MONOPULSE RADAR ANALYSIS FOR CROSS-POLARISATION JAMMING

by

Khahliso Mosoma

Submitted in partial fulfillment of the requirements for the degree

Master of Engineering (Electronic Engineering)

in the

Department of Electrical, Electronic and Computer Engineering

Faculty of Engineering, Built Environment and Information Technology

UNIVERSITY OF PRETORIA

23 November 2023

SUMMARY

MONOPULSE RADAR ANALYSIS FOR CROSS-POLARISATION JAMMING

by

Khahliso Mosoma

Supervisor:	Prof. Warren P. du Plessis
Department:	Electrical, Electronic and Computer Engineering
University:	University of Pretoria
Degree:	Master of Engineering (Electronic Engineering)
Keywords:	Angular error, co-polarisation, counter-measure, cross-polarisation, cross-polarisation Jamming, monopulse antenna, monopulse radar, monopulse ratio, polarisation purity, jammer-to-signal ratio (JSR)

Cross-polarisation jamming is an electronic attack (EA) jammer that takes advantage of the design weakness in the radar antenna. The monopulse antenna with symmetric antennas in the four quadrants and feed symmetry has Condon lobes in its cross-polarisation signal component. The peaks of the Condon lobes are in the $\pm 45^{\circ}$ and $\pm 135^{\circ}$ diagonal planes. The cross-polarisation jammer receives the tracking signal from the tracking radar, interchanges the polarisation components, and re-transmits it to the tracking radar. If the jammer has a high JSR, the tracking radar will be forced to use one of the Condon lobes as the tracking lobe.

Six monopulse antennas are analysed for cross-polarisation jamming. The jammer's effects on the radar's angle tracking accuracy are analysed as the JSR increases. How the antenna polarisation purity affects the effectiveness of cross-polarisation jamming is investigated. How the jammer polarisation inaccuracy affects its ability to induce angular tracking error is investigated. The simulated results are validated using the measurements of the manufactured antenna. The cross-polarisation jammer can induce angular tracking error but needs high polarisation accuracy. The mathematical models of the antenna cross-polarisation patterns are derived using three different approaches. These models are used to theoretically analyse cross-polarisation jamming and compare the results with the Feko simulations and measurement results..

The axial symmetry in antennas causes Condon lobes in their cross-polarisation component. Two antennas with axial symmetry will have two Condon lobes, while four antennas located in four quadrants with axial symmetry will have four Condon lobes in each quadrant. One of the six antennas was used to validate the axial-symmetry effect on the Condon lobes. The analysis shows that the antenna radiating elements must be symmetrical, and the feed network must be symmetrical to result in symmetrical Condon lobes. The size of the Condon lobes is influenced differently in different antennas. The focal-length-to-diameter (F/D) size influences the Condon lobes in the parabolic reflector antennas. To investigate the effects of F/D size on the Condon lobes, a parabolic reflector antenna with different F/D sizes is designed and analysed. The analysis shows that increasing the F/D reduces the Condon lobes and increases the polarisation purity of the antenna.

TABLE OF CONTENTS

CHAPTER 1 INTRODUCTION

1.1 PROBLEM STATEMENT

1.1.1 Context of the problem

A radar detects and acquires the position of a target in terms of range, azimuth angle, elevation angle, radial velocity, and amplitude from the received radar signal [1, 2, 3]. The radar sends an electromagnetic (EM) wave into space. Suppose a target is present; the target reflects the EM wave to the radar receiving antenna, which can be the same antenna used to transmit or a separate antenna dedicated to receiving [1]. The target skin return will be within the directional antenna beam, and the skin return will be analysed to determine the target information [1]. One of the differences among these radars is how accurately they can track a target, which depends on the antenna's beamwidth. The smaller the beamwidth, the higher the accuracy in the tracking capability [1]. Smaller beamwidth means the antenna has a narrow beamwidth in the direction of the radiation pattern [1]. The radar generates an error signal as the target deviates from the boresight (peak of the main lobe) [1]. The radar uses this error signal to track the target [1]. There are different types of radars, the difference being how they detect or track a target. A type of radar, such as a conical scanning radar, transmits many pulses to the target to achieve target tracking [1]. These radars are inaccurate because the target fluctuation results in amplitude variation from all the lobes [1].

The monopulse radar detects and tracks a target by theoretically sending a single EM pulse into space [1], [3, 4, 5, 6, 7]. If there is a target, the EM wave will reflect the target skin return [1], [3, 4, 5, 6, 7]. The sum signal is the transmitted EM pulse [1]. In a perfect target-tracking scenario, the target is at the peak of the sum signal's amplitude, and there is an alignment of the difference signal's null and the sum signal's peak amplitude [1]. This perfect alignment applies in theory. In practice, the alignment will be imperfect due to some delays in the difference channel reception of the signal containing the target information or due to tolerances. When the target shifts from its position, an error signal will be

generated from the difference signal in the elevation and azimuth planes [1], while the sum signal peak amplitude is a target reference. This error signal is used to adjust the servo system and position the antenna in the position of the target for tracking or to adjust the phase of the arrays in a phased array antenna to continue tracking the target [1], [3], [4].

Monopulse radar is a design improvement of the disadvantages of its predecessor radars. The statement does not imply that the monopulse radar does not have disadvantages. The advantage of monopulse radars is that they have fewer errors than errors caused by amplitude fluctuation in sequential lobing and conical scanning radars [1]. In a lobe-switching radar, the two lobes position the target between them while they point slightly away from the target and the lobes are switched depending on the deviation of the target. This process results in a low signal-to-noise ratio (SNR) compared to monopulse radar because the monopulse radar detects the sum signal from the target [1]. The boresight axis stability is higher in monopulse radar than in conical scanning radars because conical scan radars suffer from mechanical vibrations [1]. Monopulse radar is also preferred as it is less vulnerable to jamming than other radars because monopulse radars do not require modulation to determine direction. Other radars need modulation to determine the target direction. The modulated signal contains information such as the period and signal switching from the radar, which can be used by the jammer [1].

Antennas, including monopulse antennas, have a polarisation which can be linear, circular, or elliptic [1], [8]. In linear polarisation, the co-polarisation and cross-polarisation pattern components are present; these components are orthogonal [1], [8]. Linear polarisation is not limited to orthogonal components, i.e., 0° and 90° (horizontal and vertical), as these components can be diagonal but orthogonal. The co-polarisation and cross-polarisation patterns are the desired and undesired polarisation, respectively, and the undesired polarisation induces tracking error [1], [2].

The antenna extracts information from the sum of the two polarisation components. However, because the co-polarised component has a higher amplitude than the cross-polarised component, the target information is mainly from the component with high magnitude [1]. Cross-polarisation jammers use this antenna characteristic.

Cross-polarisation jamming is a target's EA technique to protect itself from radar [9]. This EA technique deceives the monopulse radar or any other radar by providing it with the wrong location of the target [9, 10, 11, 12]. When the location of the cross-polarisation jammer is on the target's body, it

receives the EM signal from the tracking radar. It splits the signal components into their polarisations [9], [10]. The jammer uses its two antennas to interchange the received polarisation components and re-transmit the interchanged polarisation components to the radar [9], [10], [13].

The angular error caused by the cross-polarised signal is why the cross-polarisation jammer is effective, as this signal differs from the expected co-polarised signal [14], [15]. Some antennas' co-polarisation and cross-polarisation patterns are different; the co-polarisation pattern has peaks at boresight, and the cross-polarisation patterns have peaks at $\pm 45^\circ$ and $\pm 135^\circ$ planes called Condon lobes and nulls at boresight [16], [17], [18]. The cross-polarisation jammer uses one of these Condon lobes to jam the radar. If the cross-polarisation jamming signal has high power compared to the skin return signal, it will result in the jammer forcing the radar to use the Condon lobe for tracking [10].

The problem with cross-polarisation jamming is that for it to be effective, it must have a high JSR [12], [19]. According to the literature, the cross-polarisation jammer must have a JSR of 20 to 30 dB [12], [19]. This JSR makes sense in that the cross-polarised signal produced by the jammer must be higher than the co-polarised signal expected by the tracking radar receiving antenna, and this is because all antennas attenuate cross-polarised signals to some extent. The higher JSR will result in the receiving antenna of the tracking radar analysing the cross-polarised signal, resulting in tracking error [9], [10], [14]. The purity factor (co-polarisation to cross-polarisation ratio) of the tracking radar can be a problem for the cross-polarisation jammer when the cross-polarised jamming signal is not accurate to the signal the radar is expecting; the jamming signal can act as a beacon (the jammer can assist the radar in tracking the target instead of deceiving the radar) [14], [19].

1.1.1.1 A simple scenario of a Cross-polarisation jammer

- A military base protected by a ground/land-based monostatic surveillance radar system and a ground/land-based missile system.
- The surveillance radar system uses a Cassegrain monopulse antenna.
- The surveillance radar system searches the sky for potential threat targets.
- In the sky, there is a bomber aircraft at $\sqrt{x^2+y^2}$ distance moving towards the military base.
- The bomber aircraft has a cross-polarisation jammer installed on it, which consists of a receiving antenna and a transmitting antenna.
- If the surveillance radar system detects the bomber aircraft, it communicates with the missile system and the missile system will shoot down the bomber aircraft.

- The Cassegrain monopulse antenna used by the surveillance system has a linear polarisation.
- In this case, the polarisation components of the Cassegrain monopulse antenna are transmitted vertically and horizontally.
- The surveillance system is constantly transmitting and receiving(receiving if it detects a target).
- The cross-polarisation jammer on the bomber aircraft receives a radar signal from the ground-based surveillance radar system, the received signal has both the polarisation components.
- The radar signal received by the jammer has the co-polarisation signal component as a dominant polarisation component.
- The cross-polarisation jammer re-transmit the signal back to the surveillance radar system, with signal polarisation components interchanged(the signal polarisation component received horizontally is re-transmitted as a vertical component and vice versa).
- The signal re-transmitted by the cross-polarisation jammer to the surveillance system has the cross-polarisation signal component as the dominant polarisation component.
- The cross-polarisation signal component has Condon lobes off-boresight, this characteristic will force the surveillance radar system to use one of the Condon lobes to extract target information (range, speed, and angle of arrival).
- The location information in the Condon lobes will be wrong which means the surveillance radar system will communicate incorrect target location to the missile system.
- The Surveillance radar system communicates incorrect target information to the missile system.
- Then the missile system launches missiles in the wrong target direction.
- The bomber aircraft reaches the military base and drops a bomb.
- This is a simple scenario of how a cross-polarisation jammer performs jamming.

1.1.2 Research gap

The problem to be addressed by this work is to model mathematically, and most importantly with simulations and experiments, the effect of the cross-polarised signal on the monopulse radar. Analysing the difference between the co-polarised and cross-polarised signals and the effect of the cross-polarised signal on the monopulse radar will result in the modelling of an effective cross-polarisation jamming signal. Only a little work has been done experimentally in the open literature on the effects of cross-polarised signals in the monopulse antenna and monopulse radar, focusing on cross-polarisation jamming. In [15], the monopulse radar was modelled in the presence of a cross-polarised signal but not experimentally.

It is clear that if more focus is on the monopulse radar response to a cross-polarised signal, the detailed requirements a cross-polarisation jammer must have to be effective in jamming monopulse radars can be generated. The minimum accuracy the cross-polarised jamming signal should have and the minimum JSR power needed will be determined.

The cross-polarisation patterns are used to analyse cross-polarisation jamming, however, the modelling of cross-polarisation patterns has not been given much attention. In addition to the simulation and measurement analysis, this work addresses this research gap by mathematically modelling cross-polarisation patterns and analysing cross-polarisation using the derived models.

1.2 RESEARCH OBJECTIVE AND QUESTIONS

This research aims to analyse at least two monopulse antennas and perform monopulse radar analysis based on these antennas. The behaviour of the antennas and the monopulse radar will be analysed when they receive a cross-polarised signal with different power and also at different angles within the half-power beamwidth (HPBW) and outside the HPBW, and this will also be applied using the co-polarisation signal.

- How do the antenna and the monopulse radar respond to signals with varying JSR power, and how can these responses be used to model the cross-polarisation jamming signal?
- How can the effects of the cross-polarised signal on the angular estimate in the monopulse system be used to model an effective cross-polarised jamming signal?
- What is the minimum JSR the cross-polarisation jammer must have to initiate break-lock and for successful monopulse radar jamming?

The first research question addresses the antenna and the monopulse radar because the monopulse antenna has a way of responding to the cross-polarised signal, and the monopulse radar responds by processing the signal it receives from the monopulse antenna. The type of monopulse antenna implementation influences its response to co and cross-polarised signals. How the antenna responds to the cross-polarised signal and how the monopulse radar responds to the response of the monopulse antenna must be investigated. The second research question investigates how the monopulse system interprets the cross-polarised signal. To jam the radar, the jammer deeds JSR of 25 to 30 dB [9], [10], and the third research question will investigate this range estimation.

1.3 APPROACH

At least two antennas will be analysed in transmitting and receiving modes for monopulse radar analysis. The co-polarisation and cross-polarisation signal components having various powers will be transmitted to the antennas, and monopulse processing will be applied to the signals received by the antennas. One of the antennas will be manufactured, and experiments corresponding to the simulation results will be performed to validate the theoretical analysis. After the analysis, co- and cross-polarisation monopulse antenna patterns will be modelled mathematically, and further cross-polarisation jamming analysis will be performed using the theoretical antenna pattern model.

1.4 RESEARCH GOALS

To provide detailed requirements for the cross-polarisation jamming signal to effectively induce angular error in a radar.

1.5 RESEARCH CONTRIBUTION

- The cross-polarisation sum and difference patterns are modelled, which helps analyse cross-polarisation jamming theoretically.
- Detailed requirements of a cross-polarisation jammer to successfully jam a tracking radar are presented. Specifications are reported in the literature about the minimum JSR needed for a successful cross-polarisation jamming and the polarisation accuracy specifications the jammer must have. However, there is less explanation of how these specifications were derived. This work presents the details of how these specifications were derived.
- The results show that the cross-polarisation jammer must not have a polarisation inaccuracy of more than 1°, because it loses $\approx 80\%$ of the induced angular error. The jammer induces angular error even when JSR < 0 dB. However, it breaks lock when JSR > 15 dB in the mathematically modelled analysis results and breaks lock when JSR > 30 dB in the analysed antennas.

1.6 RESEARCH OUTPUTS

1.6.1 Accepted Research Outputs

- W. P. du Plessis and K. Mosoma, “Initial results for cross-polarisation jamming of monopulse radar,” in Int. Conf. Electromagn. Adv. Appl. (ICEAA), Cape Town, South Africa, 5–9 Sep. 2022, pp. 258–263.

1.6.2 Research Output in Preparation

- K. Mosoma and W. P. du Plessis, "Modelling Cross-polarisation Patterns of Axially-symmetrical Monopulse Antennas for Cross-polarisation Jamming Analysis," IEEE Transactions on Aerospace and Electronic Systems, in preparation.

1.7 OVERVIEW OF STUDY

Chapter 2 presents the literature review, where the monopulse patterns are explained, and different types of monopulse radars, such as amplitude comparison, phase comparison, and sum-difference monopulse radars, are explained. Cross-polarisation jamming is explained, and the derivation of the minimum JSR needed by the cross-polarisation jammer to break lock is presented. Condon lobes are explained, and Ludwig's polarisation definition is presented. Chapter 3 outlines the research methodology used in the literature and shows the set-up of the simulation and experimental results. The design geometry and design parameters of the six analysed antennas are presented. Chapter 4 presents the mathematical modelling of the radiation patterns and the results of these mathematical models. The theoretical modelling of the cross-polarisation patterns is presented using three techniques, and the explanation of how the measurements and simulation experiments are investigated is outlined. Chapter Chapter 5 outlines the experimental results. The results of the wire-grid antenna, Hannan parabolic reflector antenna, Cassegrain antenna, Hannan Cassegrain antenna, Horn antenna, and aperture-coupled antenna are presented. The measurement results of the manufactured wire-grid antenna are presented. The investigated parameters are co-and-cross-polarisation patterns, monopulse ratios, polarisation purity, jammer polarisation accuracy, angular error, jamming within and outside the 3 dB beamwidth, axial symmetry effects on Condon lobes, and F/D effect on the Condon lobes size. The results are summarised and discussed in Chapter 6. The theoretical, Feko experimental, and measurement results are compared. In Chapter 7, concluding remarks are given. In Appendix A.1, the derivation of the definition of cross-polarisation is presented. In Appendix B, additional measurement results are presented.

CHAPTER 2 LITERATURE STUDY

2.1 INTRODUCTION/CHAPTER OVERVIEW/CHAPTER OBJECTIVES

This chapter presents the literature study for this dissertation. Section 2.2 discusses the amplitude and phase comparison monopulse antenna patterns. Section 2.3 discusses types of monopulse radars, Section 2.4 discusses cross-polarisation jamming, Section 2.5 presents the mathematical derivation of the minimum JSR needed to break-lock, Section 2.6 discusses the Condon lobes in monopulse antennas, and Section 2.7 discusses the antenna polarisation definitions.

2.2 MONOPULSE PATTERNS

The monopulse antenna uses two antennas to determine the target information in one plane, and other monopulse antennas use four antennas arranged in each quadrant to determine target information at both the azimuth and elevation planes. The monopulse radar uses these antennas to transmit the sum signal, which is the sum of all the signals from antennas in each quadrant and receives the signal reflected by the target in the individual antennas [20]. Figure 2.1(b) shows the radiation patterns of two antennas; the signal received in each antenna is compared using monopulse processing techniques [15]. Figures 2.1(a) and 2.1(b) show the pure amplitude comparison monopulse and pure phase comparison monopulse, respectively. In the pure amplitude comparison monopulse, the target information is within the amplitude of the patterns [15, 20, 21]. In the pure phase comparison monopulse, the information is within the phase angle of the patterns [15, 20, 21]. In the phase comparison monopulse, the antennas are separated by a distance d, resulting in each antenna having a unique phase centre. In the amplitude comparison monopulse, the antennas have equal phase centres.

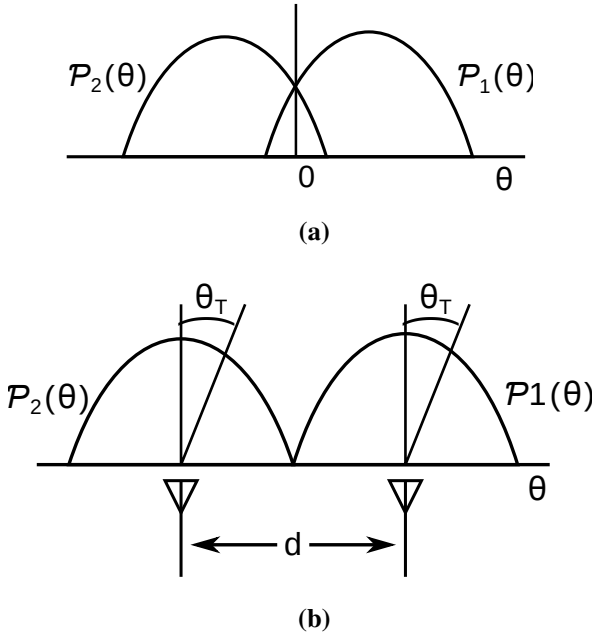

Figure 2.1. The monopulse antenna radiation pattern shows (a) the amplitude comparison monopulse and (b) the phase comparison monopulse. Taken from [15], with permission of the American Institute of Aeronautics and Astronautics, Inc.

Monopulse radar uses information from the monopulse ratio to track the target. The monopulse ratio is determined by the difference signal divided by the sum signal as follows [15, 20, 21];

$$M = \frac{P_o(\theta)}{P_e(\theta)} \tag{2.1}$$

$$= \frac{P_1(\theta) - P_2(\theta)}{P_1(\theta) + P_2(\theta)} \tag{2.2}$$

$$= \frac{\Delta(\theta)}{\Sigma(\theta)} \tag{2.3}$$

where P_o is the odd function formed by the difference of $P_1(\theta)$ and $P_2(\theta)$. The $P_e(\theta)$ is the even function formed by the sum of $P_1(\theta)$ and $P_2(\theta)$ patterns. The antenna patterns in Figure 2.1 are represented by [15, 20, 21]

$$P_1 = P(\theta)e^{j\varphi(\theta)} \tag{2.4}$$

$$P_1 = P(-\theta)e^{j\varphi(-\theta)} \tag{2.5}$$

$$= P_1(-\theta) \tag{2.6}$$

where the real magnitude and real phase of the radiation pattern are represented by $P(\theta)$ and $\varphi(\theta)$ respectively [21]. For a pure amplitude comparison monopulse, the antennas have equal phase centre

$\varphi(\theta) = \varphi(-\theta)$, as shown in Figure 2.1(a); this results in a monopulse ratio as follows [20], [21]:

$$M_a = \frac{P(\theta) - P(-\theta)}{P(\theta) + P(-\theta)} \tag{2.7}$$

$$= \frac{P_o(\theta)}{P_e(\theta)} \tag{2.8}$$

where the odd and even amplitude are given by $P_o(\theta)$ and $P_e(\theta)$ respectively [21]. In the case of the pure amplitude monopulse comparison, the radiation pattern amplitude of the antennas is equal due to the symmetry of the antennas $P(\theta) = P(-\theta)$ as shown in Figure 2.1(b), this results in a monopulse ratio as follows [20], [21]

$$M_p = \frac{e^{j\varphi(\theta)} - e^{j\varphi(-\theta)}}{e^{j\varphi(\theta)} + e^{j\varphi(-\theta)}} \tag{2.9}$$

$$= j\tan[\varphi_o(\theta)]. \tag{2.10}$$

The phase difference of the antennas is

$$\varphi(\theta) = \beta \cdot \frac{d}{2} \cdot \sin(\theta) \tag{2.11}$$

and d is the distance between the antennas, β is the free space propagation constant, and θ is the angle of arrival (AOA) with respect to the antenna pattern boresight [21].

2.3 TYPES OF MONOPULSE RADARS

The error voltage is used in monopulse radars to determine the angle of the incidence with respect to the axis of the radar [1], [15]. This section derives the error voltage from amplitude-sensing monopulse, phase-sensing monopulse, and sum-difference monopulse models. The difference between the amplitude and phase sensing monopulse was described in Section 2.2, but it is briefly mentioned in this section for the derivations. Figure 2.2 shows two antennas with patterns squinted to a θ_S, and the incidence wave reflected by the target is at an angle of θ_T. To get a phase-sensing monopulse, the squint angle must be 0°, resulting in the patterns having equal amplitudes, and the incidence wave angle information will be in the phase difference between (2.12) and (2.13) voltages [15]. To get the amplitude-sensing monopulse, the distance between the antennas must be zero, which means the target incidence wave angle is within the amplitudes of the following voltages [15].

$$v_1 = A \cdot g(\theta_s - \theta_T)\cos(\omega t + \phi), \tag{2.12}$$

$$v_2 = A \cdot g(\theta_s + \theta_T)\cos(\omega t - \phi) \tag{2.13}$$

where A is the signal amplitude, ϕ is the phase difference between the signals, and ω is the incidence wave signal radiant frequency [15].

2.3.1 Amplitude sensing monopulse

Figure 2.3 shows the amplitude-sensing monopulse radar. The radar receives two voltage signals as

$$v_1 = A \cdot g(\theta_s - \theta_T)\cos(\omega t), \tag{2.14}$$

$$v_2 = A \cdot g(\theta_s + \theta_T)\cos(\omega t) \tag{2.15}$$

where θ_s and θ_T are the squint angle and the target AOA, respectively. With the $\phi = 0^\circ$ as the antennas have zero separation, an envelope detector and a low-pass (LP) filter are applied to both the signals, and their difference forms the error signal as

$$\varepsilon = \log|v_1|_{LP} - \log|v_2|_{LP} \tag{2.16}$$

$$= \log\left|\frac{v_1}{v_2}\right|_{LP}. \tag{2.17}$$

It is unlikely to find two antennas having equal amplitude gain. Therefore, the signal after envelope detection and low-pass filtering can be linearly approximated as

$$|v_1|_{LP} = A \cdot g(\theta_s - \theta_T) \tag{2.18}$$

$$\approx g_o \cdot A(1 + k\theta_T), \tag{2.19}$$

$$|v_2|_{LP} = g_o \cdot A(1 - k\theta_T) \tag{2.20}$$

which results in an error voltage of

$$\varepsilon = \log\left(\frac{1 + k\theta_T}{1 - k\theta_T}\right) \tag{2.21}$$

$$\approx \log(1 - 2k\theta_T) \tag{2.22}$$

$$\approx \left(\frac{2k}{2.3}\theta_T\right). \tag{2.23}$$

2.3.2 Phase sensing monopulse

Figure 2.4 shows the phase-sensing monopulse radar; the antennas are separated by d and have zero squint angle. The following voltages

$$v_1 = A \cdot \cos(\omega t + \phi), \tag{2.24}$$

$$v_2 = A \cdot \cos(\omega t - \phi) \tag{2.25}$$

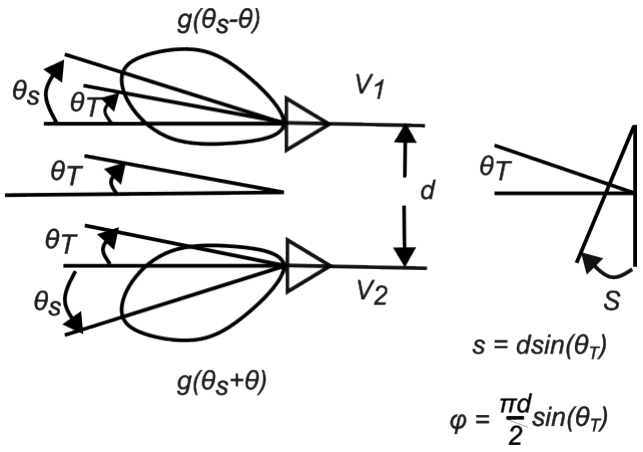

Figure 2.2. The monopulse configured antennas in one tracking plane. Taken from [15], with permission of the American Institute of Aeronautics and Astronautics, Inc.

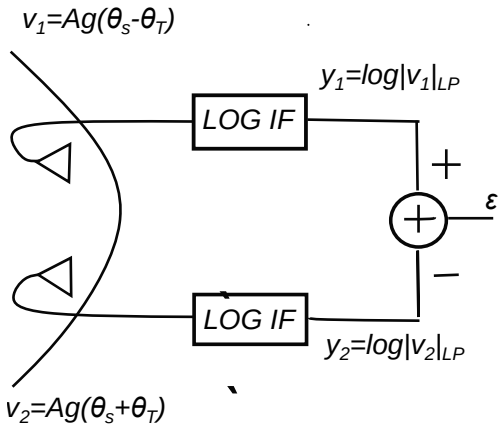

Figure 2.3. The amplitude sensing monopulse radar. Taken from [15], with permission of the American Institute of Aeronautics and Astronautics, Inc.

are received by the two antennas, and after the phase detector and phase shifting, the resulting signals are

$$y_1 = \sqrt{2}\cdot\cos(\omega t + \phi), \tag{2.26}$$

$$y_2 = \sqrt{2}\cdot\cos\left(\omega t - \phi - \frac{\pi}{2}\right) \tag{2.27}$$

$$= \sqrt{2}\sin(\omega t - \phi). \tag{2.28}$$

The (2.26) and (2.28) are multiplied, and the low-pass filter is applied to the product of the two signals to get the error voltage as

$$y_3 = y_1 \cdot y_2 \tag{2.29}$$

$$= \sin(2\omega t) + \sin(-2\phi), \tag{2.30}$$

$$\varepsilon = (y_3)_{LP} \tag{2.31}$$

$$= -\sin(2\phi) \tag{2.32}$$

$$\approx -2\phi \tag{2.33}$$

$$\approx -k \cdot d \cdot \theta_T. \tag{2.34}$$

The practical system will have some errors, and for this phase-sensing monopulse, the error can be a phase error ξ resulting from the phase shifters or other subsystems, which will result in the y_1 and y_2 as

$$y_1 = \sqrt{2}\cos(\omega t + \phi), \tag{2.35}$$

$$y_2 = \sqrt{2}\cos\left(\omega t - \phi - \frac{\pi}{2} - \xi\right) \tag{2.36}$$

and the error voltages as

$$y_3 = 2\sin(\omega t - \phi - \xi)\cos(\omega t - \phi) \tag{2.37}$$

$$= \sin(2\omega t - \xi) + \sin(-2\phi - \xi), \tag{2.38}$$

$$\varepsilon = (y_3)_{LP} \tag{2.39}$$

$$= \sin(-2\phi - \xi). \tag{2.40}$$

and when the servo system receives the error voltage it will stop when

$$2\phi = k \cdot d \cdot \sin(\theta_T) \tag{2.41}$$

$$= -\xi \tag{2.42}$$

resulting in a bias error of

$$-\theta_T = \arcsin\left(\frac{\xi}{kd}\right) \tag{2.43}$$

2.3.3 Sum-difference monopulse

The amplitude and phase comparison monopulse were explained in Sections 2.3.1 and 2.3.2, and now a sum-difference monopulse model is presented. Figure 2.5 shows the sum-difference monopulse radar [15]. The error voltage is derived using the radar model in Figure 2.5 to derive cross-polarisation

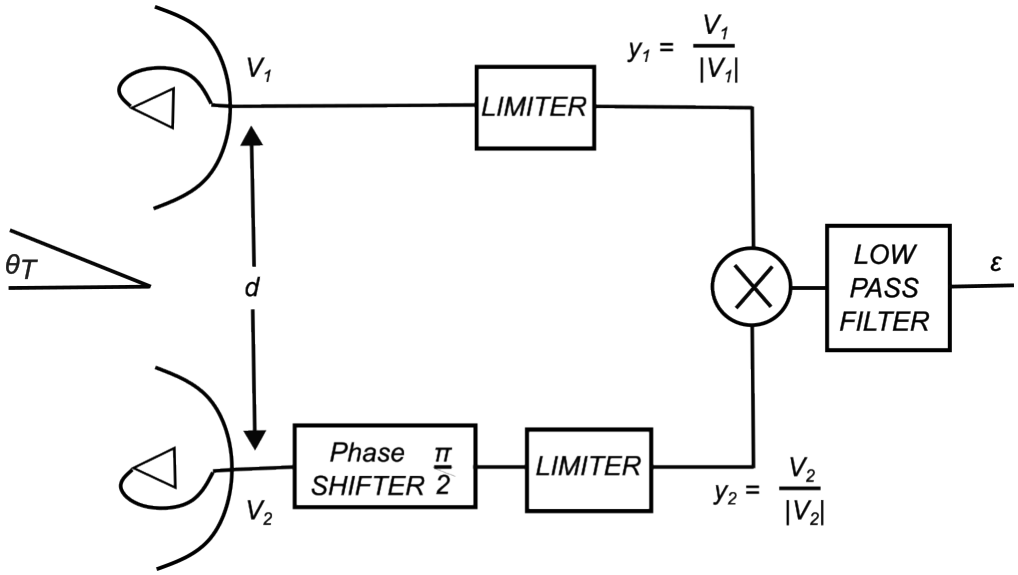

Figure 2.4. The Phase sensing monopulse radar.Taken from [15], with permission of the American Institute of Aeronautics and Astronautics, Inc.

jamming. This model can be converted to amplitude or phase monopulse radar. To convert Figure 2.5 to phase sensing monopulse, $\theta_s = 0$, $\psi_o = \pi/2$, and $d \neq 0$ [15]. For amplitude comparison, $\theta_s \neq 0$, $\psi_o = 0$, and $d = 0$ [15]. In either condition, the model will also work as a sum-difference monopulse [15]. Now, using Figure 2.5 to determine voltage error, the two antennas receive the following voltage signals

$$\upsilon_{\Sigma i} = \upsilon_1 \pm \upsilon_2 \tag{2.44}$$

$$= A \cdot [g(\theta_s - \theta_T) \cdot \cos(\omega t + \varphi) \pm g(\theta_s + \theta_T) \cdot \cos(\omega t - \varphi)] \tag{2.45}$$

where $\varphi = k \cdot d \cdot \sin(\theta_T)$ and $(k = 2\pi/\lambda)$ [15]. Now, using complex notation, the signals received at each antenna are

$$\upsilon_1 = \Re\left(V_1 e^{j\omega t}\right) \tag{2.46}$$

$$V_1 = A \cdot g(\theta_s - \theta_T) e^{j\omega} \tag{2.47}$$

$$= A \cdot g_1 \cdot e^{j\omega} \tag{2.48}$$

$$\upsilon_2 = \Re\left(V_2 e^{j\omega t}\right) \tag{2.49}$$

$$V_2 = A \cdot g_2 \cdot e^{-j\omega}. \tag{2.50}$$

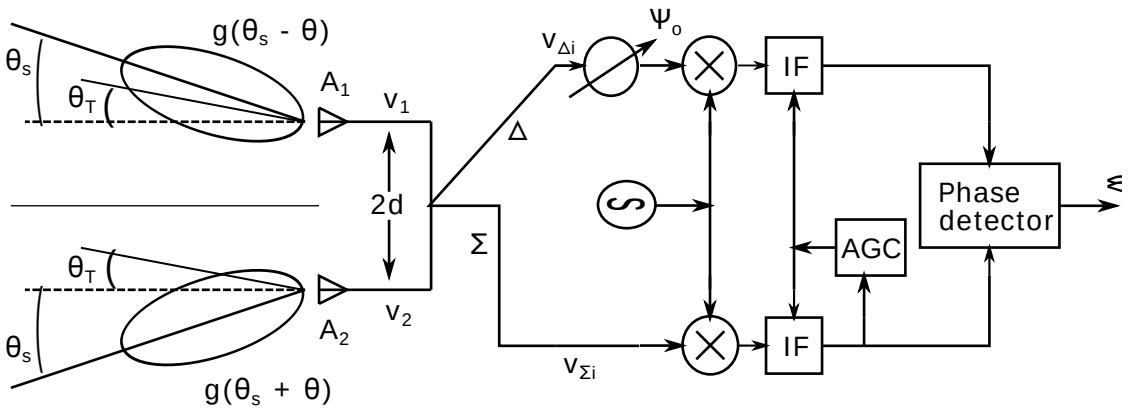

Figure 2.5. The sum-difference monopulse radar. Taken from [15], with permission of the American Institute of Aeronautics and Astronautics, Inc.

The sum voltage signal at the output of the intermediate frequency (IF) amplify is

$$V_{\Sigma o} = K_{\Sigma}(V_1 + V2) \tag{2.51}$$

$$= K_{\Sigma} \cdot A \left(g_1 \cdot e^{j\omega} + g_2 \cdot e^{-j\varphi}\right), \tag{2.52}$$

and the difference signal at the output of the IF amplifier is

$$V_{\Delta o} = e^{j\psi_o^{'}} \cdot K_{\Delta} \cdot (V_1 - V2) \tag{2.53}$$

$$= K_{\Delta} \cdot A \left(g_1 \cdot e^{j\omega} - g_2 \cdot e^{-j\varphi}\right) e^{j\psi_o^{'}} \tag{2.54}$$

where $\psi_o^{'} = \psi_o + \varphi_{\Sigma} - \varphi_{\Delta}$, ψ_o is shown in Figure 2.5 as the phase shift in the difference channel [15]. Assuming that the phase of the IF channel is matched, $\varphi_{\Delta} = \varphi_{\sigma}$ [15]. The automatic gain control shows the relationship between the input sum voltage and the gain of the IF amplifier as

$$K_{\Sigma} = K_{\Delta} \tag{2.55}$$

$$= \frac{K_o}{1 + \alpha \cdot k_g |\upsilon_{\Sigma i}|}. \tag{2.56}$$

The instantaneous voltage at the IF amplifier output is

$$V_{\Sigma i} = \Re\{A \left(g_1 \cdot e^{j\varphi} + g_2 \cdot e^{-j\varphi}\right) e^{j\omega_{IF}(t)}\}, \tag{2.57}$$

$$|V_{\Sigma i}| = A|g_1 \cdot e^{j\varphi} + g_2 \cdot e^{-j\varphi}| \tag{2.58}$$

and the patterns are given by

$$g_1 = g(\theta_s - \theta_T), \tag{2.59}$$

$$g_2 = g(\theta_s + \theta_T) \tag{2.60}$$

and the magnitude of the IF amplifier voltage is

$$|V_{\Sigma i}| = A\sqrt{g_1^2 + g_2^2 + 2 \cdot g_1 \cdot g_2 \cdot \cos(2\varphi)}. \tag{2.61}$$

The IF amplifier voltage output is passed through a low-pass filter and then through the phase detector, and the voltage error at the output of the phase detector is

$$\varepsilon = \frac{1}{2}\Re\{V_{\Sigma o} \cdot V_{\Delta o}^*\} \tag{2.62}$$

$$\varepsilon = \frac{A^2 \cdot K_\Sigma^2}{2} \cdot \Re\left\{\left(g_1 \cdot e^{j\varphi} + g_2 \cdot e^{-j\varphi}\right)\left(g_1 \cdot e^{-j(\varphi-\psi)} + g_2 \cdot e^{-j(\varphi-\psi)}\right)\right\} \tag{2.63}$$

$$= \frac{A^2 \cdot K_\Sigma^2}{2} \cdot [(g_1^2 - g_2^2)\cos(\psi_o) + 2 \cdot g_1 \cdot g_2 \cdot \sin(2\varphi)\sin(\psi_o)]. \tag{2.64}$$

Now, substituting (2.57) into (2.56) and then the resulting equation into (2.64), the error voltage is

$$\varepsilon = \frac{A^2 \cdot K_o^2}{2} \cdot \frac{(g_1^2 - g_2^2)\cos(\psi_o) + 2 \cdot g_1 \cdot g_2 \cdot \sin(2\varphi)\sin(\psi_o)}{\left[1 + \alpha \cdot k_g \cdot A \cdot \sqrt{g_1^2 + g_2^2 + 2 \cdot g_1 \cdot g_2 \cdot \cos(2\varphi)}\right]^2}. \tag{2.65}$$

Now, for the condition of amplitude comparison, $\varphi = \psi_o = 0$, the error voltage is

$$\varepsilon = \frac{\frac{A^2 \cdot K_o^2}{2}(g_1^2 - g_2^2)}{[1 + \alpha \cdot k_g \cdot A \cdot (g_1 + g_2)]^2} \tag{2.66}$$

where

$$\mu = \alpha \cdot k_g \cdot A \tag{2.67}$$

$$K_{pd} = \frac{A^2 \cdot K_o^2}{2\mu^2} \tag{2.68}$$

$$= \frac{K_o^2}{2\mu^2 \cdot k_2^2}. \tag{2.69}$$

The voltage error is

$$\varepsilon = \frac{\mu^2 \cdot K_{pd} \cdot (g_1^2 - g_2^2)}{[1 + \mu \cdot (g_1 + g_2)]^2} \tag{2.70}$$

$$\varepsilon = K_{pd} \cdot \left(\frac{g_1^2 - g_2^2}{g_1^2 + g_2^2}\right). \tag{2.71}$$

2.4 CROSS-POLARISATION JAMMING

Cross-polarisation is an angle deception electronic countermeasure (ECM) that receives a signal from the tracking radar and interchanges the polarisation of the tracking radar signal and re-transmit it back to the radar, causing an angular error [9], [22], [23]. Antennas can be designed for linear, circular, and elliptic polarisation. The linear polarisation will be used to explain cross-polarisation jamming as the antennas that will be analysed are linearly polarised. Figure 2.6 shows cross-polarisation jamming; the radar signal contains two polarisation components. The cross-polarisation jammer has two receiving

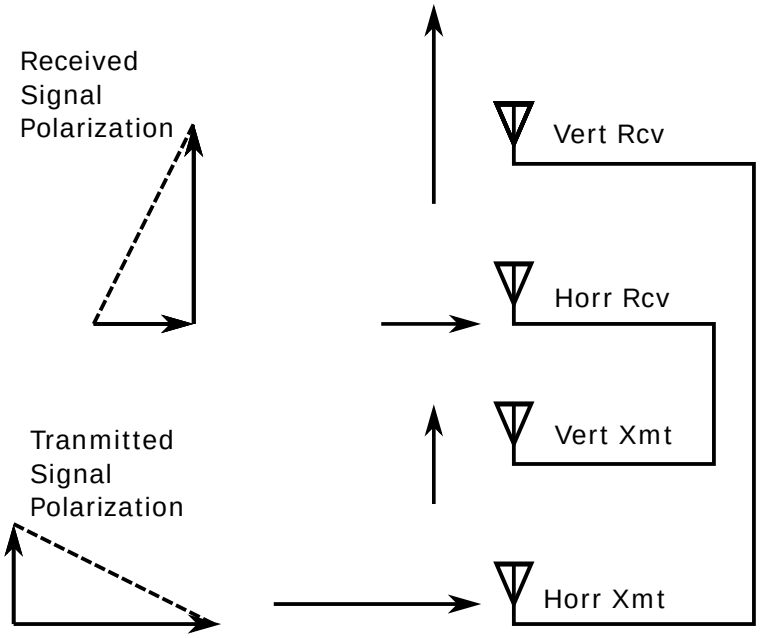

Figure 2.6. In cross-polarisation jamming, the received signal is split into the co-polarised and cross-polarised components and re-transmitted back to the radar with interchanged polarisation components. Taken from [9], with permission of Artech House Inc.

antennas that receive the tracking radar signals. They re-transmit the signal received horizontally as a vertical signal component. The signal received vertically is re-transmitted horizontally. These components will form a cross-polarised jamming signal [22]. When the tracking radar receives the cross-polarised jamming signal, it will be forced to use one of the Condon lobes to track the target, and this target will be at the wrong location [9]. The cross-polarisation jammer must have at least 20 dB to 40 dB to be able to induce angular error into the tracking radar [9], [19], [22], [24], [25]. The cross-polarisation jammer must have high polarisation sensitivity. It must sense the received signal polarisation within $\pm 5^\circ$ [24]. The cross-polarisation jammer must have a JSR more significant than the polarisation purity of the tracking radar antenna as [23]

$$\frac{J}{S} \approx \frac{J_x}{S} > \rho_R \tag{2.72}$$

where J is the jamming signal, and it is approximately equal to J_x, S is the radar skin return, and ρ_R is the radar polarisation purity. The cross-polarisation jammer must also have a polarisation purity greater than the polarisation purity of the antenna [23]

$$\rho_J = \frac{J_x}{J_0} > \rho_R. \tag{2.73}$$

2.5 DERIVING MINIMUM JSR TO BREAK-LOCK IN MONOPULSE RADAR DUE TO CROSS-POLARISATION JAMMING

Designing a jamming system requires an understanding of the system to be jammed, especially in a cross-polarisation jamming system, as this deception jamming method uses the same type of signal the victim radar expects to jam the victim. To analyze and design a cross-polarisation jammer, it is essential to understand the difference between the co-polarisation and cross-polarisation signal components. These differences must be investigated experimentally and theoretically to assist in modelling the response of the monopulse radar when it receives a cross-polarised signal. It is well known that the cross-polarised signal component induces an angular error [10], [15]. However, there are few details on how this characteristic can be used to model an effective cross-polarisation jammer. Therefore, it is essential to know the properties that the jammer must have to break lock. Figure 2.5 shows the sum-difference monopulse radar model and the voltage error resulting from the incident wave received in the antenna receiver. Figure 2.5 is the base model used to derive the model of the monopulse radar response to an incident wave containing both the co-polarised and cross-polarised signal components. When an antenna receives an incident wave, it will radiate its radiation pattern in the direction of the incident wave [15]. In a monopulse antenna, the antenna will radiate the sum signal in the direction of the incident wave. The output voltage of an antenna is represented by

$$V_{oc} = K_1 \cdot \bar{\boldsymbol{E}}_{in} \cdot \bar{\boldsymbol{E}}_a, \tag{2.74}$$

where $\bar{\boldsymbol{E}}_{in}$ is the incident wave while $\bar{\boldsymbol{E}}_a$ is the antenna radiation field in the direction of the incident wave $\bar{\boldsymbol{E}}_{in}$. The output voltage in (2.74) must be divided into the sum and difference voltage components, as a monopulse radar uses both the sum and difference radiation patterns [15]. The voltage components are passed through the IF amplifiers, and then the outputs of the IF amplifiers are the inputs to the phase detector. The phase detector output is as follows

$$\varepsilon_{az} = \frac{1}{2} \cdot \Re\{V_{\Sigma o} \cdot V_{\Delta o}^*\}, \tag{2.75}$$

where $V_{\Sigma o}$ and $V_{\Delta o}^*$ are the sum and difference voltages to the angle error detector, respectively. One of the functions of the automatic gain control is to create independence between the error voltage and the amplitude of the target, and the derived voltage error is as follows

$$\varepsilon_{az} = K_1 \cdot \Re\left\{ \left(\frac{V_\Delta \cdot \bar{E}_{in}}{V_\Sigma \cdot \bar{E}_{in}} \right)^* \right\}. \tag{2.76}$$

The incident EM signal mentioned in (2.74) can be divided into the co-polarised and cross-polarised signal components as $\bar{\boldsymbol{E}}_{in} = \bar{\boldsymbol{E}}_p + \bar{\boldsymbol{E}}_n = E_p \hat{\boldsymbol{e}}_p^* + E_n \hat{\boldsymbol{e}}_n^*$, where $\bar{\boldsymbol{E}}_p = E_p \hat{\boldsymbol{e}}_p^*$ and $\bar{\boldsymbol{E}}_n = E_n \hat{\boldsymbol{e}}_n^*$ are the cross-polarised and co-polarised signal components of the incident wave $\bar{\boldsymbol{E}}_{in}$ respectively. The nominal

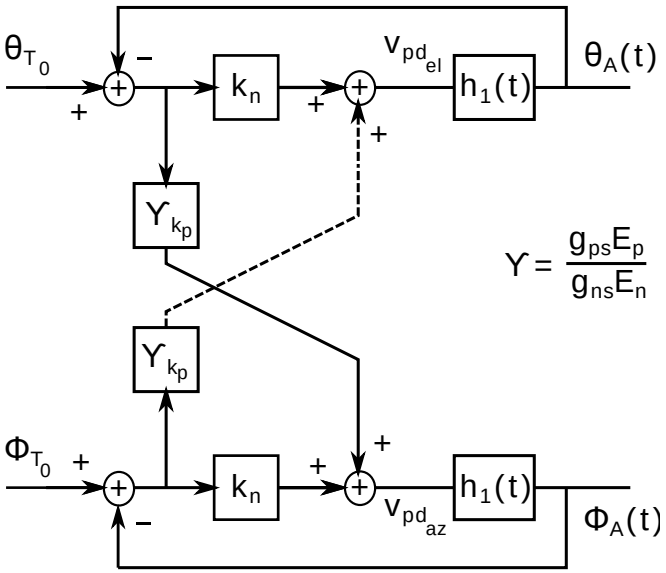

Figure 2.7. The model of a monopulse radar as it receives the incident wave having co-polarised and cross-polarised components. Taken from [15], with permission of the American Institute of Aeronautics and Astronautics, Inc.

components $\hat{\boldsymbol{e}}_p^*$ and $\hat{\boldsymbol{e}}_n^*$ are used to decompose $\bar{\boldsymbol{E}}_{in}$ into cross-polarised and co-polarised signal components respectively, and it must be noted that the time-varying component is omitted [15]. The monopulse radar model in Figure 2.7 is used to derive the azimuth and elevation errors as

$$\varepsilon_{az} = k_n \cdot \phi + k_p \cdot \Re\left\{\frac{g_{p_s} \cdot E_p}{g_{n_s} \cdot E_n}\right\}\theta, \tag{2.77}$$

$$\varepsilon_{el} = k_n \cdot \theta + k_p \cdot \Re\left\{\frac{g_{p_s} \cdot E_p}{g_{n_s} \cdot E_n}\right\}\phi \tag{2.78}$$

respectively. The components k_p and k_n are real constants for the cross-polarised and co-polarised components, respectively, ϕ is the angle of the plane and θ is the off-boresight angle, g_{n_s} and g_{p_s} are the co-polarised and cross-polarised radiation patterns, respectively. The monopulse radar model in Figure 2.7 is uncoupled in Figure 2.8. The uncoupled model is used to derive

$$S_{1,2} = -\frac{(\omega_1 + \lambda_i \cdot K) \pm \sqrt{\omega_1^2 + 2 \cdot \lambda_i \cdot K(\omega_1 - 2\omega_2) + \lambda_i^2 \cdot K^2}}{2}, \tag{2.79}$$

which is used to determine the stability of the servo system [15]. Figure 2.7 measures the input target angular position and the radar boresight angles relative to a fixed angle [15]. The instability results if there is a positive real part in the roots of (2.79) [15]. From (2.79), it is evident that deriving the effects of the cross-polarised signal on the monopulse radar will allow the modelling of an effective

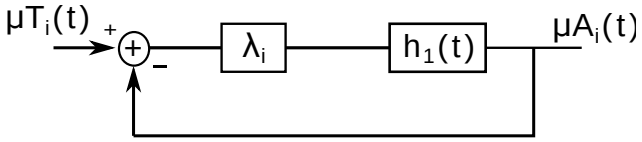

Figure 2.8. Uncoupled monopulse model. Taken from [15], with permission of the American Institute of Aeronautics and Astronautics, Inc.

cross-polarised jamming signal. The JSR is given by

$$\frac{J}{S} = \left|\Re\{\frac{E_p}{E_n}\}\right|^2 > \left(\frac{K_n \cdot g_{n_s}}{k_p \cdot g_{p_s}}\right)^2, \tag{2.80}$$

which determines the minimum JSR to initiate break-lock.

2.6 CONDON LOBES

The antenna's co-polarisation and cross-polarisation radiation pattern must be discussed before cross-polarisation jamming can be analysed. Figure 2.9(a) shows the co-polarisation and cross-polarisation of the sum and difference signal in both azimuth and elevation planes. Figure 2.9(a) shows that the co-polarisation and cross-polarisation patterns are different in the sum signal; the co-polarisation has a peak on the axis while the cross-polarisation has nulls on the axis. The nulls on the axis are caused by the axial symmetry of the antenna [26]. The antenna has four horn antennas in each quadrant, which are anti-phase to each other and result in cross-polarisation cancellation along the axis [26]. With the cross-polarisation sum pattern having nulls on the axis, they also have peaks off-axis at $\pm$ 45° planes called Condon lobes, as seen in Figure 2.9(a) [16], [17], [18], [23], [27]. In parabolic reflector antennas, the Condon lobes can be reduced by increasing the F/D ratio, and they also increase with decreasing F/D ratio [16, 17, 18]. In most antennas, the Condon lobes are less than -20 dB normalised to the co-polarisation radiation pattern [18]. The Condon lobes are not only in parabolic reflector antennas; they are seen in planar array antennas [28, Fig. 4], which shows the Condon lobes formed in the cross-polarisation pattern of the wire-grid antenna.

Figures 2.9(b) and 2.9(c) show the azimuth difference signal and elevation difference signal, respectively. The difference signal cross-polarisation pattern in the azimuth plane looks like the main lobes of the co-polarisation elevation difference signal, while the difference signal cross-polarisation in the elevation plane looks like the main lobe for the difference signal co-polarisation in the azimuth plane.

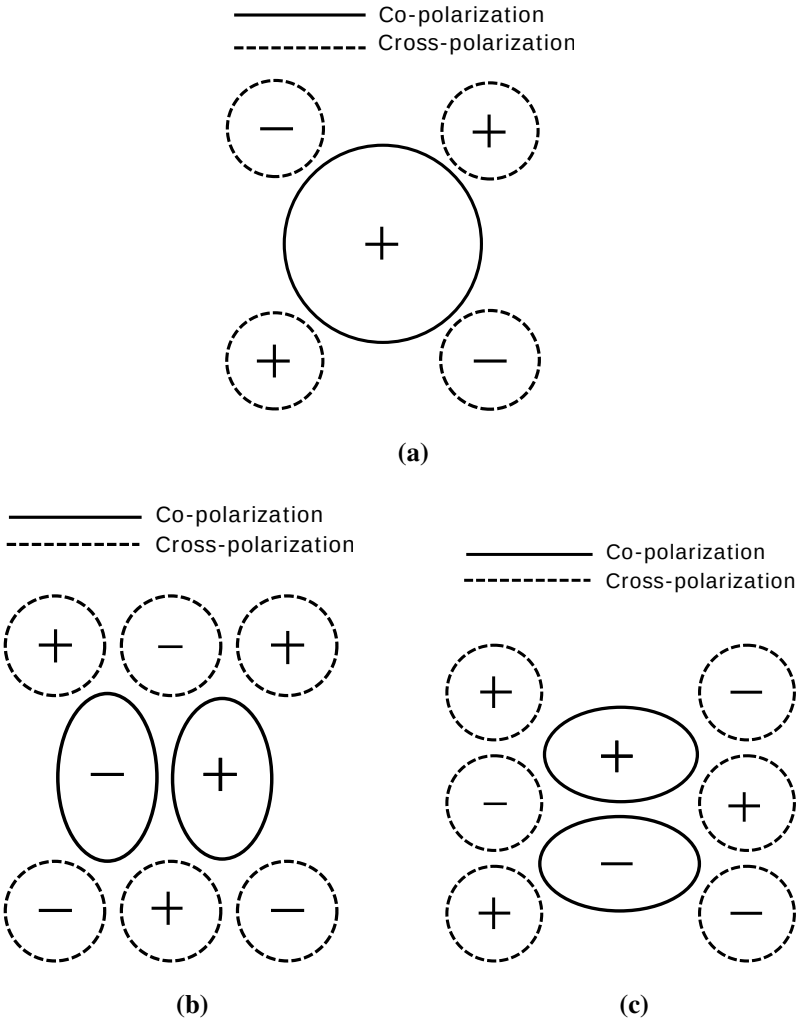

Figure 2.9. The radiation pattern of the monopulse antenna showing the co-polarisation and cross-polarisation of the (a) the sum signal, (b) the azimuth difference signal, and (c) the elevation difference signal. Taken from [16], ©1980 IEEE

2.7 LUDWID POLARISATION DEFINITION

Dr Ludwig formulated three definitions for polarisation, and the polarisation directions in definition 1 are

$$\boldsymbol{i}_C \equiv \hat{\boldsymbol{y}}, \tag{2.81}$$

$$\boldsymbol{i}_X \equiv \hat{\boldsymbol{x}}. \tag{2.82}$$

where $\boldsymbol{i}_C$ and $\boldsymbol{i}_X$ are the co and cross-polarisation components, respectively. Definition 1 defines polarisation in a two-dimensional plane as shown in Figures 2.10(a) and 2.10(d). If the co-polarisation

is along the x-axis, then the cross-polarisation is along the y-axis [29]. The polarisation definition 2 is

$$\boldsymbol{i}_C = \frac{\sin(\phi)\cos(\theta)\hat{\boldsymbol{\theta}} + \cos(\phi)\hat{\boldsymbol{\phi}}}{\sqrt{1-\sin^2(\theta)\sin^2(\phi)}} \tag{2.83}$$

$$\boldsymbol{i}_X = \frac{\cos(\phi)\hat{\boldsymbol{\theta}} - \sin(\phi)\cos(\theta)\hat{\boldsymbol{\phi}}}{\sqrt{1-\sin^2(\theta)\sin^2(\phi)}}, \tag{2.84}$$

where θ and ϕ are the directions of the radiation pattern [29]. Definition 2 considers the spherical coordinates representing how radiation patterns are distributed. Polarisation definition 3 is

$$\boldsymbol{i}_C = \sin(\phi)\hat{\boldsymbol{\theta}} + \cos(\phi)\hat{\boldsymbol{\phi}} \tag{2.85}$$

$$\boldsymbol{i}_X = \cos(\phi)\hat{\boldsymbol{\theta}} - \sin(\phi)\hat{\boldsymbol{\phi}}, \tag{2.86}$$

Definition 2 and 3 are shown in Figures 2.10(b) , 2.10(e) and Figures 2.10(c) , 2.10(f) respectively. They both represent the radiation pattern reality, and Dr Ludwig concluded that definition 3 represents antenna radiation pattern polarisation better than definitions 1 and 2. The detailed polarisation definition derivation is presented in Appendix A.1 in the Appendix.

2.8 CHAPTER SUMMARY

The success of Cross-polarisation jamming depends on the weakness of a tracking radar. The tracking radars that do not have cross-polarisation counselling techniques and have Condon lobes in their cross-polarisation components are vulnerable to cross-polarisation jamming. There are different types of monopulse radars, such as amplitude-comparison monopulse, phase-comparison monopulse, and sum-difference monopulse radars, and which one to use depends on the application and preference. There are also different ways to perform monopulse processing. Analysing the effectiveness of the cross-polarisation jamming on a monopulse radar requires understanding the monopulse antenna, monopulse radar, and monopulse radar processing. The definition of cross-polarisation must be understood for one, two, and three dimensions.

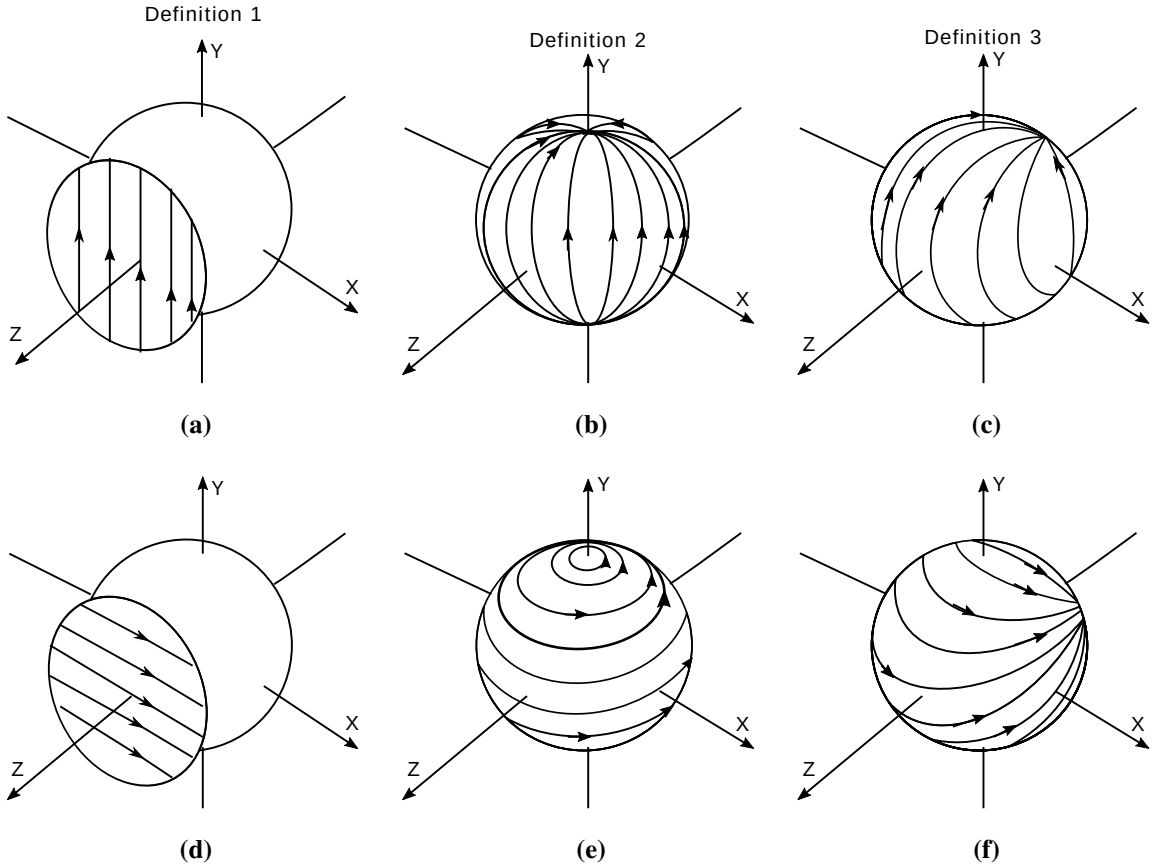

Figure 2.10. The polarisation definitions (a), (b), and (c) are the co-polarisation distribution and (d), (e), and (f) are the cross-polarisation distribution. Moreover, (a) and (d) are polarisation distributions for definition 1, (b) and (e) are polarisation distributions for definition 2, and (c) and (f) are polarisation distributions for definition 3. Taken from [29], ©1973 IEEE.

CHAPTER 3 METHODS

3.1 CHAPTER OVERVIEW

This chapter presents the research methods used in the literature and methods used in this dissertation. Section 3.2 discusses cross-polarisation research methods used in the literature. Section 3.3 discusses the cross-polarisation research methods used in this dissertation and the types of monopulse antennas analysed.

3.2 RESEARCH METHODS USED IN LITERATURE

There has been little work published on cross-polarisation jamming. Therefore, few methods are used to analyse cross-polarisation jamming, and most use mathematical modelling. In [30], the cross-polarisation jamming is analysed mathematically for phase comparison monopulse radar. In this paper, the co-polarisation and cross-polarisation models are mathematically modelled. The cross-polarisation phase patterns are randomly chosen and kept constant throughout the paper [30]. There are limited detailed mathematical models for both the sum and difference cross-polarisation phase patterns, which explains why the authors used random values for the cross-polarisation phase patterns. However, the paper does not give these random cross-polarisation phase values mentioned. The cross-polarisation jamming model introduced angular error into the radar model as the cross-polarisation jamming power was increased. The relationship between the SNR and the angular root-mean-square-error (RMSE) was analysed, which shows that when the tracking radar SNR is low, the tracking error is high even without the jammer and the cross-polarisation jammer does not make a difference. However, when the tracking radar SNR is high, the tracking error is low but increases as the cross-polarisation jammer is introduced [30]. The use of random phase values in this paper limits the analysis. There is a need to model the cross-polarisation patterns for both the sum and difference channels of a monopulse radar for analysing cross-polarisation jamming.

In [31], the same authors of [30] are mathematically analysing the performance of a polarimetric fusion monopulse radar in the presence of cross-polarisation jamming. The focus of the polarimetric fusion in this paper is to improve the radar's anti-jamming. It was concluded that the monopulse radar that uses polarimetric fusion is insensitive to cross-polarisation jamming. The cross-polarisation jammer does introduce angular error, but it is not significant; the random phase patterns are still used for the cross-polarisation components of the monopulse radar. In [13], an unmanned aerial Vehicle (UAV) model is simulated in CST microwave simulation software; two antennas are attached to the UAV model as receiving and transmitting antennas. The received signal is re-transmitted back to the monopulse radar for jamming. The authors are investigating if the cross-polarisation jammer is effective outside the radar HPBW. The results show that the cross-polarisation jamming is effective outside the radar HPBW [13].

3.3 RESEARCH METHODS USED IN THIS DOCUMENT

1. Investigate the sum and difference radiation pattern response of the monopulse antenna when it receives an incident wave with a co-polarised and cross-polarised signal with varying JSR power.
2. Investigate the monopulse ratio pattern response of a monopulse radar when it receives an incident wave with a co-polarised and cross-polarised signal with varying JSR power.
3. After the monopulse radar and antenna model patterns in the presence of co-polarised and cross-polarised signal components are understood, the cross-polarised signal pattern is modelled in Chapter 4, and further cross-polarisation jamming is performed using the new theoretical models.
4. Analyse the effects of the tracking radar polarisation purity on the effectiveness of the cross-polarisation jammer.
5. Analyse the relationship between JSR and the angular error.
6. Analyse the effects of the polarisation accuracy and polarisation inaccuracy of the jamming signal on the tracking radar accuracy.

3.3.1 Experiments and Simulations Set-up

Figure 3.1 shows the simulation setup of the antenna and the plane-wave signal in the FEKO EM software. The plane wave signal is used as a jamming signal and also as the target skin return. The four horn antennas in Figure 3.1 form a monopulse antenna that can track in both azimuth and elevation planes. Before diving into the measurement setup, it is essential to show the cross-polarisation jamming

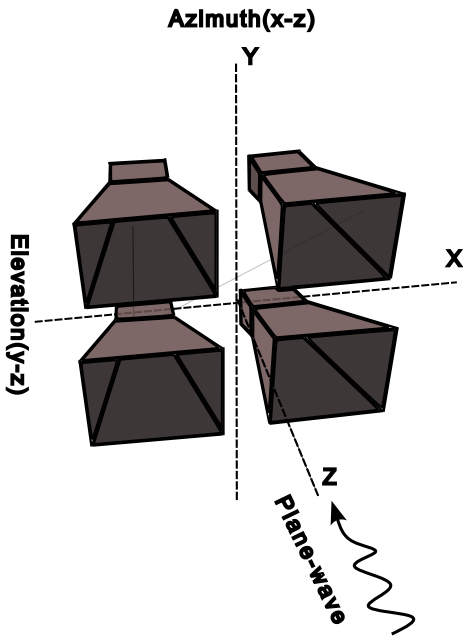

Figure 3.1. The FEKO simulation setup shows the plane wave signal transmitted to the antenna, which has four antenna elements forming a monopulse antenna.

setup. Figure 3.2 shows the cross-polarisation jamming setup with two antennas, one as the cross-polarisation jammer and the other as the tracking antenna. Instead of having two antennas for jamming, one antenna will be used. These antennas will transmit polarisation components interchangeably to the tracking radar antenna to demonstrate cross-polarisation jamming.

The measurement setup for the analysis in the anechoic chamber is shown in Figure 3.3, and the resources shown in Figure 3.3 are available at the Center for Electromagnetism at the University of Pretoria. To measure the co-polarisation and cross-polarisation of the antenna, the antenna under test (AUT) will be in the receiving mode. At the same time, another horn antenna transmits an EM wave to the AUT [32]. The transmitting antenna will be positioned horizontally or vertically, while the receiving antenna is also placed horizontally or vertically but also rotating about its position axis. When the receiving antenna is rotating, the transmitting antenna is stationary.

The measurement procedure and setup are detailed in Figure 3.4, which shows two antennas pointing at each other in the Z-direction. That is the AUT and the transmitting horn antenna. The AUT shows four horn antennas, representing the four antennas forming a monopulse antenna. The AUT is placed on a servo system, which scans over the XZ plane for an azimuth scan and across the YZ plane for

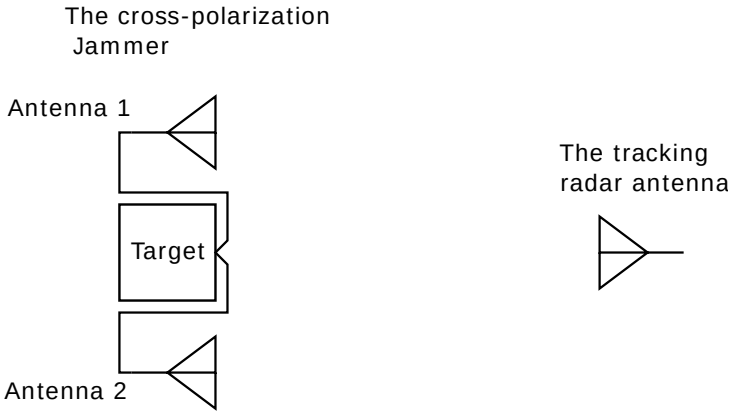

Figure 3.2. In the cross-polarisation jamming model, the jammer has two antennas that are orthogonal to each other.

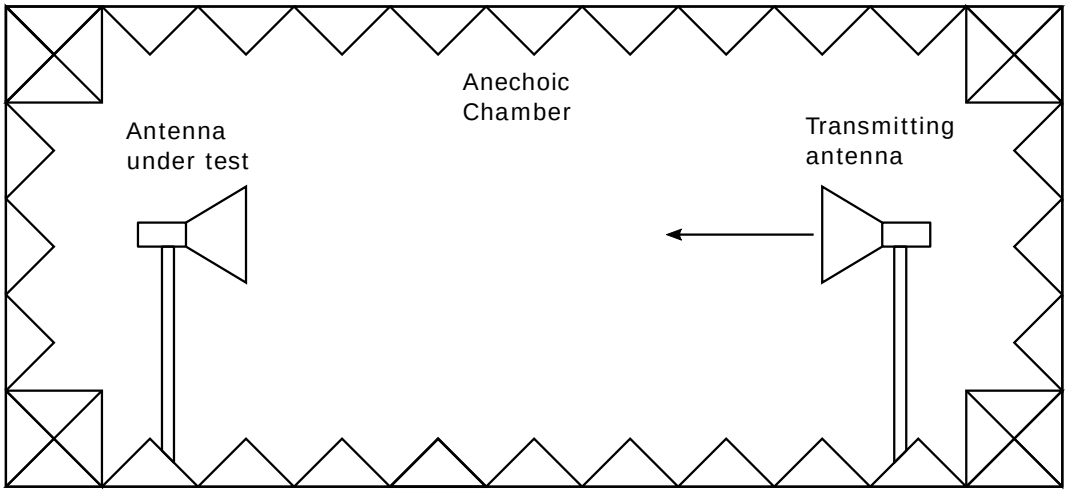

Figure 3.3. Antenna polarisation measurement setup.

an elevation scan while the transmitting antenna is transmitting. On the AUT plane, the ϕ-angles of the antenna are changed across the XY plane, and the θ angles are changed across the XZ and YZ planes. The current setup of the AUT shows each antenna in its quadrant; if the antenna scans across the XZ-plane, it will be scanning the antenna at $\phi = \pm 0^{\circ}$. If it scans across the YZ plane, it will be scanning across the antenna at $\phi = \pm 90^{\circ}$.

To scan the antenna across the diagonal planes, the four antennas must be rotated across the XY plane, which is around ϕ plane, so that each antenna is aligned to an axis, i.e., two antennas must be across the $\pm$XZ plane. In comparison, the other two antennas must be aligned to the $\pm$YZ plane. The antenna changes polarisation across the XY plane in the transmitting antenna plane. If the co-polarisation

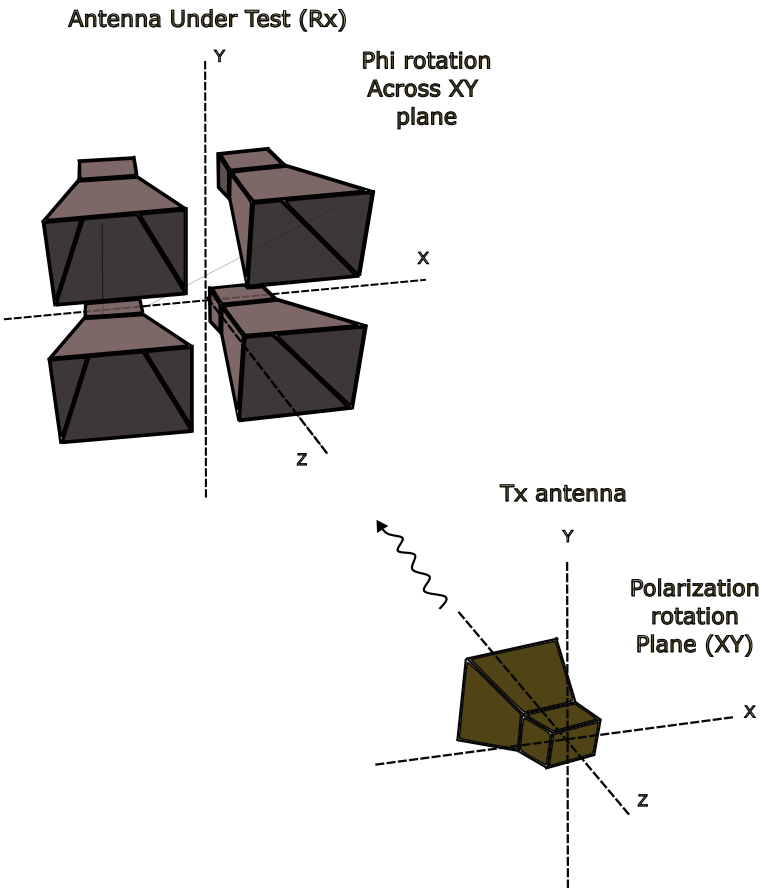

Figure 3.4. The antenna set-up during measurements.

angle of the AUT antenna is across $\pm 0^{\circ}$, the transmitting antenna must be set to $\pm 0^{\circ}$ polarisation. When the measurement is done, the transmitting antenna polarisation is changed to $\pm 90^{\circ}$ to take the cross-polarisation measurement of the AUT, but the AUT remains in the same position.

3.3.2 Analysed antennas

The analysed antennas are shown in Figure 3.5. These antennas and the simulation results in the upcoming sections were designed in Altair Feko Solver 2021.1-5769.

The antennas analysed in this work represent both planar array antennas and parabolic reflector antennas. Most radar systems use planar slotted waveguide array antennas and in this work, these types of antennas are represented by the wire-grid antenna and the aperture-coupled antenna. Other radar systems use parabolic reflector antennas, in this work, these types of antennas are represented by Hannan parabolic reflector antenna and the Cassegrain antennas.

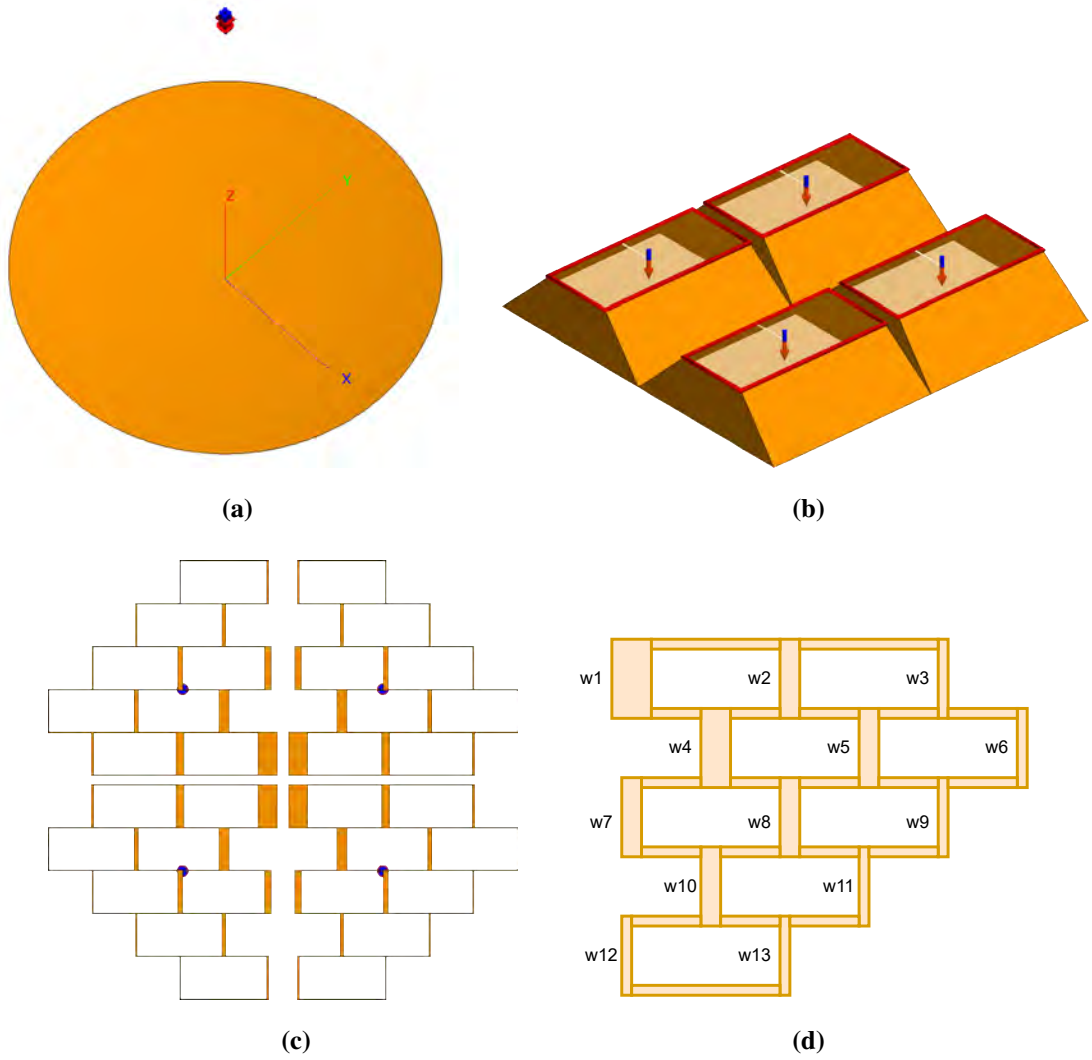

Figure 3.5. The geometry of the analysed antennas, (a) the Hannan parabolic reflector antenna, (b) the horn feed of the Hannan parabolic reflector antenna, (c) the wire-grid antenna, and (d) the quadrant of the wire-grid antenna showing micro-strip transmission line widths labels and their values are in 3.1. The coloured pins and circles represent the feed points, and the antennas operate at a 10 GHz frequency [33].

The parabolic reflector and the wire-grid antennas were designed using the guidelines described in [34, Fig. 5] and *et al.* [28, Fig. 9], respectively. The guidelines for Hannan's parabolic reflector shown in Figures 3.5(a) and 3.5(b) are as follows:

$$\frac{aA}{2\lambda F} = 0.69 \tag{3.1}$$

and

$$\frac{bB}{2\lambda F} = 0.71 \tag{3.2}$$

where a and b are the width and height of the feed horns, respectively, A and B are the dimensions of the reflector. The wavelength and the focal length are represented by λ and F, respectively. The radius of the reflector was selected to be 1 m ($A = B = 2$ m), and the horn apertures were $a = 25.0$ mm $\times$ $b = 24.3$ mm, which gives a focal length of $F = 2.35$ m at a centre frequency of 10 GHz. The waveguide feed to the horns was a WR90 waveguide with dimensions of 22.86 mm $\times$ 10.16 mm, and the long walls of the horn antenna were at an angle of 45° [33].

Figure 3.5(c) shows a wire-grid antenna designed for a 10 GHz center frequency on a substrate with a dielectric constant 2.2 and a height of 0.05 wavelength. The side lobe level (SLL) of this antenna is below -20 dB, and a gain of 21.5 dBi, and these were achieved by using the Taylor distribution tapering method, which resulted in the antenna maintaining a taper loss of 0.5 dB [33]. The wire-grid antenna was chosen to be the antenna to be manufactured. Therefore, it was designed for a C-band frequency range of 5 GHz to 6 GHz with a centre frequency of 5.5 GHz. The C-band was chosen for future antenna usage with the available software-defined radio (SDR) devices with an operating frequency of up to 6 GHz. The manufactured antenna performance will be shown in Section 5.9. The calculated parameter values for the analysed antenna at 10 GHz and the manufactured antenna at 5.5 GHz are shown in Table 3.1.

More antennas are analysed, and these antennas are shown in Figure 3.6. The Cassegrain monopulse antenna is shown in Figures 3.6(a) and 3.6(b). The hyperbolic reflector focal length, radius and segment length in Figure 3.6(a) are 266.6767 mm, 200 mm, and 5.9958 mm, respectively. The parabolic reflector focal length, radius and segment length in Figure 3.6(a) are 1500 mm, 1000 mm, and 5.9958 mm, respectively.

The Hannan Cassegrain monopulse antenna is shown in Figures 3.6(c) and 3.6(d). Its parabolic

reflector focal length and radius are 0.7833 mm and 1 m, respectively. Its hyperbolic reflector radius is 0.2657 m. Its hyperbolic reflector is placed 0.5875 m from the parabolic reflector. The horn antenna used as a feed in Figure 3.6(c) has a feed width and height of 22.86 mm and 10.16 mm, respectively. The aperture width and length of the horn are 25.00 mm. The monopulse horn antenna is shown in Figure 3.6(b), and it has a feed width and height of 22.86 mm and 10.16 mm, respectively, and an aperture width and height of 22.86 mm and a horn length of 6.35 mm.

The last antenna to be analysed is the aperture-coupled antenna designed and manufactured in [35]. This antenna is shown in Figure 3.7; its feed network is not symmetric. The non-symmetry feed network was designed to create space for phase-shifting transmission lines to introduce radiation pattern squint and a space for the monopulse comparator [35]. The current work focuses not on squinting the radiation pattern and creating space for the comparator placement; therefore, the antenna feed network was converted to have a symmetric feeding network, as shown in Figure 3.8. The symmetry and non-symmetry aperture-coupled antennas were included in this work to investigate the relationship between Condon lobes and the symmetry of the antenna feeding network. The aperture-coupled antennas operate at a C-band frequency of 5.46 GHz [35].

3.4 CHAPTER SUMMARY

Six antennas will be analysed using Feko in the transmitting and receiving mode to analyse cross-polarisation jamming. In a receiving mode, a plane wave transmits the co-and-cross-polarisation signal components to the antennas. The detailed analysis from Feko is used to model cross-polarisation patterns mathematically. One antenna will be manufactured to validate the analysis.

Table 3.1. The design parameter values for the wire-grid antenna. The analysed antenna operates at 10 GHz with $\varepsilon = 2.2$, and the manufactured antenna is designed for 5.5 GHz with $\varepsilon = 3.38$. The geometry of the widths is in Figure 3.5(d).

Parameters	Analysed antenna (values in mm)	Manufactured antenna (values in mm)
Free space λ	29.9792	34.8300
Guided λ	23.8095	31.1600
substrate height λ	1.4990	0.8130
horizontal gap	8.2550	23.4800
vertical gap	2.5654	11.7800
Radiator w1	5.3086	12.3800
Radiator w2	2.2606	9.2640
Radiator w3	0.7366	6.5680
Radiator w4	2.8194	3.0430
Radiator w5	1.1684	2.8830
Radiator w6	0.2540	8.5440
Radiator w7	1.9304	3.9670
Radiator w8	1.4732	5.1710
Radiator w9	0.3556	0.6883
Radiator w10	1.0414	0.6941
Radiator w11	0.4064	3.1140
Radiator w12	0.6096	0.6947
Radiator w13	0.3302	0.6834
Transmission line w	0.2540	0.7403

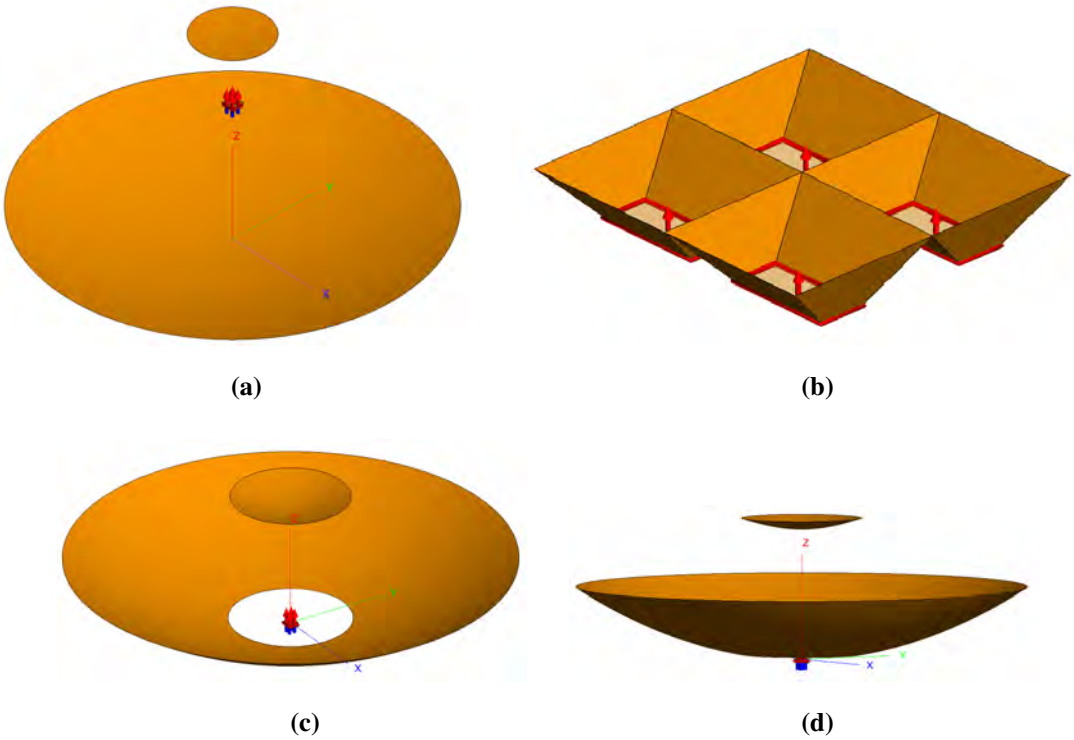

Figure 3.6. The geometry of the other analysed antennas, (a) the Cassegrain monopulse antenna full geometry, (b) the horn feed of the Cassegrain monopulse antenna, and (c), (d) Hannan Cassegrain monopulse antenna full geometry. The four-horn monopulse feed antenna in (b) was analysed on its own as a monopulse antenna. The coloured pins represent the feed points. These antennas operate at 10 GHz frequency.

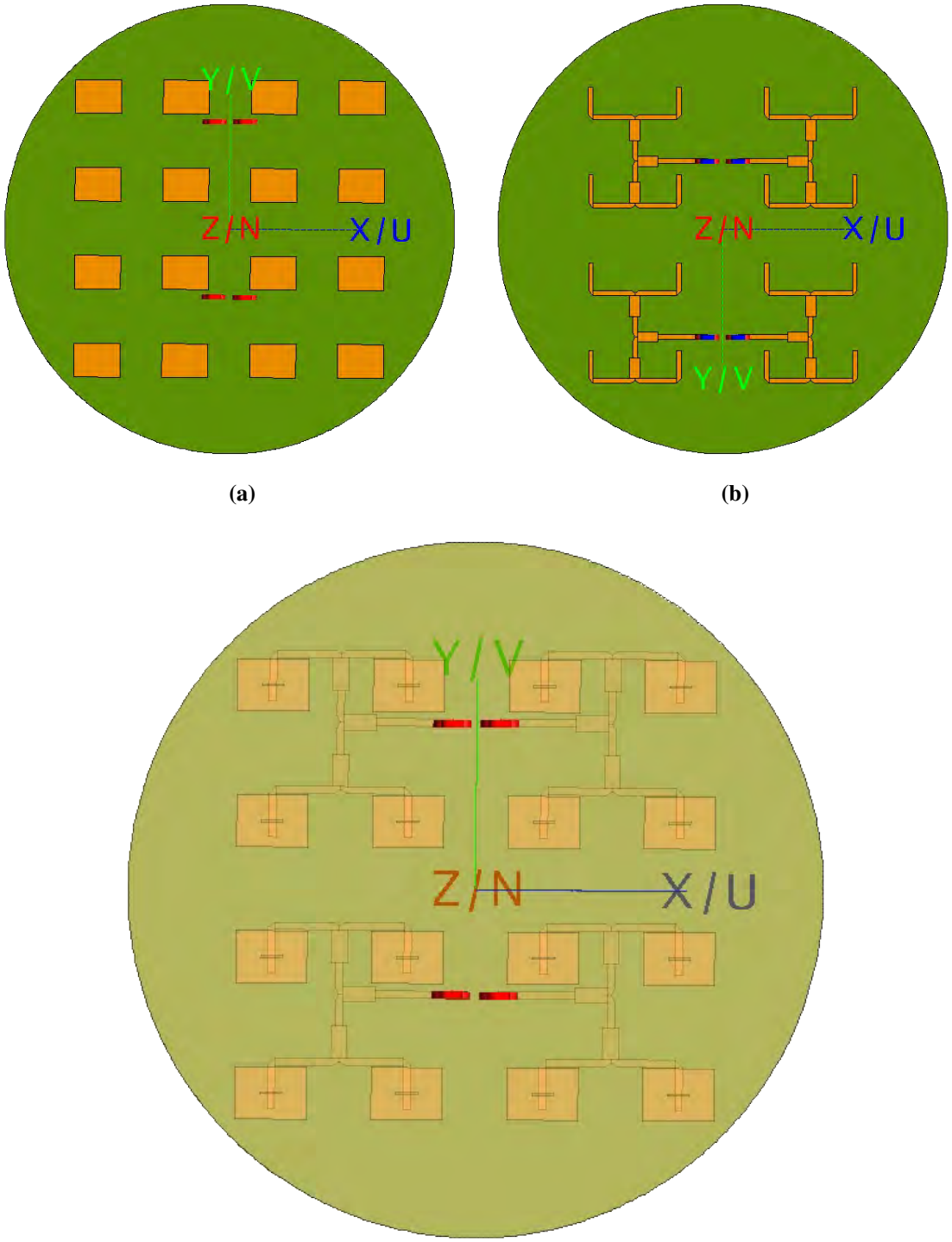

Figure 3.7. The geometry of the non-symmetric feed network of the aperture-coupled monopulse antenna showing the (a) the top, (b) the bottom feed, and (c) the full antenna showing the middle ground layer with coupling slots [35]. The antenna operates at 5.46 GHz. Figures were exported from Feko.

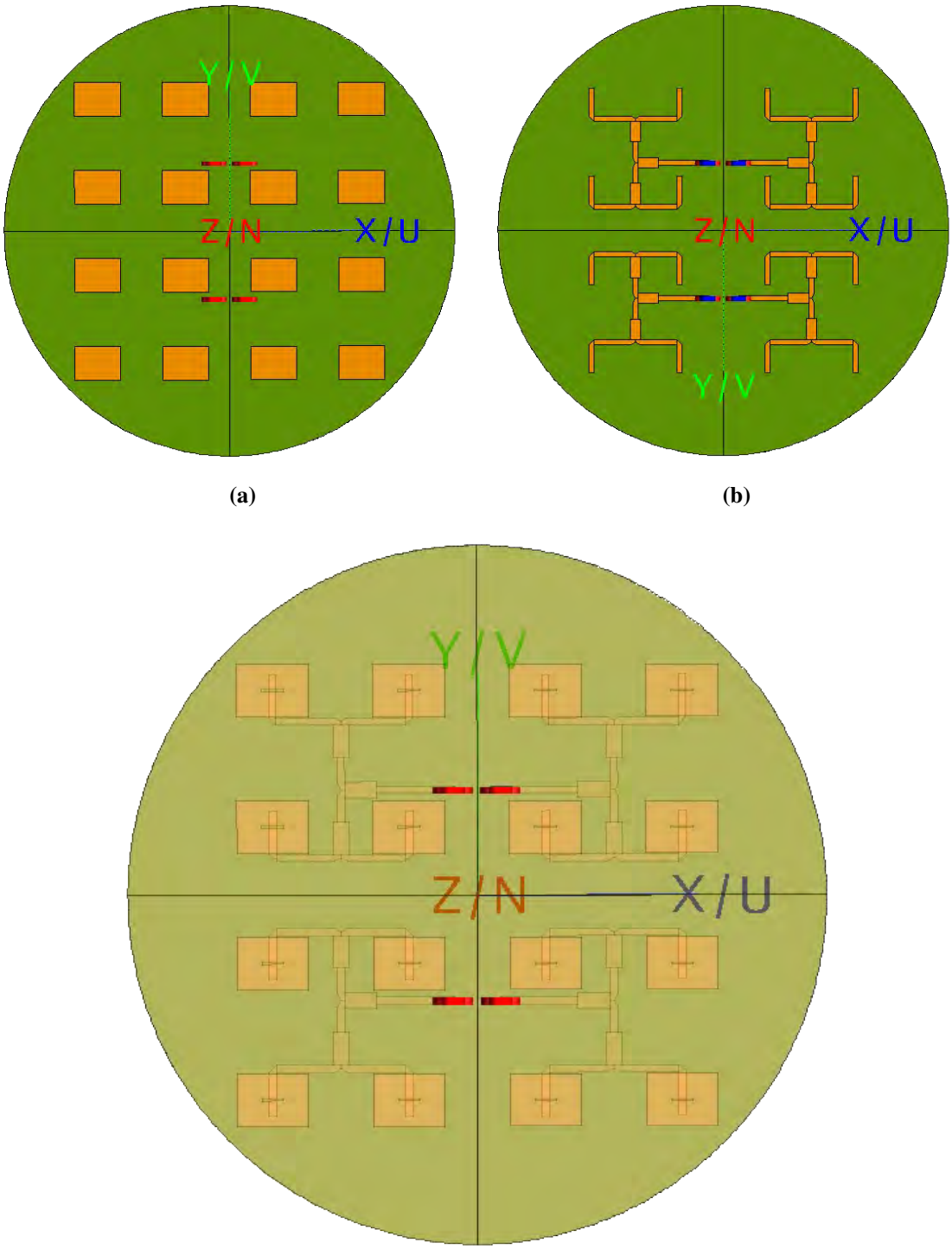

Figure 3.8. The antenna in Figure 3.7 is reshaped to illustrate symmetric feed network. The geometry of the symmetric aperture-coupled monopulse antenna showing (a) the top, (b) the bottom feed, and (c) the full antenna showing the middle ground layer with coupling slots [35]. The antenna operates at 5.46 GHz. Figures were exported from Feko.

CHAPTER 4 THEORETICAL ANALYSIS

4.1 CHAPTER OVERVIEW

This chapter presents the theoretical analysis for this dissertation. Section 4.2 presents the mathematical derivation of the monopulse co and cross-polarisation patterns and their corresponding monopulse ratios. Section 4.3 discusses the radiation patterns, monopulse ratios, and the induced angular error results generated from the derived mathematical models.

4.2 MONOPULSE ANTENNA PATTERN MODELLING FOR CROSS-POLARISATION JAMMING

Modelling the cross-polarisation jamming requires modelling the cross-polarisation patterns of the antenna the cross-polarisation jammer will be jamming. In this work, phase comparison monopulse antennas are analysed. Therefore, the monopulse patterns must be modelled. In [21], monopulse patterns are modelled, and these patterns can represent the co-polarisation patterns or the combination of both polarisation components but not the cross-polarisation patterns. The axial-symmetry antenna pattern was modelled in [36], but the modelling was for the sum pattern co- and cross-polarisation patterns. The difference pattern co- and cross-polarisation patterns are needed to calculate the monopulse ratio used in monopulse radar tracking.

This work aims to model the cross-polarisation radiation patterns for both the sum and difference patterns and analyse the effect of increasing the cross-polarisation signal power on the tracking radar accuracy. Three techniques are used to model the monopulse antenna co- and cross-polarisation patterns. The difference between the techniques is that techniques one and two in Subsection (4.2.1) and Subsection (4.2.2) use Ludwig's third polarisation definition to split the array pattern into co- and cross-polarisation patterns. In contrast, technique three in Subsection (4.2.3) uses a different technique to split the array pattern into co- and cross-polarisation patterns. These techniques use linear

polarisation. While the focus is on cross-polarisation patterns, the co-polarisation patterns are also modelled in each technique as the relationship between the polarisations plays a significant role in cross-polarisation jamming.

The main focus is on the Condon lobes located in the diagonal planes for the antennas in this work. Due to the symmetry of the Condon lobes, only one diagonal plane is analysed, the ±45° diagonal plane. These models are for phase-comparison monopulse antennas, but their results are valid for all axially-symmetrical monopulse antennas. The location of planes used in this work are as follows: in Cartesian coordinates (X, Y, Z) and spherical coordinates (ϕ, θ, radius), the ϕ angle represents the antenna planes and it is scanned in the XY plane. The θ angle is the off-boresight angle, the boresight is in the direction of Z axis.

4.2.1 Technique 1

The co and cross-polarisation radiation patterns of an antenna in a spherical coordinates system are represented by [29], [32],

$$F_C(\theta,\phi) = \boldsymbol{E}(\theta,\phi)\cdot\boldsymbol{i}_C \tag{4.1}$$

$$F_X(\theta,\phi) = \boldsymbol{E}(\theta,\phi),\cdot\boldsymbol{i}_X \tag{4.2}$$

respectively, where $\boldsymbol{i}_C$ and $\boldsymbol{i}_X$ are the components of the third polarisation definition of LUDWIG in (2.85) and (2.86), respectively. $\boldsymbol{E}(\theta,\phi)$ is the E-field in the θ and ϕ direction. The challenge is to model the $\boldsymbol{E}(\theta,\phi)$ patterns that give the expected polarisation components in the principal planes (azimuth and elevation) and the diagonal plane. Even though the modelling chapter comes before the simulations and results chapters, the antennas in Figures 3.5 , 3.6 , 3.7 , and 3.8 were analysed thoroughly to understand the antenna patterns of practical antennas. Let $\boldsymbol{E}(\theta,\phi)$ be

$$\boldsymbol{E}(\theta,\phi) = E_\theta(\theta,\phi)\hat{\boldsymbol{\theta}} + E_\phi(\theta,\phi)\hat{\boldsymbol{\phi}}, \tag{4.3}$$

where $E_\theta(\theta,\phi)$ and $E_\phi(\theta,\phi)$ are the E-fields in the θ and ϕ direction, respectively. In the analysed antennas, it is seen that at $\phi = 0°$

$$E_\theta(\theta,\phi) = 0 \tag{4.4}$$

$$E_\phi(\theta,\phi) = E_\phi(\theta,\phi), \tag{4.5}$$

at $\phi = 45°$

$$E_\theta(\theta,\phi) \approx E_\phi(\theta,\phi), \tag{4.6}$$

and at $\phi = 90^\circ$

$$E_\theta(\theta,\phi) = E_\theta(\theta,\phi) \tag{4.7}$$

$$E_\phi(\theta,\phi) = 0 \tag{4.8}$$

and this trend continues to $\phi = 360^\circ$. The $\boldsymbol{E}(\theta,\phi)$ can represent the sum or difference E-field. To model the sum channel E-field, the array factor from two antennas spaced at a distance d from each other is [36] [21],

$$AF_\Sigma(\theta,\phi) = P_1(\theta,\phi)e^{-j\varphi} + P_2(\theta,\phi)e^{j\varphi} \tag{4.9}$$

$$\varphi = \beta\frac{d}{2}\sin(\theta) \tag{4.10}$$

where β is the free-space propagation constant, θ is the pattern angle from boresight, and θ is the plane wave angle [21]. $P_1(\theta,\phi)$ and $P_2(\theta,\phi)$ are the antenna pattern magnitudes, and due to symmetry in phase comparison antennas, they are $P_1(\theta,\phi) = P_2(\theta,\phi) = P(\theta,\phi)$, then

$$AF_\Sigma(\theta,\phi) = P(\theta,\phi)\left(e^{-j\varphi} + e^{j\varphi}\right) \tag{4.11}$$

$$AF_\Sigma(\theta,\phi) = P(\theta,\phi)\left(\cos(-\varphi) + j\sin(-\varphi) + \cos(\varphi) + j\sin(\varphi)\right) \tag{4.12}$$

$$AF_\Sigma(\theta,\phi) = P(\theta,\phi)\left(2\cos(-\varphi) - j\sin(\varphi) + j\sin(\varphi)\right) \tag{4.13}$$

$$AF_\Sigma(\theta,\phi) = 2P(\theta,\phi)\cdot\cos(\varphi), \tag{4.14}$$

where Σ is the sum channel. To simplify the upcoming calculations, (4.14) is normalised to

$$AF_{\Sigma N}(\theta,\phi) = \cos(\varphi). \tag{4.15}$$

The same antennas with opposite phases are used to model the difference pattern array factor as [36],

$$AF_\Delta(\theta,\phi) = -P_1(\theta,\phi)e^{-j\varphi} + P_2(\theta,\phi)e^{j\varphi} \tag{4.16}$$

$$AF_\Delta(\theta,\phi) = P(\theta,\phi)\left(e^{j\varphi} - e^{-j\varphi}\right) \tag{4.17}$$

$$AF_\Delta(\theta,\phi) = P(\theta,\phi)\left(\cos(\varphi) + j\sin(\varphi) - cos(-\varphi) - j\sin(-\varphi)\right) \tag{4.18}$$

$$AF_\Delta(\theta,\phi) = P(\theta,\phi)\left(\cos(\varphi) - \cos(\varphi) - j\sin(\varphi) - j\sin(\varphi)\right) \tag{4.19}$$

$$AF_\Delta(\theta,\phi) = j\cdot 2P(\theta,\phi)\cdot\sin(\varphi), \tag{4.20}$$

normalising (4.20) results in

$$AF_{\Delta N}(\theta,\phi) = \sin(\varphi), \tag{4.21}$$

where Δ is the difference channel. To determine the full array pattern, the array factor is multiplied by

the element pattern [36]. The element patterns are modelled by

$$EP(\theta,\phi) = \cos(\theta). \tag{4.22}$$

The Σ array pattern is determined as

$$AP_{\Sigma}(\theta,\phi) = EP(\theta,\phi)\cdot AF_{\Sigma N}(\theta,\phi) \tag{4.23}$$

$$AP_{\Sigma}(\theta,\phi) = \cos(\theta)\cdot\cos(\varphi), \tag{4.24}$$

while the Δ array patterns are

$$AP_{\Delta}(\theta,\phi) = EP(\theta,\phi)\cdot AF_{\Delta N}(\theta,\phi) \tag{4.25}$$

$$AP_{\Delta}(\theta,\phi) = \cos(\theta)\cdot\sin(\varphi). \tag{4.26}$$

The array patterns in (4.24) and (4.26) are independent of ϕ and can represent E-fields at any plane. From (4.1), the co-polarisation Σ radiation patterns at $\phi = 0^{\circ}$ are given by [32]

$$F_{\Sigma C}(\theta,\phi) = [E_{\theta}(\theta,\phi)\hat{\boldsymbol{\theta}} + E_{\phi}(\theta,\phi)\hat{\boldsymbol{\phi}}]\cdot[\sin(\phi)\hat{\boldsymbol{\theta}} + \cos(\phi)\hat{\boldsymbol{\phi}}] \tag{4.27}$$

$$F_{\Sigma C}(\theta,0^{\circ}) = [E_{\theta}(\theta,\phi)\hat{\boldsymbol{\theta}} + E_{\phi}(\theta,\phi)\hat{\boldsymbol{\phi}}]\cdot[\sin(0^{\circ})\hat{\boldsymbol{\theta}} + \cos(0^{\circ})\hat{\boldsymbol{\phi}}] \tag{4.28}$$

$$F_{\Sigma C}(\theta,0^{\circ}) = E_{\phi}(\theta,\phi), \tag{4.29}$$

where $E_{\phi}(\theta,\phi) = AF_{\Sigma N}(\theta,\phi)$ resulting in

$$F_{\Sigma C}(\theta,0^{\circ}) = \cos(\theta)\cdot\cos(\varphi). \tag{4.30}$$

The same procedure from (4.27) to (4.30), with $E_{\phi}(\theta,\phi) = AF_{\Delta N}(\theta,\phi)$ result in the co-polarisation Δ patterns of

$$F_{\Delta C}(\theta,0^{\circ}) = \cos(\theta)\cdot\sin(\varphi). \tag{4.31}$$

For the cross-polarisation radiation pattern, (4.2) becomes

$$F_{\Sigma X}(\theta,\phi) = [E_{\theta}(\theta,\phi)\hat{\boldsymbol{\theta}} + E_{\phi}(\theta,\phi)\hat{\boldsymbol{\phi}}]\cdot[\cos(\phi)\hat{\boldsymbol{\theta}} - \sin(\phi)\hat{\boldsymbol{\phi}}] \tag{4.32}$$

$$F_{\Sigma X}(\theta,0^{\circ}) = [E_{\theta}(\theta,\phi)\hat{\boldsymbol{\theta}} + E_{\phi}(\theta,\phi)\hat{\boldsymbol{\phi}}]\cdot[\cos(0^{\circ})\hat{\boldsymbol{\theta}} - \sin(0^{\circ})\hat{\boldsymbol{\phi}}], \tag{4.33}$$

from (4.4), $E_{\theta}(\theta,\phi) = 0^{\circ}$ resulting in

$$F_{X}(\theta,0^{\circ}) = 0. \tag{4.34}$$

Therefore,

$$F_{\Sigma X}(\theta,\phi) = 0 \tag{4.35}$$

$$F_{\Delta X}(\theta,\phi) = 0. \tag{4.36}$$

The co-polarisation monopulse ratio at $\phi = 0^\circ$ is given as

$$M_C(\theta,0^\circ) = \frac{F_{\Delta C}(\theta,0^\circ)}{F_{\Sigma C}(\theta,0^\circ)} \tag{4.37}$$

$$M_C(\theta,0^\circ) = \frac{\cos(\theta)\sin(\varphi)}{\cos(\theta)\cos(\varphi)} \tag{4.38}$$

$$M_C(\theta,0^\circ) = \tan(\varphi). \tag{4.39}$$

The normalisation in (4.15) and (4.21) was done because the $P(\theta,\phi)$ antenna magnitude will cancel each other when determining the monopulse ratio. If (4.14) and (4.20) were not normalised, the monopulse ratio in (4.39) would be

$$M_C(\theta,0^\circ) = j\tan(\varphi). \tag{4.40}$$

The cross-polarisation monopulse ratio is

$$M_X(\theta,0^\circ) = 0. \tag{4.41}$$

The same procedure for $\phi = 0^\circ$ is applied to $\phi = 90^\circ$, but $E_\theta(\theta,\phi) = AF_{\Sigma N}(\theta,\phi)$ for the Σ patterns, $E_\theta(\theta,\phi) = AF_{\Delta N}(\theta,\phi)$ for the Δ patterns, and $E_\phi(\theta,\phi) = 0$ for both Σ and Δ patterns. These results in

$$F_{\Sigma C}(\theta,90^\circ) = [E_\theta\hat{\boldsymbol{\theta}} + E_\phi\hat{\boldsymbol{\phi}}]\cdot[\sin(90^\circ)\hat{\boldsymbol{\theta}} + \cos(90^\circ)\hat{\boldsymbol{\phi}}] \tag{4.42}$$

$$F_{\Sigma C}(\theta,90^\circ) = E_\theta, \tag{4.43}$$

resulting in

$$F_{\Sigma C}(\theta,90^\circ) = \cos(\theta)\cos(\varphi), \tag{4.44}$$

then

$$F_{\Delta C}(\theta,90^\circ) = \cos(\theta)\sin(\varphi). \tag{4.45}$$

For cross-polarisation radiation patterns

$$F_{\Sigma X}(\theta,90^\circ) = [E_\theta(\theta,\phi)\hat{\boldsymbol{\theta}} + E_\phi(\theta,\phi)\hat{\boldsymbol{\phi}}]\cdot[\cos(90^\circ)\hat{\boldsymbol{\theta}} - \sin(90^\circ)\hat{\boldsymbol{\phi}}] \tag{4.46}$$

$$F_{\Sigma X}(\theta,90^\circ) = F_{\Delta X}(\theta,90^\circ) = 0. \tag{4.47}$$

The general monopulse ratio at $\phi = 90^\circ$ plane is

$$M_C(\theta,90^\circ) = \tan(\varphi) \tag{4.48}$$

$$M_X(\theta,90^\circ) = 0. \tag{4.49}$$

The main focus is on the cross-polarisation patterns, and it is seen that the principle planes have zero cross-polarisation patterns. Even in the analysed antennas, the cross-polarisation patterns at ϕ $\pm0^\circ$ and ϕ $\pm90^\circ$ planes are approximately zero. The diagonal planes ϕ $\pm45^\circ$ and ϕ $\pm135^\circ$ have

non-zero cross-polarisation patterns because Condon lobes are located in these planes. Therefore, cross-polarisation patterns must be modelled for the Σ and Δ channels in these planes. There is a condition in (4.6) that at $\phi = 45^\circ$ plane, $E_\theta(\theta,\phi) \approx E_\phi(\theta,\phi)$. To achieve this condition, a constant must be introduced into (4.24) and (4.26) as

$$AP_\Sigma(\theta,\phi) = \cos(\theta)\cdot\cos(n_\Sigma\cdot\varphi) \tag{4.50}$$

$$AP_\Delta(\theta,\phi) = \cos(\theta)\cdot\sin(n_\Delta\cdot\varphi), \tag{4.51}$$

where n_Σ and n_Δ are, respectively, Σ and Δ positive integer constants used to control the beamwidth of the main lobe. Now the Σ and Δ $E_\theta(\theta,\phi)$ and $E_\phi(\theta,\phi)$ are given as

$$E_{\Sigma\theta}(\theta,\phi) = \cos(\theta)\cdot\cos(n_{\Sigma\theta}\cdot\varphi) \tag{4.52}$$

$$E_{\Sigma\phi}(\theta,\phi) = \cos(\theta)\cdot\cos(n_{\Sigma\phi}\cdot\varphi) \tag{4.53}$$

$$E_{\Delta\theta}(\theta,\phi) = \cos(\theta)\cdot\sin(n_{\Delta\theta}\cdot\varphi) \tag{4.54}$$

$$E_{\Delta\phi}(\theta,\phi) = \cos(\theta)\cdot\sin(n_{\Delta\phi}\cdot\varphi). \tag{4.55}$$

To maintain the condition that $E_\theta(\theta,\phi) \approx E_\phi(\theta,\phi)$, then $n_{\Sigma\theta} \neq n_{\Sigma\phi}$ and $n_{\Delta\theta} \neq n_{\Delta\phi}$. If $n_{\Sigma\theta} = n_{\Sigma\phi}$ or $n_{\Delta\theta} = n_{\Delta\phi}$, then $E_\theta(\theta,\phi) = E_\phi$, which results in the cross-polarisation component calculated from LUDWIG 3rd polarisation definition becoming zero, which is undesirable. The co-polarisation Σ antenna radiation patterns at $\phi = 45^\circ$ are as follows

$$F_{\Sigma C}(\theta,45^\circ) = [E_{\Sigma\theta}(\theta,\phi)\hat{\boldsymbol{\theta}} + E_{\Sigma\phi}(\theta,\phi)\hat{\boldsymbol{\phi}}]\cdot[\sin(45^\circ)\hat{\boldsymbol{\theta}} + \cos(45^\circ)\hat{\boldsymbol{\phi}}] \tag{4.56}$$

$$F_{\Sigma C}(\theta,45^\circ) = \frac{1}{\sqrt{2}}[E_{\Sigma\theta}(\theta,\phi) + E_{\Sigma\phi}(\theta,\phi)], \tag{4.57}$$

substituting (4.52) and (4.53) into (4.57) gives

$$F_{\Sigma C}(\theta,45^\circ) = \frac{1}{\sqrt{2}}[\cos(\theta)\cdot\cos(n_{\Sigma\theta}\cdot\varphi) + \cos(\theta)\cdot\cos(n_{\Sigma\phi}\cdot\varphi)]. \tag{4.58}$$

The co-polarisation Δ radiation patterns are as follows

$$F_{\Delta C}(\theta,45^\circ) = [E_{\Delta\theta}(\theta,\phi)\hat{\boldsymbol{\theta}} + E_{\Delta\phi}(\theta,\phi)\hat{\boldsymbol{\phi}}]\cdot[\sin(45^\circ)\hat{\boldsymbol{\theta}} + \cos(45^\circ)\hat{\boldsymbol{\phi}}] \tag{4.59}$$

$$F_{\Delta C}(\theta,45^\circ) = \frac{1}{\sqrt{2}}[E_{\Delta\theta} + E_{\Delta\phi}], \tag{4.60}$$

substituting (4.54) and (4.55) into (4.60) gives

$$F_{\Delta C}(\theta,45^\circ) = \frac{1}{\sqrt{2}}[\cos(\theta)\cdot\sin(n_{\Delta\theta}\cdot\varphi) + \cos(\theta)\cdot\sin(n_{\Delta\phi}\cdot\varphi)]. \tag{4.61}$$

Now, for the Σ cross-polarisation radiation patterns,

$$F_{\Sigma X}(\theta,45^\circ) = [E_{\Sigma\theta}\hat{\boldsymbol{\theta}} + E_{\Sigma\phi}\hat{\boldsymbol{\phi}}]\cdot[\cos(45^\circ)\hat{\boldsymbol{\theta}} - \sin(45^\circ)\hat{\boldsymbol{\phi}}], \tag{4.62}$$

$$F_{\Sigma X}(\theta,45^\circ) = \frac{1}{\sqrt{2}}[E_{\Sigma\theta}(\theta,\phi) - E_{\Sigma\phi}(\theta,\phi)] \tag{4.63}$$

substituting (4.52) and (4.53) into (4.63) gives

$$F_{\Sigma X}(\theta,45^\circ) = \frac{1}{\sqrt{2}}[\cos(\theta)\cdot\cos(n_{\Sigma\theta}\cdot\varphi) - \cos(\theta)\cdot\cos(n_{\Sigma\phi}\cdot\varphi)]. \tag{4.64}$$

For the Δ cross-polarisation radiation patterns,

$$F_{\Delta X}(\theta,45^\circ) = [E_{\Delta\theta}(\theta,\phi)\hat{\boldsymbol{\theta}} + E_{\Delta\phi}(\theta,\phi)\hat{\boldsymbol{\phi}}]\cdot[\cos(45^\circ)\hat{\boldsymbol{\theta}} - \sin(45^\circ)\hat{\boldsymbol{\phi}}] \tag{4.65}$$

$$F_{\Delta X}(\theta,45^\circ) = \frac{1}{\sqrt{2}}[E_{\Delta\theta}(\theta,\phi) - E_{\Delta\phi}(\theta,\phi)], \tag{4.66}$$

substituting (4.54) and (4.55) into (4.66) gives

$$F_{\Delta X}(\theta,45^\circ) = \frac{1}{\sqrt{2}}[\cos(\theta)\cdot\sin(n_{\Delta\theta}\cdot\varphi) - \cos(\theta)\cdot\sin(n_{\Delta\phi}\cdot\varphi)]. \tag{4.67}$$

The co-polarisation monopulse ratio at $\phi = 45^\circ$ is

$$M_C(\theta,45^\circ) = \frac{F_{\Delta C}(\theta,45^\circ)}{F_{\Sigma C}(\theta,45^\circ)}. \tag{4.68}$$

Substituting (4.58) and (4.61) into (4.68) gives

$$M_C(\theta,45^\circ) = \left(\frac{\frac{1}{\sqrt{2}}[\cos(\theta)\cdot\sin(n_{\Delta\theta}\cdot\varphi) + \cos(\theta)\cdot\sin(n_{\Delta\phi}\cdot\varphi)]}{\frac{1}{\sqrt{2}}[\cos(\theta)\cdot\cos(n_{\Sigma\theta}\cdot\varphi) + \cos(\theta)\cdot\cos(n_{\Sigma\phi}\cdot\varphi)]}\right) \tag{4.69}$$

$$M_C(\theta,45^\circ) = \frac{\sin(n_{\Delta\theta}\cdot\varphi) + \sin(n_{\Delta\phi}\cdot\varphi)}{\cos(n_{\Sigma\theta}\cdot\varphi) + \cos(n_{\Sigma\phi}\cdot\varphi)}. \tag{4.70}$$

Then, the cross-polarisation monopulse ratio is

$$M_X(\theta,45^\circ) = \frac{F_{\Delta X}(\theta,45^\circ)}{F_{\Sigma X}(\theta,45^\circ)}, \tag{4.71}$$

substituting (4.64) and (4.67) into (4.71) gives

$$M_X(\theta,45^\circ) = \left(\frac{\frac{1}{\sqrt{2}}[\cos(\theta)\cdot\sin(n_{\Delta\theta}\cdot\varphi) - \cos(\theta)\cdot\sin(n_{\Delta\phi}\cdot\varphi)]}{\frac{1}{\sqrt{2}}[\cos(\theta)\cdot\cos(n_{\Sigma\theta}\cdot\varphi) - \cos(\theta)\cdot\cos(n_{\Sigma\phi}\cdot\varphi)]}\right) \tag{4.72}$$

$$M_X(\theta,45^\circ) = \frac{\sin(n_{\Delta\theta}\cdot\varphi) - \sin(n_{\Delta\phi}\cdot\varphi)}{\cos(n_{\Sigma\theta}\cdot\varphi) - \cos(n_{\Sigma\phi}\cdot\varphi)}. \tag{4.73}$$

The co- and cross-polarisation monopulse ratios in (4.70) and (4.73) result in the expected polarisation components at the diagonal planes.

4.2.2 Technique 2

This technique uses the same LUDWIG's 3rd polarisation definition as Technique One. Still, this technique focuses on modelling the full array pattern without defining which component is the element pattern or array factor. The Σ and Δ E-fields are given as follow

$$E_{\Sigma\theta}(\theta,\phi) = \cos(n_{\Sigma\theta1}\theta)\cdot\mathrm{sinc}(n_{\Sigma\theta2}\cdot\theta) \tag{4.74}$$

$$E_{\Sigma\phi}(\theta,\phi) = \cos(n_{\Sigma\phi1}\theta)\cdot\mathrm{sinc}(n_{\Sigma\phi2}\cdot\theta) \tag{4.75}$$

$$E_{\Delta\theta}(\theta,\phi) = \sin(n_{\Delta\theta1}\theta)\cdot\text{sinc}(n_{\Delta\theta2}\cdot\theta) \tag{4.76}$$

$$E_{\Delta\phi}(\theta,\phi) = \sin(n_{\Delta\phi1}\theta)\cdot\text{sinc}(n_{\Delta\phi2}\cdot\theta), \tag{4.77}$$

where

$$\text{sinc}(n\theta) = \frac{\sin(n\theta)}{n\theta} \tag{4.78}$$

and $n_{\Sigma\theta1}$, $n_{\Sigma\theta2}$, $n_{\Sigma\phi1}$, $n_{\Sigma\phi2}$, $n_{\Delta\theta1}$, $n_{\Delta\theta2}$, $n_{\Delta\phi1}$, and $n_{\Delta\phi2}$ are used to control the beamwidth of the antenna pattern. At ϕ = 0° plane the Σ and Δ E-fields are

$$E_{\Sigma\theta}(\theta,\phi) = 0 \tag{4.79}$$

$$E_{\Sigma\phi}(\theta,\phi) = \cos(n_{\Sigma\phi1}\theta)\cdot\text{sinc}(n_{\Sigma\phi2}\cdot\theta), \tag{4.80}$$

substituting (4.79) and (4.80) into (4.27), results in the radiation patterns

$$F_{\Sigma C}(\theta,\phi) = [E_{\Sigma\theta}(\theta,\phi)\hat{\boldsymbol{\theta}} + E_{\Sigma\phi}(\theta,\phi)\hat{\boldsymbol{\phi}}]\cdot[\sin(0^\circ)\hat{\boldsymbol{\theta}} + \cos(0^\circ)\hat{\boldsymbol{\phi}}] \tag{4.81}$$

$$F_{\Sigma C}(\theta,0^\circ) = \cos(n_{\Sigma\phi1}\theta)\cdot\text{sinc}(n_{\Sigma\phi2}\cdot\theta). \tag{4.82}$$

For the Δ radiation patterns, substituting (4.79) and (4.80) into (4.32), gives

$$F_{\Delta C}(\theta,0^\circ) = \sin(n_{\Delta\phi1}\theta)\cdot\text{sinc}(n_{\Delta\phi2}\cdot\theta). \tag{4.83}$$

The cross-polarisation radiation patterns are

$$F_{\Sigma X}(\theta,\phi) = [E_{\Sigma\theta}(\theta,\phi)\hat{\boldsymbol{\theta}} + E_{\Sigma\phi}(\theta,\phi)\hat{\boldsymbol{\phi}}]\cdot[\cos(0^\circ)\hat{\boldsymbol{\theta}} - \sin(0^\circ)\hat{\boldsymbol{\phi}}] \tag{4.84}$$

$$F_{\Sigma X}(\theta,0^\circ) = 0 \tag{4.85}$$

$$F_{\Delta X}(\theta,\phi) = [E_{\Delta\theta}(\theta,\phi)\hat{\boldsymbol{\theta}} + E_{\Delta\phi}(\theta,\phi)\hat{\boldsymbol{\phi}}]\cdot[\cos(0^\circ)\hat{\boldsymbol{\theta}} - \sin(0^\circ)\hat{\boldsymbol{\phi}}] \tag{4.86}$$

$$F_{\Delta X}(\theta,0^\circ) = 0. \tag{4.87}$$

The co-polarisation monopulse ratios are

$$M_C(\theta,0^\circ) = \frac{F_{\Delta C}(\theta,0^\circ)}{F_{\Sigma C}(\theta,0^\circ)} \tag{4.88}$$

$$M_C(\theta,0^\circ) = \frac{\sin(n_{\Delta\phi1}\theta)\cdot\text{sinc}(n_{\Delta\phi2}\cdot\theta)}{\cos(n_{\Sigma\phi1}\theta)\cdot\text{sinc}(n_{\Sigma\phi2}\cdot\theta)}. \tag{4.89}$$

The cross-polarisation monopulse ratios are

$$M_X(\theta,0^\circ) = \frac{F_{\Delta C}(\theta,0^\circ)}{F_{\Delta C}(\theta,0^\circ)} \tag{4.90}$$

$$M_X(\theta,0^\circ) = 0. \tag{4.91}$$

Now, modelling the ϕ = 90° plane, the Σ E-fields are

$$E_{\Sigma\theta}(\theta,\phi) = \cos(n_{\Sigma\theta1}\theta)\cdot\text{sinc}(n_{\Sigma\theta2}\cdot\theta) \tag{4.92}$$

$$E_{\Sigma\phi}(\theta,\phi) = 0, \tag{4.93}$$

substituting (4.92) and (4.93) into (4.27), results in radiation patterns

$$F_{\Sigma C}(\theta,\phi) = [E_{\Sigma\theta}(\theta,\phi)\hat{\boldsymbol{\theta}} + E_{\Sigma\phi}(\theta,\phi)\hat{\boldsymbol{\phi}}]\cdot[\sin(90^\circ)\hat{\boldsymbol{\theta}} + \cos(90^\circ)\hat{\boldsymbol{\phi}}] \tag{4.94}$$

$$F_{\Sigma C}(\theta,90^\circ) = \cos(n_{\Sigma\theta 1}\theta)\cdot\mathrm{sinc}(n_{\Sigma\theta 2}\cdot\theta). \tag{4.95}$$

For the Δ radiation patterns, substituting (4.92) and (4.93) into (4.32), gives

$$F_{\Delta C}(\theta,90^\circ) = \sin(n_{\Delta\theta 1}\theta)\cdot\mathrm{sinc}(n_{\Delta\theta 2}\cdot\theta). \tag{4.96}$$

The cross-polarisation radiation patterns are

$$F_{\Sigma X}(\theta,\phi) = [E_{\Sigma\theta}(\theta,\phi)\hat{\boldsymbol{\theta}} + E_{\Sigma\phi}(\theta,\phi)\hat{\boldsymbol{\phi}}]\cdot[\cos(90^\circ)\hat{\boldsymbol{\theta}} - \sin(90^\circ)\hat{\boldsymbol{\phi}}] \tag{4.97}$$

$$F_{\Sigma X}(\theta,90^\circ) = 0 \tag{4.98}$$

$$F_{\Delta X}(\theta,\phi) = [E_{\Delta\theta}(\theta,\phi)\hat{\boldsymbol{\theta}} + E_{\Delta\phi}(\theta,\phi)\hat{\boldsymbol{\phi}}]\cdot[\cos(90^\circ)\hat{\boldsymbol{\theta}} - \sin(90^\circ)\hat{\boldsymbol{\phi}}] \tag{4.99}$$

$$F_{\Delta X}(\theta,90^\circ) = 0. \tag{4.100}$$

The co-polarisation monopulse ratios are

$$M_C(\theta,90^\circ) = \frac{F_{\Delta C}(\theta,90^\circ)}{F_{\Sigma C}(\theta,90^\circ)} \tag{4.101}$$

$$M_C(\theta,90^\circ) = \frac{\sin(n_{\Delta\theta 1}\theta)\cdot\mathrm{sinc}(n_{\Delta\theta 2}\cdot\theta)}{\cos(n_{\Sigma\theta 1}\theta)\cdot\mathrm{sinc}(n_{\Sigma\theta 2}\cdot\theta)}. \tag{4.102}$$

The cross-polarisation monopulse ratios are

$$M_X(\theta,90^\circ) = \frac{F_{\Delta X}(\theta,90^\circ)}{F_{\Sigma X}(\theta,90^\circ)} \tag{4.103}$$

$$M_X(\theta,90^\circ) = 0. \tag{4.104}$$

Modeling at ϕ = 45° plane, the Σ and Δ E-fields are (4.74 - 4.77). Substituting (4.74) and (4.75) into (4.27) and (4.32), gives the Σ radiation patterns

$$F_{\Sigma C}(\theta,45^\circ) = [E_{\Sigma\theta}(\theta,\phi)\hat{\boldsymbol{\theta}} + E_{\Sigma\phi}(\theta,\phi)\hat{\boldsymbol{\phi}}]\cdot[\sin(45^\circ)\hat{\boldsymbol{\theta}} + \cos(45^\circ)\hat{\boldsymbol{\phi}}] \tag{4.105}$$

$$F_{\Sigma C}(\theta,45^\circ) = [\cos(n_{\Sigma\theta 1}\theta)\mathrm{sinc}(n_{\Sigma\theta 2}\theta)\hat{\boldsymbol{\theta}} + \cos(n_{\Sigma\phi 1}\theta)\mathrm{sinc}(n_{\Sigma\phi 2}\theta)\hat{\boldsymbol{\phi}}]\cdot[\sin(45^\circ)\hat{\boldsymbol{\theta}} + \cos(45^\circ)\hat{\boldsymbol{\phi}}] \tag{4.106}$$

$$F_{\Sigma C}(\theta,45^\circ) = \frac{1}{\sqrt{2}}[\cos(n_{\Sigma\theta 1}\theta)\mathrm{sinc}(n_{\Sigma\theta 2}\theta) + \cos(n_{\Sigma\phi 1}\theta)\mathrm{sinc}(n_{\Sigma\phi 2}\theta)] \tag{4.107}$$

$$F_{\Sigma X}(\theta,45^\circ) = [E_{\Sigma\theta}(\theta,\phi)\hat{\boldsymbol{\theta}} + E_{\Sigma\phi}(\theta,\phi)\hat{\boldsymbol{\phi}}]\cdot[\cos(45^\circ)\hat{\boldsymbol{\theta}} - \sin(45^\circ)\hat{\boldsymbol{\phi}}] \tag{4.108}$$

$$F_{\Sigma X}(\theta,45^\circ) = [\cos(n_{\Sigma\theta 1}\theta)\mathrm{sinc}(n_{\Sigma\theta 2}\theta)\hat{\boldsymbol{\theta}} + \cos(n_{\Sigma\phi 1}\theta)\mathrm{sinc}(n_{\Sigma\phi 2}\theta)\hat{\boldsymbol{\phi}}]\cdot[\cos(45^\circ)\hat{\boldsymbol{\theta}} - \sin(45^\circ)\hat{\boldsymbol{\phi}}] \tag{4.109}$$

$$F_{\Sigma X}(\theta,45^\circ) = \frac{1}{\sqrt{2}}[\cos(n_{\Sigma\theta 1}\theta)\mathrm{sinc}(n_{\Sigma\theta 2}\theta) - \cos(n_{\Sigma\phi 1}\theta)\mathrm{sinc}(n_{\Sigma\phi 2}\theta)]. \tag{4.110}$$

Substituting (4.76) and (4.77) into (4.27) and (4.32), gives the Δ radiation patterns as

$$F_{\Delta C}(\theta,45^\circ) = [E_{\Delta\theta}(\theta,\phi)\hat{\boldsymbol{\theta}} + E_{\Delta\phi}(\theta,\phi)\hat{\boldsymbol{\phi}}]\cdot[\sin(45^\circ)\hat{\boldsymbol{\theta}} + \cos(45^\circ)\hat{\boldsymbol{\phi}}] \tag{4.111}$$

$$F_{\Delta C}(\theta,45^\circ) = [\cos(n_{\Delta\theta1}\theta)\mathrm{sinc}(n_{\Delta\theta2}\theta)\hat{\boldsymbol{\theta}} + \cos(n_{\Delta\phi1}\theta)\mathrm{sinc}(n_{\Delta\phi2}\theta)\hat{\boldsymbol{\phi}}]\cdot[\sin(45^\circ)\hat{\boldsymbol{\theta}} + \cos(45^\circ)\hat{\boldsymbol{\phi}}] \tag{4.112}$$

$$F_{\Delta C}(\theta,45^\circ) = \frac{1}{\sqrt{2}}[\cos(n_{\Delta\theta1}\theta)\mathrm{sinc}(n_{\Delta\theta2}\theta) + \cos(n_{\Delta\phi1}\theta)\mathrm{sinc}(n_{\Delta\phi2}\theta)] \tag{4.113}$$

$$F_{\Delta X}(\theta,45^\circ) = [E_{\Delta\theta}(\theta,\phi)\hat{\boldsymbol{\theta}} + E_{\Delta\phi}(\theta,\phi)\hat{\boldsymbol{\phi}}]\cdot[\cos(45^\circ)\hat{\boldsymbol{\theta}} - \sin(45^\circ)\hat{\boldsymbol{\phi}}] \tag{4.114}$$

$$F_{\Delta X}(\theta,45^\circ) = [\cos(n_{\Delta\theta1})\theta)\mathrm{sinc}(n_{\Delta\theta2}\theta)\hat{\boldsymbol{\theta}} + \cos(n_{\Delta\phi1}\theta)\mathrm{sinc}(n_{\Delta\phi2}\theta)\hat{\boldsymbol{\phi}}]\cdot[\cos(45^\circ)\hat{\boldsymbol{\theta}} - \sin(45^\circ)\hat{\boldsymbol{\phi}}] \tag{4.115}$$

$$F_{\Delta X}(\theta,45^\circ) = \frac{1}{\sqrt{2}}[\cos(n_{\Delta\theta1}\theta)\mathrm{sinc}(n_{\Delta\theta2}\theta) - \cos(n_{\Delta\phi1}\theta)\mathrm{sinc}(n_{\Delta\phi2}\theta)]. \tag{4.116}$$

Using (4.107) and (4.113) to get the co-polarisation monopulse ratio

$$M_C(\theta,45^\circ) = \frac{F_{\Delta C}(\theta,45^\circ)}{F_{\Sigma C}(\theta,45^\circ)} \tag{4.117}$$

$$M_C(\theta,45^\circ) = \frac{\cos(n_5\theta)\mathrm{sinc}(n_6\theta) + \cos(n_7\theta)\mathrm{sinc}(n_8\theta}{\cos(n_1\theta)\mathrm{sinc}(n_2\theta) + \cos(n_3\theta)\mathrm{sinc}(n_4\theta)}. \tag{4.118}$$

Using (4.116) and (4.110) to get the cross-polarisation monopulse ratio

$$M_X(\theta,45^\circ) = \frac{F_{\Delta X}(\theta,45^\circ)}{F_{\Sigma X}(\theta,45^\circ)} \tag{4.119}$$

$$M_X(\theta,45^\circ) = \frac{\cos(n_5\theta)\mathrm{sinc}(n_6\theta) - \cos(n_7\theta)\mathrm{sinc}(n_8\theta)}{\cos(n_1\theta)\mathrm{sinc}(n_2\theta) - \cos(n_3\theta)\mathrm{sinc}(n_4\theta)}. \tag{4.120}$$

4.2.3 Technique 3

This technique differs from Technique One because it does not directly use Ludwig's polarisation definitions. The co- and cross-polarisation components for an axially-symmetrical parabolic reflector antenna are modelled [36], but only the sum patterns. The co- and cross-polarisation components sum antenna radiation patterns are given as [36],

$$F_{\Sigma C}(\theta,\phi) = AP_{\Sigma C}(\theta,\phi)\, i_C(\theta,\phi), \tag{4.121}$$

$$F_{\Sigma X}(\theta,\phi) = AP_{\Sigma X}(\theta,\phi)\, i_X(\theta,\phi), \tag{4.122}$$

where $AP_{\Sigma C}(\theta,\phi)$ and $AP_{\Sigma X}(\theta,\phi)$ are array patterns, and in this work, they are modelled differently from [36] to suit the goals of this work. $i_C(\theta,\phi)$ and $i_X(\theta,\phi)$ are the functions used to convert the

array pattern function to co- and cross-polarisation components, and they are [36]

$$i_C(\theta,\phi) = \left[C_e \cos^2(\phi) + C_h \sin^2(\phi)\right], \tag{4.123}$$

$$i_X(\theta,\phi) = \left[(C_e - C_h)\sin(\phi)\cos(\phi)\right], \tag{4.124}$$

where $C_e = \cos(\theta)$ and $C_h = 1$. The array patterns are modelled as

$$AP_{\Sigma C}(\theta,\phi) = \cos(n_{\Sigma C}\theta)\,\mathrm{sinc}(n_{\Sigma C}\theta), \tag{4.125}$$

$$AP_{\Sigma X}(\theta,\phi) = \cos(n_{\Sigma X}\theta)\,\mathrm{sinc}(n_{\Sigma X}\theta), \tag{4.126}$$

where $n_{\Sigma C}$ and $n_{\Sigma X}$ are used to control the beamwidth of the patterns. Technique one determines the sum co- and cross-polarisation patterns from the same array pattern function. However, in this technique, the beamwidth of the array pattern (4.125) is not equal to that of the array pattern (4.126). If (4.125) equals (4.126), the Condon lobes will be located at location A in Figure 4.1, which is undesirable. Regarding the antennas analysed in this work, the Condon lobes must be located at location B in Figure 4.1. They do not have to be located precisely at location B, and they must not be within the sum co-polarisation pattern (location A) as it does not represent a practical monopulse antenna with Condon lobes.

The focus was on the sum patterns [36], not the difference patterns. For (4.121) and (4.122) to be useful for cross-polarisation analysis, the difference patterns must be modelled. The azimuth co- and cross-polarisation difference antenna radiation patterns are modelled as

$$F_{az\Delta C}(\theta,\phi) = AP_\Delta(\theta,\phi)\left[\cos(\phi)\right] \tag{4.127}$$

$$F_{az\Delta X}(\theta,\phi) = k \times AP_\Delta(\theta,\phi)\left[\sin(\phi)\right], \tag{4.128}$$

where k is the constant used to set the magnitude of the cross-polarisation component. $AP_\Delta(\theta,\phi)$ is

$$AP_\Delta(\theta,\phi) = \sin(n_\Delta\theta)\,\mathrm{sinc}(n_\Delta\theta), \tag{4.129}$$

where n_Δ is the integer value used to control the beamwidth of the radiation pattern. The elevation antenna radiation patterns are

$$F_{el\Delta C}(\theta,\phi) = F_{az\Delta X}(\theta,\phi) \tag{4.130}$$

$$F_{el\Delta X}(\theta,\phi) = kF_{az\Delta C}(\theta,\phi). \tag{4.131}$$

The azimuth monopulse ratios are as follows

$$M_{azC}(\theta,\phi) = \frac{F_{az\Delta C}(\theta,\phi)}{F_{\Sigma C}(\theta,\phi)} \tag{4.132}$$

$$= \frac{AP_{\Delta}(\theta,\phi)[\cos(\phi)]}{AP_{\Sigma C}(\theta,\phi)\left[C_e\cos^2(\phi)+C_h\sin^2(\phi)\right]} \tag{4.133}$$

$$M_{azX}(\theta,\phi) = \frac{F_{az\Delta X}(\theta,\phi)}{F_{\Sigma X}(\theta,\phi)} \tag{4.134}$$

$$= \frac{k_X \times AP_{\Delta}(\theta,\phi)[\sin(\phi)]}{AP_{\Sigma X}(\theta,\phi)[(C_e-C_h)\sin(\phi)\cos(\phi)]}. \tag{4.135}$$

The elevation monopulse ratio

$$M_{elC}(\theta,\phi) = \frac{F_{el\Delta C}(\theta,\phi)}{F_{\Sigma C}(\theta,\phi)} \tag{4.136}$$

$$= \frac{AP_{\Delta}(\theta,\phi)[\sin(\phi)]}{AP_{\Sigma C}(\theta,\phi)\left[C_e\cos^2(\phi)+C_h\sin^2(\phi)\right]} \tag{4.137}$$

$$M_{elX}(\theta,\phi) = \frac{F_{el\Delta X}(\theta,\phi)}{F_{\Sigma X}(\theta,\phi)} \tag{4.138}$$

$$= \frac{k_X \times AP_{\Delta}(\theta,\phi)[\cos(\phi)]}{AP_{\Sigma X}(\theta,\phi)[(C_e-C_h)\sin(\phi)\cos(\phi)]}, \tag{4.139}$$

where k_X is the scaling factor used to scale the magnitude of the cross-polarisation patterns.

4.3 THEORETICAL RESULTS

4.3.1 Technique 1

The modelling in Section 4.2 generates the results in Figures 4.2 to 4.8. Figure 4.2 shows the modelling results from Technique 1 in Subsection 4.2.1. For azimuth plane $\phi = 0^\circ$ and elevation plane $\phi = 90^\circ$, the exact variable n location in (4.50) and (4.51) is introduced to (4.30), (4.31), (4.44), and (4.45) as $n = 5$. The variable n reduces the patterns' HPBW of the patterns; therefore, if there is no need to reduce the HPBW, it can be $n = 1$. The Σ and Δ patterns generated using $n = 5$ are shown in Figures 4.2(a) and 4.2(b), respectively. These results show only the co-polarisation patterns because the cross-polarisation patterns are zero. The Σ pattern has a peak magnitude at boresight, while the Δ pattern has a null at boresight as expected. The co-polarisation monopulse ratio of these principle planes is shown in Figure 4.2(e), and it must be noted that with the cross-polarisation patterns being zero, the cross-polarisation monopulse ratio is zero, resulting in the co-polarisation monopulse ratio being approximately equal to the combination of co and cross-polarisation monopulse ratios.

To generate the results for all the techniques at the $\phi = 45^\circ$ diagonal plane, the $E_\theta(\theta,45^\circ)$ and $E_\phi(\theta,45^\circ)$ of the designed antennas were analysed, and they showed similar behaviour $E_\theta(\theta,45^\circ)$ $\neq E_\phi(\theta,45^\circ)$. The $E_\theta(\theta,45^\circ)$ and $E_\phi(\theta,45^\circ)$ magnitudes for both sum and difference patterns were

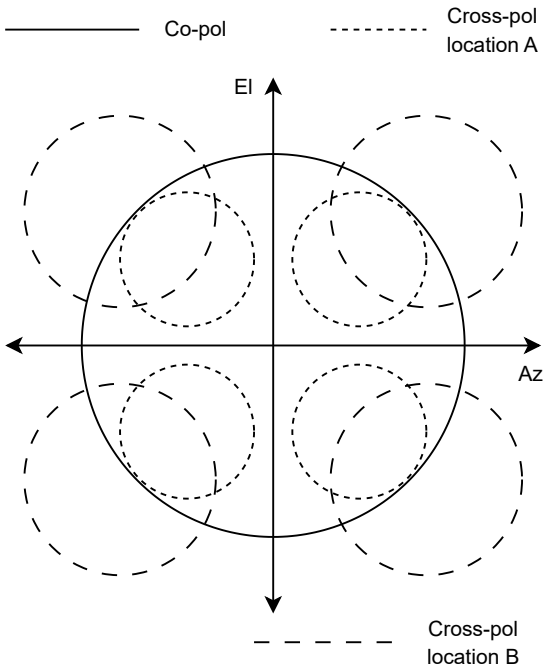

Figure 4.1. The effect of using the antenna pattern models with equal and unequal beamwidth to determine the sum co- and cross-polarisation pattern components. Location A happens when the antenna pattern model for sum co-and cross-polarisation has equal beamwidth, and location B happens when their beamwidth is unequal.

averaged at the main lobes of the wire-grid antenna. The values are $n_{\Sigma\theta} = 4.6180$, $n_{\Sigma\theta} = 5.2963$, $n_{\Delta\theta} = 2.8643$, and $n_{\Delta\phi} = 2.4919$. When these values are used as they are, they result in the second null of the cross-polarisation difference pattern not being aligned with the peak of the Condon lobe, which results in the offset not being aligned to the Condon lobe peak. These values are optimised to align the offset to the Condon lobe peaks, as shown in Figure 4.2(c).

At the $\phi = 45°$ diagonal plane, $n_{\Sigma\theta} = 5$, $n_{\Sigma\phi} = 4$ in (4.58) and (4.64). Then $n_{\Delta\theta} = 4$, $n_{\Delta\phi} = 3$ in (4.61) and (4.67). The diagonal plane results are shown in Figures 4.2(c) and 4.2(d). The Σ co-polarisation patterns have a peak at boresight, and their cross-polarisation patterns have a null at boresight. Condon lobes appear on their cross-polarisation patterns at ≈-22 dB less than the co-polarisation peak pattern. The cross-polarisation jammer uses the Condon lobes to jam the tracking radar; if the jammer has enough power to dominate the co-polarisation signal, the tracking radar is forced to use one of the Condon lobes as an Σ lobe [12]. The co and cross-polarisation Δ patterns both have a null at boresight. The tracking radar uses boresight as the tracking equilibrium. As the cross-polarisation jamming

is introduced, a new tracking equilibrium is introduced, as shown in Figure 4.2(c). An offset of 20° from boresight tracking equilibrium to a new equilibrium is seen. The tracking radar will use this new peak lobe and the difference patterns. The monopulse ratios in Figure 4.2(d) show that the cross-polarisation pattern results in a distorted monopulse ratio at boresight, but at the offset angle of 20° the cross-polarisation monopulse ratio behaves like the co-polarisation monopulse ratio.

The angular error is investigated by determining the minimum JSR needed to break lock, to determine the angular error (2.7) and (2.8) are derived into,

$$M_s = \tan\left\{\beta \cdot \frac{d}{2} \cdot \sin(\theta)\right\} \tag{4.140}$$

$$\sin(\theta) = \frac{2}{\beta \cdot d}\tan^{-1}(M_s) \tag{4.141}$$

$$\theta = \sin^{-1}\left\{\frac{2}{\beta \cdot d}\tan^{-1}(M_s)\right\}. \tag{4.142}$$

In a practical cross-polarisation jamming situation, the monopulse ratio (M_s) contains both the jammer (J) co- and cross-polarisation components and both the radar (R) co- and cross-polarisation components as

$$M_s = \frac{E_{\Delta R} + E_{\Delta J}}{E_{\Sigma R} + E_{\Sigma J}} \tag{4.143}$$

$$E_{\Delta R} = E_{\Delta R(C)} + E_{\Delta R(X)} \tag{4.144}$$

$$E_{\Delta J} = E_{\Delta J(C)} + E_{\Delta J(X)} \tag{4.145}$$

$$E_{\Sigma R} = E_{\Sigma R(C)} + E_{\Sigma R(X)} \tag{4.146}$$

$$E_{\Sigma J} = E_{\Sigma J(C)} + E_{\Sigma J(X)}, \tag{4.147}$$

Then

$$M_s = \frac{(E_{\Delta R(C)} + E_{\Delta R(X)}) + (E_{\Delta J(C)} + E_{\Delta J(X)})}{(E_{\Sigma R(C)} + E_{\Sigma R(X)}) + (E_{\Sigma J(C)} + E_{\Sigma J(X)})}. \tag{4.148}$$

In this analysis, the objective is to see the direct influence of the cross-polarisation signal on the tracking accuracy. Therefore, the monopulse ratio is used as

$$M_s = \frac{E_{\Delta R}}{E_{\Sigma R}} \tag{4.149}$$

$$E_{\Delta} = E_{\Delta C} + E_{\Delta X} \tag{4.150}$$

$$E_{\Sigma} = E_{\Sigma C} + E_{\Sigma X}, \tag{4.151}$$

then

$$M_s = \frac{E_{\Delta C} + E_{\Delta X}}{E_{\Sigma C} + E_{\Sigma X}}, \tag{4.152}$$

where $E_{\Delta X}$ and $E_{\Sigma X}$ are the difference and sum patterns of the cross-polarisation jammer, respectively, and $E_{\Delta C}$ and $E_{\Sigma C}$ are the difference and sum patterns of the tracking radar respectively. In a practical cross-polarisation jamming scenario, the tracking radar will receive both the target skin-return and the jamming signal, and both of them have co- and cross-polarisation components. But in this work, a cross-polarisation component is used as the cross-polarisation jamming signal, and the co-polarisation component is the target skin-return to determine the induced angular error in Fig. 4.8. This is because around boresight in Figure 4.2(c), the cross-polarisation signal is so small that it may be ignored. The co-polarisation signal may be used on its own as the tracking signal, and the cross-polarisation signal may be used as a jamming signal. This also shows the direct effect of increasing the cross-polarisation signal power while the co-polarisation signal is constant because the JSR is determined as the ratio of the cross-polarisation signal to the co-polarisation signal.

The angular error is analysed in the diagonal plane as this plane has Condon lobe peaks in the cross-polarisation patterns, while the principal planes have zero cross-polarisation. Initially, the co- and cross-polarisation patterns are as shown in Figure 4.2(c), with he AOA being off-boresight at $\theta = 1^\circ$ and $\phi = 45^\circ$. The effect of increasing the cross-polarisation signal while keeping the co-polarisation signal constant is seen in Figure 4.8(a). There are three stages: S1, S2, and S3. Stage S1 is where the cross-polarisation jamming power does not affect the tracking radar as the polarisation purity is high. As the JSR reaches ≈-40 dB, the angular error starts to increase, and when it reaches JSR = 0 dB, it stabilises. In stage S2, the angular error is increasing, but this is not a break-lock stage because the tracking radar still shows influence. However, in stage S3, the angular error is constant, showing that the tracking radar does not have an influence, and this is the break-lock stage. The results show that the cross-polarisation jammer reaches break-lock when JSR > 15 dB for Technique One.

4.3.2 Technique 2

The results generated from the mathematical modelling in Subsection 4.2.2 are shown in Figure 4.3. In the $\phi = 0^\circ$ azimuth plane, $n_{\Sigma\phi 1} = n_{\Sigma\phi 2} = 2$ in (4.82) and $n_{\Delta\phi 1} = 5$, $n_{\Delta\phi 2} = 2$ in (4.83). In the $\phi = 90^\circ$ elevation plane $n_{\Sigma\theta 1} = 3$, $n_{\Sigma\theta 2} = 2$ in (4.95) and $n_{\Delta\theta 1} = 5$, $n_{\Delta\theta 2} = 2$ in (4.96). The focus of Technique 2 is demonstrating how cross-polarisation jamming works. It is seen that the SLLs are high, but this is not the focus, and the Σ SLL does not help in analysing cross-polarisation jamming. The Σ patterns for azimuth and elevation planes are shown in Figure 4.3(a), and they have a peak at boresight as expected. The Δ patterns have a null at boresight, as seen in Figure 4.3(b). The monopulse ratio in azimuth and elevation planes are shown in Figure 4.3(e); with the cross-polarisation patterns being zero, the

cross-polarisation monopulse ratio is also zero.

In the $\phi = 45^\circ$ diagonal plane, $n_{\Sigma\theta 1} = 1$, $n_{\Sigma\theta 2} = 3$, $n_{\Sigma\phi 1} = 1$, and $n_{\Sigma\phi 2} = 2$ in (4.107) and (4.110). Then $n_{\Delta\theta 1} = 3$, $n_{\Delta\theta 2} = 1$, $n_{\Delta\phi 1} = 6$, and $n_{\Delta\phi 2} = 1$ in (4.113) and (4.116). The co and cross-polarisation patterns are shown in Figure 4.3(c), where the Σ co-polarisation patterns have a peak at boresight, and its cross-polarisation patterns have a null at boresight with Condon lobes $\approx$ -25 dB less than the co-polarisation pattern peak. Both the co- and cross-polarisation Δ patterns have a null at boresight. The tracking equilibrium is shifted from boresight (0°, 0) to a new tracking equilibrium (35°, 0) by an offset angle of 35°. The monopulse ratios in Figure 4.3(e) also show the new tracking equilibrium.

The same procedure used in subsection 4.3.1 is used in this Subsection. Initially, the co and cross-polarisation patterns are as shown in Figure 4.3(c) with $\theta = 1^\circ$ off-boresight. The angular error results for increasing the cross-polarisation signal power while keeping the co-polarisation signal constant are shown in Figure 4.8(a). Three stages are shown; in stage S1, the jammer does not induce angular error but starts to induce angular error in stage S2, where the angular error reaches stabilisation at JSR > 0 dB. Stage S3 is the break-lock stage, as the angular error is constant, and the tracking radar signal shows no influence. In Technique 2, the jammer reaches break-lock at JSR $\geq$ 20 dB.

4.3.3 Technique 3

The results generated from mathematical modelling in Subsection 4.2.3 are presented in this subsection. $n_{\Sigma C} = 4$ in (4.125), $n_{\Sigma X} = 2$ in (4.126), $n_{\Delta} = 5$ in (4.129), and $k_X = 0.05$. This technique demonstrates an axially symmetrical monopulse antenna with four sub-antennas. For a parabolic monopulse antenna, this representation would be referenced as a parabolic reflector antenna with four horn feeds. The radiation patterns are shown in Figure 4.4. The Σ co-polarisation pattern in Figure 4.4(a) shows a peak at boresight, and its cross-polarisation pattern in Figure 4.4(b) has a null at boresight and across the azimuth and elevation planes, and Condon lobes in the diagonal planes. The co- and cross-polarisation Δ patterns are shown in Figure 4.4(c) and Figure 4.4(d) respectively. The azimuth Δ co-polarisation pattern has lobes across the azimuth axis, and a null across the elevation axis, and its cross-polarisation patterns have a null across the azimuth axis and lobes across the elevation axis. The elevation Δ co-polarisation pattern has lobes across the elevation axis, and a null across the azimuth axis, and its cross-polarisation patterns have a null across the elevation axis and lobes across the azimuth axis as seen in Figures 4.4(e) and 4.4(f).

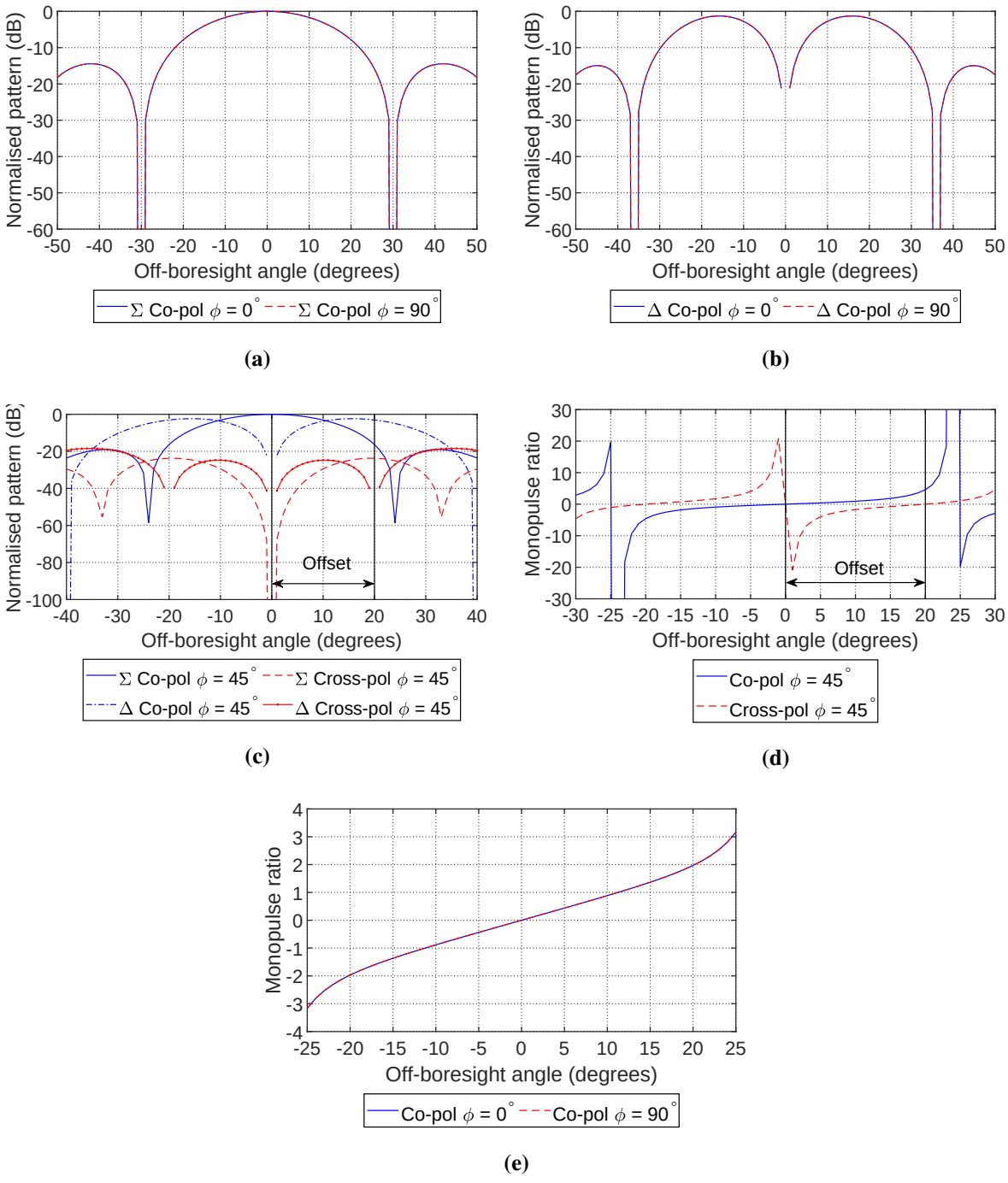

Figure 4.2. Technique 1 simulation results, (a) sum pattern in both azimuth and elevation planes, (b) difference patterns in both azimuth and elevation planes, (c) sum and difference patterns in the diagonal plane, (d) monopulse ratio at the diagonal plane, and (e) azimuth and elevation plane monopulse ratios.

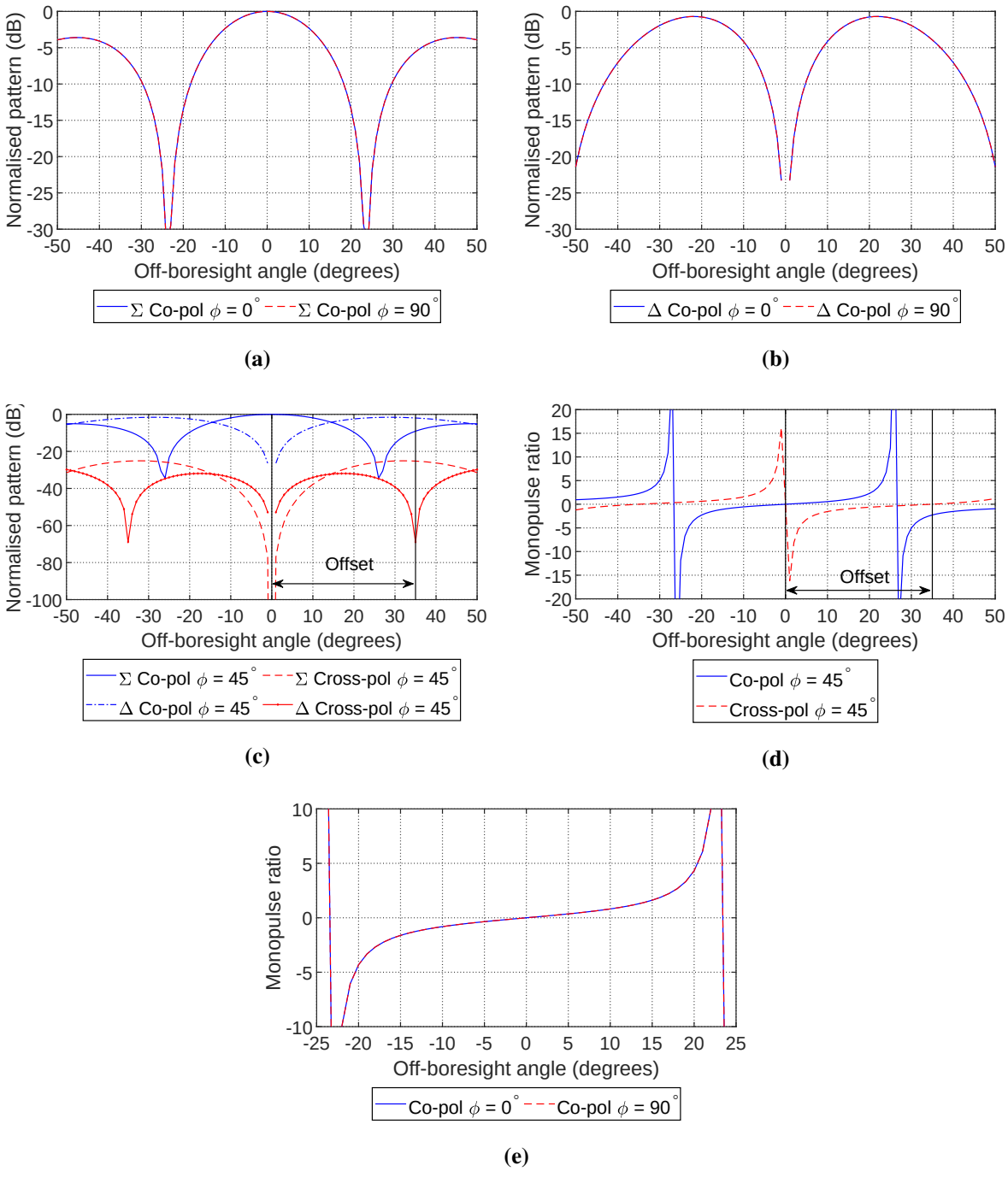

Figure 4.3. Technique 2 simulation results, (a) sum pattern in both azimuth and elevation planes, (b) difference patterns in both azimuth and elevation planes, (c) sum and difference patterns in the diagonal plane, (d) monopulse ratios at the diagonal plane, and (e) azimuth and elevation plane monopulse ratio.

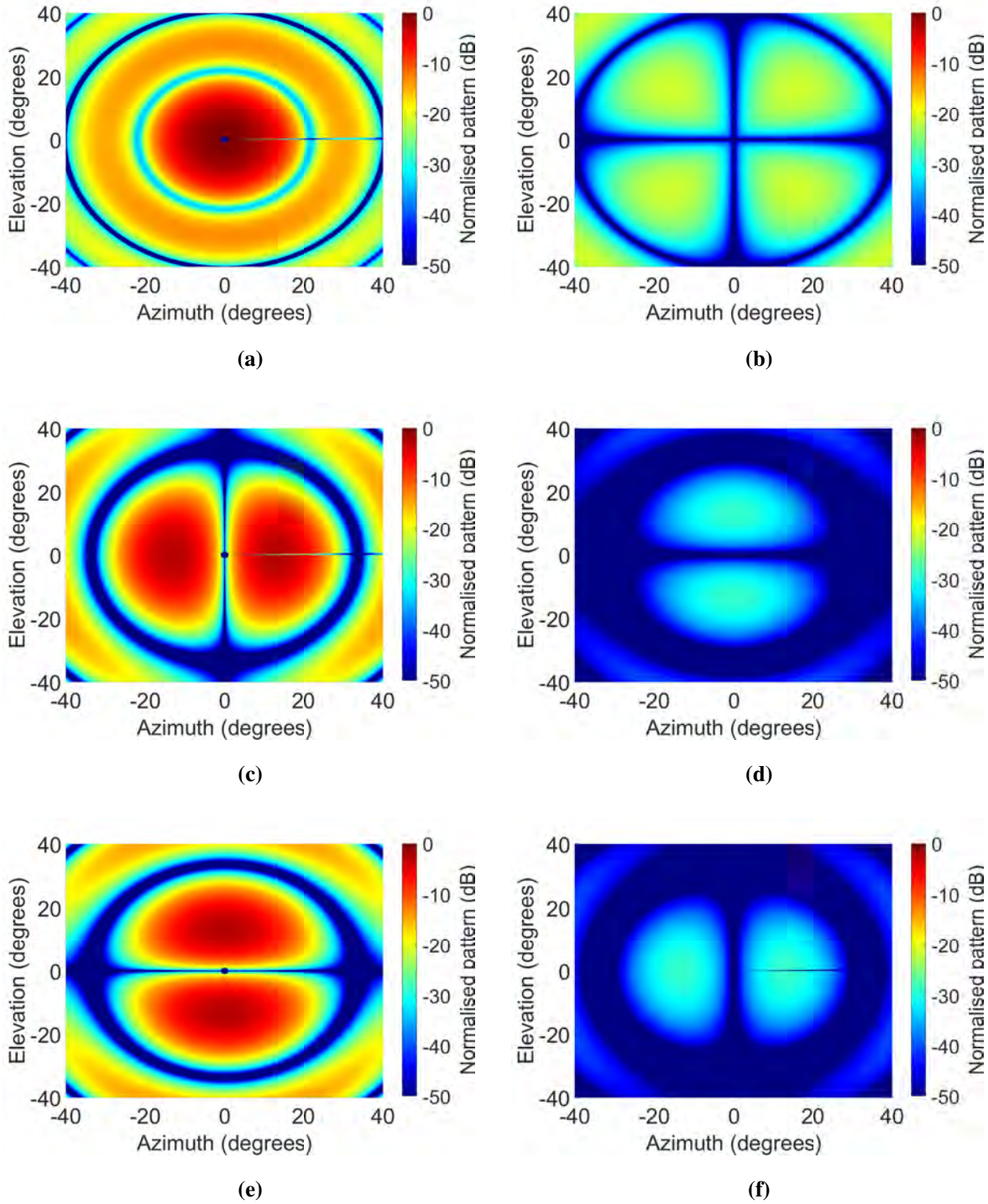

Figure 4.4. Technique 3 simulation results, (a) co-polarisation sum pattern, (b) cross-polarisation sum pattern, (c), co-polarisation azimuth difference pattern, (d) cross-polarisation azimuth difference pattern, (e) co-polarisation elevation difference pattern, and (f) cross-polarisation elevation difference pattern.

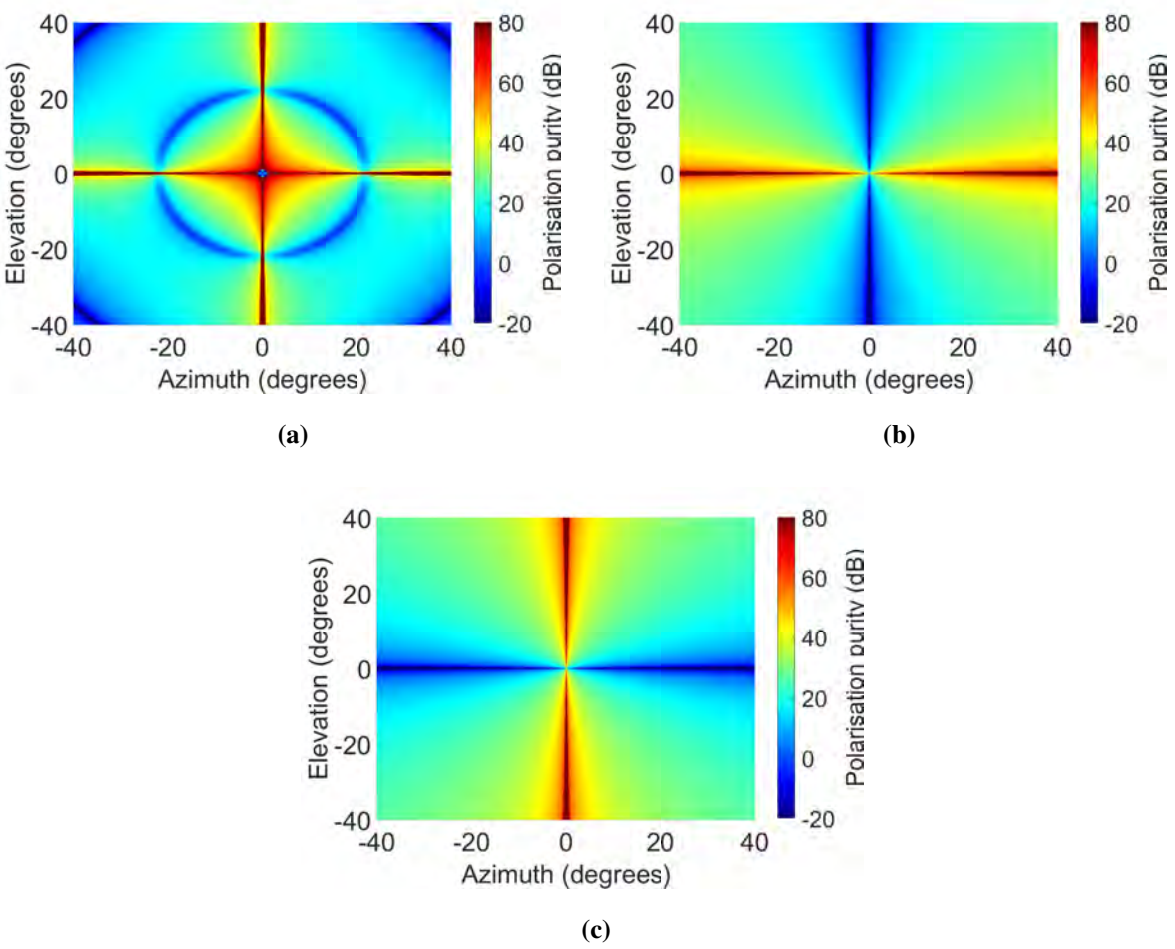

Figure 4.5. Technique 3 polarisation purity simulation results, (a) sum channel, (b) azimuth difference channel, (c), elevation difference channel.

The polarisation purity results are shown in Figure 4.5. They are computed by dividing the co-polarisation patterns by the cross-polarisation patterns. The higher the polarisation purity, the higher the JSR to jam the radar. The Σ polarisation purity is shown in Figure 4.5(a); the polarisation purity is higher across the azimuth and elevation axis, and it is due to the nulls in the Σ cross-polarisation patterns azimuth and elevation axes; the polarisation purity is also higher, close to boresight. The polarisation purity is less in the diagonal planes, which is expected as these planes have Condon lobes. The azimuth and elevation polarisation purity are shown in Figures 4.5(b) and 4.5(c), respectively. It is seen that for the azimuth polarisation purity, the purity is high across the azimuth axis. In the elevation polarisation purity, the purity is high across the elevation axis. However, the purity is less towards the diagonal plane. The decrease in the polarisation purity in the diagonal plane favours the cross-polarisation jammer as it will need less JSR compared to jamming at the principal planes.

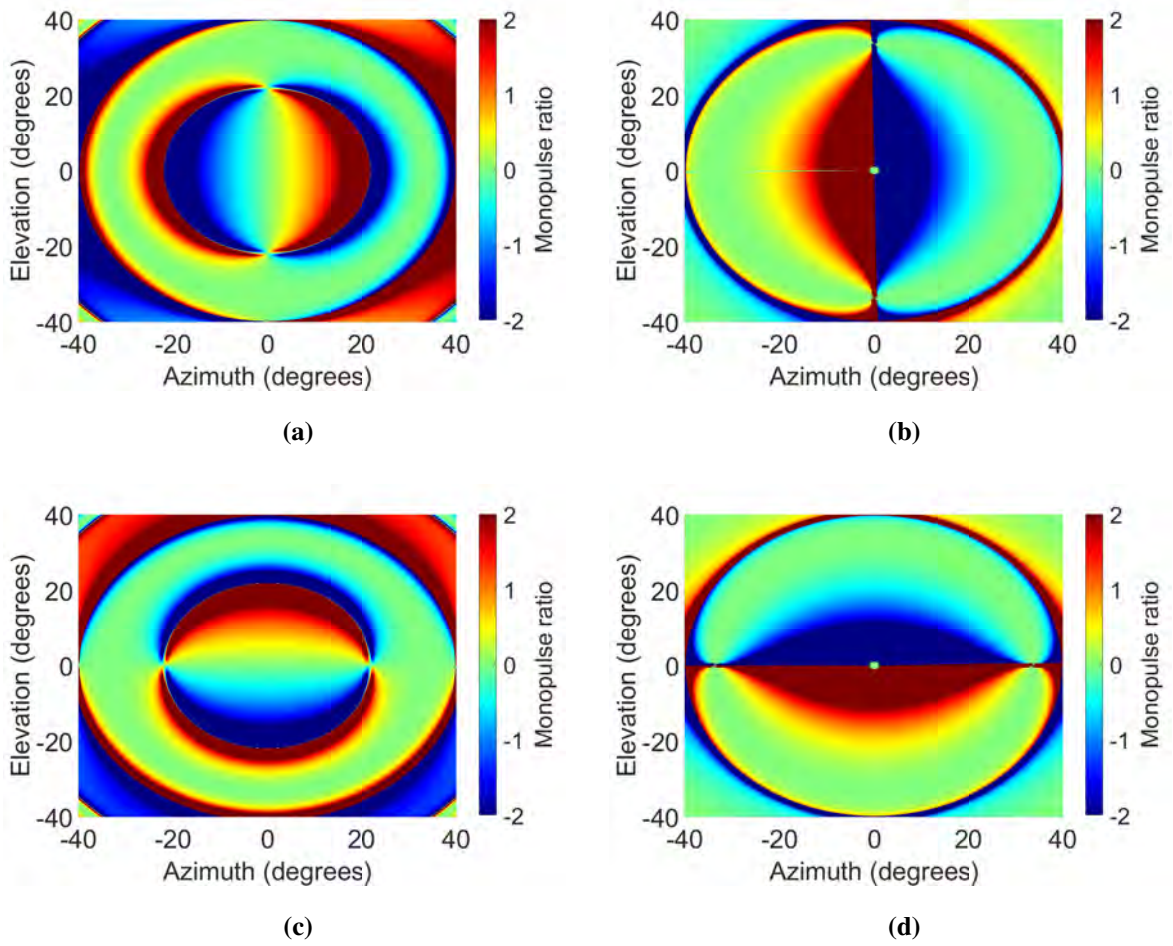

Figure 4.6. Technique 3 monopulse ratio simulation results, (a) co-polarisation azimuth plane, (b) cross-polarisation azimuth plane, (c), co-polarisation elevation plane, and (d), cross-polarisation elevation plane.

The monopulse ratios are shown in Figure 4.6. For the co-polarisation monopulse ratios, there is a smooth transition from high to low in both the azimuth and elevation axis. The cross-polarisation monopulse ratio shows a steep transition from low to high across the relevant axis. The spherical coordinate results for Technique 3 are presented, but it is essential to show the results when the patterns in Figures 4.4 and 4.6 are cut at the diagonal plane. Figure 4.7 shows the diagonal plane results, and it is seen that the offset tracking equilibrium is at 35° off-boresight, and the cross-polarisation patterns are $\approx$ -32 dB less than the co-polarisation patterns. The angular error results are shown in Figure 4.8(c). These angular error results show that the jammer in Technique 3 reaches break-lock at JSR $\geq$ 15 dB. The angular error results for all the techniques show that the jammer break-lock at different JSR, but for all of them, the break-lock happens at JSR $\geq$ 0 dB and at different angular error values.

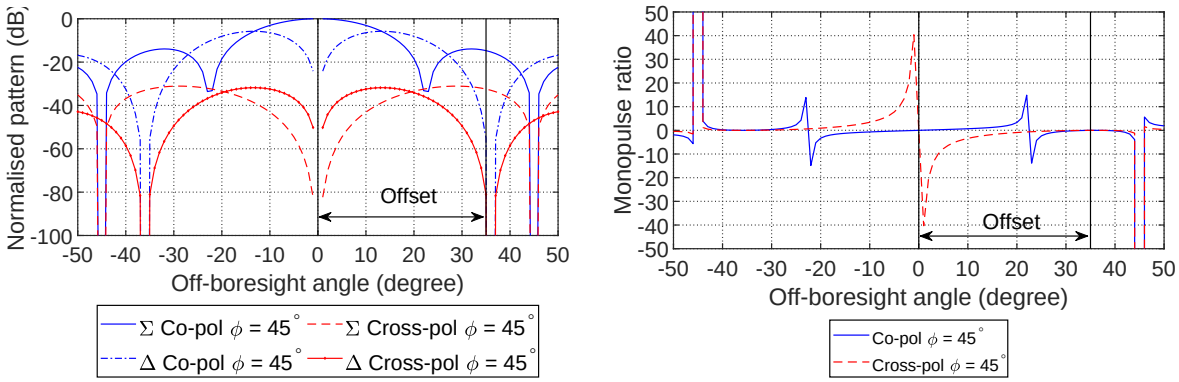

(a) **(b)**

Figure 4.7. Technique 3 diagonal plane simulation results, (a), sum and difference patterns and (b) diagonal plane monopulse ratios.

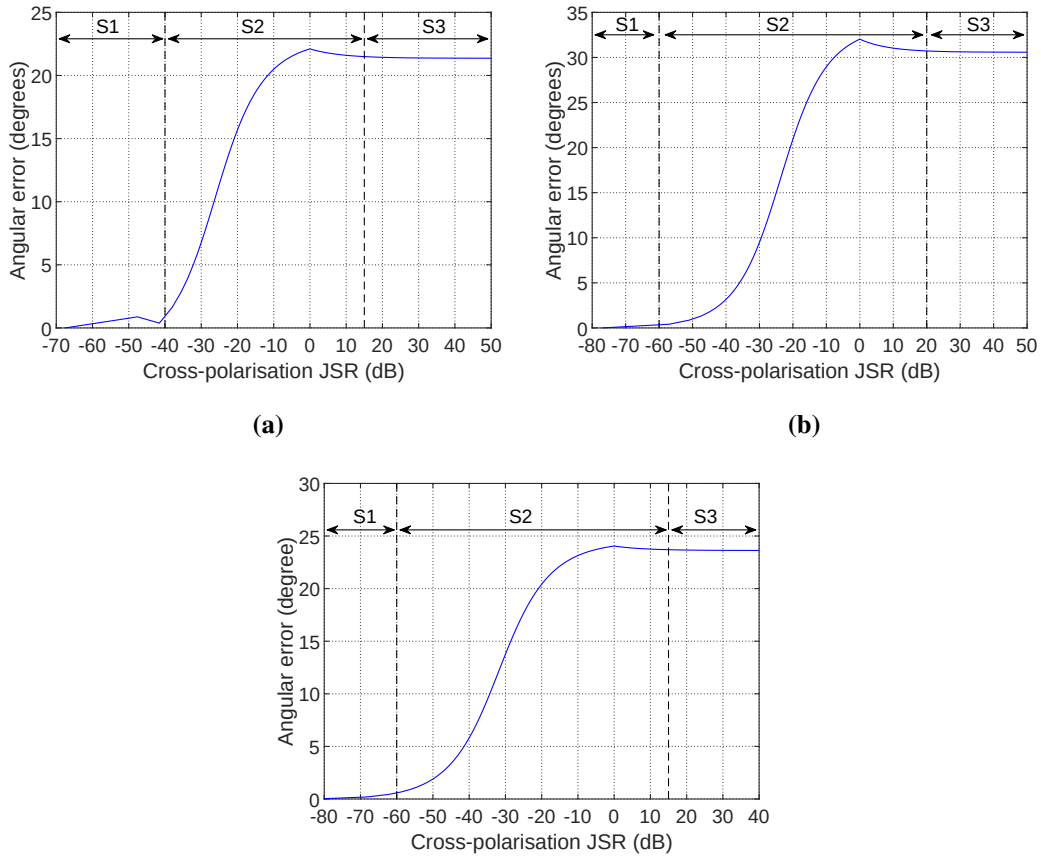

(a) **(b)**

(c)

Figure 4.8. The diagonal plane angular error results for the three techniques, (a), technique 1 $\theta = 1°$, (b) technique 2 $\theta = 1°$, and(c) technique 3 $\theta = 1°$.

4.4 CHAPTER SUMMARY

The co-and cross-polarisation patterns are modelled mathematically. These models have characteristics seen in the analysed antennas, which are characteristics of phase-comparison monopulse antennas. The theoretical results are also presented, and they show that the three techniques used to model the patterns have similar characteristics to the analysed antennas.

CHAPTER 5 RESULTS

5.1 CHAPTER OVERVIEW

This chapter presents the simulation and measurement results for this dissertation. Section 5.2 discusses the Feko simulation results between the wire-grid antenna and the Hannan parabolic reflector antenna in the transmitting and receiving modes. Section 5.3 discusses the Feko simulation results of the Cassegrain monopulse antenna in the transmitting and receiving modes. Section 5.4 discusses the Feko simulation results of the Hanna Cassegrain monopulse antenna results in the transmitting and receiving modes, and Section 5.5 discusses the Feko simulation results of the monopulse horn antenna in the transmitting and receiving modes. Section 5.6 discusses the induced angular error when the target moves from boresight towards and outside the 3 dB beamwidth. Section 5.7 discusses the effects of symmetry and asymmetry of the antenna radiating elements and the symmetry and asymmetry of the antenna feeding network on the Condon lobes using an aperture-coupled monopulse antenna. Section 5.8 discusses the effects of F/D on the Condon lobes in parabolic reflector antennas, and Section 5.9 discusses the measurement results of the wire-grid antenna.

5.2 MICROSTRIP PLANAR ANTENNA AND PARABOLIC REFLECTOR ANTENNA

5.2.1 Transmitting mode of the microstrip planar antenna vs parabolic reflector antenna

The co-polarisation and cross-polarisation monopulse antenna radiation patterns are shown in Figures 5.1 and 5.2, respectively. In the results, θ is the off-boresight angle and ϕ angle represents the antenna pattern planes. The azimuth plane $\phi = \pm 0^\circ$ is the XZ plane, the elevation plane $\phi = \pm 90^\circ$ is the YZ plane, and the diagonal planes are between +X+Y plane, -X+Y plane, +X-Y plane, and -X-Y plane. The azimuth plane is also referred to as $\phi = \pm 0^\circ$ plane, the elevation plane is referred to as $\phi = \pm 90^\circ$ plane, and the diagonal plane is the $\phi = \pm 45^\circ$ plane. For the wire-grid antenna co-polarisation results, the sum channel has a peak on the boresight axis, and the azimuth difference channel and elevation difference channel have nulls at their axis; this is seen in Figures 5.1(a), 5.1(c), and 5.1(e)

respectively.

The wire-grid antenna has similarities to the Hannan parabolic reflector antenna co-polarisation results shown in Figures 5.1(b), 5.1(d), and 5.1(f). The cross-polarisation results in Figure 5.2 differ from the co-polarisation results. The cross-polarisation sum channel in Figures 5.2(a) and 5.2(b) has nulls at the boresight axis and peaks at $\pm 45^\circ$ and $\pm 135^\circ$ planes. Suppose a power that is greater than that of the co-polarisation signal is applied to the cross-polarisation signal; the tracking radar will be forced to use one of the Condon lobes for tracking, which is located at a different orientation to the co-polarisation main lobe [9], and this will steer the tracking radar away from the target. In the difference patterns, the nulls are interchanged in the co-polarisation and cross-polarisation. The co-polarisation azimuth difference pattern has a null along the elevation boresight axis. The cross-polarisation azimuth difference pattern has a null along the azimuth boresight axis, and the same applies to the elevation difference signals. These co-polarisation and cross-polarisation patterns differ, which may cause tracking distortion if the cross-polarisation component is used as a main polarisation component for tracking. The cross-polarisation patterns in Figure 5.2 show that the wire-grid antenna has Condon lobes with higher magnitude compared to the Hannan parabolic reflector antenna; these are the results of how the antennas were designed. The Hannan parabolic reflector has a lower cross-polarisation because it has a higher F/D, and this means more power is needed to jam the Hannan parabolic reflector than the wire-grid antenna using the cross-polarisation jamming technique [33].

The polarisation purity is given by the co-polarisation pattern divided by the cross-polarisation pattern. The polarisation purity of the Hannan parabolic reflector antenna is higher than that of the wire-grid antenna; the reason for this is that the Hannan parabolic antenna has low cross-polarisation compared to the wire-grid antenna, as explained in the previous paragraph. The polarisation purity of the antenna pattern is shown in Figure 5.3. There is a higher polarisation purity along the azimuth and elevation boresight axis for the sum channel in Figures 5.3(a) and 5.3(b). The polarisation purity is also higher across the ϕ angles for the sum pattern. However, the cross-polarisation jamming takes advantage of the Condon lobes at $\phi = \pm 45^\circ$ diagonal plane. It is seen in the difference patterns in Figures 5.3(c), 5.3(e), 5.3(d), and 5.3(f) that the polarisation purity in these diagonal angles is lower than at the boresight axis, and this may be the weakness the cross-polarisation jammer can explore [33].

The monopulse radar uses the monopulse ratio to track the target [33]. The monopulse ratio of the

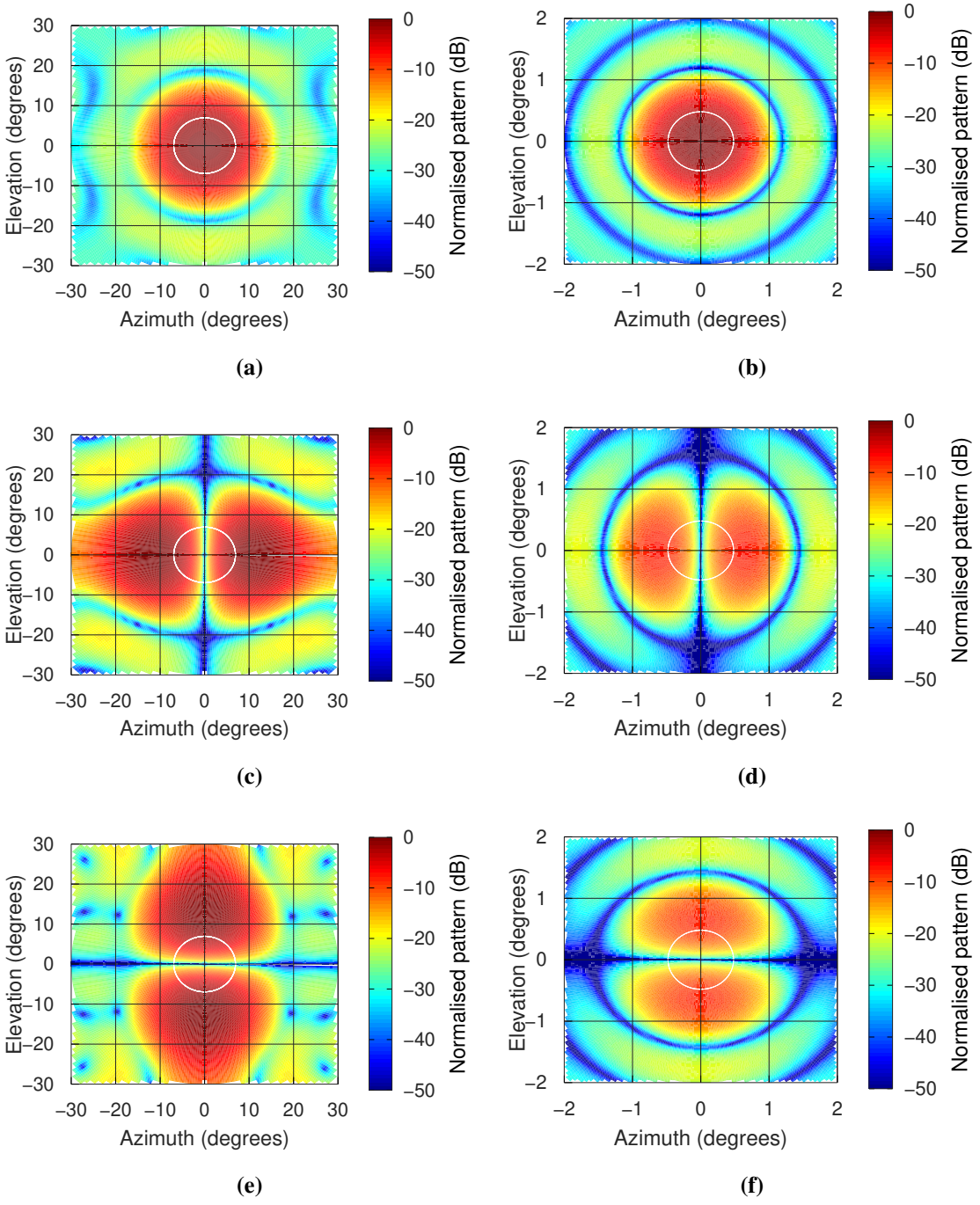

Figure 5.1. The co-polarisation monopulse antenna patterns at the (a) sum pattern, (c) azimuth difference pattern, and (e) elevation difference pattern for the wire-grid antenna. The (b) sum pattern, (d) azimuth pattern, and (f) elevation pattern for the Hannan reflector antenna. The white circle is the -3 dB beamwidth of the antennas [33].

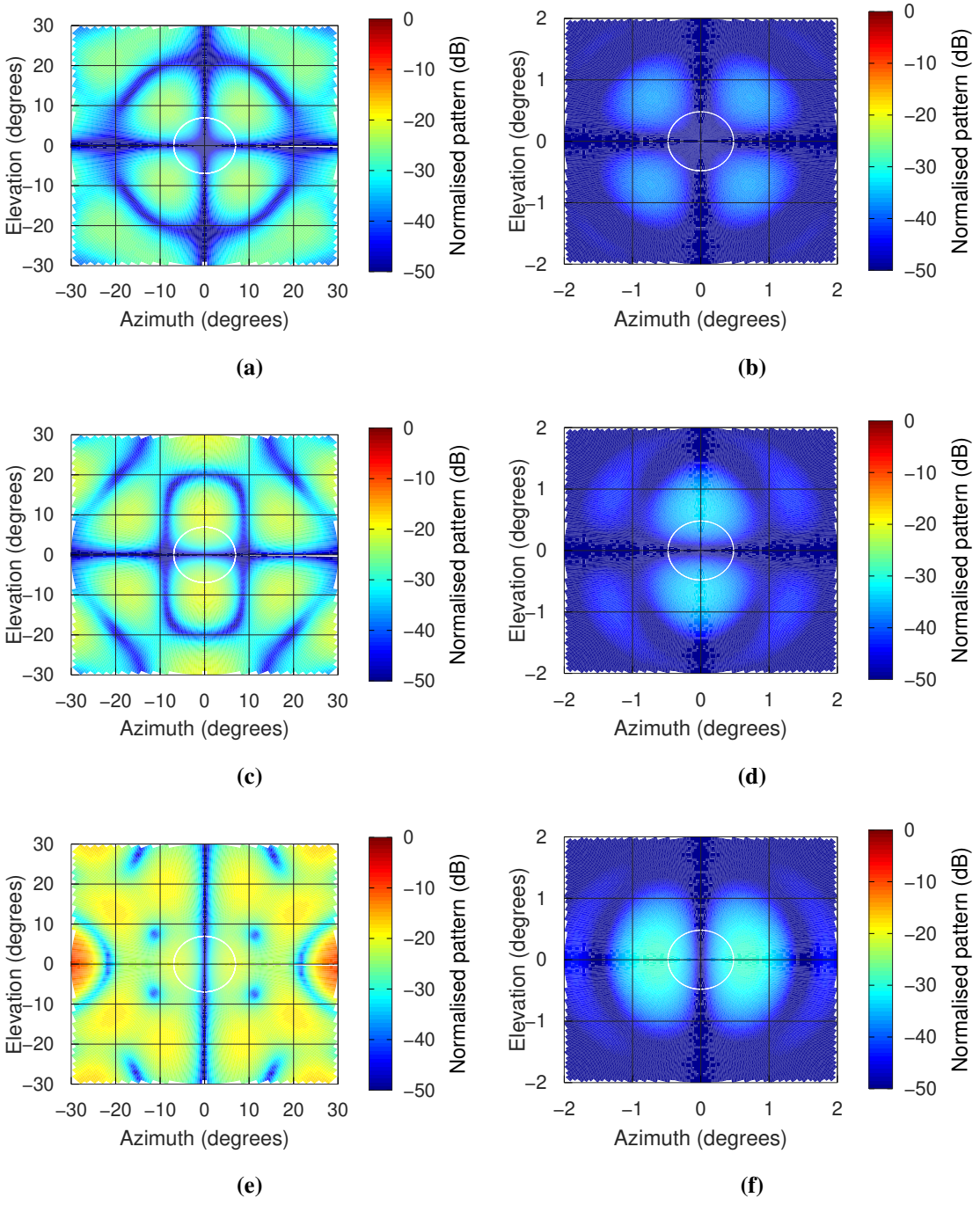

Figure 5.2. The cross-polarisation monopulse antenna patterns at the (a) sum pattern, (c) azimuth difference pattern, and (e) elevation difference pattern for the wire-grid antenna. The (b) sum pattern, (d) azimuth pattern, and (f) elevation pattern for the Hannan reflector antenna. The white circle is the –3 dB beamwidth of the antennas [33].

antennas in the azimuth and elevation planes is shown in Figures 5.4 and 5.5, respectively. There is a higher slope difference in the co-polarisation and cross-polarisation monopulse ratio, as shown in Figures 5.4(a) and 5.4(b); this is because of the peak at the co-polarisation sum pattern and the null at the cross-polarisation sum pattern. The peak at the co-polarisation sum patterns results in a monopulse ratio with a smooth transition slope from high to low, and the null at the cross-polarisation sum patterns results in a steep transition from low to high monopulse ratio.

5.2.2 Receiving mode of the microstrip planar antenna vs parabolic reflector antenna

The radar antennas are analysed in the receiving mode to investigate their response to the co-polarised and cross-polarised signal components. The plane-wave in Feko EM software is used to transmit the jamming signal, and the setup is shown in Figure 3.1. The .out file in Feko EM software gives the Ludwig-III polarisation angles used in the plane wave. Assuming β represents the co-polarisation angle of the antenna at a specific (ϕ,θ) coordinate, the cross-polarisation is [29]

$$X = \beta \pm 90^{\circ}, \tag{5.1}$$

and it is used to find the equivalent orthogonal polarisation angles to the angles calculated by Feko EM software. Tables 5.1 and 5.2 show the polarisation angles and (ϕ,θ) directions used in the plane wave that was used to generate the following results. In [29], the basic polarisation alignment concept is that at the antenna plane ϕ, the antenna co-polarisation (β) is $\beta = \phi$, and the cross-polarisation is $\beta \pm 90^{\circ}$ [29]. It also states that it depends on the position of the measured antenna [29]. Therefore, the angles in the tables are used in the plane wave.

5.2.2.1 Monopulse antennas radiation patterns

The radiation patterns of the two antennas in the three planes are shown in Figure 5.6. These are the same as the results shown in the spherical coordinates in Figures 5.1 and 5.2 transmitting mode. The similarities between the transmitting and receiving modes are due to the antennas' reciprocity [37]. The azimuth plane results $\phi = 0^{\circ}$ for the wire-grid antenna and the Hannan parabolic reflector are shown in Figures 5.6(a) and 5.6(b), respectively. The wire-grid antenna cross-polarisation patterns cannot be used for cross-polarisation jamming because, in this plane, the polarisation isolation is $\approx$ 100 dB. For the Hannan parabolic reflector, the cross-polarisation pattern has the same shape as the co-polarisation patterns. However, their magnitude is different, with the polarisation isolation being $\approx$ 65 dB, which is still high and cannot be used for cross-polarisation jamming. The elevation plane $\phi = 90^{\circ}$ results in Figures 5.6(e) and 5.6(f) are almost identical to the azimuth results. The results in the diagonal plane $\phi = 45^{\circ}$ are shown in Figures 5.6(c) and 5.6(d); the cross-polarisation sum channel signal has a null at $\theta = 0^{\circ}$ instead of a peak. This effect is expected as both antennas have the Condon

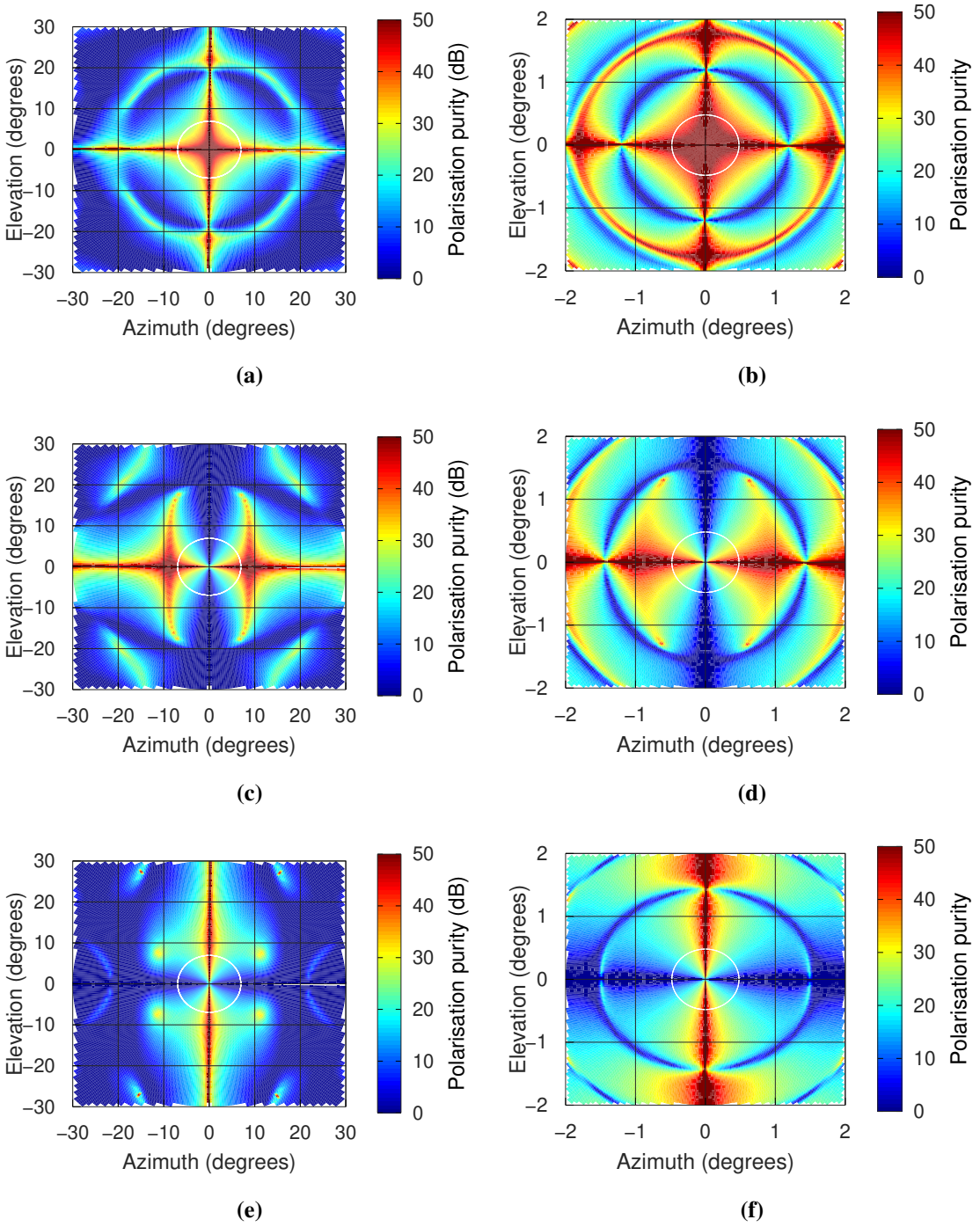

Figure 5.3. The polarisation purity of the (a) sum signals, (c) azimuth difference signals, and (e) elevation difference signal for the wire-grid antenna. The the (b) sum signal, (d) azimuth signal, and (f) elevation signal for the Hannan reflector antenna. The white circle is the –3 dB beamwidth of the antennas [33].

Table 5.1. The polarisation angles of the plane wave received by the wire-grid antenna.

θ	ϕ	Co-Pol	Cross-Pol	ϕ	Co-Pol	Cross-Pol	ϕ	Co-Pol	Cross-Pol
0	0	90	0	45	135.00	45.00	90	180	90
1	0	90	0	45	135.06	45.06	90	180	90
2	0	90	0	45	135.24	45.24	90	180	90
3	0	90	0	45	135.55	45.55	90	180	90
4	0	90	0	45	135.99	45.99	90	180	90
5	0	90	0	45	136.57	46.57	90	180	90
6	0	90	0	45	137.30	47.30	90	180	90
7	0	90	0	45	138.19	48.27	90	180	90
8	0	90	0	45	139.27	49.27	90	180	90
9	0	90	0	45	140.55	50.55	90	180	90
10	0	90	0	45	142.02	52.02	90	180	90
11	0	90	0	45	143.90	53.90	90	180	90
12	0	90	0	45	146.08	56.08	90	180	90
13	0	90	0	45	148.73	58.73	90	180	90
14	0	90	0	45	151.99	61.99	90	180	90
15	0	90	0	45	156.11	66.11	90	180	90

Table 5.2. The polarisation angles of the plane wave received by the Hannan parabolic reflector antenna.

θ	ϕ	Co-Pol	Cross-Pol	ϕ	Co-Pol	Cross-Pol	ϕ	Co-Pol	Cross-Pol
0	0	89.95	-0.05	45	134.95	44.95	90	180	90
0.1	0	89.95	-0.05	45	134.96	44.94	90	180	90
0.2	0	89.95	-0.05	45	135.02	45.02	90	180	90
0.4	0	89.95	-0.05	45	135.27	45.27	90	180	90
0.6	0	89.94	-0.06	45	135.79	45.79	90	180	90
0.8	0	89.94	-0.06	45	136.91	46.91	90	180	90
1	0	89.95	-0.07	45	140.18	50.18	90	180	90

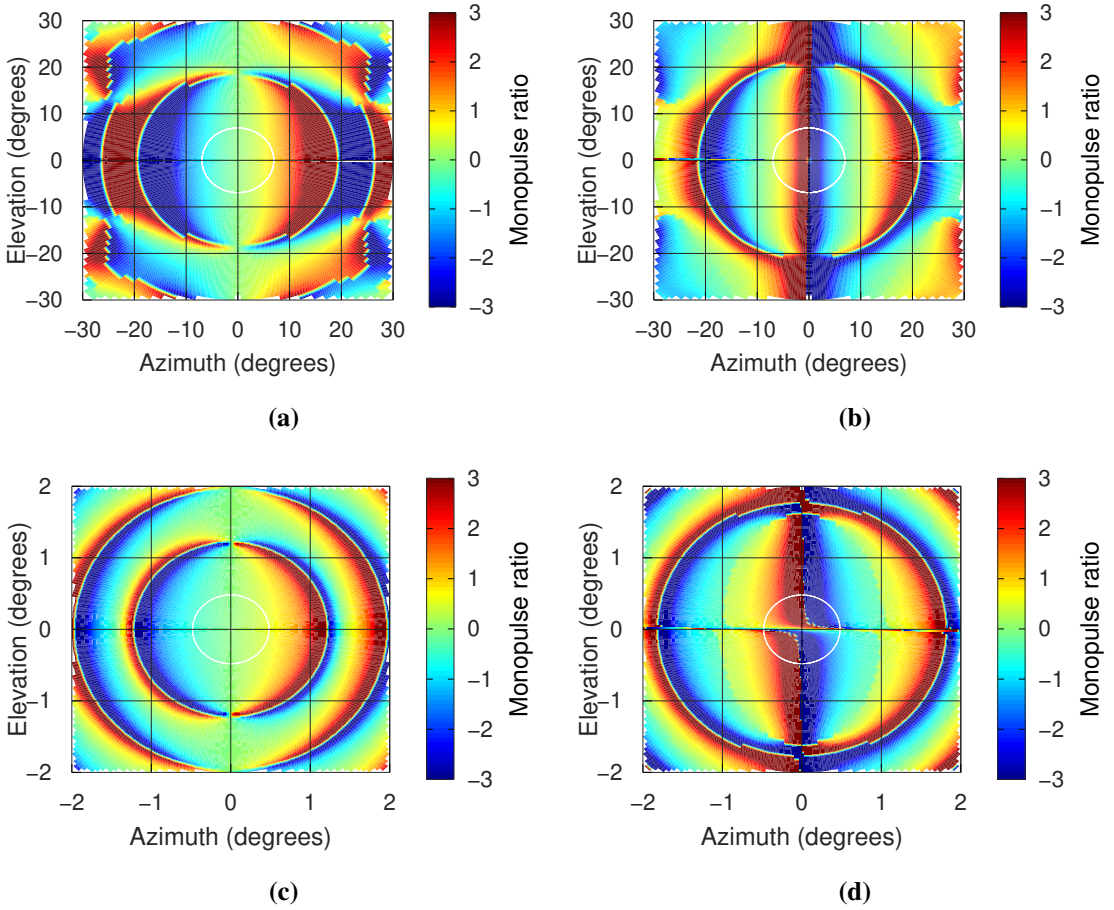

Figure 5.4. The azimuth plane monopulse ratio at (a) co-polarisation, and (b) cross-polarisation for the wire-grid antenna. Then at (c) co-polarisation, and (d) cross-polarisation for the Hannan parabolic reflector. The white circle is the –3 dB beamwidth of the antennas [33].

lobes at the diagonal planes. Cross-polarisation uses this effect to induce angular error in the tracking radar. The polarisation isolation between the co- and cross-polarisation sum channels is $\approx$ 20 dB for the wire-grid antenna, and it is $\approx$ 30 dB for the Hannan parabolic reflector, which is understandable, as it was previously noted in Figure 5.3, that the parabolic reflector has a higher polarisation purity than the wire-grid antenna.

5.2.2.2 Monopulse ratio

The monopulse ratio of the antennas is shown in Figure 5.7. The monopulse ratio in the azimuth plane for the wire-grid antenna and the Hannan parabolic reflector is shown in Figures 5.7(a) and 5.7(b), respectively. The elevation plane monopulse ratios are in Figures 5.7(e) and 5.7(f); these results show that the antennas have no cross-polarisation at the boresight axis. The diagonal plane results in

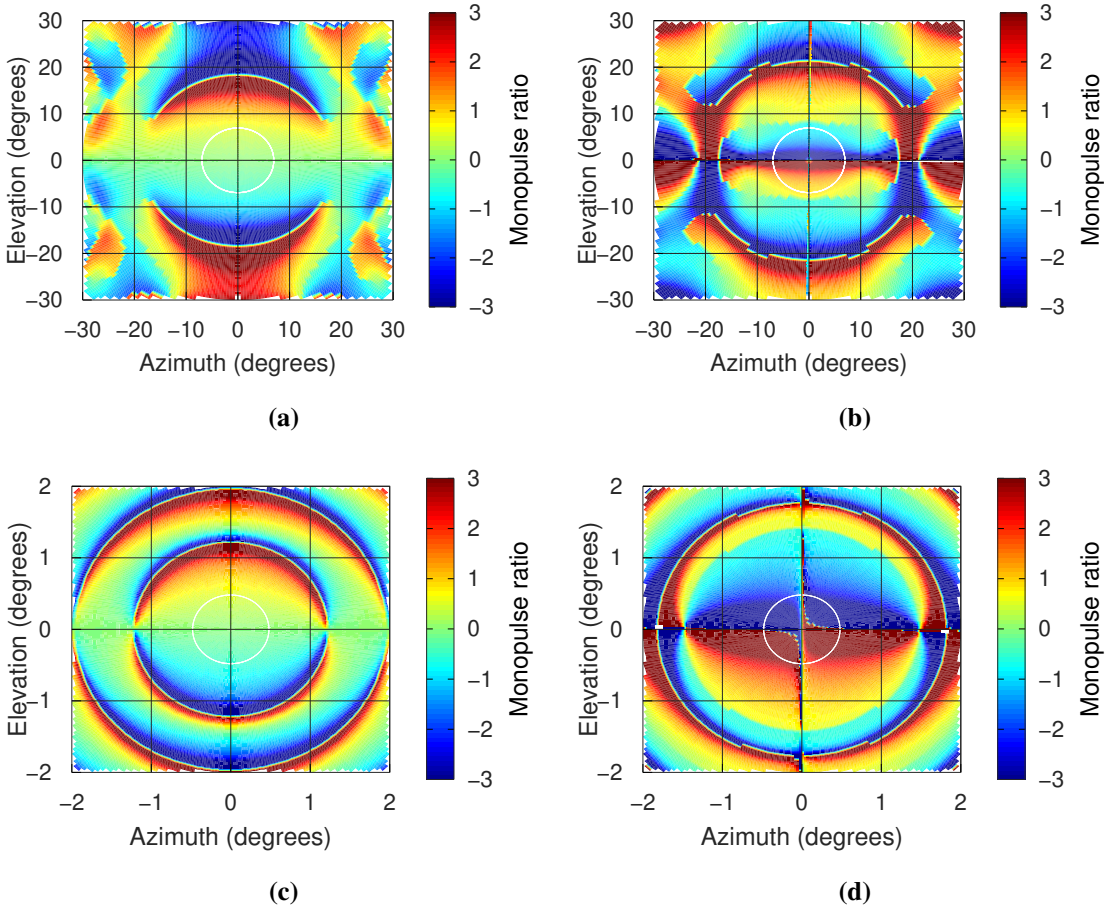

Figure 5.5. The elevation plane monopulse ratio at (a) co-polarisation, and (b) cross-polarisation for the wire-grid antenna. Then at (c) co-polarisation, and (d) cross-polarisation for the Hannan parabolic reflector antenna. The white circle is the –3 dB beamwidth of the antennas [33].

Figures 5.7(c) and 5.7(d) shows the cross-polarisation monopulse ratio that is crossed oppositely with the co-polarisation monopulse ratio; since this was generated from the monopulse patterns that have polarisation isolation between 20 to 30 dB, it is what the tracking radar will use if the jammer generates a cross - polarised jamming signal with power that is above the co-polarised signal power. One thing to note is that from boresight towards the Condon lobes jamming region, the cross-polarisation monopulse ratio takes the shape of the co-polarisation monopulse ratio.

5.2.2.3 Induced angular error

The angular error in Figure 5.8 is determined using (4.142) and (4.152), where M_s is the imaginary monopulse ratio, E_Σ and E_Δ are the sum and difference patterns. These patterns have co-polarisation and cross-polarisation components. The reference θ plane-wave AOA is determined initially when

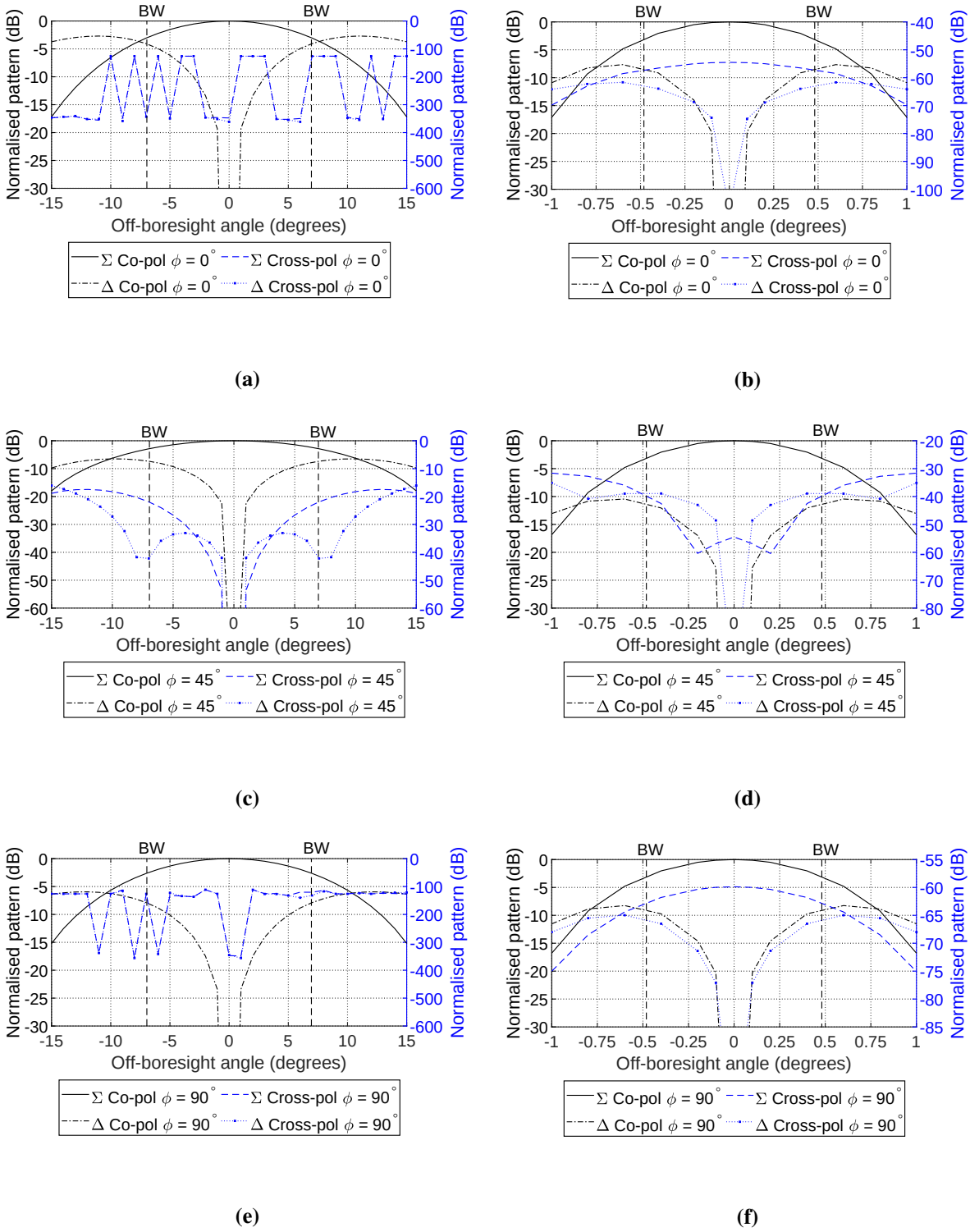

Figure 5.6. The monopulse antenna patterns resulting from the received incident wave at (a) $\phi = 0°$ azimuth plane, (c) $\phi = 45°$ diagonal plane, (e) $\phi = 90°$ for the wire-grid antenna, at (b) $\phi = 0°$ azimuth plane, (d) $\phi = 45°$ diagonal plane, and (f) $\phi = 90$ elevation plane for the Hannan parabolic reflector antenna. The dashed lines are the -3 dB beamwidth(BW).

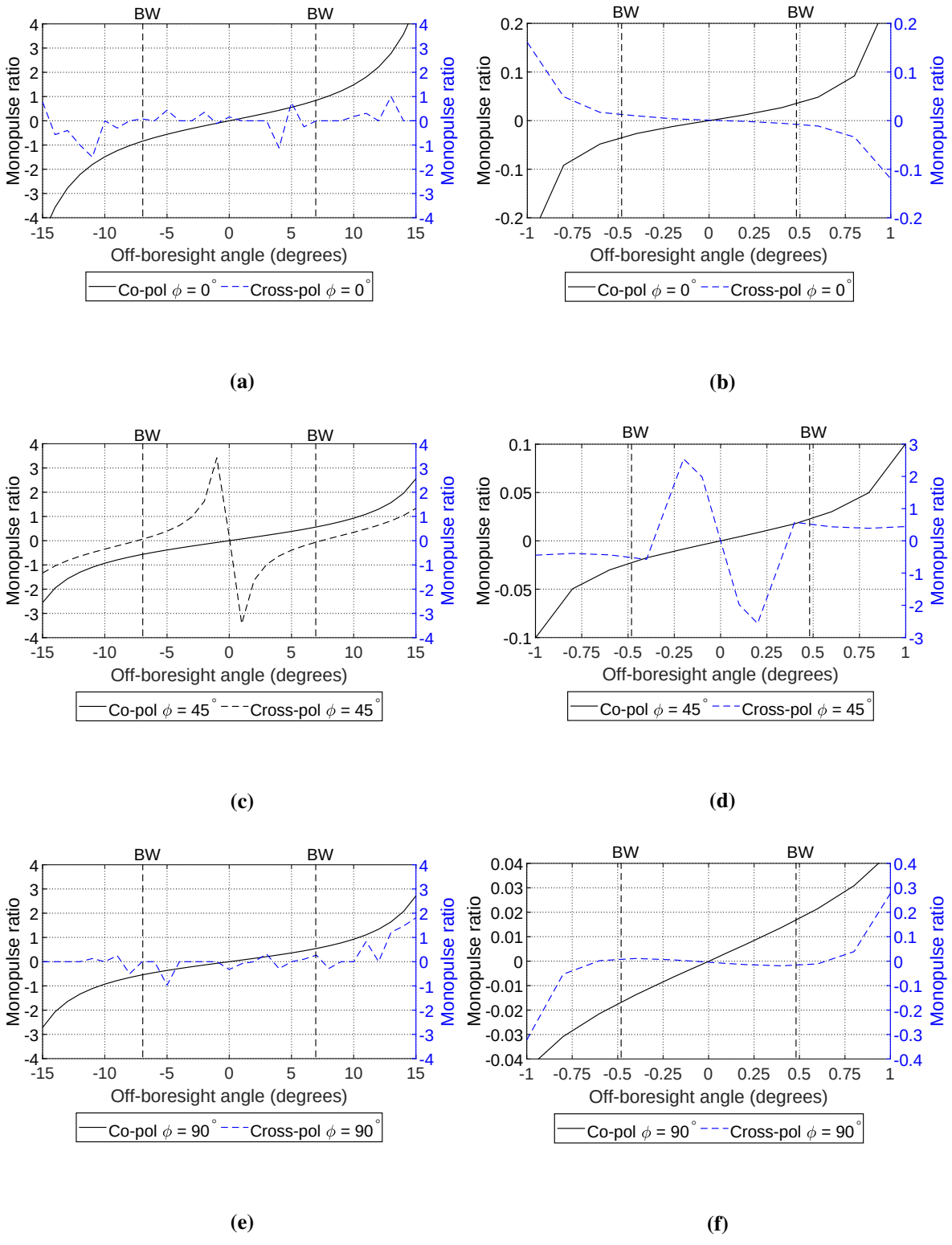

Figure 5.7. The imaginary monopulse ratios resulting from the received incident wave at (a) $\phi = 0°$ azimuth plane, (c) $\phi = 45°$ diagonal plane, (e) $\phi = 90°$ for the wire-grid antenna, at (b) $\phi = 0°$ azimuth plane, (d) $\phi = 45°$ diagonal plane, and (f) $\phi = 90$ elevation plane for the Hannan parabolic reflector antenna. The dashed lines are the -3 dB beamwidth(BW).

equal power is applied to both the co- and cross-polarisation components. On the transmissions that follow, the cross-polarisation component signal power is increased while its co-polarisation component is kept constant; this results in an induced angular error; this way of calculating angular error assumes that the radar antenna receives only two signal components: the co-polarisation component is the target skin return, and the cross-polarisation component is the jamming signal. In a practical environment, the radar antenna will receive both the tracking signal (with both co- and cross-polarisation components) and the jamming signal(with both co and cross-polarisation components).

The polarisation purity plays a crucial role in successfully jamming the tracking radar. It is said that for the jammer to induce angular error in the tracking radar, it must have a JSR greater than the polarisation purity of the radar [23]. The induced angular error for both antennas is shown in Figure 5.8. The angular error at the azimuth and elevation planes for both antennas is shown in Figures 5.8(a) , 5.8(b), Figures 5.8(e) , and 5.8(f), and the induced angular error in the diagonal plane for both antennas is shown in Figures 5.8(c) and 5.8(d). Comparing the induced angular error in all the planes, the induced angular error in the azimuth and elevation planes is significantly small. The induced angular error in the diagonal plane is higher and desirable for cross-polarisation jamming. The diagonal plane angular error for the wire-grid antenna is higher than the Hannan parabolic reflector due to their difference in polarisation purity. The induced angular error in the diagonal planes shows three stages: S1, S2, and S3. S1 is where the increase in the cross-polarisation jamming power does not affect the tracking accuracy due to high polarisation isolation. S2 is where the jammer induces angular error into the tracking radar. S3 is the break-lock stage; the radar does not have an effect and is no longer locked to the target using the co-polarisation component, but it is locked onto the target using the jamming signal. This is seen with a constant error that the co-polarisation signal does not have an effect.

5.2.2.4 Jammer polarisation accuracy

The ability of the jammer to re-transmit a cross-polarised signal with power higher than the co-polarised signal component is not the only cross-polarisation jamming requirement. The jammer must have higher polarisation sensitivity, which is the ability to receive the tracking signal with the correct polarisation angles and re-transmit it back with the correct polarisation angles [22], [25], [24]. The polarisation accuracy results for the two antennas are shown in Figure 5.9. There are two approaches used to analyse the jammer polarisation accuracy; the first approach was to use the plane-wave signal having a starting polarisation angle as the co-polarisation angle, then increment the polarisation angle until it reaches the cross-polarisation angle. The plane-wave jamming signal has a constant signal

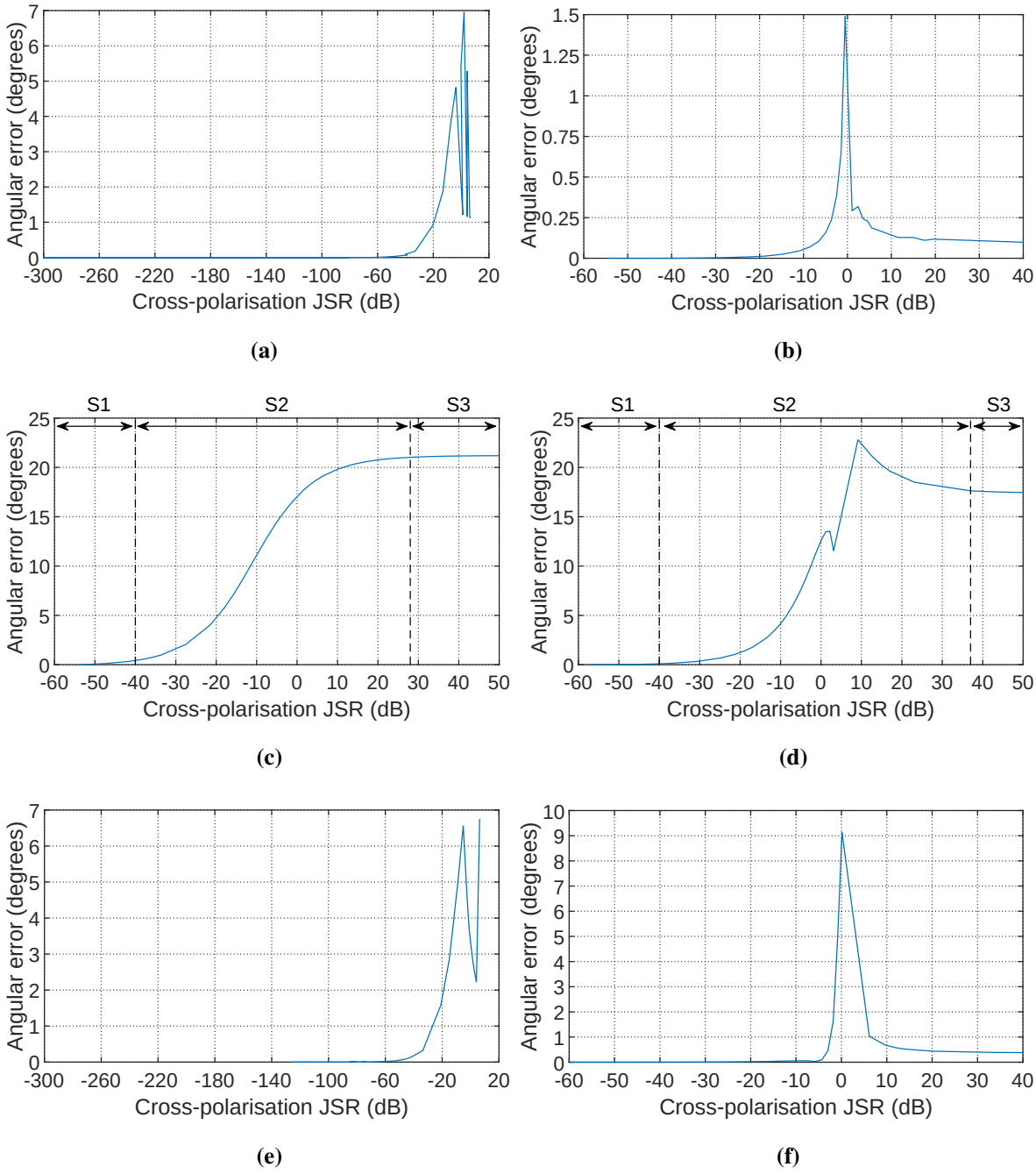

Figure 5.8. The induced angular error due to the plane wave from off-boresight angle of 1° for wire-grid antenna at (a) $\phi = 0°$ azimuth plane, (c) $\phi = 45°$ diagonal plane, and (e) $\phi = 90°$ elevation plane. Then from off-boresight angle of 0.1° for Hannan parabolic reflector antenna at (b) $\phi = 0°$ azimuth plane, (d) $\phi = 45°$ diagonal plane, and (f) $\phi = 90°$ elevation plane.

power. The results for this approach are shown in Figure 5.9; in Figures 5.9(e) and 5.9(f), the horizontal axis shows the jammer polarisation angle accuracy where 45° angle represents the cross-polarisation angle and the 135° angle represents the co-polarisation angle, the vertical axis is the induced angular error.

The results in Figures 5.9(e) and 5.9(f) are similar to the reported results in [22]. These results show that if the jammer polarisation angle is off by $\approx 2°$, for the Hannan parabolic reflector in Figure 5.9(f), the induced angular error is reduced significantly from its highest angular error of 12° to $\approx 2°$, which is an $\approx 83\%$ reduction. If the jammer polarisation accuracy is off by $\approx 2°$, the induced angular error in the wire-grid antenna in Figure 5.9(e) is reduced from its highest angular error of 16° to $\approx 3°$, which is a reduction of $\approx 81\%$, and this shows that the induced angular error is sensitive to the cross-polarisation angle. Comparing the wire-grid radar antenna results in Figure. 5.9(e) and the Hannan parabolic reflector radar antenna results in Figure. 5.9(f), the antenna with the higher polarisation purity needs higher jammer polarisation accuracy; in this case, the parabolic reflector needs higher jammer polarisation accuracy than the wire-grid antenna. In the wire-grid antenna results, the plane wave has an off-boresight angle of 1° while it has an off-boresight angle of 0.1° in the Hannan parabolic reflector antenna results.

The second approach in analysing the jammer polarisation accuracy was to use three inaccurate angles that deviate from the correct cross-polarisation angle and increase the jammer signal power. The results of this approach are shown in Figure. 5.9(a) to 5.9(d). The monopulse ratio in both figures shows distortion when the jammer polarisation accuracy is off by 1°, and the distortion increases as the inaccuracy increases. This distortion of the monopulse ratio will continue until the cross-polarisation monopulse ratio is the same as the co-polarisation monopulse ratio in Figures 5.7(c) and Figure 5.7(d). As shown in Figures. 5.9(c) and 5.9(d), the monopulse ratio distortion reduces angular error.

When the jammer is off by 1° the angular error for the wire-grid antenna decreases from $\approx 16°$ in Figure 5.7(c) to $\approx 5°$ in Figure 5.9(c). When the jammer is off by 1°, the induced angular error for the Hannan parabolic reflector antenna decreases from $\approx 12°$ in Figure 5.7(d) to $\approx 2°$ in Figure 5.9(d), which are significant induced angular error reductions. It is reported that the cross-polarisation jammer must have polarisation accuracy of at least $\pm 1°$ to $\pm 5°$ [22], [25], [24]. Looking at the analysis of the results, 1° to 5° polarisation inaccuracy results in a significant angular error reduction. Polarisation accuracy is strict in cross-polarisation jamming. The induced angular error will be reduced if the

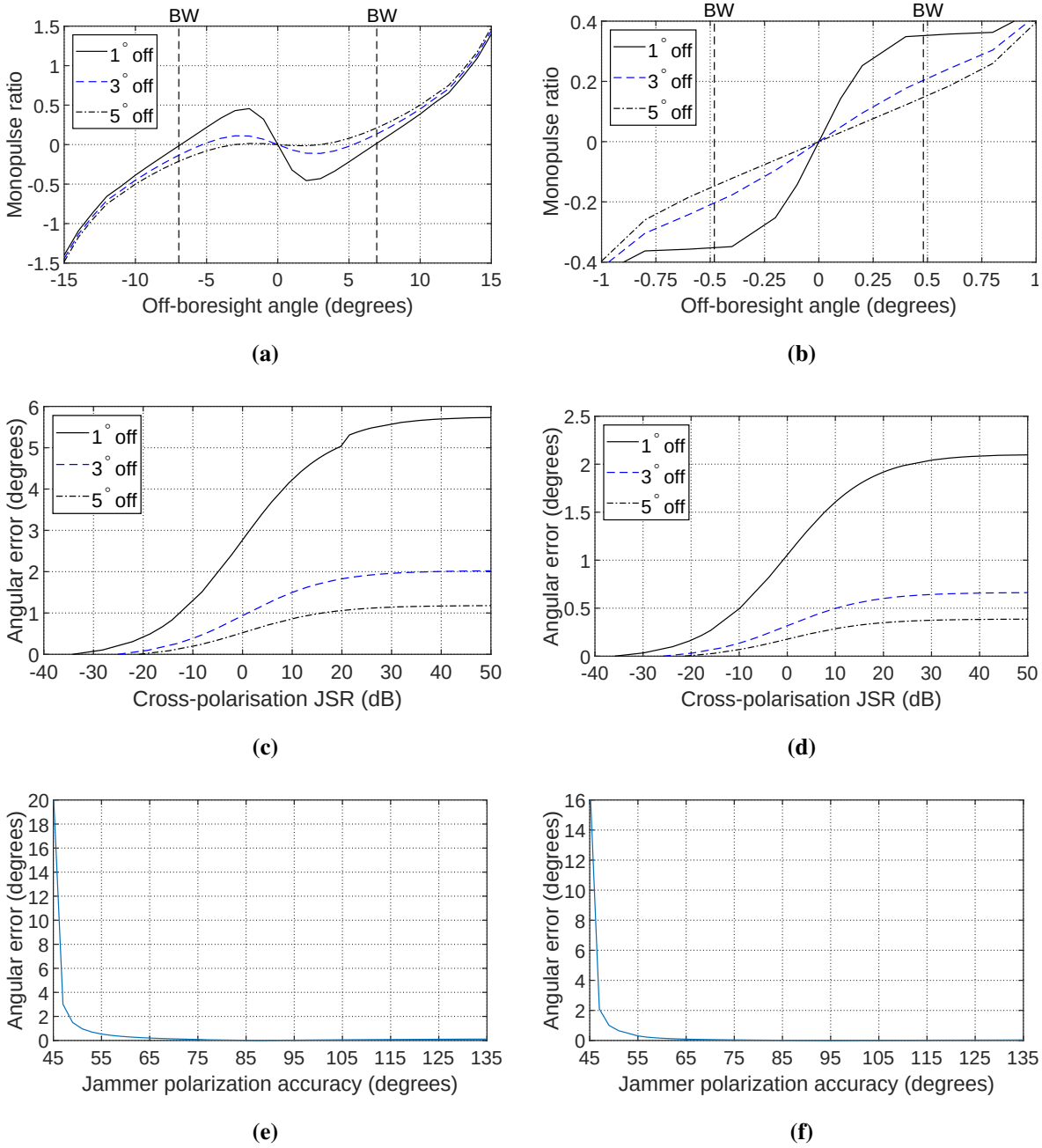

Figure 5.9. The Jammer cross-polarisation accuracy sensitivity demonstrated by the (a) imaginary monopulse ratio with (c) and (e) being the induced angular error at $\phi = 45^\circ$ diagonal plane for the wire-grid antenna. The (b) imaginary monopulse ratio with (d) and (f) being the induced angular error at $\phi = 45^\circ$ diagonal plane for Hannan parabolic reflector antenna.

cross-polarisation jammer with inaccurate polarisation detection is implemented in practice.

5.3 CASSEGRAIN MONOPULSE ANTENNA

5.3.1 Transmitting mode

The antenna analysed in this section is the Cassegrain antenna and the same procedure used to analyse the previous antennas is used for all the other antennas. The radiation patterns of the Cassegrain monopulse antenna are shown in Figure 5.10, and the co-polarisation patterns are well-defined. The cross-polarisation patterns are also well-defined; the cross-polarisation sum patterns have Condon lobes in the diagonal planes as expected. The co- and cross-polarisation difference patterns have nulls at their respective axis. The monopulse ratio is shown in Figure 5.11, and the cross-polarisation patterns in the azimuth and elevation plane are distorted. Figure 5.12 shows the polarisation purity; the sum channel has high polarisation purity at the azimuth and elevation axis, while the difference channels have high polarisation purity on one axis. In Figures 5.12(b) and 5.12(c), the polarisation purity decreases when moving away from the azimuth and elevation axis; hence, the diagonal planes have less polarisation purity compared to the azimuth and elevation axis [33]. The reduced polarisation purity trend in the difference pattern is seen in all six antennas. The cross-polarisation jamming takes advantage of this characteristic [33].

5.3.2 Receiving mode

The Cassegrain monopulse antenna is analysed when it receives a plane wave with polarisation and direction angles shown in Table 5.3. The radiation patterns are shown in Figure 5.13. The cross-polarisation patterns are distorted in the azimuth and elevation planes. In the diagonal plane, the sum channel has a null at boresight, and Condon lobes off-boresight. These patterns show high polarisation isolation of $\approx$ 70 dB in the azimuth and elevation plane, while the diagonal plane has a reduced polarisation isolation of $\approx$ 35 dB. Figures 5.13(b) and 5.13(f) show the monopulse ratios with the cross-polarisation monopulse ratio distorted; however, Figure 5.13(d) show the desired distorted diagonal plane monopulse ratio. Figures 5.14(a), 5.14(c), and 5.14(e) show the angular error in the azimuth, elevation, and diagonal plane, respectively. The diagonal plane has a higher induced angular error than the azimuth and elevation planes. The diagonal plane angular error in Figure 5.14(e) shows three stages. In S2, the jamming signal induces angular error into the tracking radar, but between JSR = -5 dB to 10 dB, the tracking radar reduces the angular tracking error. However, the jammer increases it again because the JSR > 0 and eventually reaches break-lock. Figures 5.14(b), 5.14(d), and 5.14(f) show the monopulse ratio for three inaccurate polarisation angles, the angular error due to the three inaccurate polarisation angles, and the polarisation accuracy analysis, respectively. As the polarisation

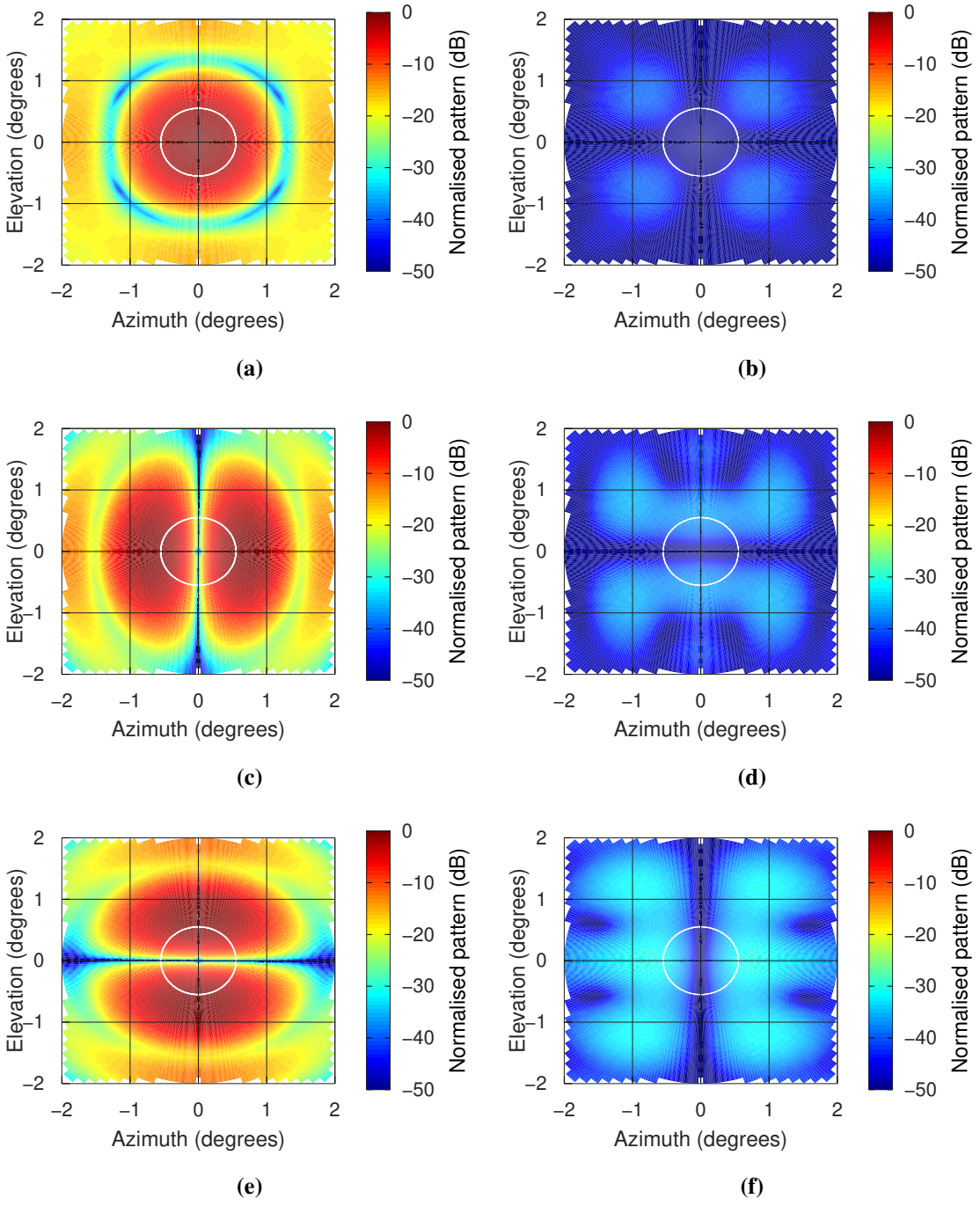

Figure 5.10. The monopulse radiation patterns of the Cassegrain monopulse antenna, the co-polarisation patterns for (a) sum channel, (c) azimuth channel, (e) elevation channel and the cross-polarisation patterns for (b) sum channel, (d) azimuth channel, and (f) elevation channel. The white circle is the –3 dB beamwidth of the antennas.

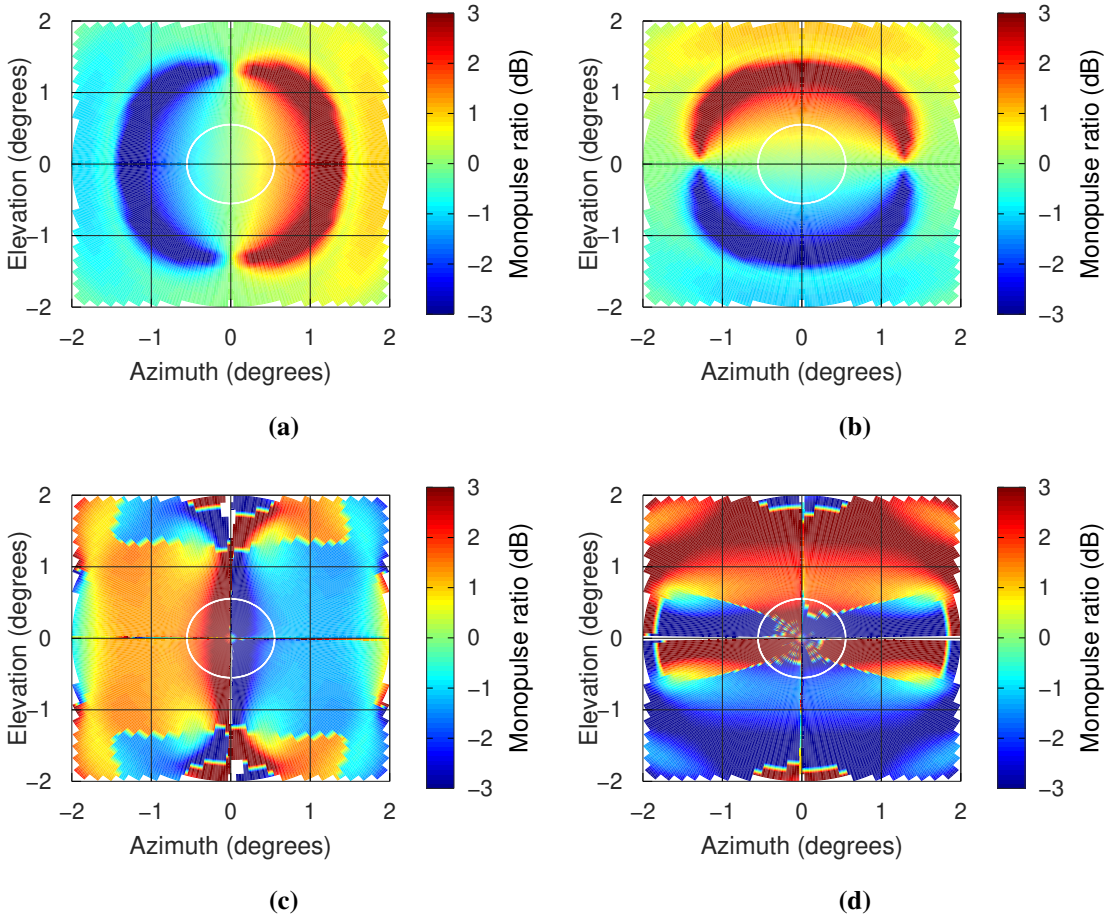

Figure 5.11. The monopulse ratio of the Cassegrain monopulse antenna, for co-polarisation at (a) azimuth channel, (b) elevation channel and for cross-polarisation at (c) azimuth channel, (d) elevation channel. The white circle is the –3 dB beamwidth of the antennas.

accuracy decreases, the monopulse ratio is distorted; It changes its shape to that of the co-polarisation monopulse ratio, which will assist the tracking radar in tracking the target. The angular error decreases as the polarisation accuracy decreases.

5.4 HANNAN CASSEGRAIN MONOPULSE ANTENNA

5.4.1 Transmitting mode

The antenna analyzed in this section is the Hannan Cassegrain antenna. The radiation patterns of the Hannan Cassegrain horn antenna are shown in Figure 5.15. The cross-polarisation patterns are $\approx$ 30 dB less than the co-polarisation patterns, and they have the Condon lobes in their diagonal planes. Figure 5.16 shows the monopulse ratio, and the cross-polarisation monopulse ratio is distorted. Figure 5.17 shows the polarisation purity of the sum signal and the difference signals in the azimuth

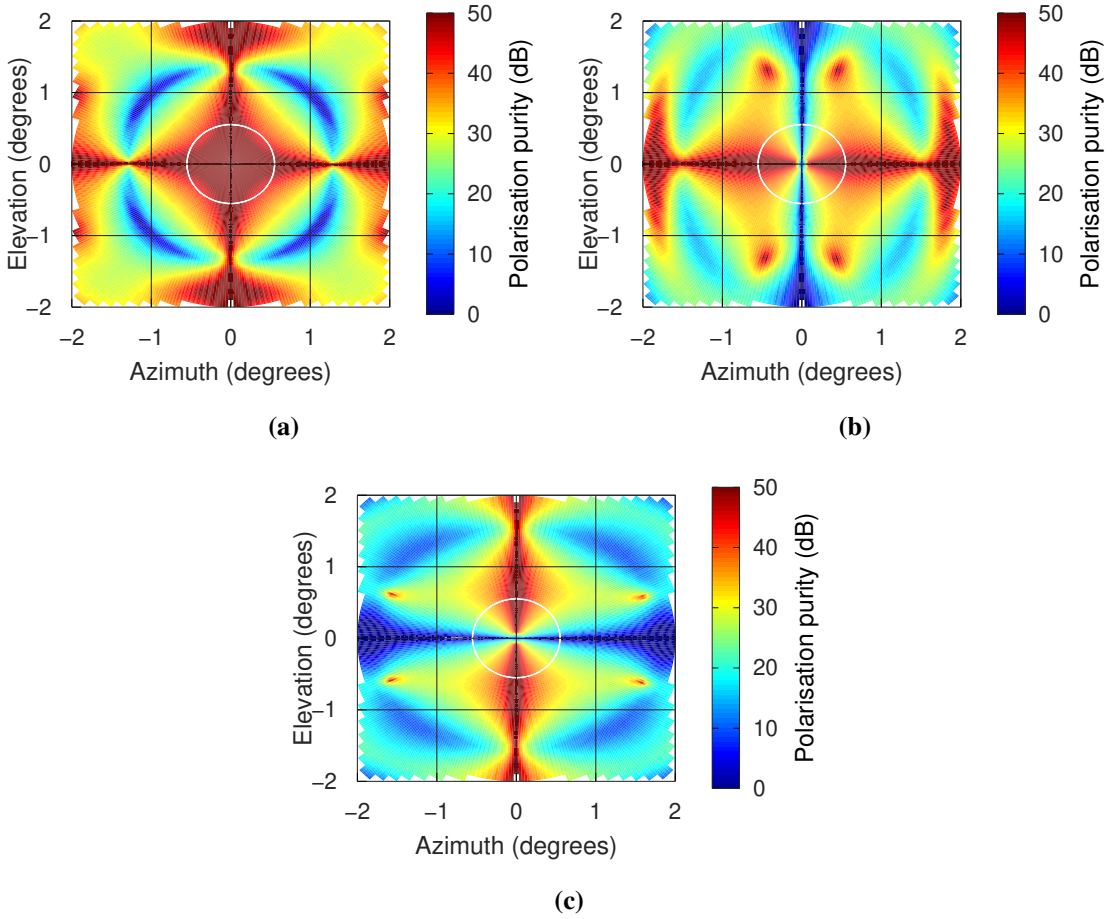

Figure 5.12. The polarisation purity of the Cassegrain monopulse antenna for (a) sum channel, (b) azimuth difference channel and for (c) elevation difference channel. The white circle is the —3 dB beamwidth of the antennas.

and elevation. The azimuth and elevation planes show higher polarisation purity in the relevant axis, while the polarisation purity is reduced around the diagonal plane axis.

5.4.2 Receiving mode

The direction and polarisation angles of the plane wave received by the Hannan Cassegrain antenna are shown in Table 5.4. The radiation patterns of the Hannan Cassegrain monopulse horn antenna are shown in Figure 5.18; the cross-polarisation patterns in the diagonal planes have Condon lobes. The polarisation isolation in the azimuth and elevation planes is $\approx$ 70 dB, and for the diagonal plane it is $\approx$ 30 dB. The monopulse ratios are shown in Figures 5.18(b), 5.18(d), and 5.18(f). Figures 5.19(a), 5.19(c), and 5.19(e) show the induced angular error in the azimuth, elevation, and diagonal plane, respectively. Figures 5.19(b), 5.19(d), and 5.19(f) shows the monopulse ratio for three

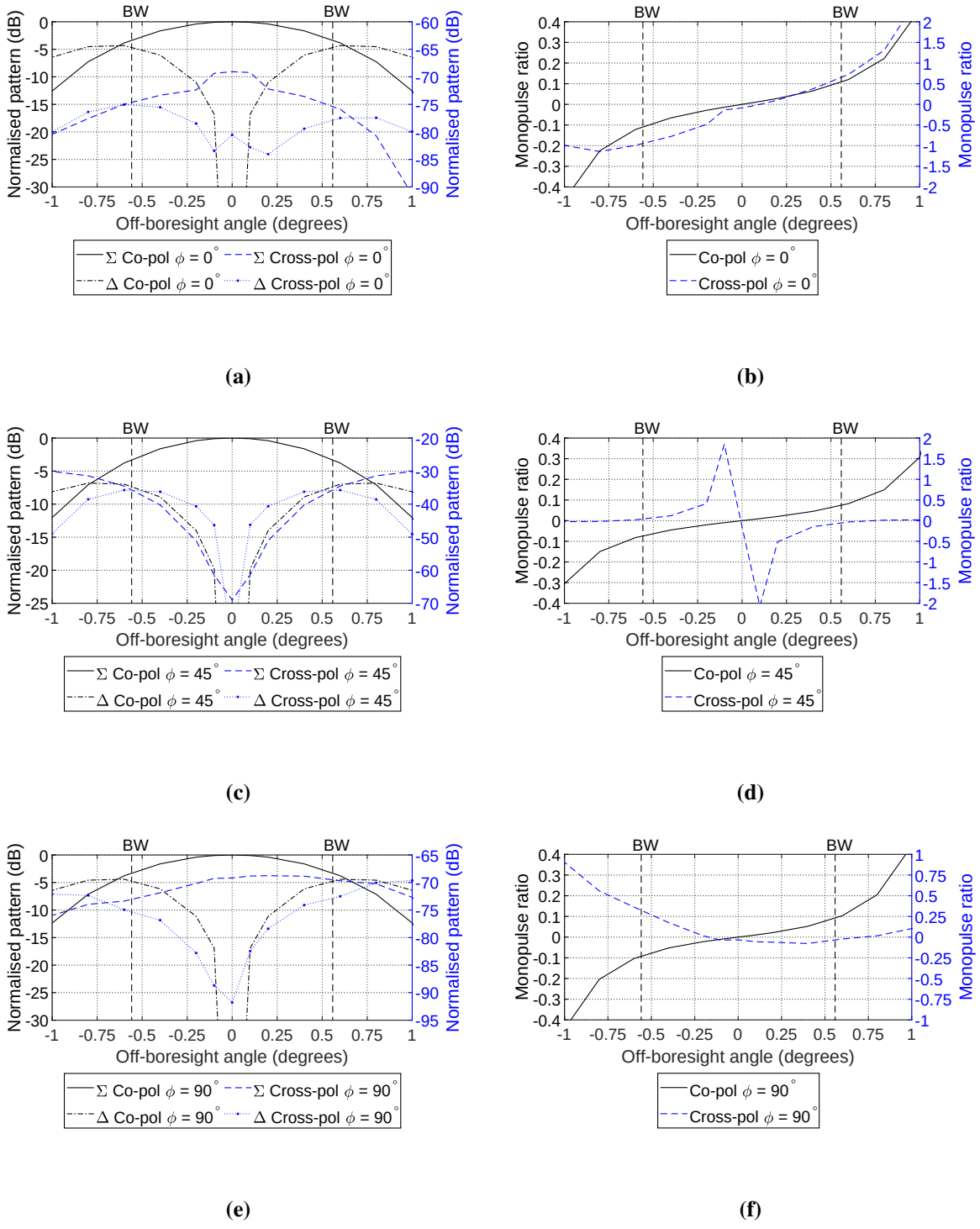

Figure 5.13. The radiation patterns of the Cassegrain monopulse antenna resulting from the received incident wave at (a) $\phi = 0°$ azimuth plane, (c) $\phi = 45°$ diagonal plane and at (e) $\phi = 90°$ elevation plane. The imaginary monopulse ratios at (b) $\phi = 0°$ azimuth plane, (d) $\phi = 45°$ diagonal plane and at (f) $\phi = 90°$ elevation plane.

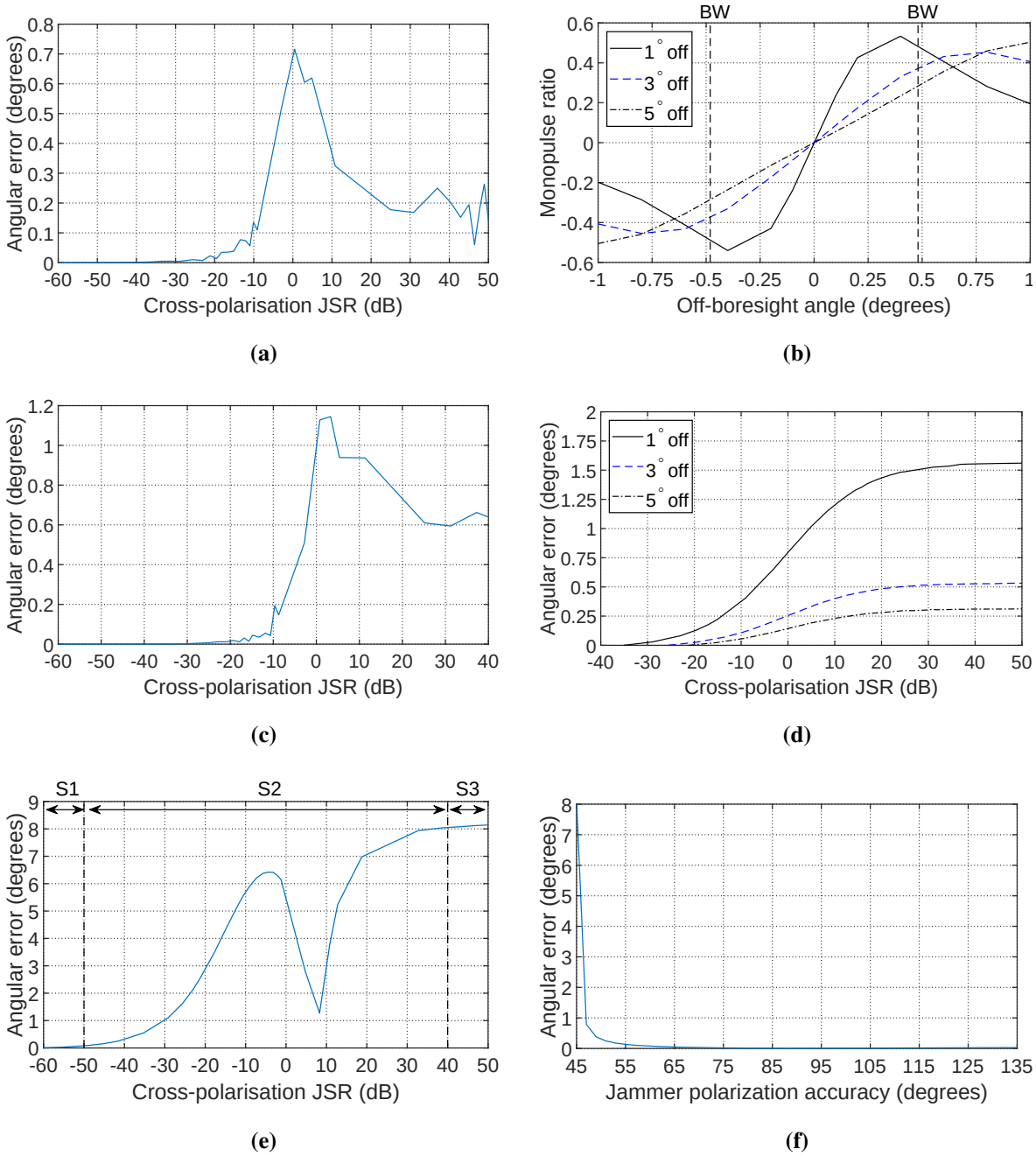

Figure 5.14. The Cassegrain monopulse antenna showing the (a) induced angular error at $\phi = 0°$ azimuth plane, (c) induced angular error at $\phi = 90°$ elevation plane, and (e) the induced angular error at $\phi = 45°$ diagonal plane. The polarisation accuracy analysis results at $\phi = 45°$ diagonal plane, (b) the monopulse ratios, (d) the induced angular error, and (f) induced angular error as the polarisation angle inaccuracy increases.

Table 5.3. The polarisation angles of the plane wave received by the Cassegrain monopulse antenna.

θ	ϕ	Co-Pol	Cross-Pol	ϕ	Co-Pol	Cross-Pol	ϕ	Co-Pol	Cross-Pol
0.0	0	89.99	-0.01	45	134.99	44.99	90	-0.01	-90.01
0.1	0	89.99	-0.01	45	134.99	44.99	90	-0.01	-90.01
0.2	0	90.00	0.00	45	134.97	44.97	90	-0.01	-90.01
0.4	0	90.00	0.00	45	134.87	44.87	90	-0.01	-90.01
0.6	0	90.00	0.00	45	134.70	44.70	90	-0.01	-90.01
0.8	0	90.00	0.00	45	134.37	44.39	90	-0.02	-90.02
1.0	0	90.00	0.00	45	133.80	43.80	90	-0.03	-90.02
1.2	0	90.02	0.02	45	132.21	42.21	90	-0.04	-90.04
1.4	0	-90.06	-180.06	45	100.71	10.71	90	-179.91	-269.91
1.6	0	-90.03	-180.03	45	-43.30	-133.3	90	-180.00	-270
1.8	0	-90.03	-180.03	45	-44.86	-134.86	90	179.98	89.98
2.0	0	-90.03	-180.03	45	-45.72	-135.72	90	179.97	89.97

inaccurate polarisation angles, the induced angular error at three inaccurate polarisation angles, and the polarisation accuracy analysis. The jammer induces an angular error in Figure 5.19(e) at an off-boresight angle of 0.4°. In Figure 5.19(e), the jamming signal reaches break-lock when JSR > 50 dB, but the angular error is induced before reaching break-lock.

5.5 MONOPULSE HORN ANTENNA

5.5.1 Transmitting mode

The antenna analyzed in this section is the monopulse horn antenna. The radiation patterns of the monopulse horn antenna are shown in Figure 5.20. As expected, the sum cross-polarisation patterns have Condon lobes in the diagonal plane. There is an interchange of the co- and cross-polarisation patterns' axes in the difference patterns, a behaviour seen in all the antennas analysed in the previous sections. The monopulse ratio is shown in Figure 5.21, and the polarisation purity is shown in Figure 5.22.

5.5.2 Receiving mode

The direction and polarisation angles of the plane wave received by the Horn antenna are shown in Table 5.5. The radiation patterns of the monopulse horn antenna are shown in Figure 5.23. The cross-polarisation sum pattern in the azimuth and elevation plane are the same as the co-polarisation sum

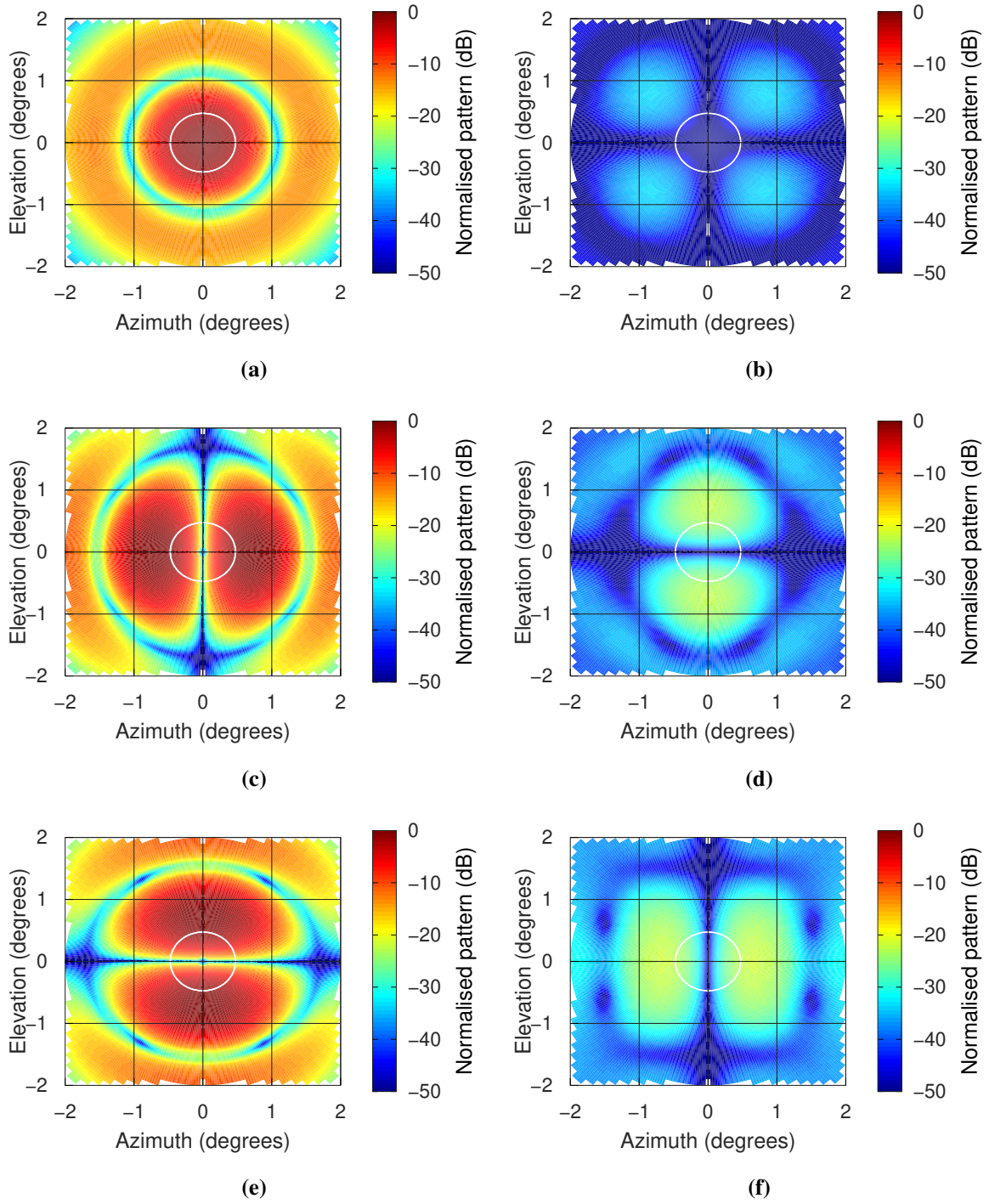

Figure 5.15. The monopulse radiation patterns of the Hannan Cassegrain monopulse horn antenna, the co-polarisation patterns for (a) sum channel, (c) azimuth channel, (e) elevation channel and the cross-polarisation patterns for (b) sum channel, (d) azimuth channel, and (f) elevation channel.

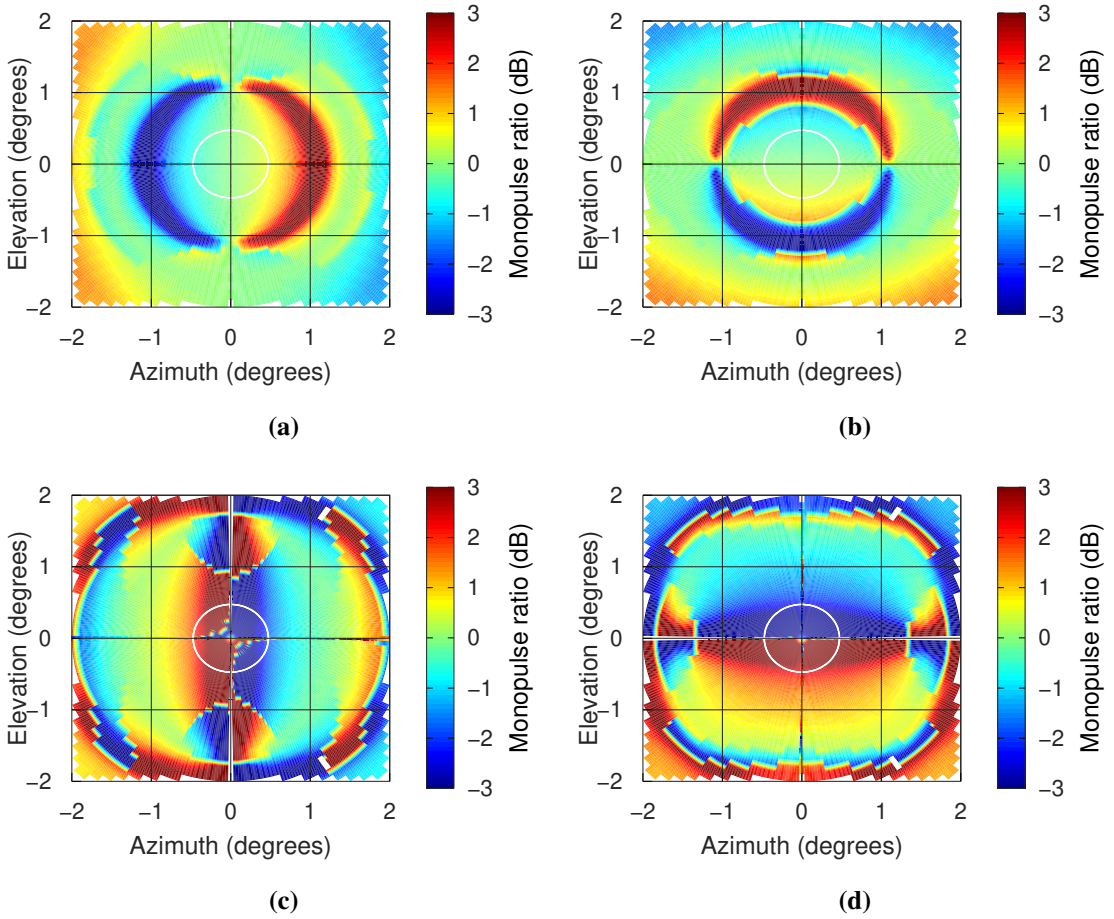

Figure 5.16. The monopulse ratio of the Hannan Cassegrain monopulse horn antenna, for co-polarisation at (a) azimuth channel, (b) elevation channel and for cross-polarisation at (c) azimuth channel, (d) elevation channel.

patterns but with different magnitudes, and the cross-polarisation sum channel at the diagonal plane has a null at $\theta = 0°$. The polarisation isolation in the azimuth and elevation planes is ≈ 70 dB, while it is ≈ 27 dB in the diagonal planes. The monopulse ratio is shown in Figures 5.23(b), 5.23(d), and 5.23(f); in the azimuth and elevation planes, the cross-polarisation monopulse ratio is approximate to the co-polarisation monopulse ratio, meaning the tracking radar can use any of the polarisation components for tracking. The monopulse ratio at the diagonal plane is distorted at boresight. The induced angular errors due to the cross-polarisation jamming power and the polarisation accuracy are shown in Figure 5.24. The angular error in Figure 5.24(e) is induced by the jammer when the jamming signal off-boresight angle is 1°. In Figure 5.24(e), the jamming signal reaches break-lock when JSR > 30 dB.

Table 5.4. The direction and polarisation angles of the plane wave received by the Hannan Cassegrain horn antenna.

θ	ϕ	Co-Pol	Cross-Pol	ϕ	Co-Pol	Cross-Pol	ϕ	Co-Pol	Cross-Pol
0.0	0	90.00	0.00	45	135.00	45.00	90	-0	-90
0.1	0	90.00	0.00	45	135.02	45.02	90	-0	-90
0.2	0	90.00	0.00	45	135.07	45.07	90	-0	-90
0.3	0	90.00	0.00	45	135.17	45.17	90	-0	-90
0.4	0	90.00	0.00	45	135.33	45.33	90	-0	-90
0.5	0	90.00	0.00	45	135.56	45.56	90	-0	-90
0.6	0	90.00	0.00	45	135.90	45.90	90	-0	-90
0.7	0	89.99	-0.01	45	136.43	46.43	90	0	-90
0.8	0	89.99	-0.01	45	137.34	47.34	90	0	-90
0.9	0	89.99	-0.01	45	139.11	49.11	90	0	-90
1.0	0	-90.04	-180.04	45	-35.98	-125.998	90	0	-90

Table 5.5. The direction and polarisation angles of the plane wave received by the horn antenna.

θ	ϕ	Co-Pol	Cross-Pol	ϕ	Co-Pol	Cross-Pol	ϕ	Co-Pol	Cross-Pol
0	0	90	0	45	135.00	45.00	90	0.00	-90.00
1	0	90	0	45	135.00	45.00	90	0.00	-90.00
2	0	90	0	45	134.99	44.99	90	0.00	-90.00
4	0	90	0	45	134.95	44.95	90	0.00	-90.00
6	0	90	0	45	134.88	44.88	90	0.00	-90.00
8	0	90	0	45	134.78	44.78	90	0.00	-90.00
10	0	90	0	45	134.65	44.65	90	0.00	-90.00
12	0	90	0	45	134.49	44.49	90	0.00	-90.00
14	0	90	0	45	134.29	44.29	90	0.00	-90.00
16	0	90	0	45	134.06	44.06	90	0.00	-90.00
18	0	90	0	45	133.79	43.79	90	0.00	-90.00
20	0	90	0	45	133.48	43.48	90	-0.01	-90.01

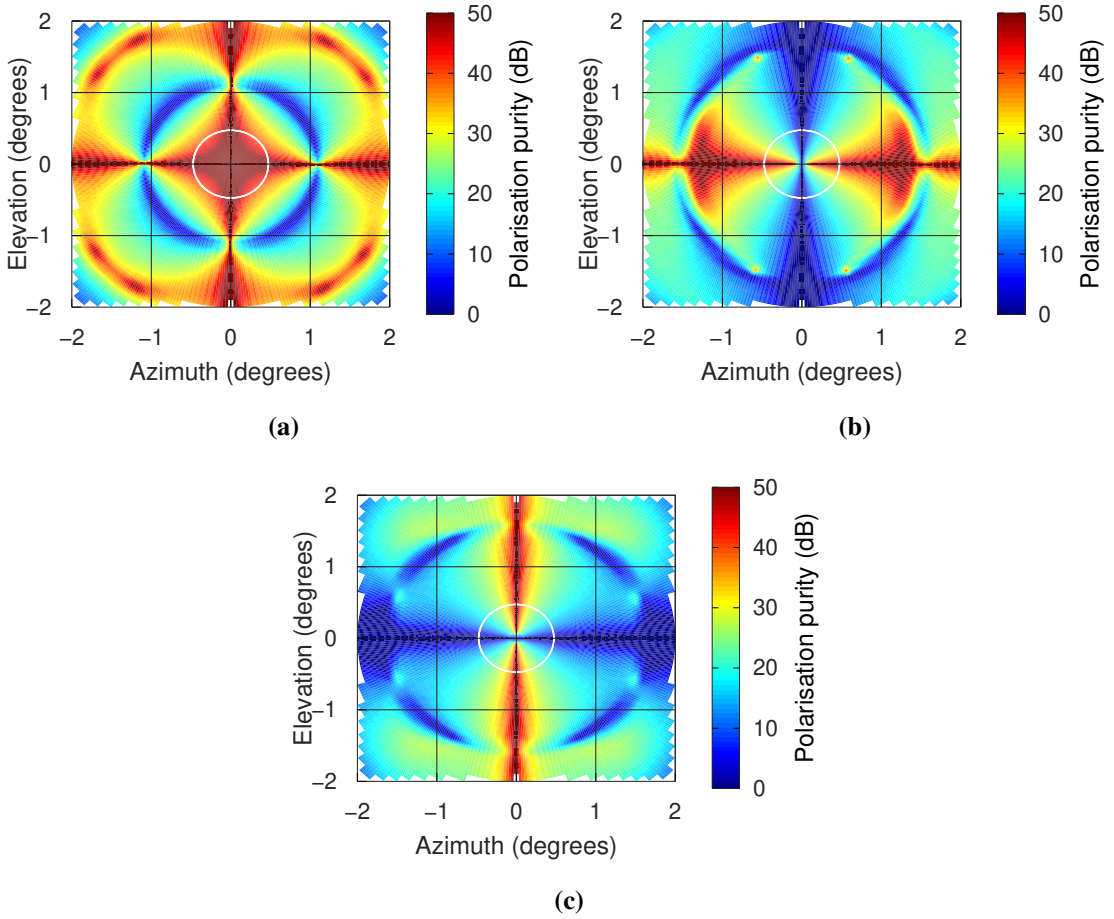

Figure 5.17. The polarisation purity of the Hannan Cassegrain monopulse horn antenna for (a) sum channel, (b) azimuth channel and for (c) elevation channel.

5.6 3 DB HPBW TRACKING ANALYSIS

The analysis of the angular error caused by the cross-polarisation jamming is extended from boresight towards the 3 dB beamwidth edge and outside. Even though monopulse radars use monopulse ratios to perform target tracking, the magnitude of the polarisation components signal plays a crucial role in determining which polarisation component is dominant, which will, in turn, influence the monopulse ratio shape. Looking at the co-polarisation sum pattern in Figures 5.6(c) and 5.6(d) for the wire-grid antenna and the Hanna parabolic reflector antenna, respectively, the side lobes follow the main lobe. When looking at the cross-polarisation sum pattern, the null at boresight is followed by the Condon lobes; this means different AOAs are analysed from boresight towards the 3 dB beamwidth edge in the co-polarisation component, that is, towards the Condon lobes in the cross-polarisation component, which are the lobes the tracking radar will use if the cross-polarisation jammer has enough jamming

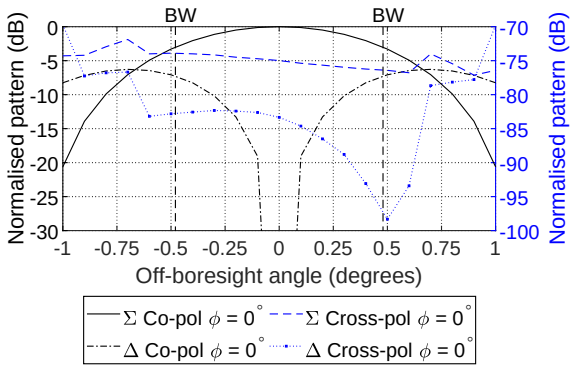

(a)

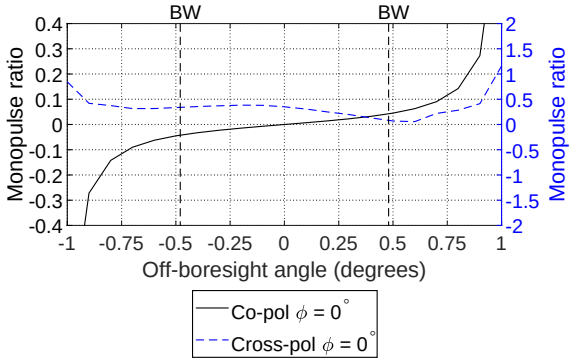

(b)

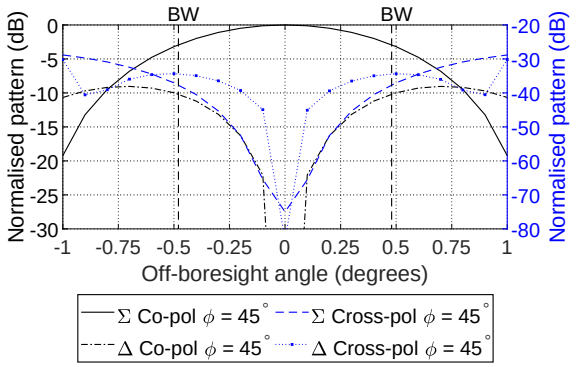

(c)

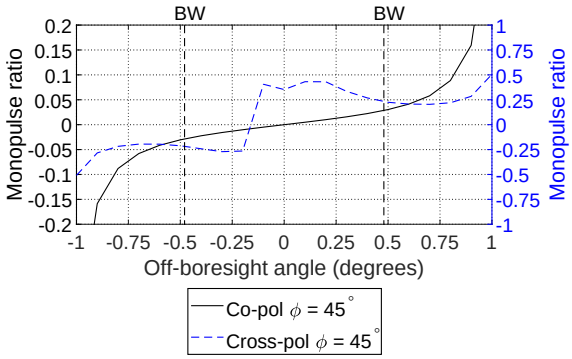

(d)

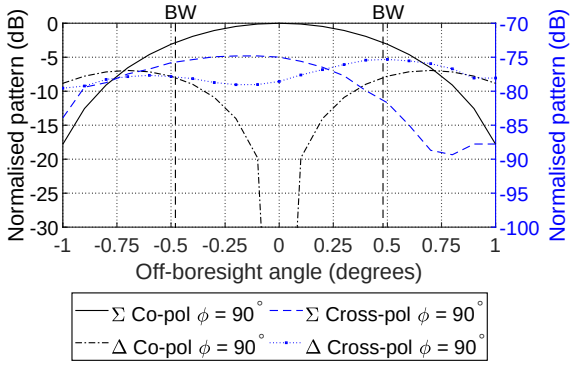

(e)

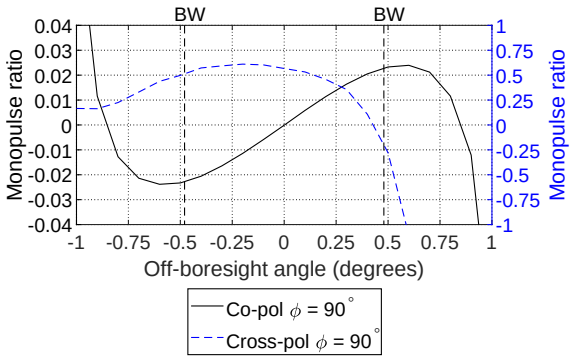

(f)

Figure 5.18. The radiation patterns of the Hannan Cassegrain monopulse horn antenna resulting from the received incident wave at (a) $\phi = 0°$ azimuth plane, (c) $\phi = 45°$ diagonal plane, and at (e) $\phi = 90°$ elevation plane. The imaginary monopulse ratio at (b) $\phi = 0°$ azimuth plane, (d) $\phi = 45°$ diagonal plane and at (f) $\phi = 90°$ elevation plane.

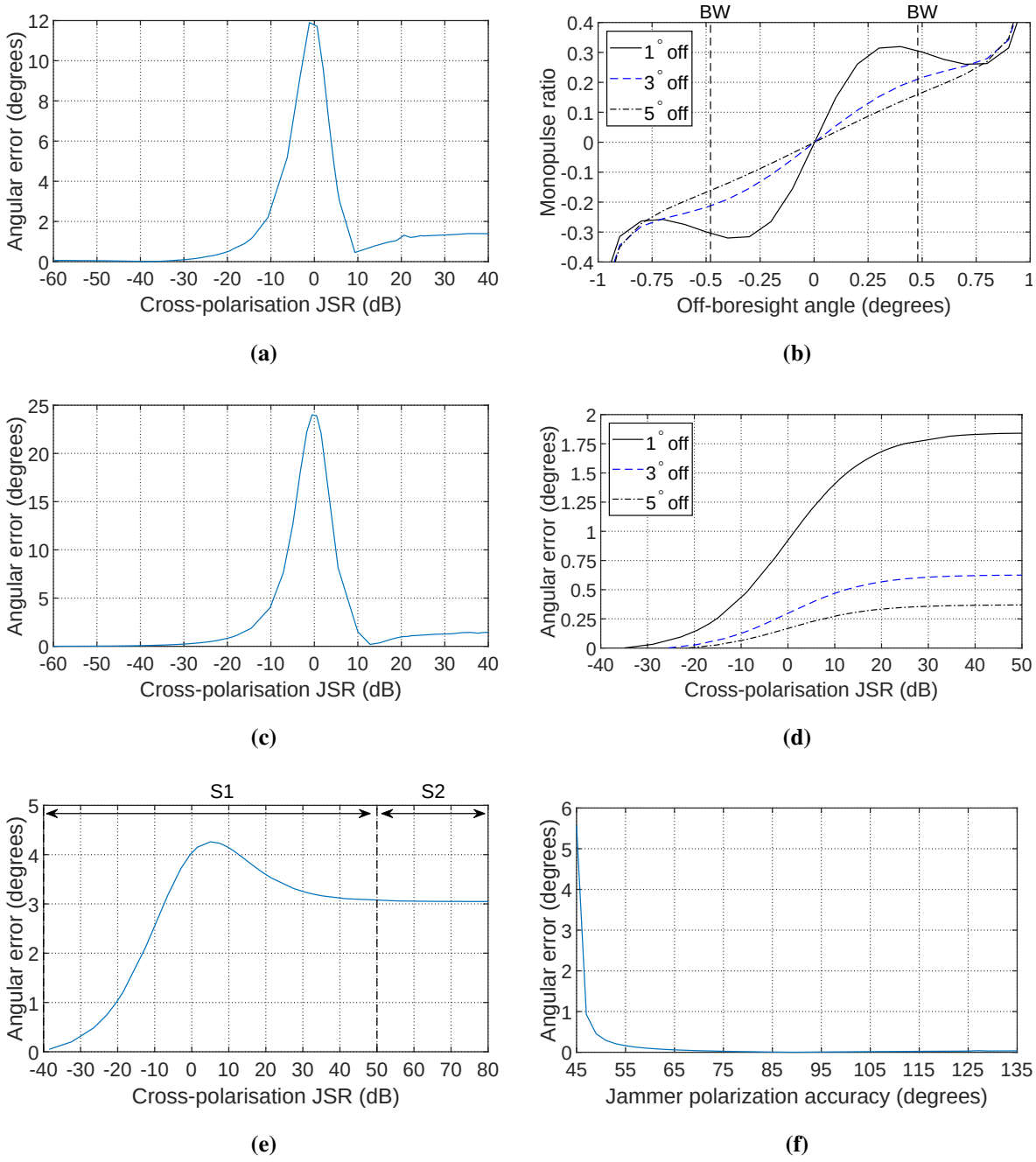

Figure 5.19. The Hannan Cassegrain monopulse horn antenna showing the (a) the induced angular error at $\phi = 0°$ azimuth plane, (c) the induced angular error at $\phi = 90°$ elevation plane, and (e) the induced angular error at $\phi = 45°$ diagonal plane. The polarisation accuracy analysis results at $\phi = 45°$ diagonal plane, (b) the monopulse ratios, (d) the induced angular error, and (f) induced angular error as the polarisation angle inaccuracy increases.

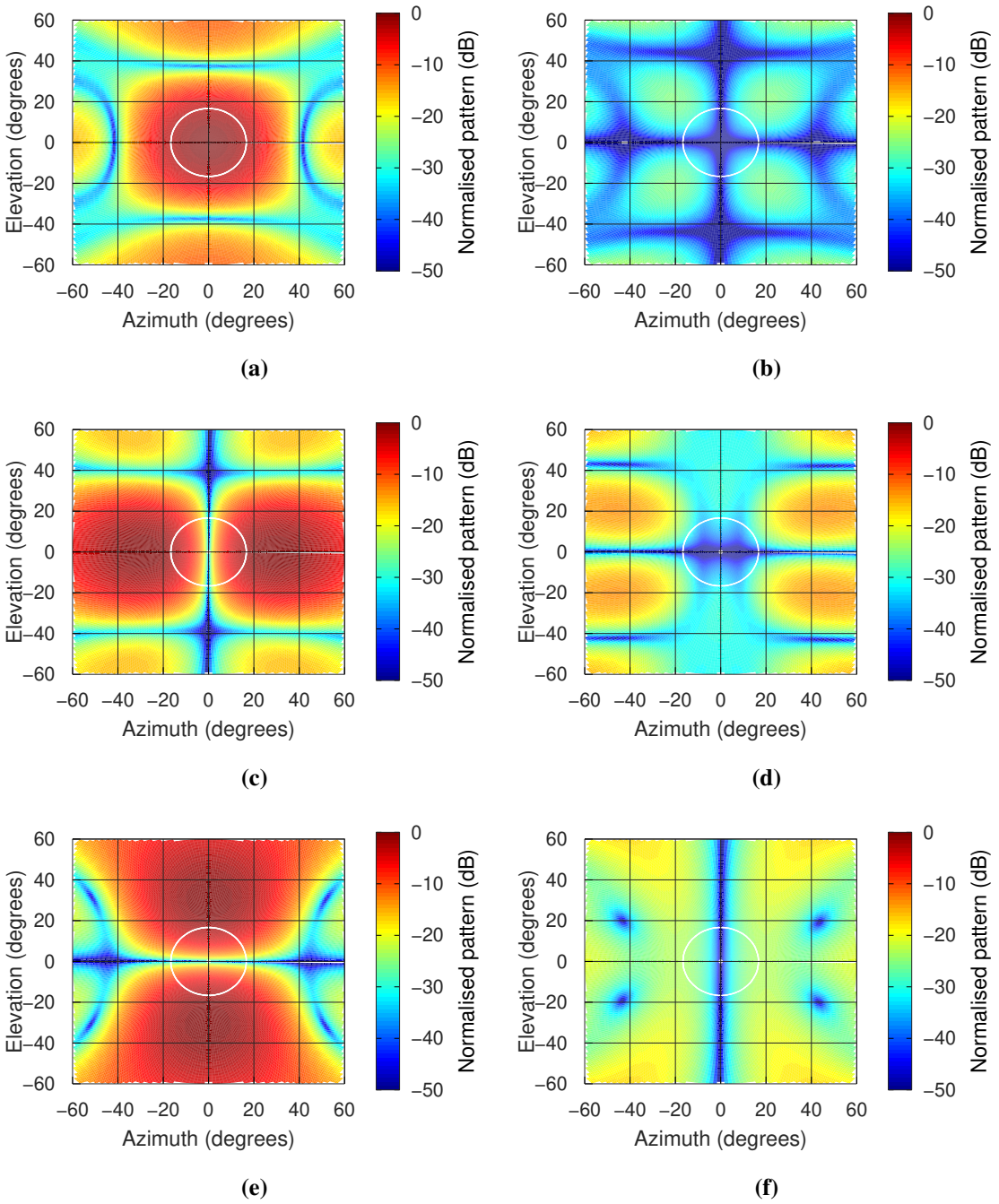

Figure 5.20. The monopulse radiation patterns of the monopulse horn antenna, the co-polarisation patterns for (a) sum channel, (c) azimuth channel, (e) elevation channel and the cross-polarisation patterns for (b) sum channel, (d) azimuth channel, and (f) elevation channel.

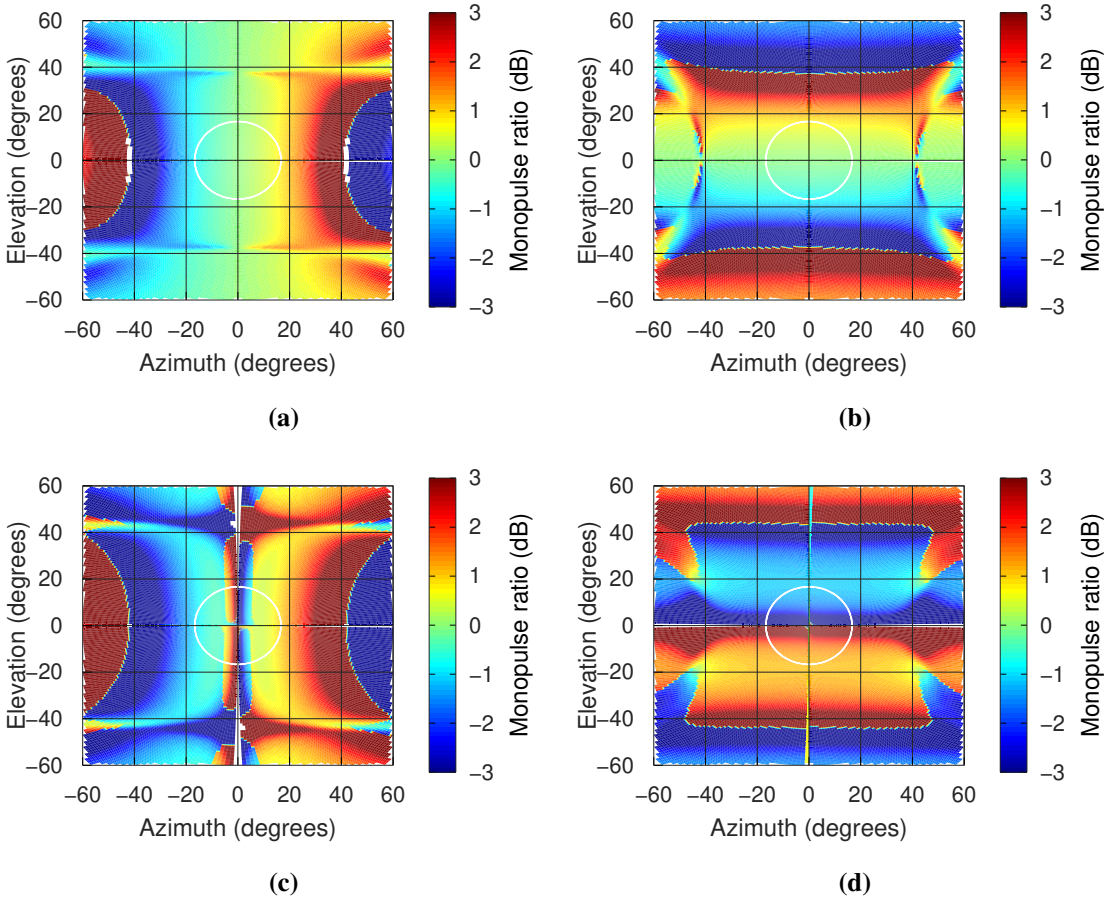

Figure 5.21. The monopulse ratio of the monopulse horn antenna, for co-polarisation at (a) azimuth channel, (b) elevation channel and for cross-polarisation at (c) azimuth channel, (d) elevation channel.

power. Figure 5.25(a) show the angular error when AOA = 2°, Figure 5.25(b) show the angular error when AOA = 4°, Figure 5.25(c) show the angular error when AOA = 6°, Figure 5.25(d) show the angular error when AOA = 8°. The trend in these angular errors is that, as the *AOA* moves away from the boresight, the angular error induced by the jammer into the tracking radar is reduced. This also shows that as the AOA move away from boresight, the tracking ability of the radar is reduced; this is seen in Figure 5.25(c) and Figure 5.25(d) at JSR = -40 dB, the error is supposed to be 0° to show that initially before the jamming signal power is increased, the tracking radar must have an accurate signal track.

The Hannan parabolic reflector angular error results are shown in Figure 5.26(a), Figures 5.26(b), and 5.26(c). The trend in these angular errors is similar to that in the wire-grid antenna. The induced angular error decreases when the AOA moves towards the 3 dB beamwidth edge and

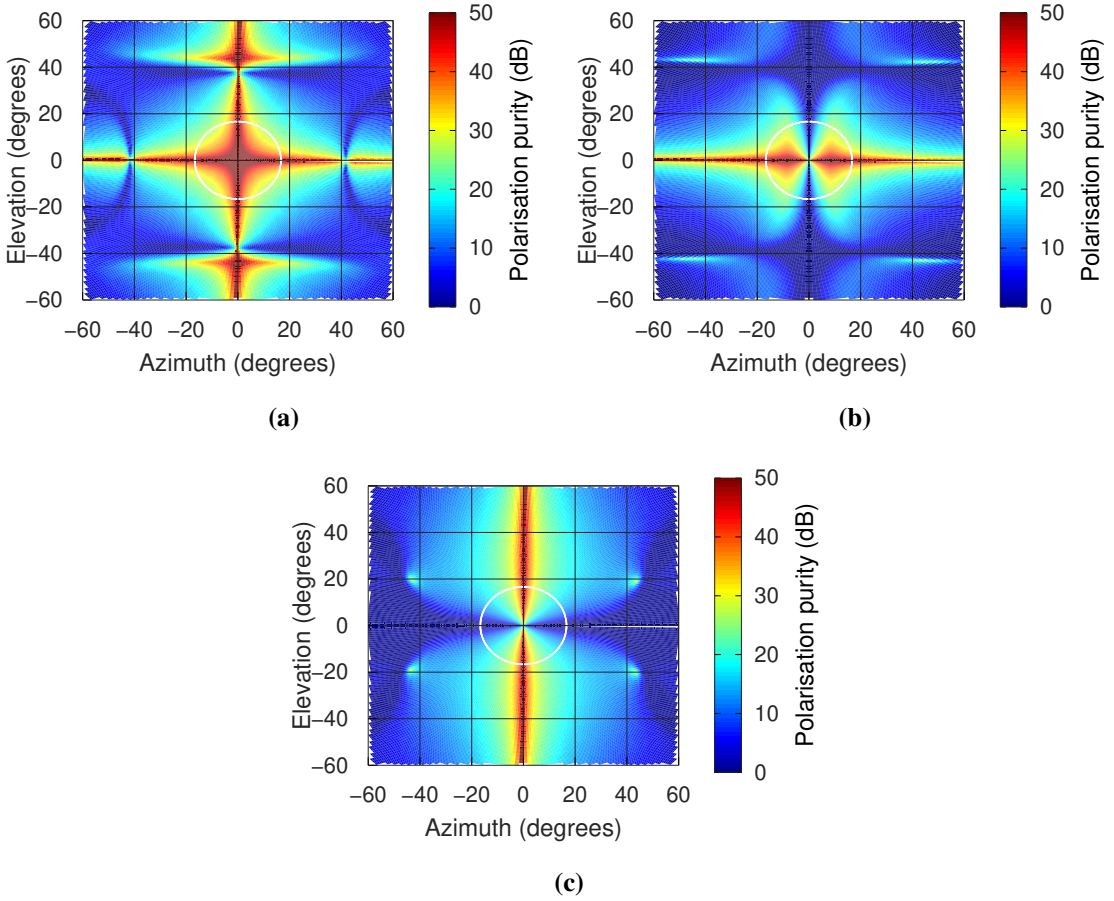

Figure 5.22. The polarisation purity of the monopulse horn antenna for (a) sum channel, (b) azimuth channel and for (c) elevation channel.

outside. In Figure 5.26(c), the initial angular error is $\approx 0.5^{\circ}$, which is supposed to be 0° because the jamming signal power is not increased at this point; this shows how tracking outside the 3 dB beamwidth does not give an accurate tracking angle.

5.7 ANTENNA FEED NETWORK SYMMETRY ANALYSIS IN APERTURE COUPLED MICROSTRIP MONOPULSE ANTENNA

The axially symmetric antennas were researched in [26] but for parabolic reflector antennas. It was found that if the antenna radiating elements are axially symmetrical, the antenna does not produce cross-polarisation on its axes because 1) the parabolic reflector quadrants have antiphase polarisations [26]", 2) due to symmetry, all rays have a constant distance from the focus to any plane normal to the axis [26]. The above statements apply not only to the reflector antennas; this effect is seen in the aperture-coupled antenna. Figure 5.27 shows the radiation patterns of the aperture-coupled antenna

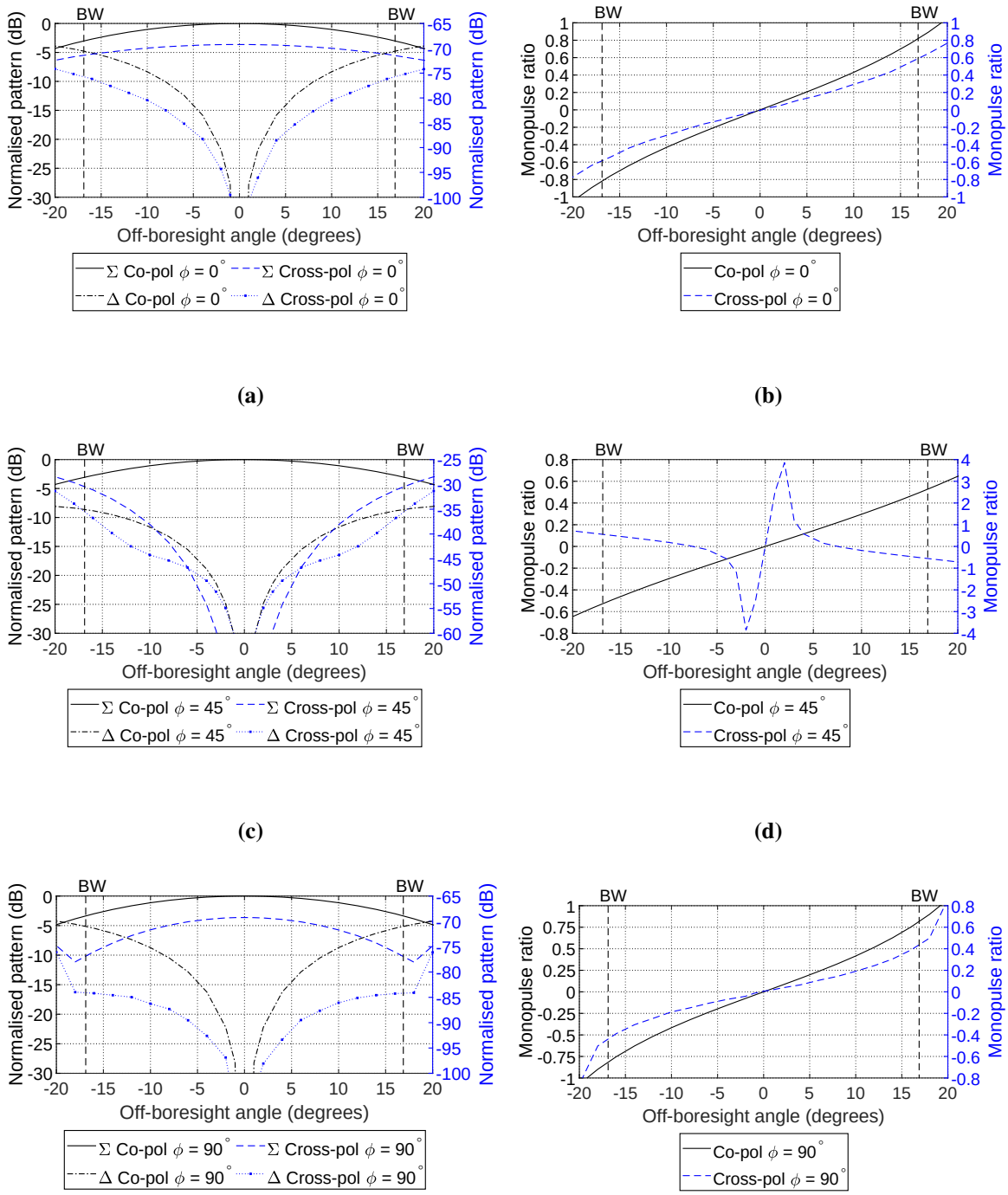

Figure 5.23. The radiation patterns of the monopulse horn antenna resulting from the received incident wave at (a) $\phi = 0°$ azimuth plane, (c) $\phi = 45°$ diagonal plane, and at (e) $\phi = 90°$ elevation plane. The imaginary monopulse ratios at (b) $\phi = 0°$ azimuth plane, (d) $\phi = 45°$ diagonal plane, and at (f) $\phi = 90°$ elevation plane.

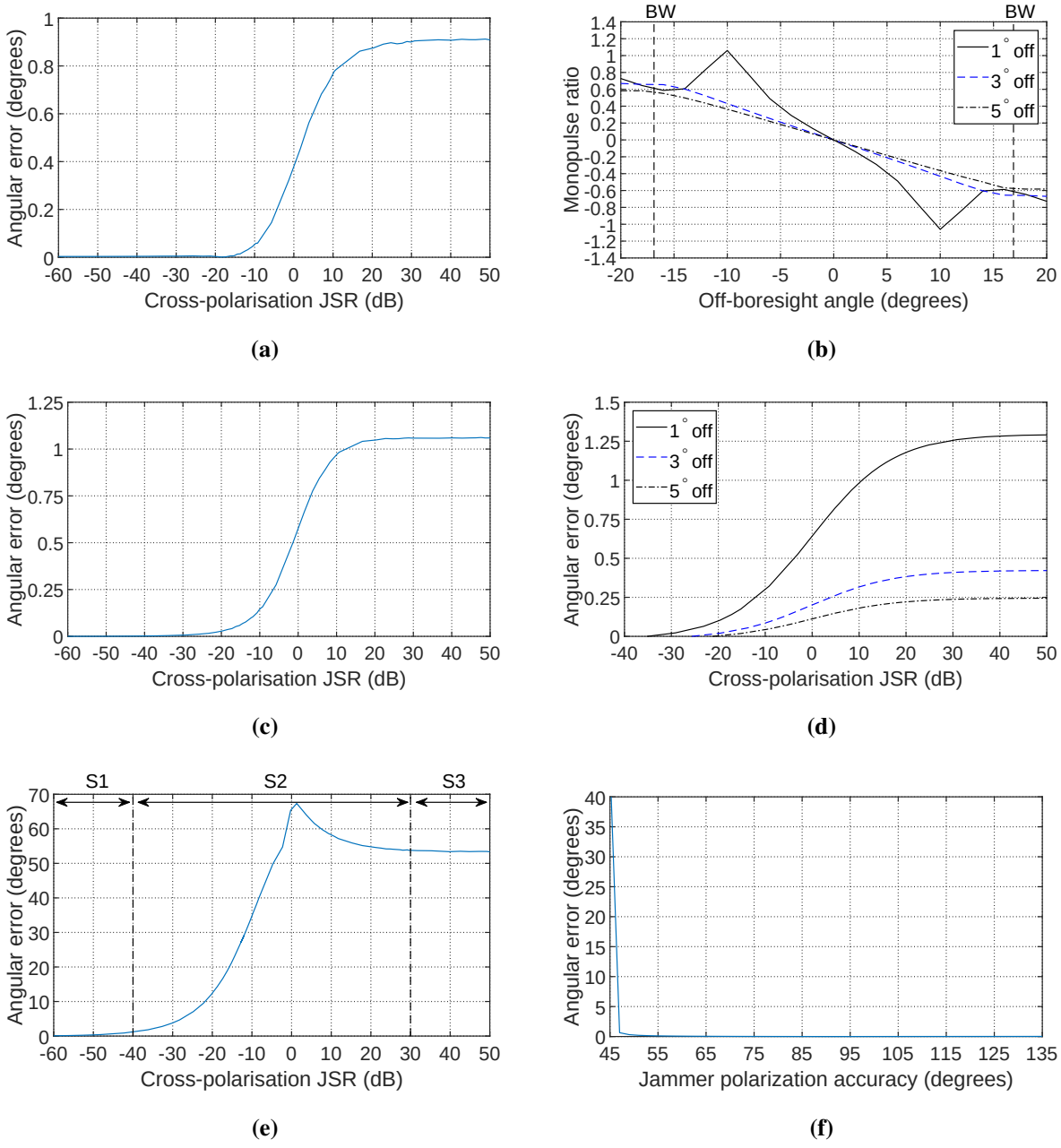

Figure 5.24. The monopulse horn antenna showing the (a) the induced angular error at $\phi = 0°$ azimuth plane, (c) the induced angular error at $\phi = 90°$ elevation plane, and (e) the induced angular error at $\phi = 45°$ diagonal plane. Polarisation accuracy analysis results at $\phi = 45°$ diagonal plane, (b) the monopulse ratios, (d) the induced angular error, and (f) induced angular error as the polarisation angle inaccuracy increases

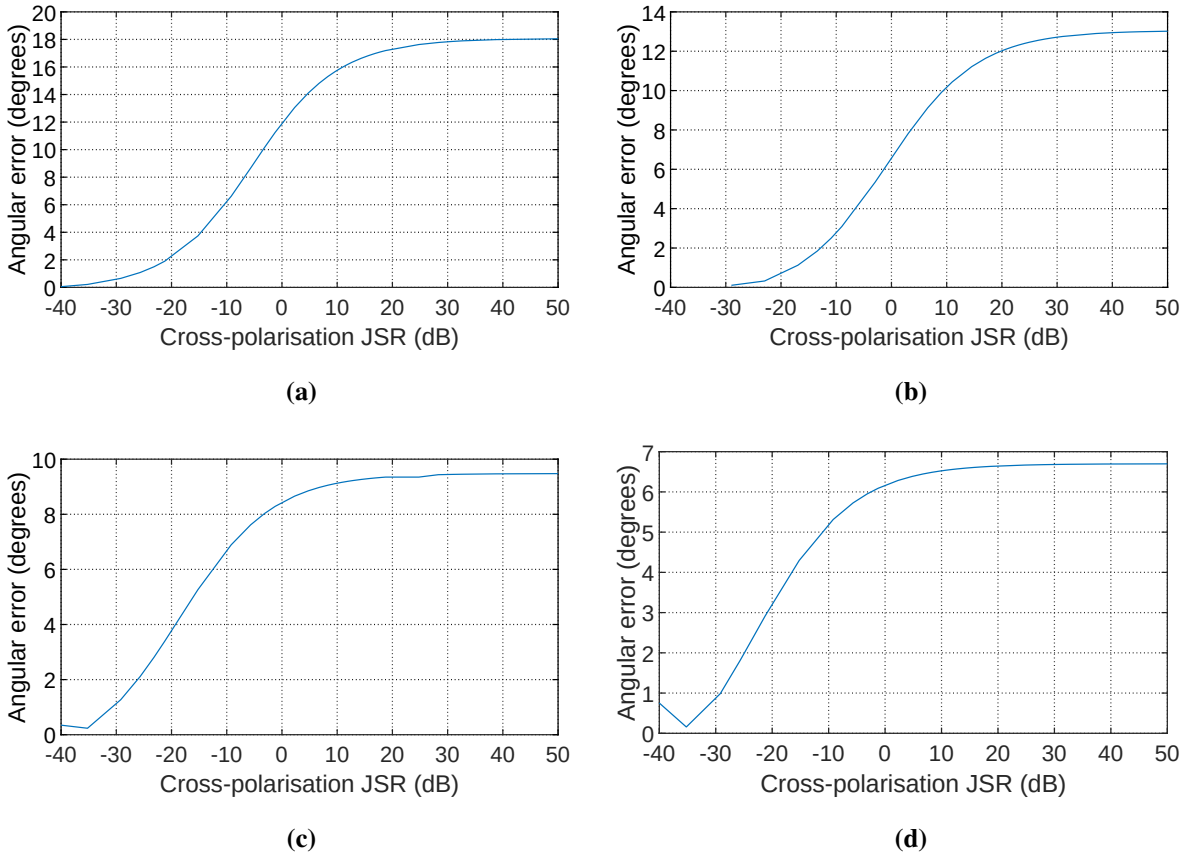

Figure 5.25. The tracking accuracy when the incident wave varies from boresight towards the 3 dB beamwidth for the wire-grid antenna. The cross-polarisation jammer at AOA (a) 2° within the 3 dB beamwidth, (b) 4° within the 3 dB beamwidth, (c) 6° within the 3 dB beamwidth, and (d) 8° outside the 3 dB beamwidth.

having asymmetric and symmetric feeding networks, as shown in Figures 3.7 and 3.8. Even though the feed network is not symmetrical in all four quadrants, they are still equal. The equality in the feed network is seen in the co-polarisation patterns, showing no difference for the symmetric and asymmetric feed network antenna. The difference is seen in the cross-polarisation patterns in Figure 5.28. Looking specifically at the sum channel cross-polarisation in Figures 5.28(a) and 5.28(b), it is seen that the antenna with the symmetric feeding network has Condon lobes in all four quadrants. In comparison, the antenna with the asymmetric feeding network has Condon lobes in the top two quadrants because the antenna feed network is only symmetric on one axis. The co-polarisation monopulse ratio does not show much difference in Figure 5.29, but the cross-polarisation monopulse ratio in Figure 5.30 shows a significant difference. The cross-polarisation monopulse ratio of the asymmetric feeding network is completely distorted in the azimuth and elevation planes in Figure 5.30(a) and 5.30(c), respectively.

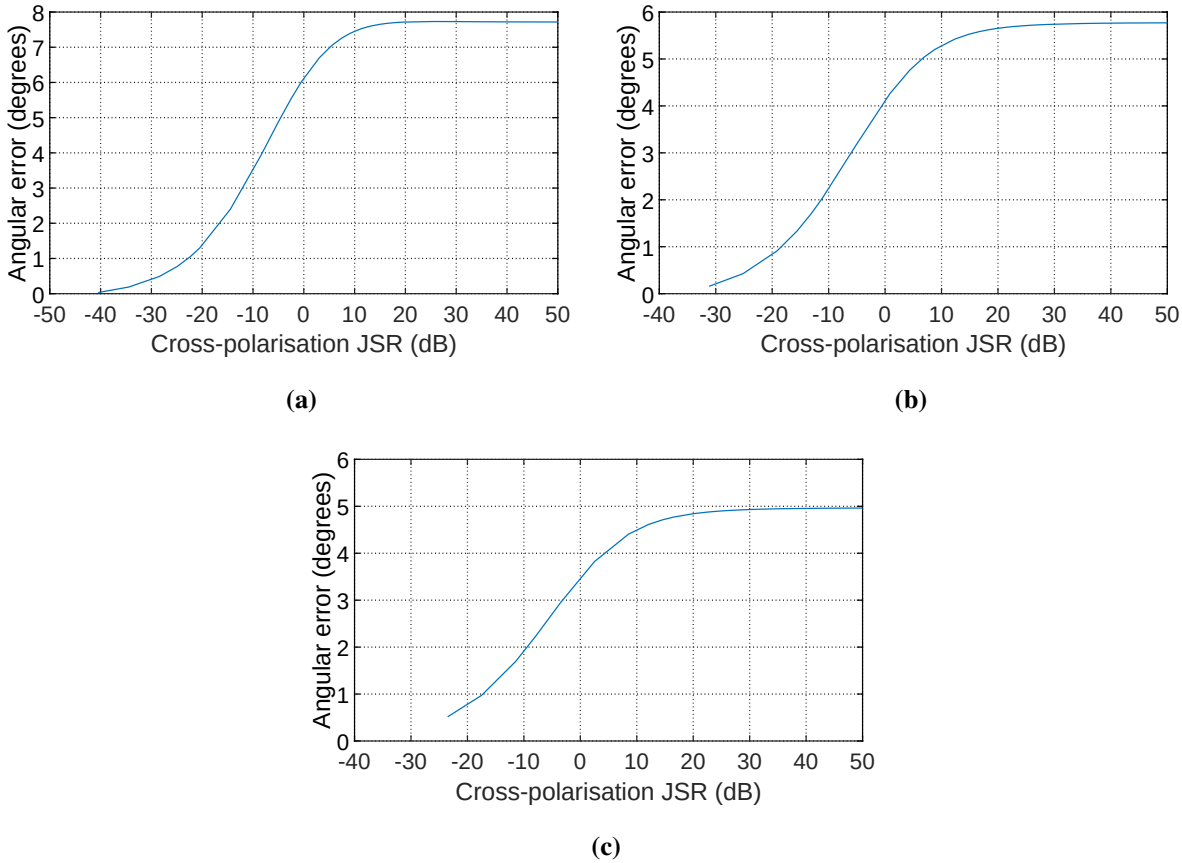

Figure 5.26. The tracking accuracy when the incident wave varies from boresight towards the 3 dB beamwidth for the Hannan parabolic reflector antenna. The cross-polarisation jammer at AOA (a) 0.4° within the 3 dB beamwidth, (b) 0.6° outside the 3 dB beamwidth, and (c) 0.8° outside the 3 dB beamwidth.

This effect is also seen in the polarisation purity in Figure 5.31; in the sum channel, the polarisation purity is offset away from the boresight.

5.8 PARABOLIC REFLECTOR FOCAL-LENGTH-TO-DIAMETER F/D ANALYSIS

The magnitude of the Condon lobes plays a crucial role in cross-polarisation jamming because they appear in the signal's cross-polarisation component. The higher the Condon lobes of the tracking radar antenna, the higher the induced angular error in the tracking radar by the cross-polarisation jammer. This statement is seen in Section 5.2, where the cross-polarisation jammer induces higher angular error into the wire-grid antenna than it induces into the Hannan parabolic reflector antenna because the designed Hannan parabolic reflector has lower Condon lobes than the wire-grid antenna. Low Condon lobes result in high polarisation purity compared to an antenna with high Condon lobes. The F/D of

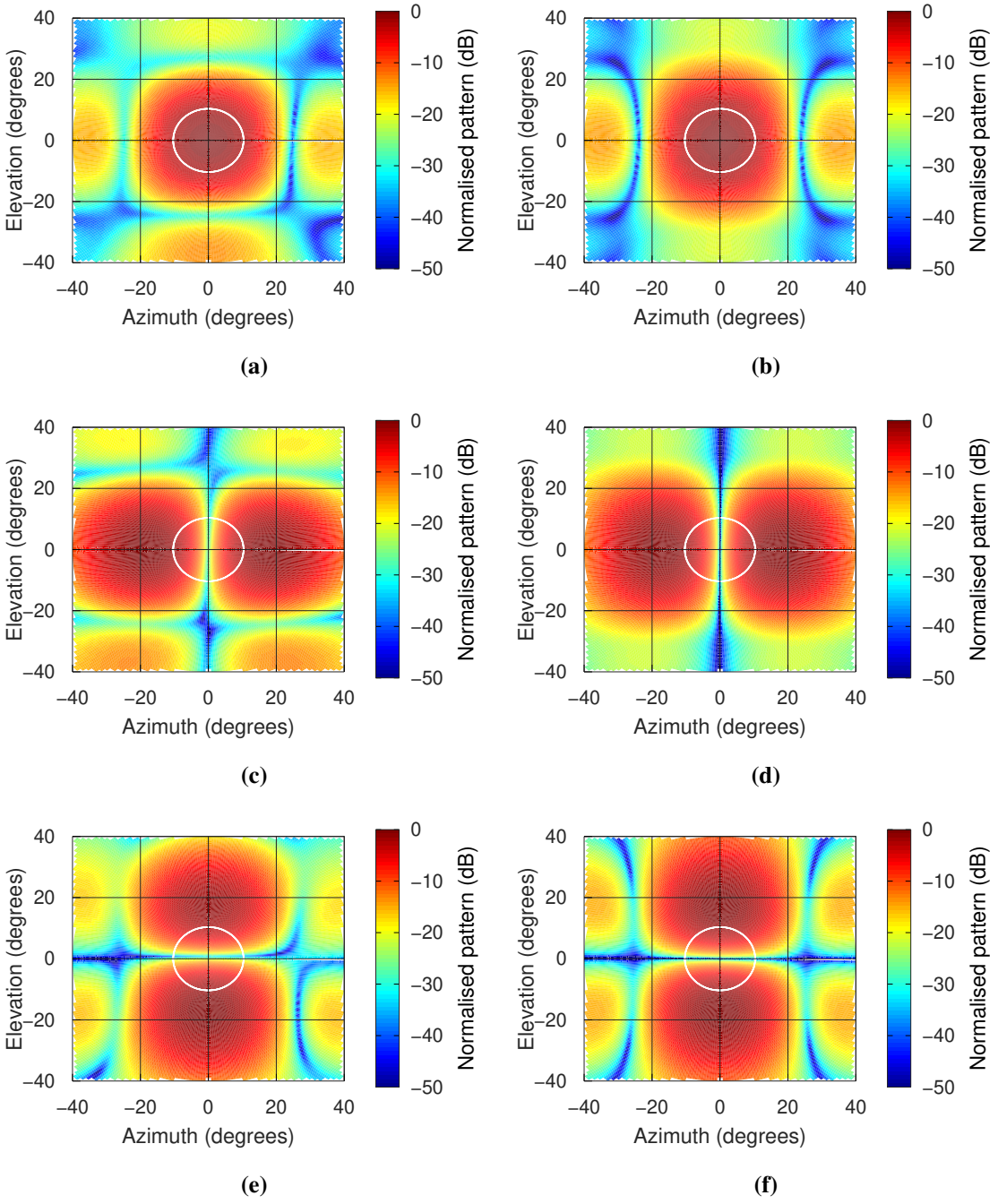

Figure 5.27. The co-polarisation patterns for the aperture-coupled antenna with symmetry and asymmetry feed network. (a), (c), and (e) are the sum, azimuth difference, elevation difference respectively for the asymmetry feed network. (b), (d), and (f) are the sum, azimuth difference, elevation difference respectively for the symmetry feed network. The white circle is the -3 dB beamwidth of the antenna

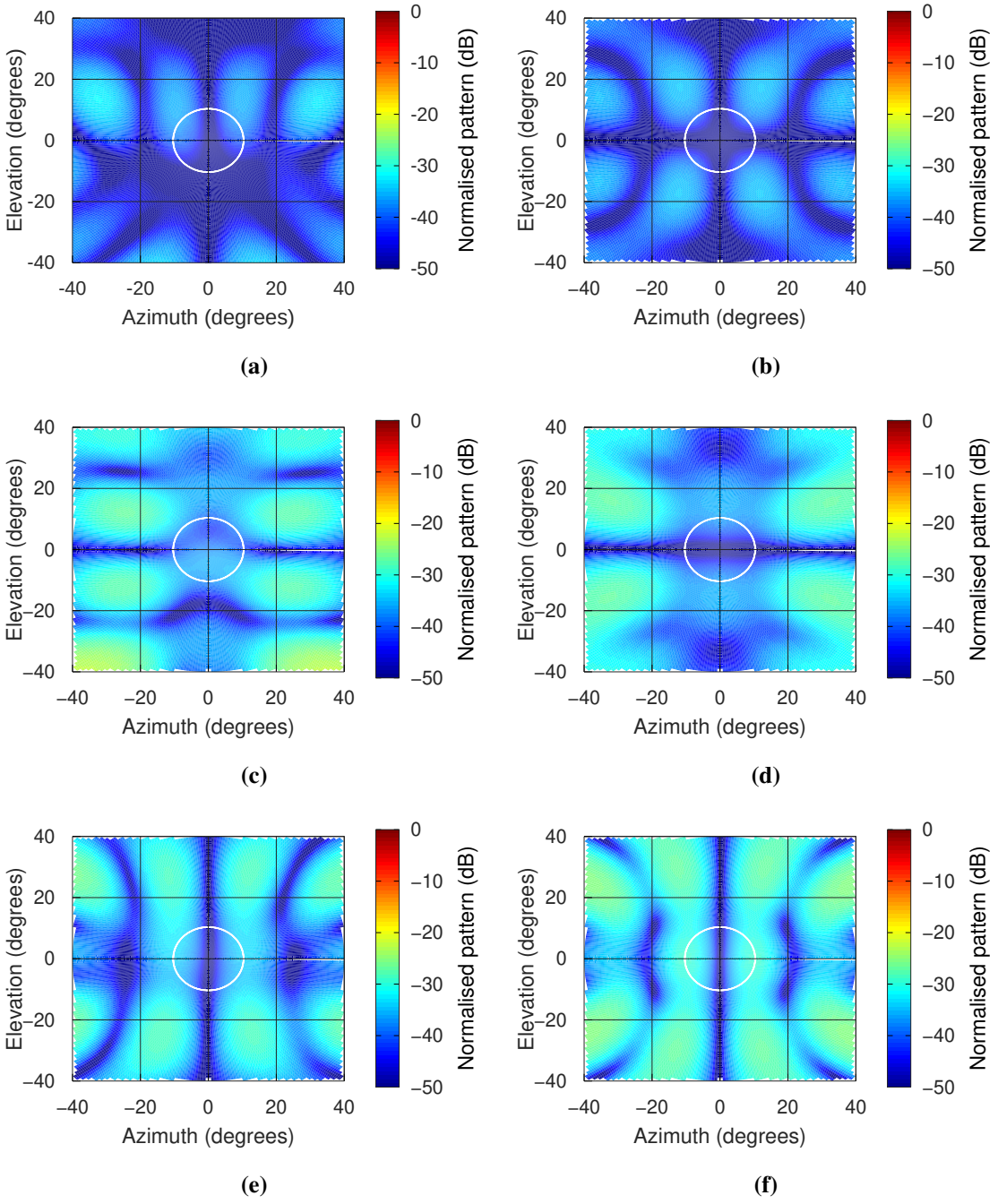

Figure 5.28. The cross-polarisation patterns for the aperture-coupled antenna with symmetry and asymmetry feed network. (a), (c), and (e) are the sum, azimuth difference, elevation difference respectively for the asymmetry feed network. (b), (d), and (f) are the sum, azimuth difference, elevation difference respectively for the symmetry feed network. The white circle is the -3 dB beamwidth of the antenna

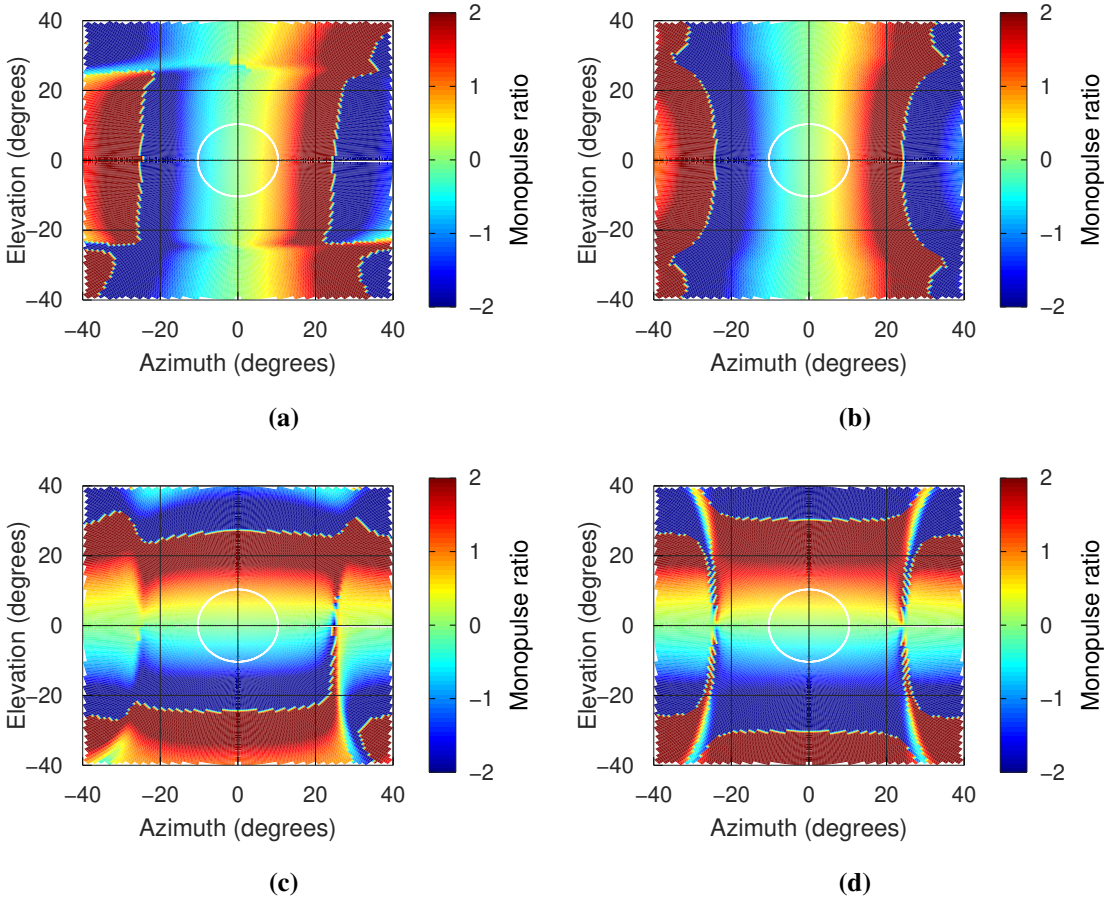

Figure 5.29. The co-polarisation monopulse ratio for the aperture-coupled antenna with symmetry and asymmetry feed network. (a), and (c) are for the azimuth and elevation planes respectively, for the asymmetry feed network. (b), and (d) are for the azimuth and elevation planes respectively, for the symmetry feed network. The white circle is the -3 dB beamwidth of the antenna

the antenna influences the size and magnitude of the Condon lobes in the parabolic reflector. This section analyses the effect of the F/D on the Condon lobes and the polarisation purity.

The parabolic reflector with different F/D is shown in Figures 5.32, 5.33, and 5.34. The co-polarisation sum patterns of the parabolic reflector are shown in Figure 5.32. Figures 5.32(a), 5.32(b), 5.32(c), 5.32(d), and 5.32(e) represent the F/Ds of 0.705, 0.94, 1.175, 1.29, and 1.41, respectively. The sum channel does not show a significant difference; the difference is noticed in the cross-polarisation patterns in Figure 5.33. The Condon lobes decrease from Figures 5.33(a) to 5.33(e) as the F/D increases from 0.705 to 1.41. The Condon lobes do not only decrease in magnitude, they decrease in size, but they do not become zero; this is seen in Figure 5.33(e) for

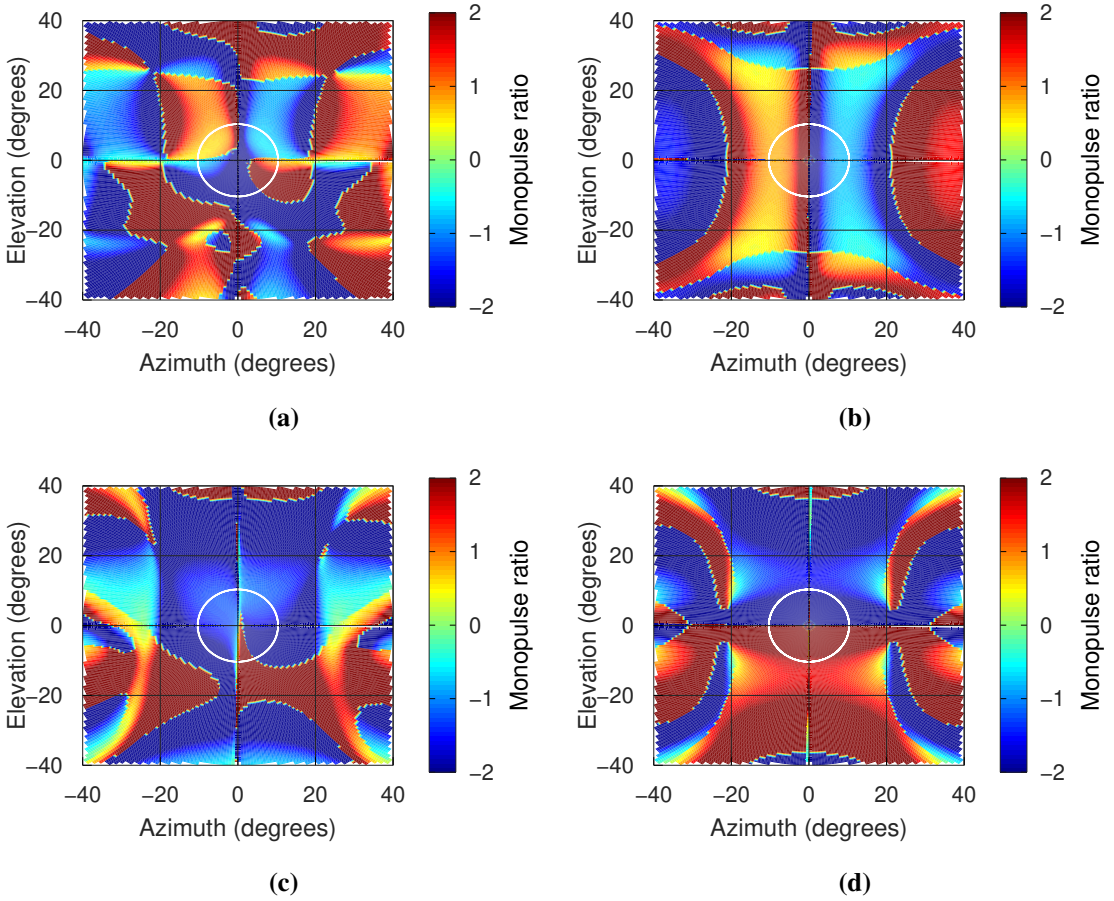

Figure 5.30. The cross-polarisation monopulse ratio for the aperture-coupled antenna with symmetry and asymmetry feed network. (a) and (c) are for the azimuth and elevation planes respectively, for the asymmetry feed network. (b) and (d) are for the azimuth and elevation planes respectively, for the symmetry feed network. The white circle is the -3 dB beamwidth of the antenna.

F/D of 1.29. It looks like they are completely erased, but that is because of the normalised pattern range of 0 to -50 dB. Figure 5.33(e) is zoomed in Figure 5.33(f), where the normalised pattern range is increased from 0 to -60 dB. The zoomed-in figure shows that the Condon lobes can be reduced, but they will always be there, especially for the parabolic reflector. The polarisation purity is shown in Figure 5.34; there are two things to focus on in these polarisation purity figures: the magnitude at the center and the circle outside the 3 dB beamwidth. The outside circle is not connected in Figure 5.34(a) but starts to connect from Figure 5.32(b) to Figure 5.34(e). The circle outside the 3 dB beamwidth is explained in this context to show the influence of the decreasing Condon lobes.

The important thing is the polarisation purity at boresight, and it increases in size from being almost

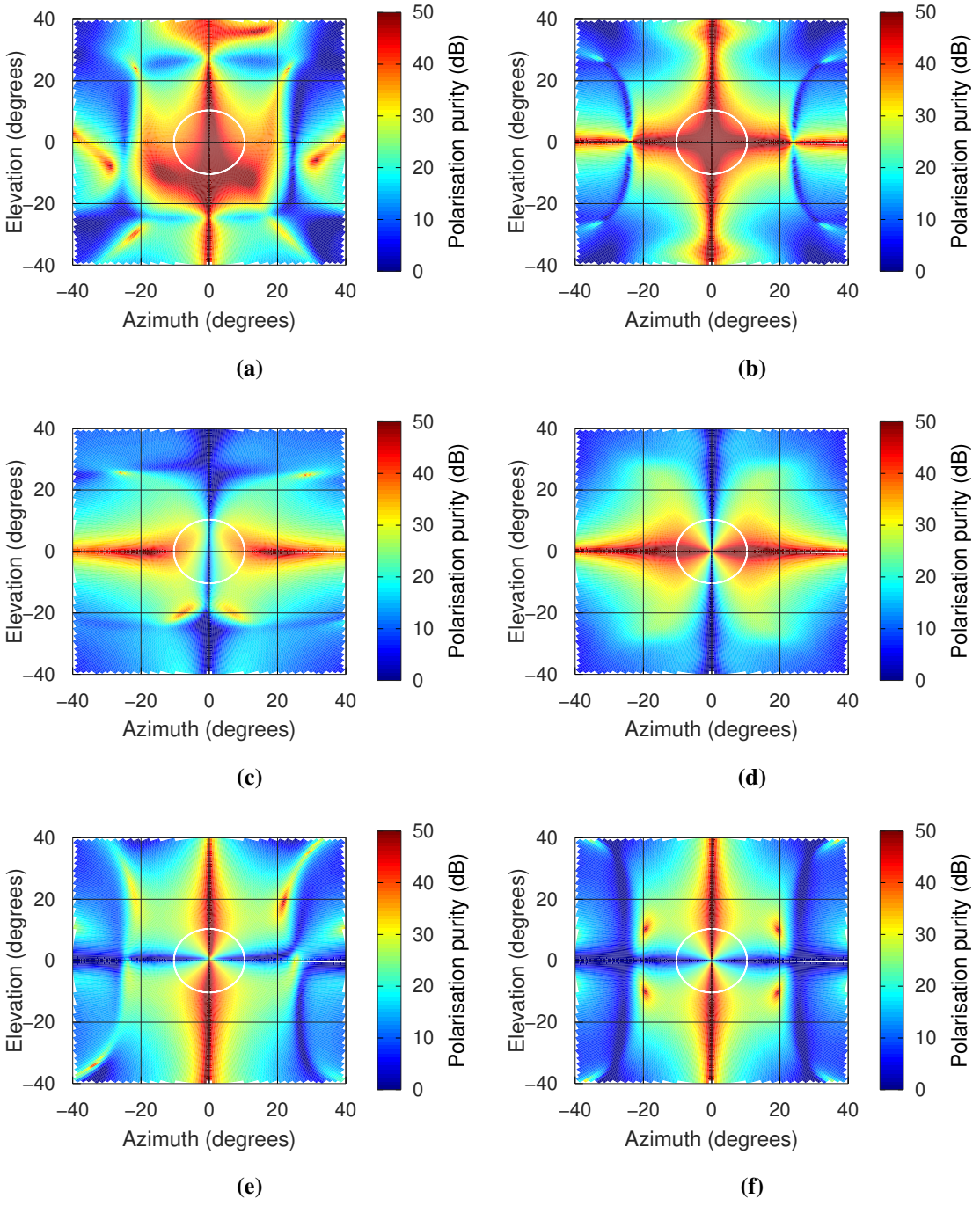

Figure 5.31. The polarisation purity of the aperture-coupled antenna with symmetry and asymmetry feed network. (a), (c), and (e) are the sum, azimuth difference, elevation difference respectively for the asymmetry feed network. (b), (d), and (f) are the sum, azimuth difference, elevation difference respectively for the symmetry feed network. The white circle is the -3 dB beamwidth of the antenna.

Table 5.6. The Hannan parabolic reflector focal-length-to-diameter (F/D) analysis

Plane	($\phi = 0°$, $\theta = 0°$)	($\phi = 90°$, $\theta = 0°$)	($\phi = 45°$, $\theta = 0°$)	($\phi = 45°$, $\theta = 1°$)
F/D		0.705		
Co-pol (dB)	53.900	53.900	53.900	39.551
Cross-pol (dB)	-13.626	-13.626	-13.626	19.310
polarisation purity (dB)	67.527	67.527	67.527	20.24
F/D		0.94		
Co-pol (dB)	54.071	54.071	54.071	38.304
Cross-pol (dB)	-13.819	-13.819	-13.819	19.197
polarisation purity (dB)	67.890	67.890	67.890	19.107
F/D		1.175		
Co-pol (dB)	53.569	53.569	53.569	36.812
Cross-pol (dB)	-6.946	-6.946	-6.946	16.952
polarisation purity (dB)	60.514	60.514	60.514	19.860
F/D		1.29		
Co-pol (dB)	53.695	53.695	53.695	36.201
Cross-pol (dB)	-22.930	-22.930	-22.930	11.845
polarisation purity (dB)	76.625	76.625	76.625	24.356
F/D		1.41		
Co-pol (dB)	53.326	53.326	53.326	36.151
Cross-pol (dB)	-24.070	-24.070	-24.070	4.887
polarisation purity (dB)	77.396	77.396	77.396	31.264

a star shape in Figure 5.34(a) to being almost a square shape in Figure 5.34(e). The plots do not show the highest magnitude; therefore, Table 5.6 shows the highest peaks at the boresight and the Condon lobes. The yellow cells show the magnitude of the Condon lobes decreasing from 19.310 dB, 19.197 dB, 16.952 dB, and 11.845 dB to 4.887 dB. The polarisation purity increases from 20.240 dB, 19.107 dB, 19.860 dB, and 24.356 dB to 31.264 dB. The F/D of 0.705, 0.940, and 1.175 do not show much difference in the polarisation purity, but a clear difference is seen in F/D of 1.175, 1.290, and 1.410.

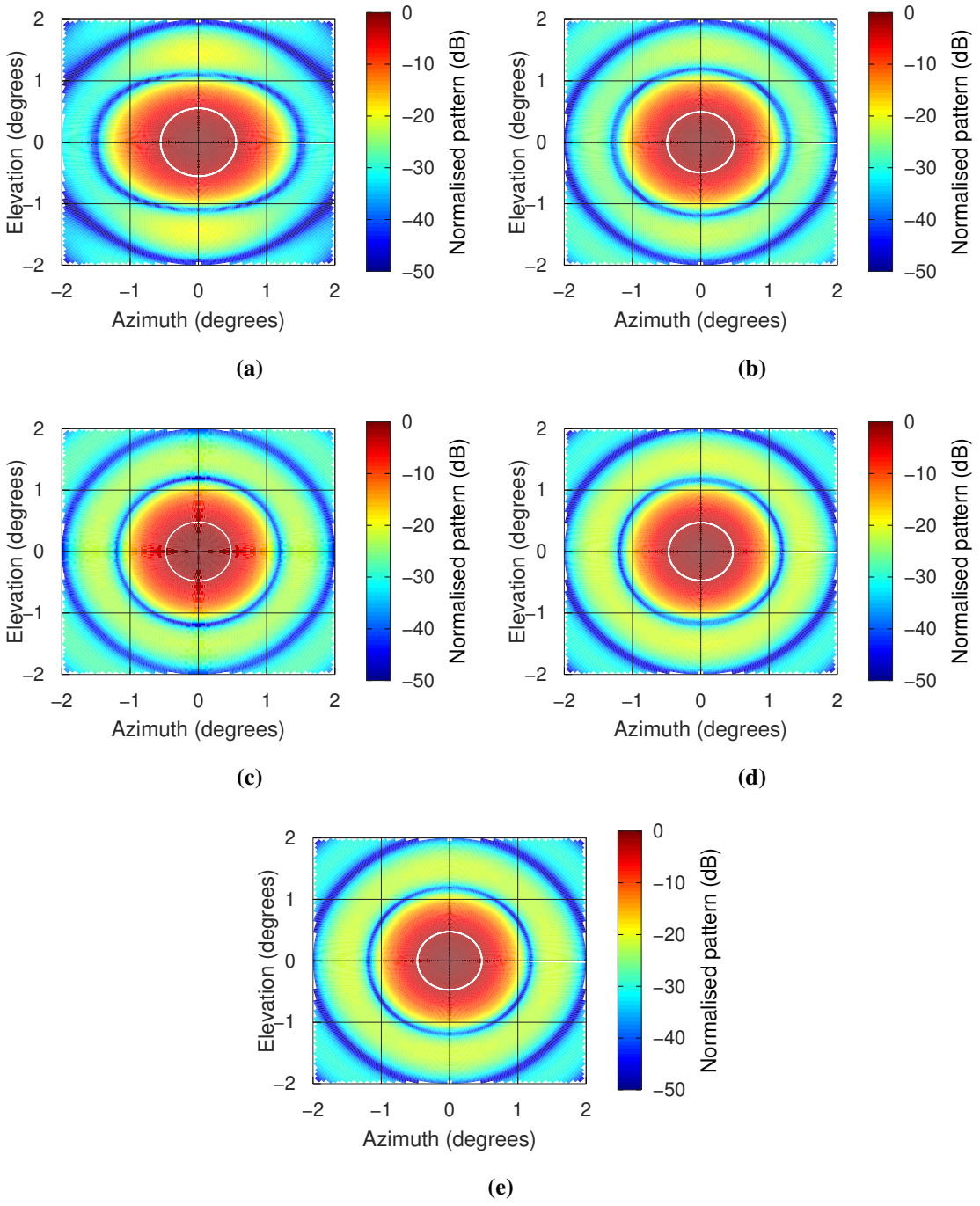

Figure 5.32. Investigating the effects of F/D on the Condon lobe size, the co-pol sum signal patterns of the parabolic reflector with different F/D sizes, (a) F/D = 0.705, (b) F/D = 0.94, (c) F/D = 1.175, (d) F/D = 1.29, and (e) F/D = 1.41. The white circle is the -3 dB beamwidth of the antenna

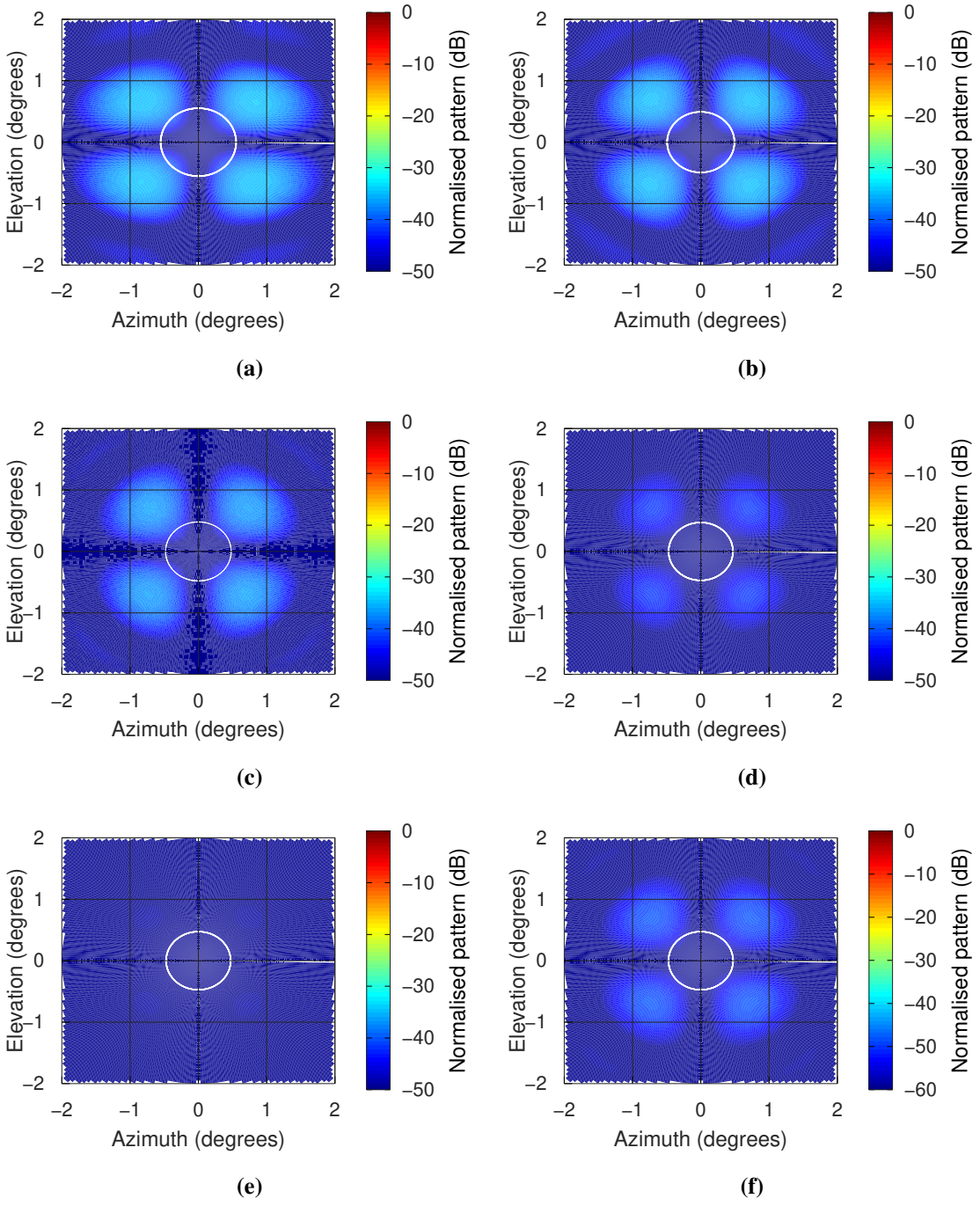

Figure 5.33. Investigating the effects of F/D on the Condon lobe size, the cross-pol sum signal patterns of the parabolic reflector with different F/D sizes, (a) F/D = 0.705, (b) F/D = 0.94, (c) F/D = 1.175, (d) F/D = 1.29, and (e) F/D = 1.41, (e) F/D = 1.41 zoomed in. The white circle is the -3 dB beamwidth of the antenna

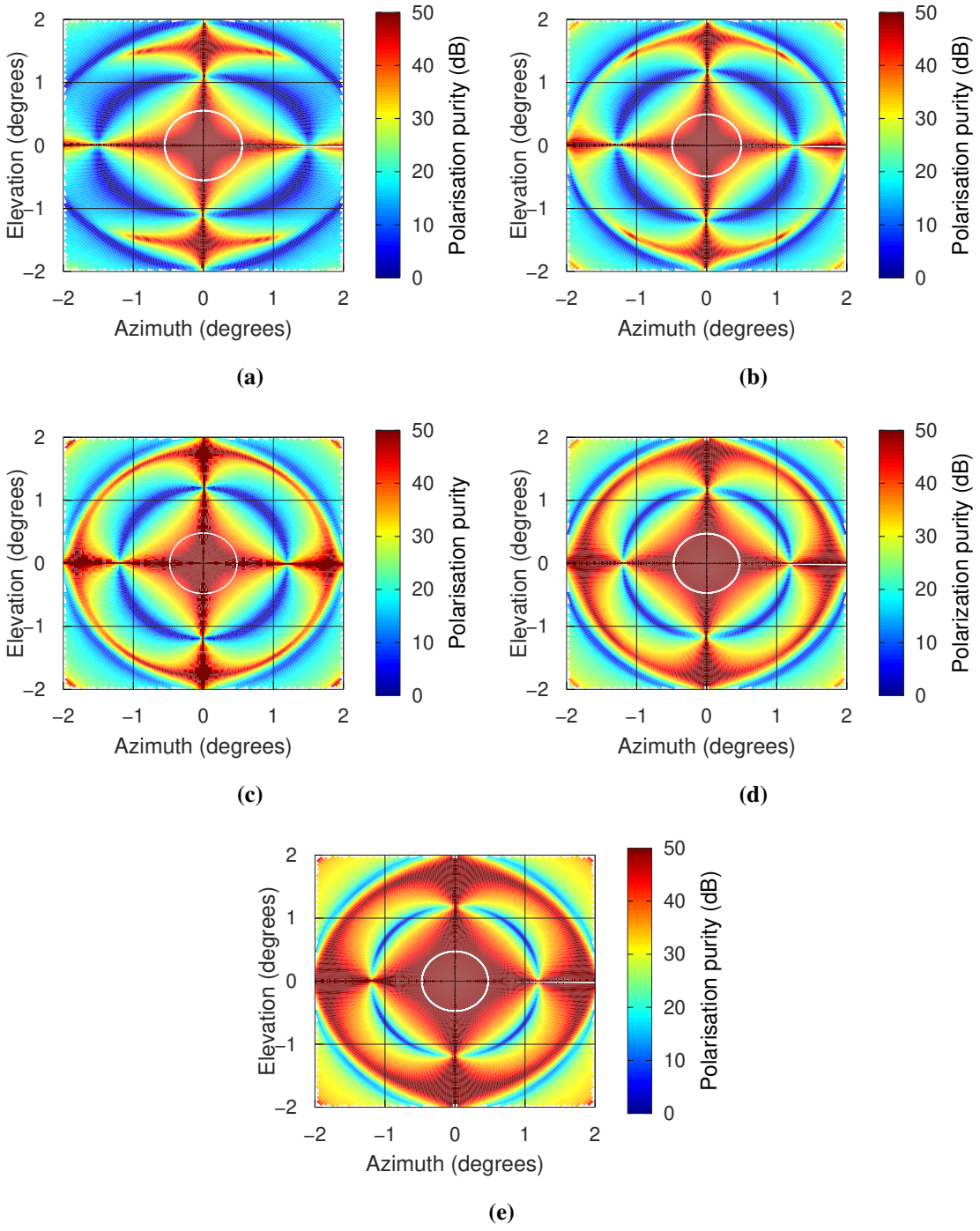

Figure 5.34. Investigating the effects of F/D on the Condon lobe size, sum signal polarisation purity of the parabolic reflector with different F/D sizes, (a) F/D = 0.705, (b) F/D = 0.94, (c) F/D = 1.175, (d) F/D = 1.29, and (e) F/D = 1.645. The white circle is the -3 dB beamwidth of the antenna

5.9 WIRE-GRID ANTENNA MEASUREMENT RESULTS

The wire-grid antenna was chosen as the antenna to be manufactured and analysed. The original antenna by [28] was operating at X-band with a center frequency of 10 GHz. The same wire-grid antenna was analysed at 10 GHz, but the manufactured antenna was re-designed to C-band with a center frequency of 5.5 GHz. The final design performance results of the wire-grid antenna in FEKO are shown in Figure 5.36. In the reflection coefficient results, it is seen that the antenna is matched at 5.48 GHz, but the 5.5 GHz is still below -10 dB, the antenna has a narrow band of $\approx$ 50 MHz, the SLL for all the selected frequencies in Figure 5.36 is above 18 dB. The antenna performs well across various frequencies, not just the selected frequencies. The diagonal planes show the Condon lobes.

The antenna was designed using RO4003C substrate with a dielectric constant of 3.38 and a thickness of 0.813 mm; the antenna geometry is shown in Figure 5.37. Figures 5.37(a), 5.37(c), and 5.37(e) show the measurement setup at the anechoic chamber A (University of Pretoria). In anechoic chamber A, the transmitting antenna was only changed from azimuth, elevation, and diagonal planes. The anechoic chamber B Council for Scientific and Industrial Research (CSIR) shown in Figures 5.37(b), 5.37(d), and 5.37(f) was used to measure antenna polarisation accuracy because the transmitting antenna polarisation can be changed electronically, meaning the polarisation can be incremented from co-polarisation to cross-polarisation angles using the chosen angle increments. In contrast, anechoic chamber A cannot perform these increments. In both chambers, the mechanical servor the AUT is placed on can scan in the XZ and YZ planes. To take measurements for the azimuth and elevation planes, the antenna is placed as shown in Figures 5.37(a) and 5.37(b), and for the diagonal plane measurements, the antenna must be rotated as shown in Figures 5.37(c) and 5.37(d). In the anechoic chamber A, only the XZ plane scan was used, meaning that, to scan the elevation and diagonal planes, the antenna must be rotated to align with the scanning plane.

The antenna reflection coefficients are shown in Figure 5.38. These results show that the antenna is matched but at a center frequency different from the simulated design frequency; however, it is matched within the designed frequency bandwidth. The antenna port isolation is $\approx$ 40 dB for all the ports, resulting in less coupling between the ports. The antenna was measured at the propagating matched frequencies.

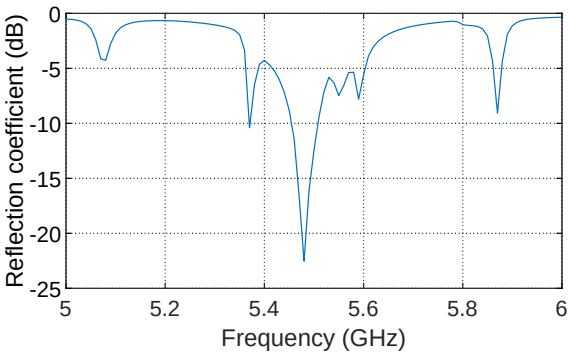

(a)

Figure 5.35. The final design results of the wire-grid antenna in FEKO software before manufacturing. (a) is the reflection coefficient of the four symmetric ports

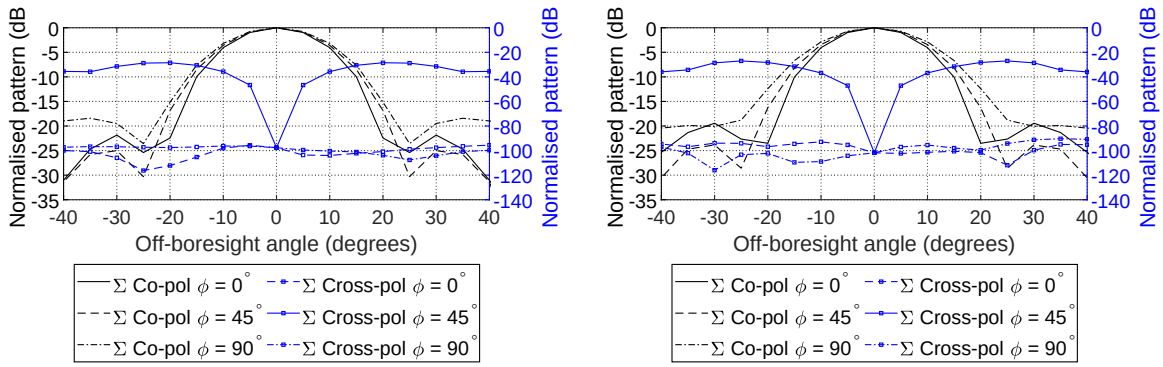

(a) **(b)**

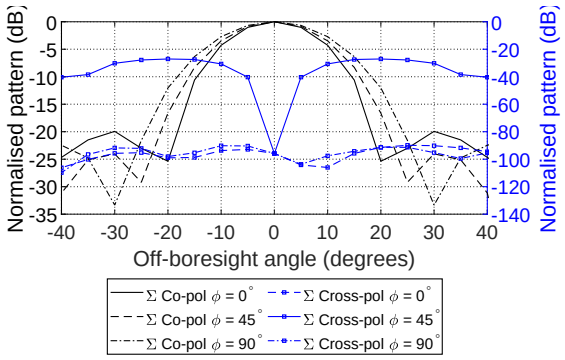

(c)

Figure 5.36. The final design results of the wire-grid antenna in FEKO software before manufacturing. The radiation patterns performance at (a) 5.47 GHz, (b), 5.48 GHz, and (c) 5.5 GHz.

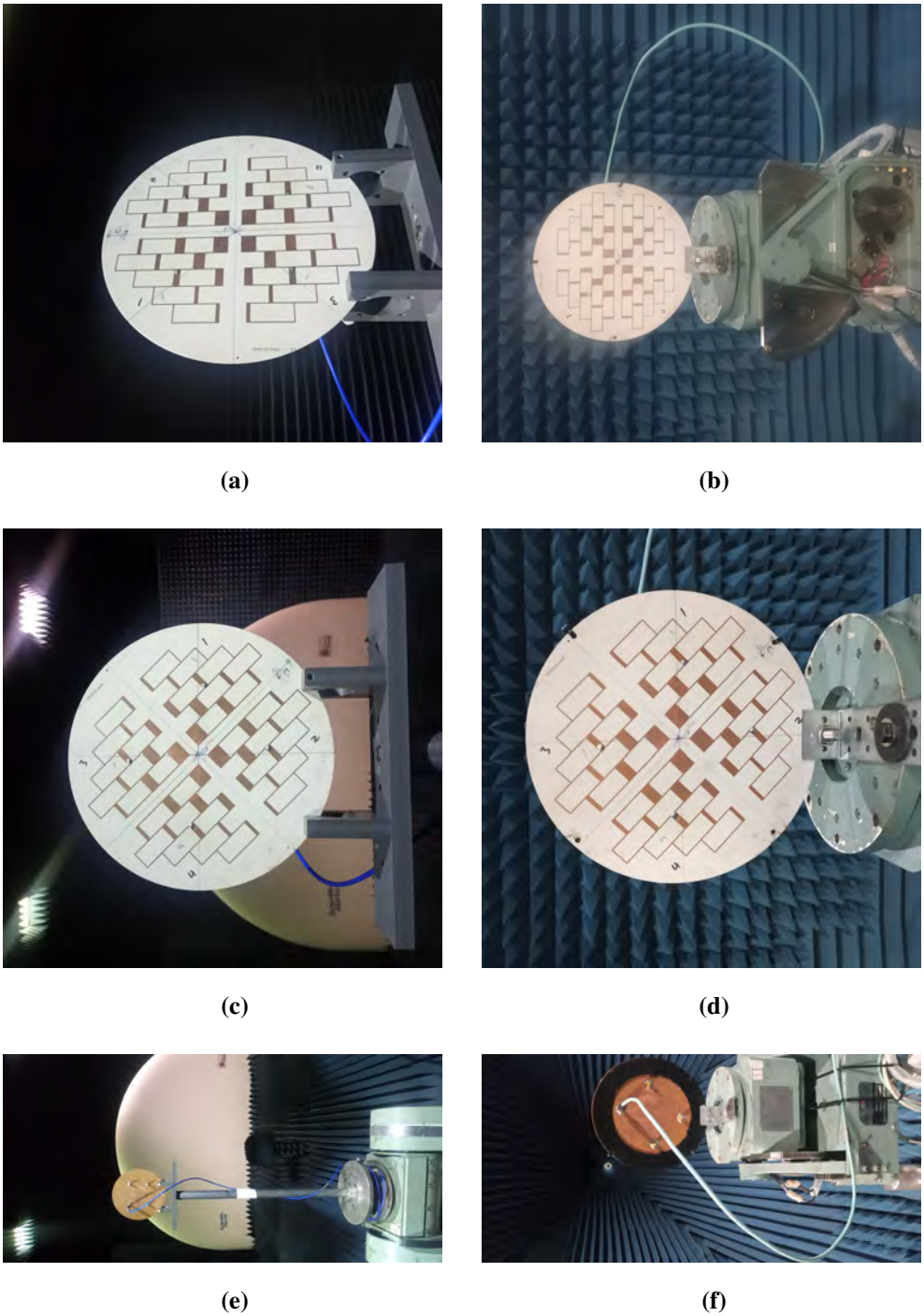

(a) **(b)**

(c) **(d)**

(e) **(f)**

Figure 5.37. The results were taken at two different anechoic chambers. The setup for anechoic chamber A is (a), (c), and (e). Then the setup for anechoic chamber B is (b), (d), and (f).

The radiation patterns from Chamber A in the azimuth and elevation planes are shown in Figures 5.39(a) and 5.39(b). They show the sum patterns having SLL $\approx$ 16 dB and $\approx$ 14 dB, respectively, in the diagonal plane in Figure B.3. The diagonal plane radiation patterns in Figure 5.39(c) show SLL $\approx$ 16 dB, and the cross-polarisation patterns have a null at boresight. However, it is not well defined and the Condon lobes are also not well defined. The monopulse ratio for the azimuth, elevation, and diagonal planes are shown in Figures 5.39(d) , 5.39(e), and 5.39(f), respectively. The co-polarisation monopulse ratios are as expected and pass through boresight at 0. The cross-polarisation monopulse ratio is expected to pass through boresight at 0, but it does not because the cross-polarisation patterns nulls are not at boresight.

Chamber B measurements are shown in Figure 5.40, and the radiation patterns and monopulse ratios in the diagonal planes are shown in Figures 5.40(a) and 5.40(b), respectively. It is seen that the co-polarisation radiation pattern has an SLL > 20 dB, and the cross-polarisation patterns have well-defined Condon lobes. The effect of having a null at boresight is seen in the monopulse ratio crossing boresight at 0. The cross-polarisation monopulse ratios do not always cross the co-polarisation monopulse ratio at off-boresight angle $\theta = 0°$. This deviation from the axis is due to the antenna not being aligned 100% correctly to the azimuth, elevation or diagonal plane during measurement. If the antenna is off by as little as 0.5°, it will show a little squint; this is shown in Figure B.3 when the difference patterns null is not precisely at boresight angle $\theta = 0°$.

The results show that cross-polarisation measurements need higher measurement accuracy than co-polarisation measurements. The cross-polarisation patterns have similar behaviour; all the monopulse ratios cross the boresight at 0, and the radiation patterns have a peak at boresight. However, the cross-polarisation patterns do not all have nulls at boresight. Appendix B shows the measurement results at different frequencies.

The polarisation accuracy at different frequencies is shown in Figure 5.40(c); at the cross-polarisation angle of 135°, the cross-polarisation jammer has induced angular error into the tracking radar as it has 100% cross-polarisation accuracy, but as the polarisation angle becomes inaccurate, the induced angular error is reduced significantly. The polarisation is moving towards the co-polarisation angle, which means the tracking radar is now tracking accurately; the tracking angular error is reduced and becomes 0° when the co-polarisation angle is 45°. The results are shown at six different frequency points: 5.67 GHz, 5.68 GHz, 5.69 GHz, 5.70 GHz, 5.71 GHz, and 5.72 GHz.

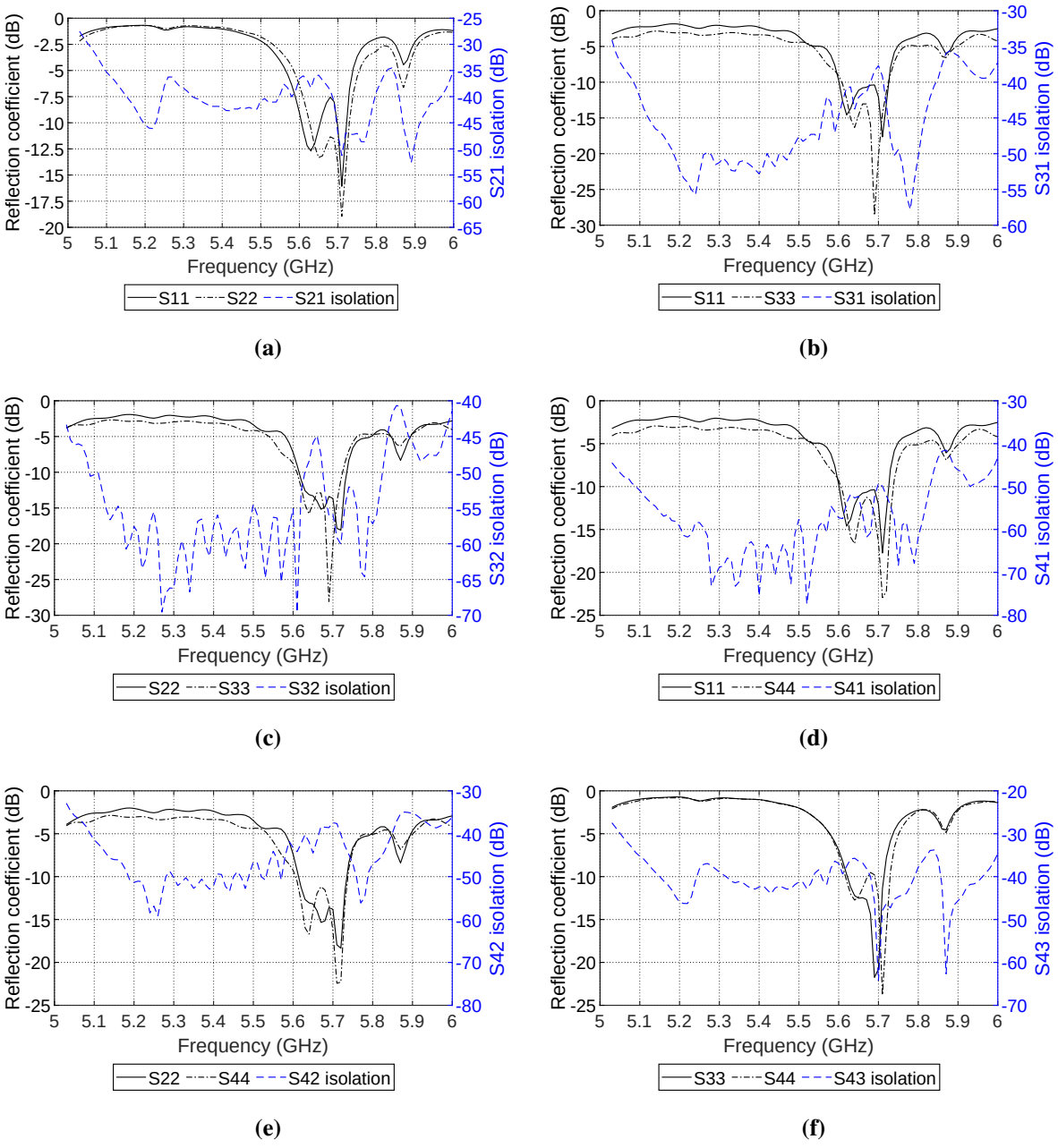

Figure 5.38. The measured reflection coefficient and ports isolation for (a) port 2 and 1, (b) port 3 and 1, (c) port 3 and 2, (d) port 4 and 1, (e) port 4 and 2, and (f) port 4 and 3.

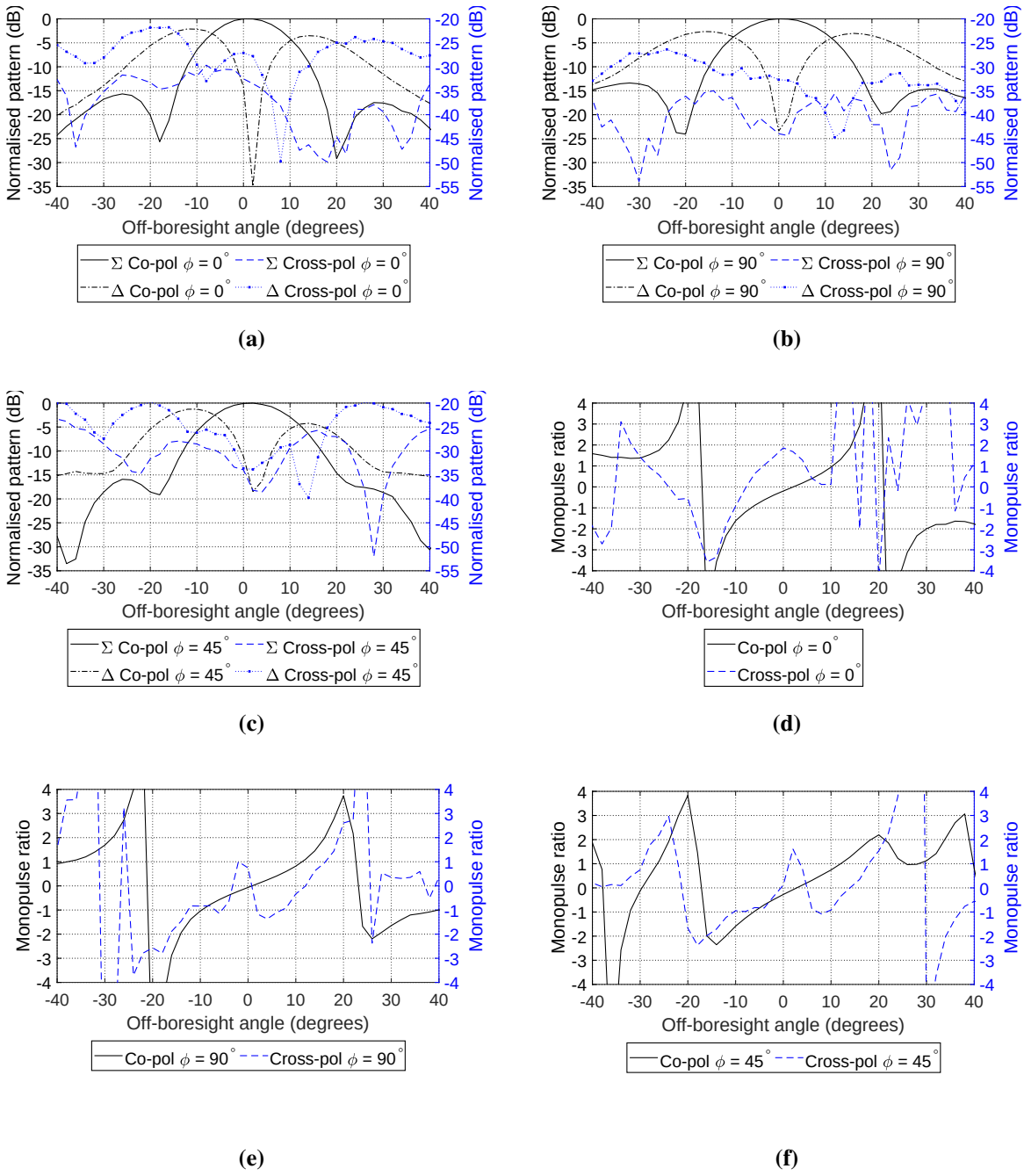

Figure 5.39. The wire-grid antenna results measured in the anechoic chamber A at 5.70 GHz (a) azimuth plane radiation patterns, (b) elevation plane radiation patterns, (c) diagonal plane radiation patterns, (d) imaginary monopulse ratio in the azimuth plane, (e) imaginary monopulse ratio in the elevation plane, and (f) imaginary monopulse ratio in the diagonal planes.

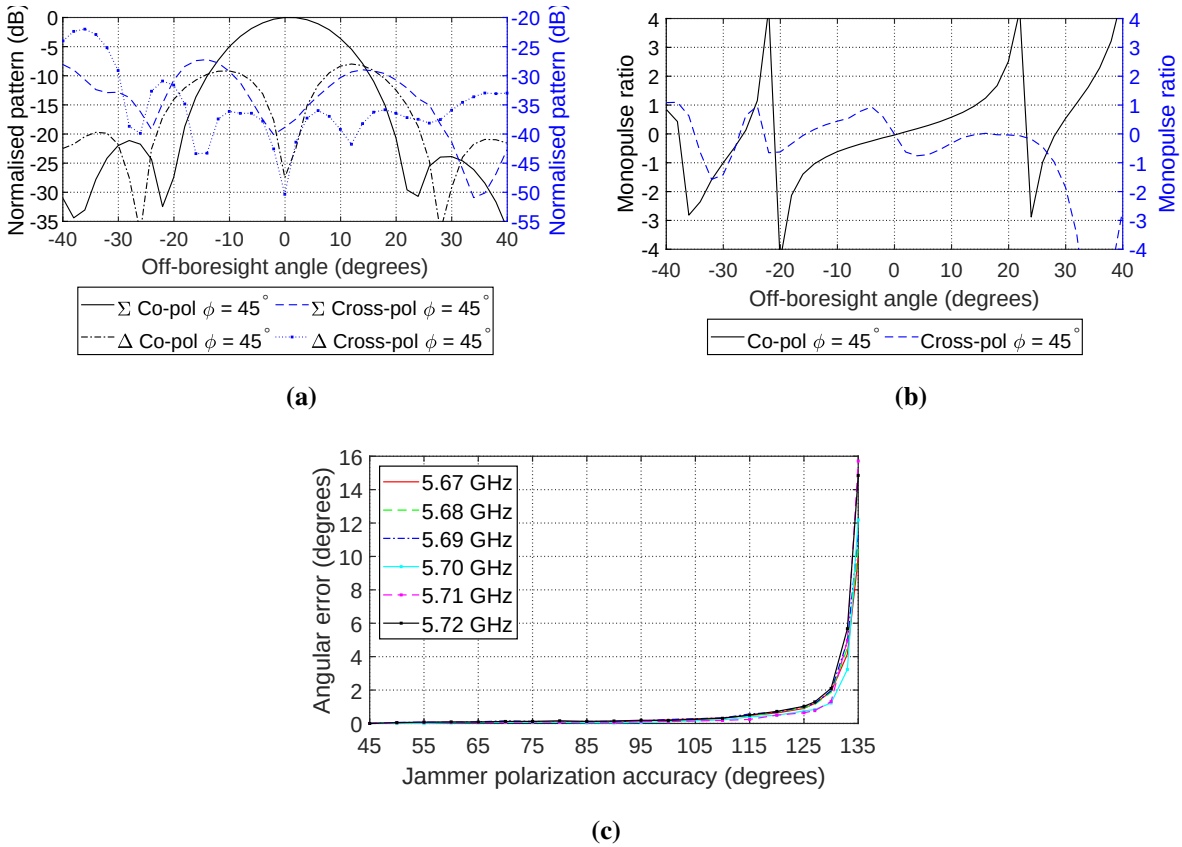

Figure 5.40. The diagonal plane results of the wire-grid antenna measured in the anechoic chamber B at 5.68 GHz (a) radiation patterns, (b) imaginary monopulse ratio, (c) and the polarisation accuracy.

5.9.1 Experimental setup limitations

The experiments were performed at two measurement facilities, chamber A and chamber B. In chamber A, only azimuth, elevation, and diagonal plane measurements can be made, which means that angular error vs. jammer polarisation accuracy measurements cannot be made there. The angular error vs. jammer polarisation accuracy measurements were made at Chamber B. Even though it was possible to take measurements for angular error vs jammer polarisation accuracy at chamber B, the minimum polarisation increment angle is 2°. From the results, it is seen that when the jammer polarisation accuracy is off by 1° to 5°, the induced angular error decreases rapidly. These results can be refined if Chamber B could increment the polarisation angle with angles less than 2°. In a practical cross-polarisation jammer, the jammer receives the radar signal with both polarisations at the same time, however, the experiments in this work use one antenna to receive the co-polarisation signal and it is rotated to the appropriate angle to receive a cross-polarisation signal. This can be improved by using

two antennas as receiving antennas, one antenna receives a cross-polarisation signal while the other antenna receives a co-polarisation signal. The work can benefit from performing cross-polarisation experiments in a way that a real system would perform, however, the way this work performs the cross-polarisation jamming is sufficient for the analysis. There is a limitation that applies to both the experimental and the simulation setup. The limitation is that they do not take into consideration the jammer platform. In a practical setup, the cross-polarisation jammer will be installed on a platform such as an aircraft. This can be achieved by using a UAV as a jammer platform. This is important as it takes into consideration the radar cross section (RCS) of the jammer platform. The jammer platform will scatter the radar signal in different directions.

5.10 SUMMARY OF THE PRACTICAL IMPLICATIONS OF THE RESULTS

The cross-polarisation jamming is effective on antennas with Condon lobes in their cross-polarisation signal component. This means the jammer will not be effective on antennas that do not have Condon lobes. Antennas with Condon lobes have different polarisation purity, this means antennas with high polarisation purity would require a jammer to have high JSR. The cross-polarisation jammer must have high polarisation accuracy in a practical environment.

5.11 CHAPTER SUMMARY

The radiation patterns of the six antennas are presented, and they show that the antennas qualify to be used to analyse cross-polarisation jamming. Condon lobes are seen in the diagonal planes of the antennas. The polarisation purity of the antennas is presented. It shows that the jammer induces less angular error in radar antennas with high polarisation purity than those with low polarisation purity. The polarisation purity is influenced by the Condon lobe size; the higher the Condon lobes, the lower the polarisation purity and vice versa. Cross-polarisation accuracy is vital in cross-polarisation jamming. Condon lobes are caused by the axial symmetry in the antenna radiating elements and the feed network.

CHAPTER 6 DISCUSSION

6.1 CHAPTER OVERVIEW

This chapter presents the research discussion for this dissertation. Section 6.2 discusses the antenna radiation patterns, monopulse ratio, and polarisation purity in the transmitting mode. Section 6.3 discusses the radiation patterns, monopulse ratios, induced angular error, polarisation accuracy, and the measurement results in the receiving mode. Section 6.4 discusses the cross-polarisation pattern modelling and Section 6.5 compares the theoretical, simulation, and measurement results.

6.2 TRANSMITTING MODE

6.2.1 Radiation Patterns

In all the antenna radiation patterns, the sum channel has a well-defined peak at boresight. All the difference patterns in the azimuth and elevation planes have a well-defined null at their relevant axis. The radiation patterns show that these antennas are suitable for target detection and tracking and are suitable for analysing cross-polarisation jamming. As mentioned in the previous sections, the sum signal is transmitted, and on reception, the difference signals are formed and, together with the sum signal, are used to track the target.

The cross-polarisation sum patterns do not have a peak at boresight; instead, it has peak lobes at $\pm 45^{\circ}$ and $\pm 135^{\circ}$ planes called Condon lobes. A cross-polarisation jammer uses these lobes to jam the tracking radar. The cross-polarisation difference channels are interchanged with the co-polarisation difference channels. The cross-polarisation azimuth difference pattern has a null in the axis that the co-polarisation elevation difference pattern has a null; the cross-polarisation elevation difference pattern has a null in the axis that the co-polarisation azimuth difference pattern has a null. The cross-polarisation patterns are normalised to the co-polarisation sum pattern; comparing the parabolic reflector antenna and the wire-grid antenna, the parabolic reflector has high polarisation purity. The

polarisation isolation of the sum pattern is ≈ 25 dB for the wire-grid antenna in Figure 5.2(a) and ≈ 30 dB for the parabolic reflector in Figure 5.2(b); this means it will require more signal power to jam the parabolic reflector than to jam the wire-grid antenna. The polarisation isolation for the Cassegrain antenna in Figure 5.10(b) is ≈ 38 dB, the Hannan Cassegrain antenna in Figure 5.15(b) is ≈ 31 dB, and the horn antenna in Figure 5.20(b) is ≈ 25 dB. These parabolic isolation results show that the Cassegrain antenna in Figure 5.10(b) will be challenging to jam compared to other antennas.

6.2.2 Monopulse ratio

The monopulse AOA equation uses the monopulse ratio to determine the AOA, making the monopulse ratio essential. The radiation patterns of the antenna are not used on their own to determine the target AOA; the difference signal is divided by the sum signal to determine the monopulse ratio. The co-polarisation monopulse ratios of the wire-grid antenna, parabolic reflector antenna, Cassegrain antenna, and Hannan Cassegrain antenna in the azimuth plane are shown in Figures 5.4(a), 5.4(c), 5.11(a), 5.16(a), and 5.21(a), respectively. In the elevation plane, they are shown in Figures 5.5(a), 5.5(c), 5.11(b), 5.16(b), and 5.21(b), respectively. In both the azimuth and elevation planes, the cross-polarisation monopulse ratio is distorted and has an interchanged direction; the positive side is now the negative side. The cross-polarisation monopulse ratio in the azimuth plane is shown in Figures 5.4(b), 5.4(d), 5.11(c), 5.16(c), and 5.21(c), respectively. In the elevation plane, they are shown in Figures 5.5(b), 5.5(d), 5.11(d), 5.16(d), and 5.21(d), respectively.

6.2.3 Polarisation purity

The polarisation purity is the ratio of co-polarisation to the cross-polarisation component. The higher the polarisation purity of the tracking radar, the higher the power the jammer will need to jam the tracking radar. The polarisation purity of the wire-grid antenna and the parabolic reflector is shown in Figure 5.3. The Cassegrain antenna, Hannan Cassegrain antenna, and Horn antenna are shown in Figures. 5.12, 5.17, and 5.22, respectively. The sum signal has a high polarisation purity in all the axes, while the difference signal has a high polarisation purity at the azimuth or elevation plane axis. The difference signals show low polarisation purity around $\pm 45^\circ$ and $\pm 135^\circ$ diagonal planes, which is useful in cross-polarisation jamming as the Condon lobes are at $\pm 45^\circ$ and $\pm 135^\circ$ diagonal planes.

6.3 RECEIVING MODE

6.3.1 Radiation Patterns

Most antenna results, such as the radiation patterns, monopulse ratio and polarisation purity, have been analysed in the three-dimensional (3-D) results in the transmitting mode. In the receiving mode, the focus will be on the $\phi = \pm 0^\circ$ azimuth plane, $\phi = \pm 45^\circ$ diagonal plane, and $\phi = \pm 90^\circ$ elevation plane, but more focus is on the $\phi = \pm 45^\circ$ plane as it is one of the planes where the Condon lobes are situated. The cross-polarisation pattern for the wire-grid antenna at $\phi = \pm 0^\circ$ and $\phi = \pm 90^\circ$ in Figures 5.6(a) and 5.6(e), respectively, are zero, which is expected because it was seen in the spherical 3-D results that it is null at the axis. However, for the Hannan parabolic reflector, the cross-polarisation patterns are similar to the cross-polarisation, with the difference being that they have ≈ 55 dB polarisation isolation as seen in Figures 5.6(b) and 5.6(f). The above-described patterns will not induce an error as they do not have Condon lobes.

The cross-polarisation pattern of the wire-grid antenna at $\phi = \pm 45^\circ$ has nulls at $\theta = \pm 0^\circ$ axis, and the Condon lobes off-axis and either one of the Condon lobes will be used as a tracking lobe. These peaks are shown in Figures 5.6(c) and 5.6(d). The Cassegrain antenna cross-polarisation patterns at $\phi = \pm 0^\circ$ and $\phi = \pm 90^\circ$ planes in Figures 5.13(a) and 5.13(e), respectively, are distorted and practically zero, while at $\phi = \pm 45^\circ$ plane in Figure 5.13(c), the sum signal has a null at the axis. This explanation also applies to the Hannan Cassegrain antenna cross-polarisation patterns at $\phi = \pm 0^\circ$, $\phi = \pm 45^\circ$, and $\phi = \pm 90^\circ$ in Figures 5.18(a), 5.18(c), and 5.18(e), respectively. This also applies to the horn antenna. However, the horn antenna cross-polarisation patterns at $\phi = \pm 0^\circ$ and $\phi = \pm 90^\circ$ are similar to the co-polarisation sum and difference patterns, with the difference being that they are isolated from each other by ≈ 70 dB, which is the same as in the parabolic reflector. However, the cross-polarisation signal at the $\phi = \pm 45^\circ$ plane has a null like other antennas.

6.3.2 Monopulse ratio

The wire-grid antenna and parabolic reflector antenna monopulse ratio are shown in Figure 5.7. The co-polarisation monopulse ratio at $\phi = \pm 0^\circ$, $\phi = \pm 45^\circ$, and $\phi = \pm 90^\circ$ are facing the same direction and have the same pattern while the cross-polarisation at $\phi = \pm 0^\circ$ and $\phi = \pm 90^\circ$ planes for the wire-grid antenna are practically zero and for the parabolic reflector is the inverse of the co-polarisation monopulse ratio. At $\phi = \pm 45^\circ$, the cross-polarisation is the inverse of the co-polarisation, but it has a different shape, which will result in an induced angular error. The monopulse ratio of the Cassegrain antenna is shown in Figures 5.13, the cross-polarisation monopulse ratio at $\phi = \pm 0^\circ$ and $\phi = \pm 90^\circ$

are practically zero while at $\phi = \pm 45°$, it is useful. The explanations apply to the Hannan Cassegrain antenna monopulse ratio in Figure 5.18 and to the horn antenna monopulse ratio in Figure 5.23.

6.3.3 The induced angular error

The induced angular error in the wire-grid antenna in Figure 5.8(c) is higher than that of the parabolic reflector in Figure 5.8(d); this is expected because the parabolic reflector has higher polarisation purity than the wire-grid antenna. The induced angular error at $\phi = \pm 0°$ and $\phi = \pm 90°$ are practically zero, as shown in Figures 5.8(a) and 5.8(f). The polarisation purity of the Cassegrain antenna is shown in Figure 5.12; the radar polarisation purity is higher than that of the wire-grid antenna and the parabolic reflector antenna, and the induced angular error in the Cassegrain antenna at $\phi = \pm 45°$ is shown in Figure 5.14(e) which is smaller than that of the wire-grid antenna and the parabolic reflector because it has higher polarisation purity. For the Hannan Cassegrain antenna, the polarisation purity is in Figure 5.17, and its induced angular error at $\phi = \pm 45°$ is shown in Figure 5.19(e); this angular error is supposed to be smaller than that of the Cassegrain antenna because its radar polarisation purity is higher than the above-described antennas. The horn antenna angular error at $\phi = \pm 45°$ is shown in Figure 5.24(e); the results show that the jammer reaches break-lock when JSR > 0 dB.

6.3.4 polarisation accuracy

To investigate how the jammer polarisation accuracy affects the jamming success, the jamming signal was investigated with cross-polarisation angles that are 1°, 3°, and 5° off from the accurate polarisation angle; it is seen in Figure 5.9(a) for the wire-grid antenna. The cross-polarisation monopulse ratio is destroyed, and it is changing its shape to the shape of the co-polarisation monopulse ratio; the induced angular errors for the three angle off-sets are shown in Figure 5.9(c); it is understandable because the monopulse ratio is taking the shape of a co-polarisation monopulse ratio, meaning the induced angular error will decrease. The same applies to the Hannan parabolic reflector in Figures 5.9(b) and 5.9(d). The polarisation accuracy is also shown in Figures 5.9(e) and 5.9(f), these show that the induced angular error decreases as the jammer polarisation accuracy decreases. These apply to the Cassegrain, Hannan Cassegrain, and horn antenna.

6.3.5 Measurement results

The polarisation isolation in the azimuth and elevation planes is ≈ 30 dB. In the FEKO Simulations, the isolation is ≈ 100 dB, which is understandable as the anechoic chamber is not the same as the simulation software, and these results might change further when the antenna is operating in a practical environment. In the diagonal plane, the polarisation isolation is ≈ 25 dB in both the simulated and measured results. Depending on the tracking angular error magnitude that the jammer wants to induce

into the tracking radar, theoretically, the jammer will need at least 25 dB jamming signal power to jam the tracking radar. The simulation results show that the jammer reaches a break-lock between JSR of 30 dB to 40 dB, depending on the antenna. The measured polarisation accuracy has the same shape/trend as the simulated polarisation accuracy, as seen in Figures 5.9(e) and 5.40(c). The induced angular error decreases by $\approx 80\%$ when cross-polarisation angle is off by $\approx 5^{\circ}$.

6.4 CROSS-POLARISATION PATTERN MODELING

To perform cross-polarisation jamming in simulations, there must be a way to model the cross-polarisation patterns. This work uses these methods to model the cross-polarisation patterns; the methods represent phase comparison monopulse antenna. The simulation results of the three modelling methods correspond to the patterns seen in the six antennas. The radiation patterns of the methods and the cross-polarisation jamming angular error simulated show the same trend seen in the analysed antennas. The angular error analysis shows three stages: the first stage is where the increased jamming power does not induce angular error in the tracking radar; the second stage is when the jamming signal is inducing angular error, but the tracking radar is still dominant because JSR < 0 dB, stage three happens after JSR > 0 but between JSR of 15 - 40 dB. Stage three is the break-lock stage.

6.5 COMPARISON

The co-and cross-polarisation radiation patterns of the Feko simulated antennas are similar to the theoretical and measurement results. They have peaks at boresight for the co-polarisation sum channel and approximately zero patterns for the cross-polarisation sum channel at azimuth and elevation plane. However, they all have Condon lobes in the diagonal planes off-boresight. The angular error caused by the increasing JSR of the cross-polarisation jamming shows a similar trend in both the simulations and the theoretical results. However, the theoretical results show jamming break lock when JSR > 15 dB, while the Feko simulation results show jamming break lock when JSR > 30 dB. The polarisation accuracy analysis from the measurement shows a similar trend to the analysis in Feko simulations. The jammer must be within 0° to 1° in accuracy to be effective against the antennas analysed in this work.

6.6 CHAPTER SUMMARY

When the jammer breaks lock, the radar is forced to use one of the Condon lobes as the peak tracking lobe, which results in a wrong target AOA. Condon lobes are located in the diagonal planes of the monopulse antennas, having axial symmetry in both azimuth and elevation axes. Cross-polarisation jammer must have JSR > 15 dB to 40 dB for successful jamming, and it is highly sensitive to polarisation. Therefore, it needs to have high polarisation accuracy (within 0 to 1° in accuracy). The

cross-polarisation jammer induces higher angular error in antennas with lower polarisation purity and lower angular error in antennas with higher polarisation purity.

CHAPTER 7 CONCLUSION

From the analysis of the six monopulse antennas, it was confirmed that the co-polarisation patterns are 20 dB to 40 dB higher than the cross-polarisation patterns [19], [24], and the diagonal planes show polarisation isolation of around 25 dB. Even though it is said that the cross-polarisation jammer will need 20 dB to 40 dB to induce angular error into the tracking radar [24], the analysis in this work shows that the cross-polarisation jammer induces angular error into the tracking radar even when the JSR < 0 dB.

It is reported in the literature that the JSR must be greater than the radar polarisation purity for the jammer to be effective against the tracking radar [23]. The minimum JSR needed to induce angular error was analysed, and it is seen that the minimum JSR depends on the magnitude of the angular error the jammer wants to induce into the tracking radar. The main point about the minimum JSR is that in this analysis, the jammer induces angular error even when the JSR < 0 dB. Inducing angular error leads to break-lock, which is the goal of the cross-polarisation jammer. The break-lock stage is achieved after JSR > 0 dB, but to be more specific, it is achieved when JSR is > 30 dB to 40 dB, depending on the radar antenna being jammed; this supports the statement that the JSR must be greater than the radar polarisation purity for the jammer to be effective against the tracking radar [23].

The polarisation accuracy of the cross-polarisation jammer must be $\pm 5^{\circ}$ [11], [24], [19]. Cross-polarisation jamming shows high polarisation sensitivity, which depends on the antenna being jammed. In this work, it was found that if the antenna being jammed is the Hannan parabolic reflector and the jammer is off by $\pm 2^{\circ}$, the jammer is useless, while for the wire-grid antenna, the jammer will be useless if it is off by $\pm 2^{\circ}$ to 5°; this is because the Hannan parabolic reflector has high polarisation purity, which means the jammer must have higher polarisation accuracy than it needs when jamming radar antennas with less polarisation purity. Therefore, the jammer will be useless if it has a high

JSR but has polarisation inaccuracies. The measurement results show that if the cross-polarisation angle is off by $\approx 5°$, the induced angular error is reduced by $\approx 80\%$, which is a significantly high loss; therefore, the jammer must be within 0 to $1°$ in accuracy.

The induced angular error decreases as the AOA moves away from the boresight towards the 3 dB beam-width edge and outside it. The cross-polarisation jammer has jamming potential if it accurately detects and re-transmits the signal components in their accurate polarisation angles. Three mathematical models to represent the cross-polarisation patterns are presented, which generate the type of monopulse ratio seen in the simulated antennas. These models are used to model cross-polarisation jamming.

7.1 FUTURE WORK

In the measurements results, only the radiation patterns were taken. Co-polarisation patterns were as expected in these patterns. However, the cross-polarization patterns did not have well-defined Condon lobes because of the high sensitivity in measuring cross-polarisation patterns. This sensitivity is seen in the simulation results, which show that the cross-polarisation jammer polarisation inaccuracy results in degraded monopulse ratios. Experiments need to be done where jamming antennas jam the tracking antenna in an anechoic chamber set-up specifically for high cross-polarisation measurement accuracy. The same jammer will need to have the ability to increase the JSR because, in the presented work, constant power is used, which is why the relationship between the angular error and JSR is only performed theoretically and in Feko EM simulation software. Not all antennas have peak Condon lobes at the diagonal planes, and this work must be extended to those antennas.

Another approach is to analyse the effects of cross-polarisation jamming on the monopulse radar's tracking accuracy when used with range gate pull-off and velocity gate pull-off jamming techniques.

REFERENCES

[1] S. M. Sherman and D. K. Barton, *Monopulse Principles and Techniques*, 2nd ed. Boston, London: Artech House, 2011.

[2] (Nov, 2000) Electronic warfare fundamentals. [Online]. Available: https://falcon.blu3wolf.com/Docs/Electronic-Warfare-Fundamentals.pdf

[3] M. I. Skolnik, *Radar Handbook*, 2nd ed. New York: McGraw-Hill, 1990.

[4] A. I. Leonov and K. I. Fominchev, *Monopulse Radar*. United States of America: Foreign Technology Division, 1970.

[5] Z. Yu, G. Wang, and C. Zhang, "A broadband planar monopulse antenna array of C-band," *IEEE Antennas and Wireless Propagation Letters*, vol. 8, pp. 1325–1328, Dec. 2009.

[6] J. B. Hoffman, B. L. Galebach, and K. R. Johnson, "Four-channel monopulse for main beam nulling and tracking," in *IEEE National Radar Conference*, Syracuse, NY, USA, May 1997, pp. 94–98.

[7] P. Zheng, G. Q. Zhao, S. H. Xu, F. Yang, and H. J. Sun, "Design of a W-band full-polarization monopulse Cassegrain antenna," *IEEE Antennas and Wireless Propagation Letters*, vol. 16, pp. 99–103, Apr 2017.

[8] X. LI and Q. Zhang, "Alternate orthogonally polarization jamming on ASLC system," *Applied Mechanics and Materials*, vol. 385–386, pp. 1449–1452, Aug. 2013.

[9] D. Adamy, *EW 104: EW against a New Generation of Threats*. Boston, USA: Artech House, 2015.

[10] D. Adamy, *EW 101 - A First Course in Electronic Warfare*. Boston, USA: Artech House, 2001.

[11] F. Neri, *Introduction to Electronic Defense Systems*, 3rd ed. Boston, London: Artech House, 2018.

[12] A. De Martino, *Introduction to Modern EW Systems*, 2nd ed. Boston, MA: Artech House, 2018.

[13] I. Kalinbacak, M. Pehlivan, and K. Yegin, "Cross polarization monopulse jammer located on UAV," in *International Conference on Recent Advances in Space Technologies, RAST*, Istanbul, Turkey, Aug. 2017, pp. 337–341.

[14] F. Neri, "Anti-monopulse jamming techniques," in *SBMO/IEEE MTT-S International Microwave and Optoelectronics Conference Proceedings*, Belem, Brazil, Aug. 2001, pp. 43–50.

[15] A. Golden, *Radar Electronic Warfare*. Washington, DC: American Institute of Aeronautics and Astronautics, 1987.

[16] D. Bodnar, "Cross-polarized characteristics of monopulse difference patterns," in *Antennas and Propagation Society International Symposium*, Syracuse, NY, USA, 2–6 Jun. 1980, pp. 477–480.

[17] S. Ghobrial, "Co-polar and cross-polar diffraction images in the focal plane of paraboloidal reflectors: A comparison between linear and circular polarization," *IEEE Transactions on Antennas and Propagation*, vol. 24, no. 4, pp. 418–424, Jul. 1976.

[18] E. Jones, "Paraboloid reflector and hyperboloid lens antennas," *Transactions of the IRE Professional Group on Antennas and Propagation*, vol. 2, no. 3, pp. 119–127, Jul. 1954.

[19] E. J. Chrzanowski, *Active Radar Electronic Countermeasures*. Norwood, MA: Artech House, 1990.

[20] D. R. Rhodes, *Introduction to monopulse*. Artech House: Artech House, 1980.

[21] W. P. du Plessis, "Modelling monopulse antenna patterns," in *Saudi International Electronics, Communications and Photonics Conference*, Riyadh, Saudi Arabia, Apr. 2013, pp. 1–5.

[22] L. B. Van Brunt, *Applied ECM*. Dunn Loring, USA: EW Engineering, Inc., 1978, vol. 1.

[23] R. N. Lothes, M. B. Szymanski, and R. G. Wiley, *Radar Vulnerability to Jamming*. Norwood, MA: Artech House, 1990.

[24] D. C. Schleher, *Introduction to Electronic Warfare*. Norwood, MA: Artech House, 1986.

[25] ——, *Electronic Warfare in the Information Age*. Norwood, MA: Artech House, 1999.

[26] S. Ghobrial, "Axial cross polarization in reflector antennas with surface imperfection," *IEEE Transactions on Antennas and Propagation*, vol. 28, no. 5, pp. 610–616, Sep. 1980.

[27] R. Lehmensiek and D. I. L. de Villiers, "On reflector feeds with unidirectional axially symmetric radiation patterns: Their cross-polarization performance and efficiencies," *IEEE Antennas and Propagation Magazine*, vol. 56, no. 1, pp. 39–61, Feb. 2014.

[28] R. Conti, J. Toth, T. Dowling, and J. Weiss, "The wire grid microstrip antenna," *IEEE Transactions on Antennas and Propagation*, vol. 29, no. 1, pp. 157–166, Jan. 1981.

[29] A. C. Ludwig, "The definition of cross polarization," *IEEE Transactions on Antennas and Propagation*, vol. 21, pp. 116 – 119, Jan. 1973.

[30] H. Han, X. Xu, H. Wang, and H. Dai, "Analysis of cross-polarization jamming for phase comparison monopulse radars," in *IEEE 2nd International Conference on Electronic Information and Communication Technology, ICEICT*, Harbin, China, Jan. 2019, pp. 404–407.

[31] H. Dai *et al.*, "Cross polarization jamming and ecm performance of polarimetric fusion monopulse radars," in *The 10th International Conference on Computer Engineering and Networks*, vol. 1274.

Singapore: Springer, Oct. 2020, pp. 612–622.

[32] W. L. Stutzman, *Polarization in Electromagnetic Systems*, 2nd ed. Norwood, MA: Artech House, Feb. 2018.

[33] W. P. du Plessis and K. Mosoma, "Initial results for cross-polarisation jamming of monopulse radar," in *International Conference on Electromagnetics in Advanced Applications (ICEAA)*, Cape Town, South Africa, 5–9 Sep. 2022, pp. 258–263.

[34] P. Hannan, "Optimum feeds for all three modes of a monopulse antenna II: Practice," *IRE Transactions on Antennas and Propagation*, vol. 9, no. 5, pp. 454–461, Sep. 1961.

[35] K. Mosoma, "Monopulse antenna," University of Pretoria, Pretoria, South Africa, Final year Report 1, Nov. 2020.

[36] W. L. Stutzman and G. A. Thiele, *Antenna Theory and Design*, 3rd ed. Hoboken, NJ: Wilery, 2013.

[37] M. S. Neiman, "The principle of reciprocity in antenna theory," in *Proceedings of the IRE.*, Dec. 1943, pp. 666–671.

APPENDIX A DERIVATION OF HIGHER ORDER MODELS

A.1 THE DEFINITION OF CROSS POLARISATION

A brief cross-polarisation definition was introduced in Section 2.7. In this section, the cross-polarisation definition will be derived in more detail. The radiation patterns shown in Figure 2.10 are used to define the three polarisation definitions [29], and unit vectors $\hat{i}_{ref}$ and $\hat{i}_{cross}$ are used as follows [29]

$$E\cdot\hat{\boldsymbol{i}}_{ref} \equiv \text{the reference polarisation component of E} \tag{A.1}$$

$$E\cdot\hat{\boldsymbol{i}}_{cross} \equiv \text{the cross polarisation component of E.} \tag{A.2}$$

The polarisation definition 1 is as follows

$$\hat{\boldsymbol{i}}^{(1)}_{ref} = \hat{\boldsymbol{y}} \tag{A.3}$$

$$\equiv \sin(\theta)\sin(\theta)\hat{\boldsymbol{i}}_r + \cos(\theta)\sin(\phi)\hat{\boldsymbol{i}}_\theta + \cos(\phi)\hat{\boldsymbol{i}}_\phi \tag{A.4}$$

$$\hat{\boldsymbol{i}}^{(1)}_{cross} = \hat{\boldsymbol{x}} \tag{A.5}$$

$$\equiv \sin(\theta)\sin(\theta)\hat{\boldsymbol{i}}_r + \cos(\theta)\sin(\phi)\hat{\boldsymbol{i}}_\theta - \cos(\phi)\hat{\boldsymbol{i}}_\phi. \tag{A.6}$$

Definition 1 describes the two-plane coordinate system polarisation, i.e., if reference polarisation is across the y-axis, then the cross-polarisation is in the x-axis. In Figure 2.10, definition 2 is described using the rectangular and spherical coordinates as [29]

$$\hat{\boldsymbol{x}} = x \quad \hat{\boldsymbol{y}} = y \quad \hat{\boldsymbol{z}} = -y, \tag{A.7}$$

resulting in definition 2 as

$$\hat{\boldsymbol{i}}_{ref}^{(2)} \equiv \hat{\boldsymbol{i}}_{\theta} \tag{A.8}$$

$$= \frac{-\sin(\theta)^2\sin(\phi)\cos(\phi)\hat{\boldsymbol{i}}_x + (1-\sin(\theta)^2\sin(\phi)^2)\hat{\boldsymbol{i}}_y - \sin(\theta)\cos(\theta)\sin(\phi)\hat{\boldsymbol{i}}_z}{\{1-\sin(\theta)^2\sin(\phi)^2\}^{1/2}} \tag{A.9}$$

$$= \frac{\sin(\phi)\cos(\theta)\hat{\boldsymbol{i}}_{\theta} + \cos(\phi)\hat{\boldsymbol{i}}_{\phi}}{\{1-\sin(\theta)^2\sin(\phi)^2\}^{1/2}} \tag{A.10}$$

$$\hat{\boldsymbol{i}}_{cross}^{(2)} \equiv -\hat{\boldsymbol{i}}_{\phi} \tag{A.11}$$

$$= \frac{\cos(\theta)\hat{\boldsymbol{i}}_x - \sin(\theta)\cos(\phi)\hat{\boldsymbol{i}}_z}{\{1-\sin(\theta)^2\sin(\phi)^2\}^{1/2}} \tag{A.12}$$

$$= \frac{\cos(\phi)\hat{\boldsymbol{i}}_{\theta} - \cos(\theta)\sin(\phi)\hat{\boldsymbol{i}}_{\phi}}{\{1-\sin(\theta)^2\sin(\phi)^2\}^{1/2}}. \tag{A.13}$$

To explain definition 3, the practical antenna pattern measurement procedure must be understood. Assuming that the AUT is positioned in such a way that the XZ plane is horizontal and is represented by $\phi = 0^{\circ}$ and the YZ plane is vertical and is represented by $\phi = 90^{\circ}$, and all other ϕ planes are in between two planes; the θ measurement is scanned in the Z-direction with respect to the ϕ plane; this is a commonly used way of measuring antennas [29]. Definition 3 is represented as follows [29]

$$R_{eff}(\theta,\phi) = E(\theta,\phi)\cdot\{\sin(\phi)\hat{\boldsymbol{i}}_{\theta} + \cos(\phi)\hat{\boldsymbol{i}}_{\phi}\} \tag{A.14}$$

$$C_{ross}(\theta,\phi) = E(\theta,\phi)\cdot\{\cos(\phi)\hat{\boldsymbol{i}}_{\theta} - \sin(\phi)\hat{\boldsymbol{i}}_{\phi}\}, \tag{A.15}$$

where $E(\theta,\phi)$ is the radiation pattern from the transmitting antenna. This is equivalent to [29]

$$\hat{\boldsymbol{i}}_{reff}^{(3)} \equiv \{\sin(\phi)\hat{\boldsymbol{i}}_{\theta} + \cos(\phi)\hat{\boldsymbol{i}}_{\phi}\} \tag{A.16}$$

$$= -\{1-\cos(\theta)\}\sin(\phi)\cos(\phi)\hat{\boldsymbol{i}}_x + \left[1-\sin(\phi)^2\{1-\cos(\theta)\}\right]\hat{\boldsymbol{i}}_y - \sin(\theta)\sin(\phi)\hat{\boldsymbol{i}}_z \tag{A.17}$$

$$\hat{\boldsymbol{i}}_{cross}^{(3)} \equiv \{\cos(\phi)\hat{\boldsymbol{i}}_{\theta} - \sin(\phi)\hat{\boldsymbol{i}}_{\phi}\} \tag{A.18}$$

$$= \left[1-\cos(\phi)^2\{1-\cos(\theta)\}\right]\hat{\boldsymbol{i}}_x - \{1-\cos(\theta)\}\sin(\phi)\cos(\phi)\hat{\boldsymbol{i}}_y - \sin(\theta)\cos(\phi)\hat{\boldsymbol{i}}_z. \tag{A.19}$$

APPENDIX B ADDITIONAL MEASUREMENTS OF THE WIRE-GRID ANTENNA

The radiation patterns in the azimuth and elevation planes shown in Figures B.1 and B.2, show the sum patterns having SLL ≈ 16 dB and ≈ 19 dB in the diagonal plane in Figure B.3. The polarisation isolation in the azimuth and elevation plane is ≈ 30 dB, and at the diagonal plane is ≈ 25 dB. The monopulse ratio in the azimuth and elevation plane is shown in Figures B.4 and B.5, respectively, and they are as expected. The co-polarisation monopulse ratios are as expected, while the cross-polarisation monopulse ratios are distorted. The monopulse ratios at the diagonal planes are shown in Figures B.6 and B.8 for anechoic chambers A and B, respectively. The cross-polarisation monopulse ratios do not always cross the co-polarisation monopulse ratio at boresight angle $\theta = 0°$. This deviation from the axis is due to the antenna not being aligned 100% correctly to the azimuth, elevation or diagonal plane. If the antenna is off by as little as 0.5°, the antenna will show a little squint. This is shown in Figure B.3 when the difference patterns null is not precisely at boresight angle $\theta = 0°$. These results show that cross-polarisation measurements have high sensitivity.

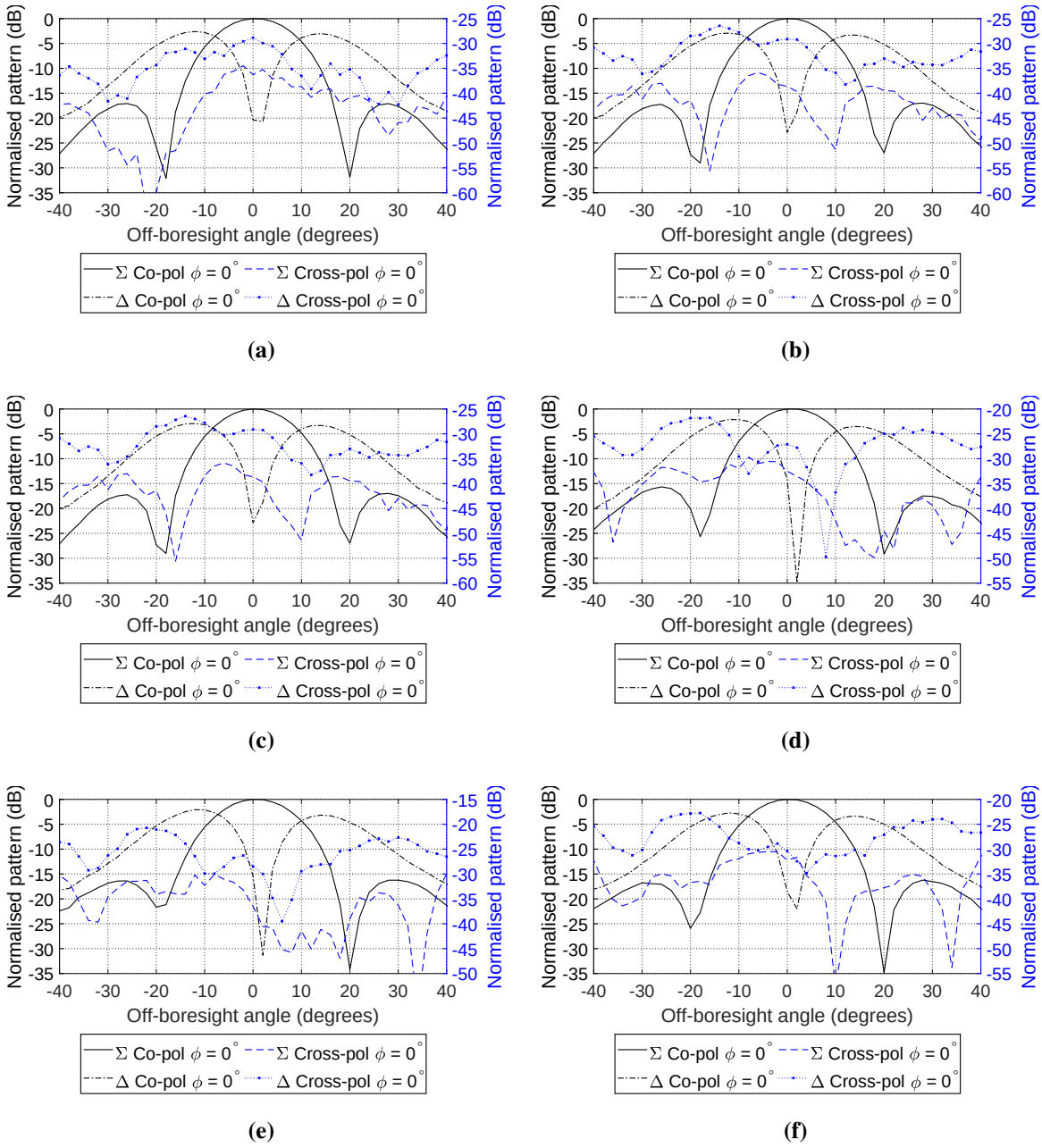

Figure B.1. The azimuth plane radiation patterns measured in the anechoic chamber A at (a) 5.67 GHz, (b) 5.68 GHz, (c) 5.69 GHz, (d) 5.70 GHz, (e) 5.71 GHz, and (f) 5.72 GHz frequencies.

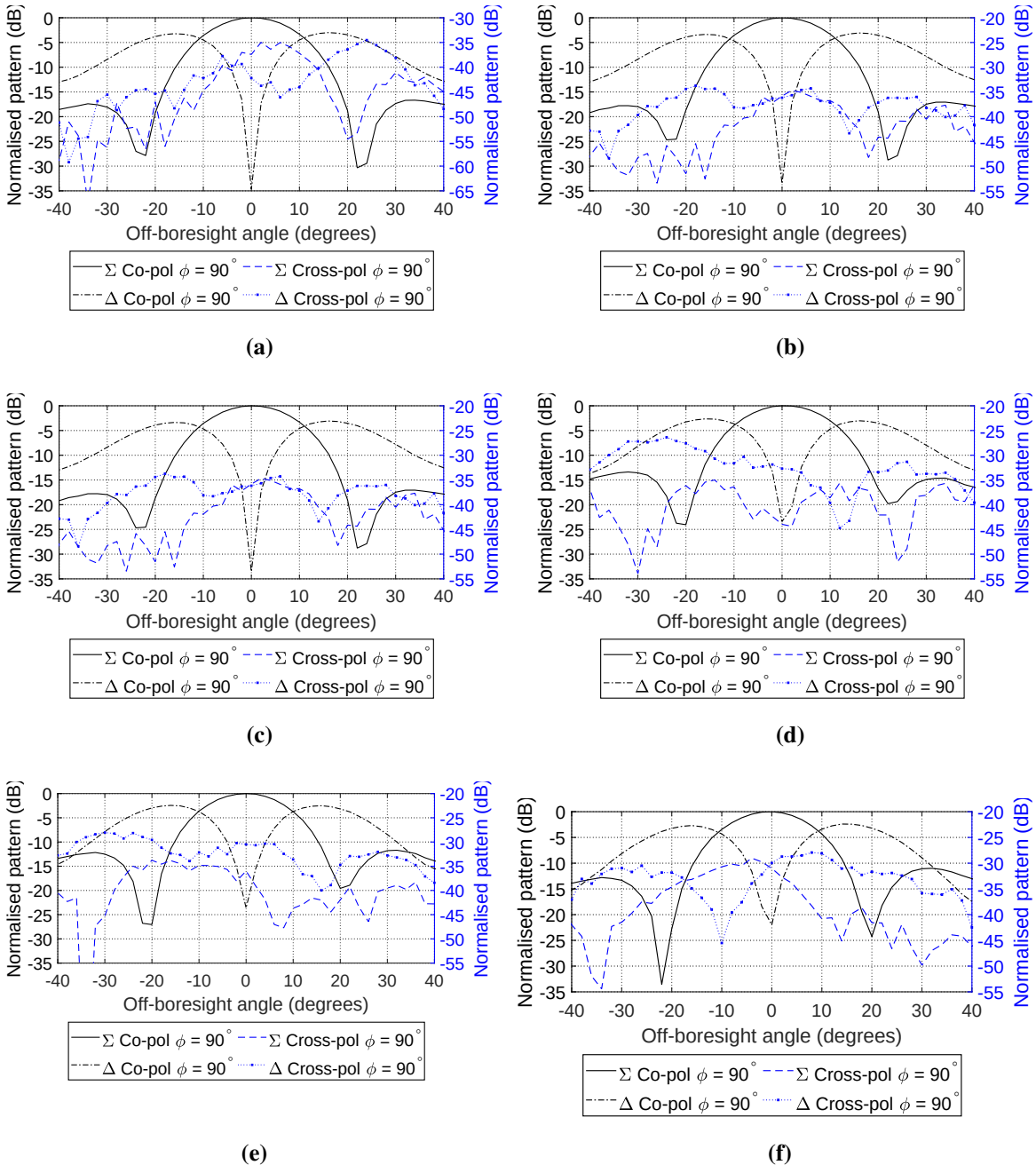

Figure B.2. The elevation plane radiation patterns measured in the anechoic chamber A at (a) 5.67 GHz, (b) 5.68 GHz, (c) 5.69 GHz, (d) 5.70 GHz, (e) 5.71 GHz, and (f) 5.72 GHz frequencies.

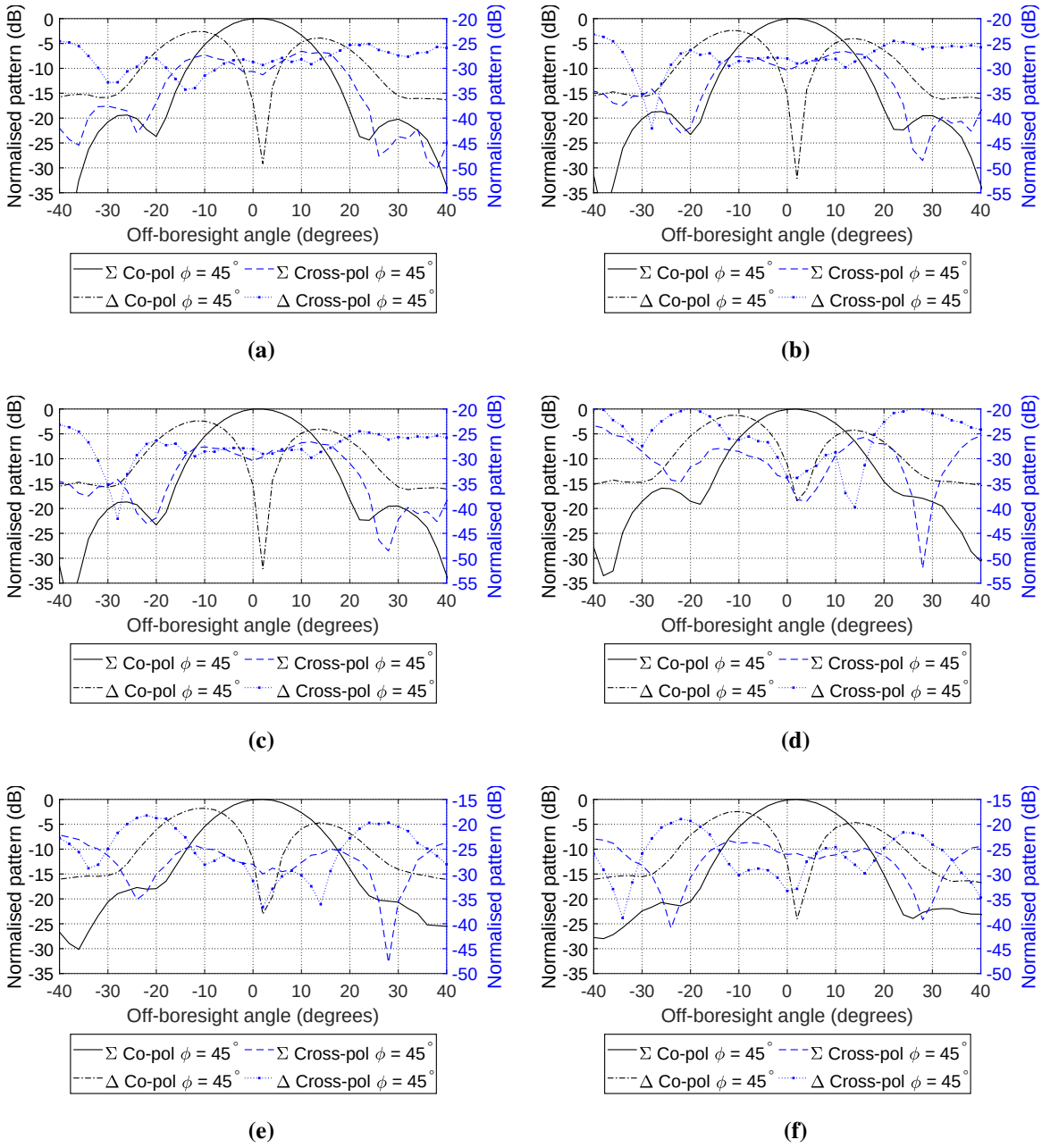

Figure B.3. The diagonal plane radiation patterns measured in the anechoic chamber A at (a) 5.67 GHz, (b) 5.68 GHz, (c) 5.69 GHz, (d) 5.70 GHz, (e) 5.71 GHz, and (f) 5.72 GHz frequencies.

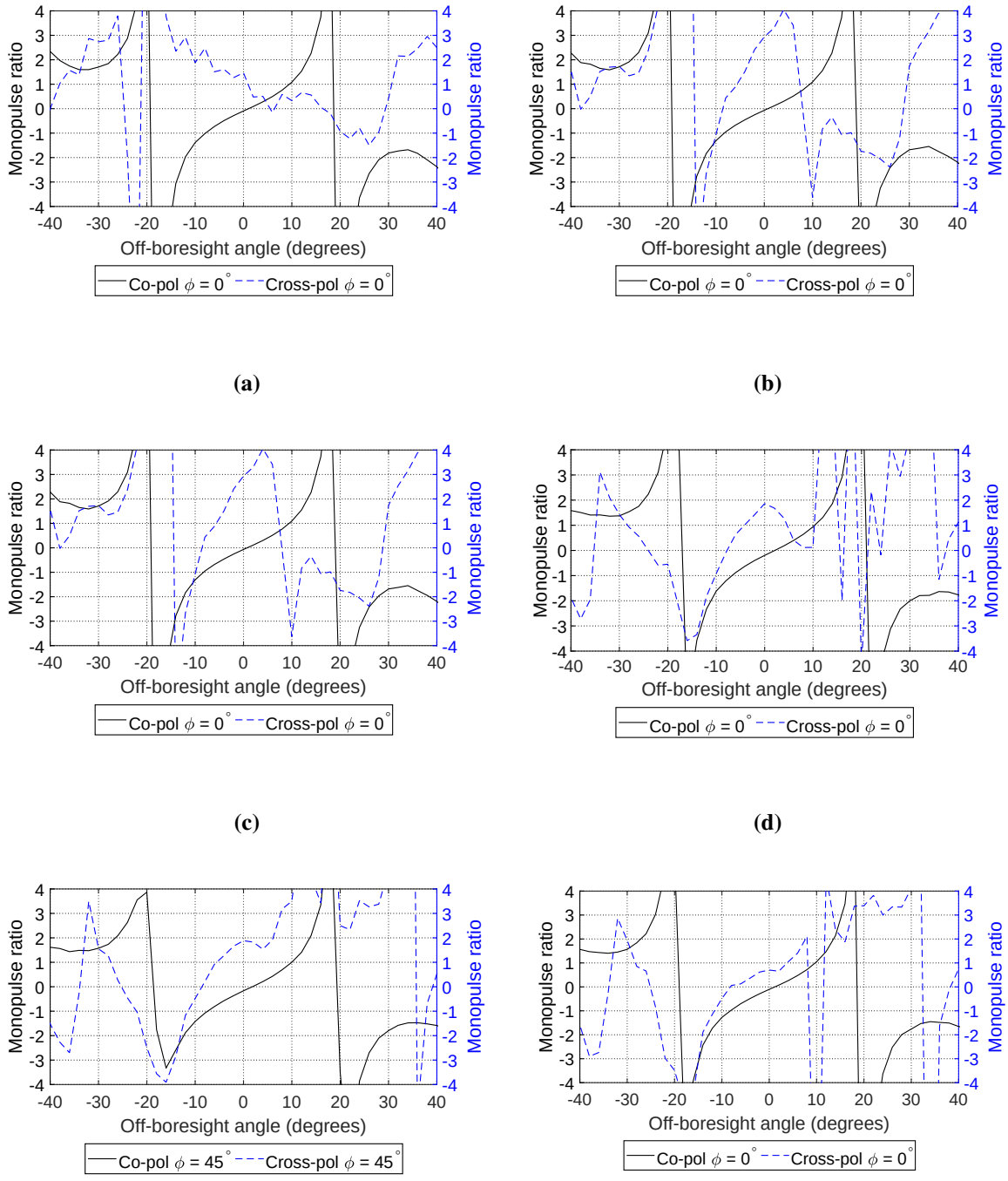

Figure B.4. The azimuth plane imaginary monopulse ratios calculated from measurements in the anechoic chamber A at (a) 5.67 GHz, (b) 5.68 GHz, (c) 5.69 GHz, (d) 5.70 GHz, (e) 5.71 GHz, and (f) 5.72 GHz frequencies.

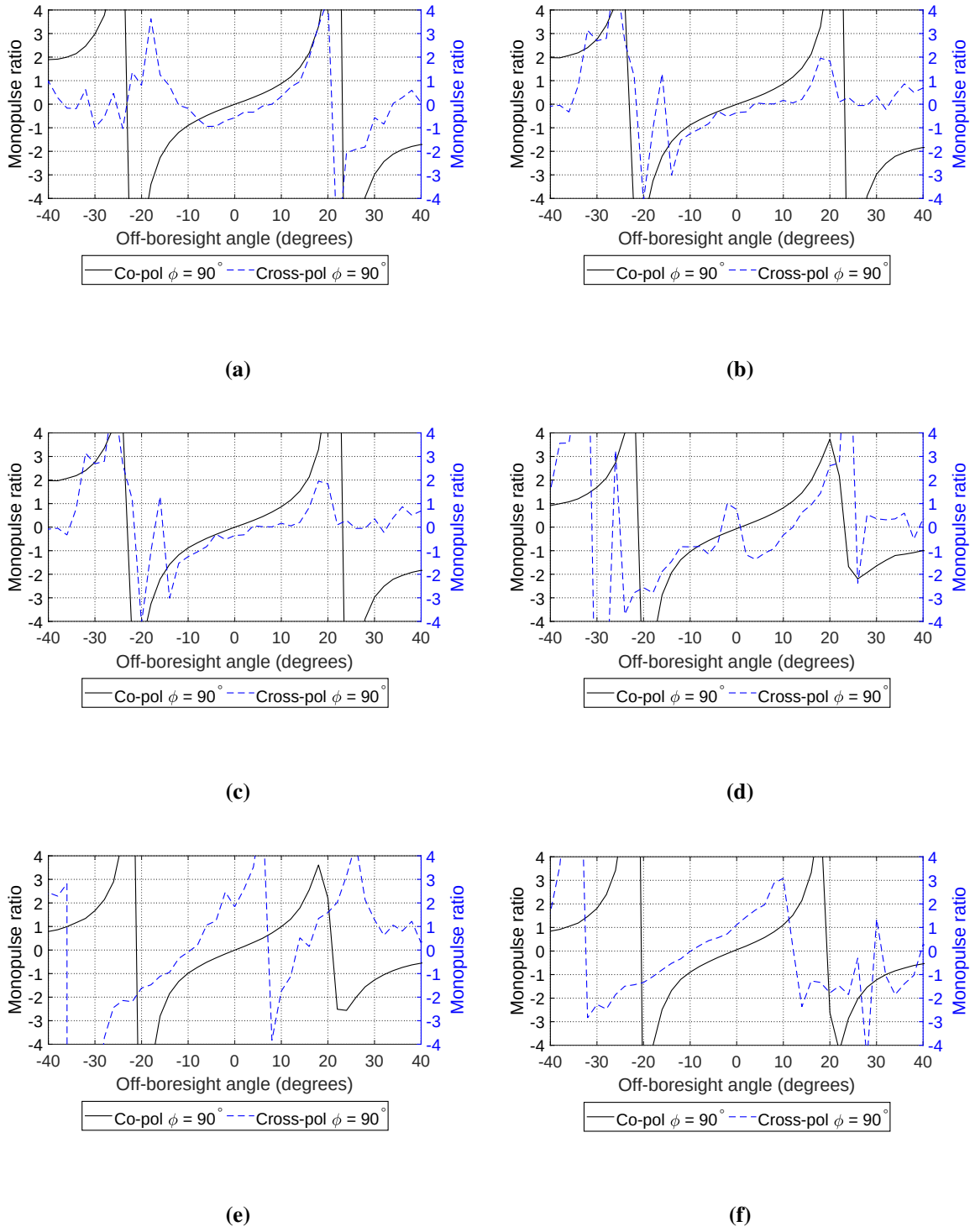

Figure B.5. The elevation plane imaginary monopulse ratios calculated from measurements in the anechoic chamber A at (a) 5.67 GHz, (b) 5.68 GHz, (c) 5.69 GHz, (d) 5.70 GHz, (e) 5.71 GHz, and (f) 5.72 GHz frequencies.

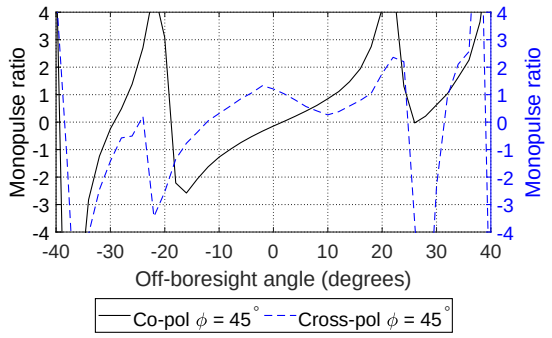

(a)

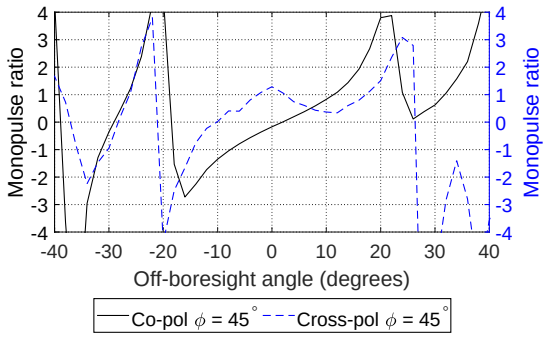

(b)

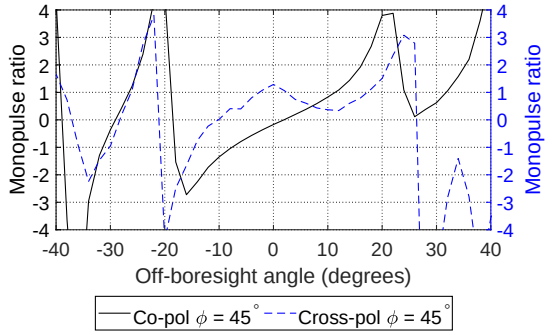

(c)

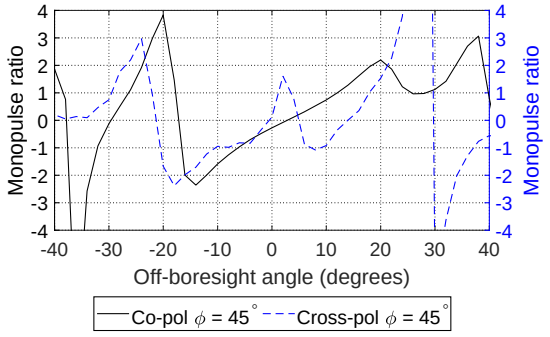

(d)

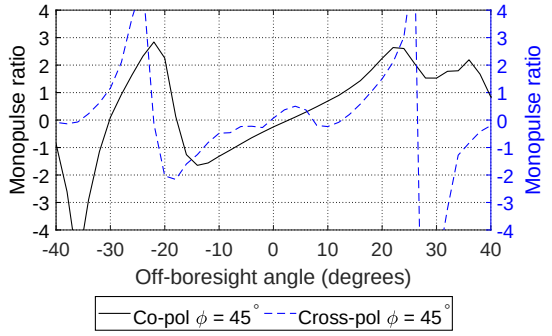

(e)

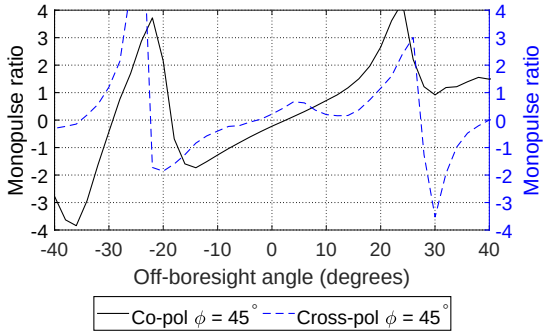

(f)

Figure B.6. The azimuth plane imaginary monopulse ratios calculated from measurements in the anechoic chamber A at (a) 5.67 GHz, (b) 5.68 GHz, (c) 5.69 GHz, (d) 5.70 GHz, (e) 5.71 GHz, and (f) 5.72 GHz frequencies.

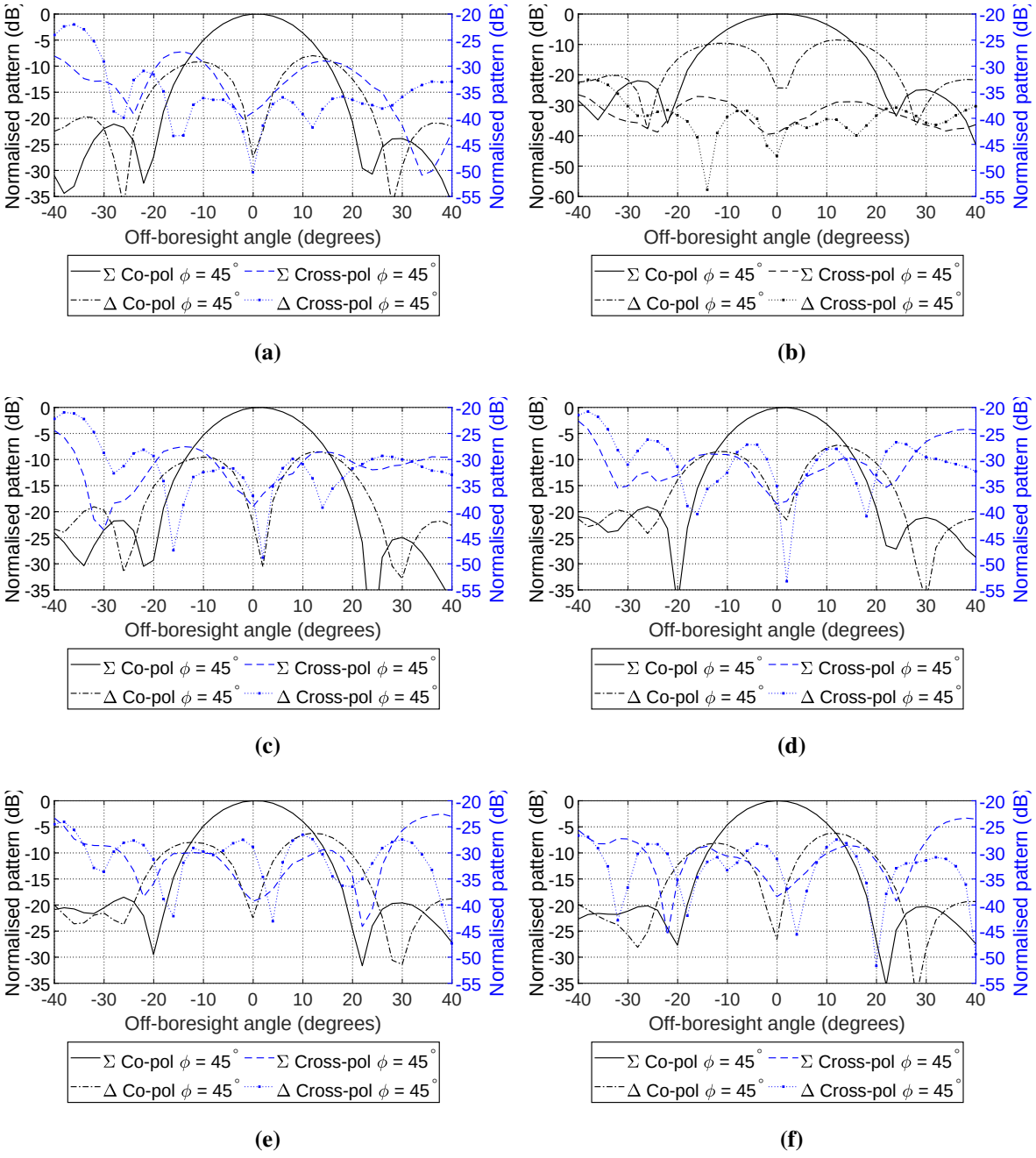

Figure B.7. The diagonal plane radiation patterns measured in the anechoic chamber B at (a) 5.67 GHz, (b) 5.68 GHz, (c) 5.69 GHz, (d) 5.70 GHz, (e) 5.71 GHz, and (f) 5.72 GHz frequencies.

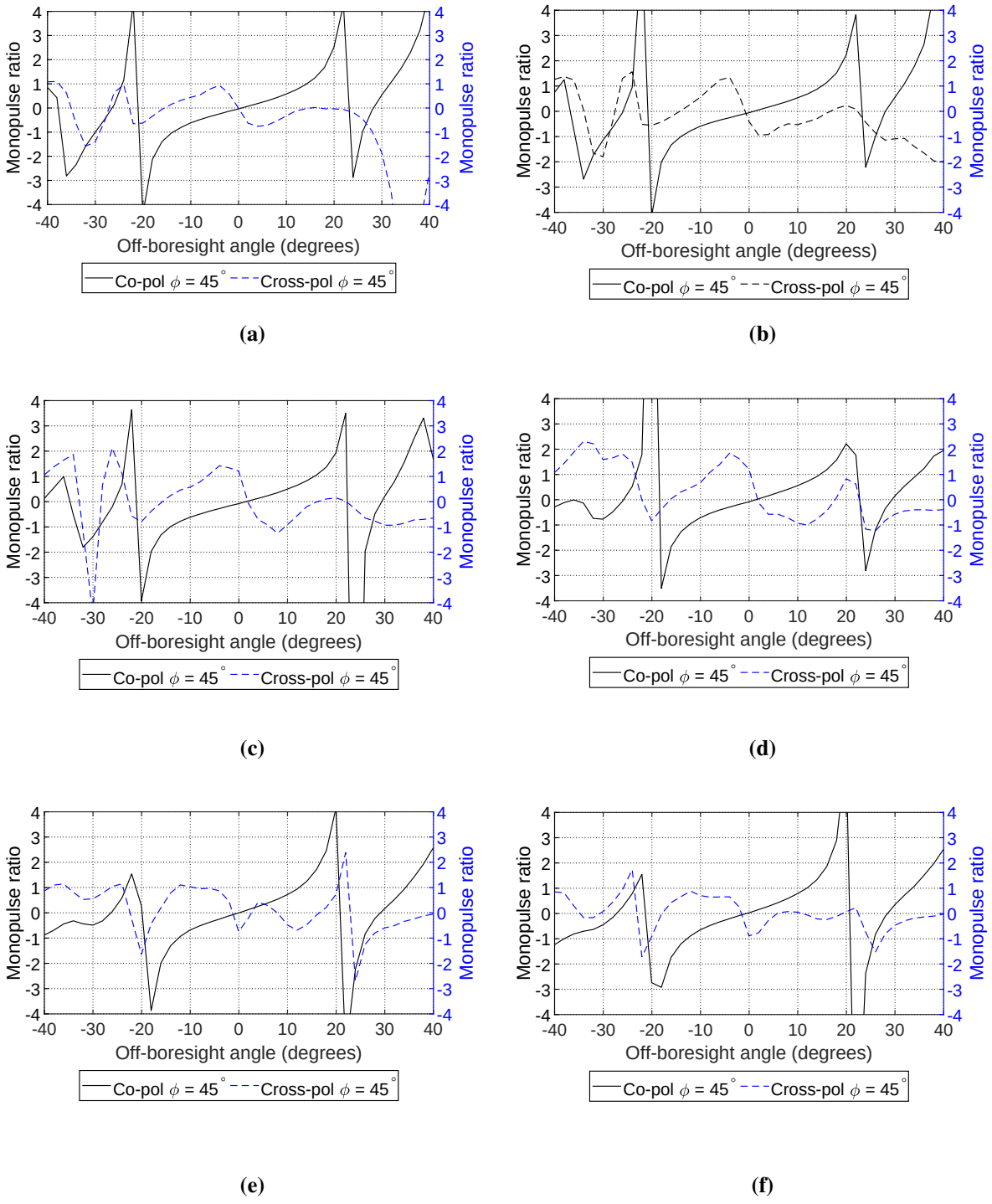

Figure B.8. The diagonal plane imaginary monopulse ratios calculated from measurements in the anechoic chamber B at (a) 5.67 GHz, (b) 5.68 GHz, (c) 5.69 GHz, (d) 5.70 GHz, (e) 5.71 GHz, and (f) 5.72 GHz frequencies.